DYNAMIC ANALYSIS OF FAST-ACTING SOLENOID ACTUATORS

A DISSERTATION SUBMITTED TO

THE DEPARTMENT OF ELECTRONICS AND ELECTRICAL ENGINEERING

OF

THE UNIVERSITY OF GLASGOW

FOR THE DEGREE OF

DOCTOR OF PHILOSOPHY

By

Marielle Piron

March 1999

To Duncan and my family

Abstract

There has been a recent revival of interest in the design of fast-acting solenoid actuators. This is due to the emergence of new control applications in the automotive industry constrained by tighter emission and noise regulations. In the context of developing a rapid computer-aided design tool for such applications, the thesis proposes several methods for computing the static and dynamic electromagnetic performance of solenoid actuators with a particular attention given to two actuator types : an axisymmetric and a rectangular solenoid actuator with a flat-faced armature.

The magnetostatic performance of both actuator types is first evaluated by developing a detailed magnetic equivalent circuit in which the actuator geometry, saturation and end-effects are all taken into account. A comparison of the analytical model, based on the computation of the magnetisation characteristics and static forces for several airgap lengths, is given with finite-elements and measurements.

In order to increase the computational speed of the static performance, the concept of magnetic gauge curve is presented. It is shown that this approach is in principle valid for any type of variable reluctance machine. Although the complexity of the gauge curve expression varies significantly from one device to another, it is shown that this method is an efficient way to store the magnetic data for a rapid computer aided-design or a real time application. When applied to the two previous types of solenoid actuator, it also leads to a very fast and accurate static force computation.

The dynamic performance of the solid iron actuators requires the evaluation of the magnetic damping due to eddy currents. Based on a 1D model of the flux and eddy current diffusion within an iron bar, an electromagnetic equivalent circuit of the axisymmetric is derived, in which the material nonlinearity, armature movement and eddy currents, a function of the previous parameters, actuator geometry and driving conditions, are modelled. A dynamic model of the partly solid iron rectangular actuator is also proposed and evaluated. In both

cases a comparison of the transient current and force waveforms with 2D or 3D finite elements and measurements is given under various driving conditions.

Acknowledgements

This work has been carried out under a CASE PhD studentship. I gratefully acknowledge the financial support of Lucas Varity Advance Electrical and Electronics Systems, Lucas Varity Diesel Systems and the Engineering and Physical Sciences Research Council of the United Kingdom. I am also very grateful to the University of Glasgow for the technical support brought to this project during the last three years.

I would like to thank my supervisors Mr. Jeff Coles, Technical Manager of Lucas Varity Advance Electrical and Electronics Systems and Professor Timothy J.E Miller, Director of the SPEED Consortium.

Many thanks to Dr. Prem Sangha, Mr. Gordon Reid, Mr. Harvey Smith, Mr. Yoshi Hori and Professor Mike Russell for their technical support and discussions. A special acknowledgement to Mr. Jeff Coles for his technical support, discussions and encouragement. Many thanks to Dr. Dan Ionel, Mr. Malcom McGilp, Mr. Calum Cossar, Miss Lynne Kelly, Mr. Peter Miller, Mr. Ian Young, Mr. Jimmy Kelly, Miss Saffron Alsford and Mrs Karen Phillips for their precious technical support at Glasgow University. I am also very grateful to Switched Reluctance Drives Ltd. and in particular to Dr. Roy Blake, Dr. Mike McClelland and Mr. Bryn Griffiths for their technical support and understanding during the last months of this project.

I would like to thank all my former colleagues of the SPEED laboratory for their encouragement and understanding. Many thanks to Dr. Gabriel Gallegos-Lopez, Dr. Tadashi Sawata for their continious support and discussions.

Contents

List of Tables

List of Figures

List of symbols

AC	Alternating current	
ANN	Artificial neural network	
CAD	Computer-aided design	
DC	Direct current	
ECU	Electronic control unit	
EUI	Electronic unit injector	
FEA	Finite element analysis	
IGBT	Insulated gate bipolar transistor	
MEC	Magnetic equivalent circuit	
MMF	Magnetomotive force	
PC	Personal computer	
PWM	Pulse width modulation	
SR	Switched reluctance	
SRM	Switched reluctance machine/motor	
$\overline{a_n}$	Material surface normal vector	
$a(\psi)$	Parameter in interpolation function	[rad.$^{-3}$]
A	Outer diameter for an axisymmetric solenoid	[m]
A	Total width for a rectangular actuator	[m]
$Astk$	Armature stack length	[m]
$Abcoil$	Limb height above the coil	[m]
$b(\psi)$	Parameter in interpolation function	[rad.$^{-2}$]
B	Armature diameter or width	[m]

$\overline{B}$	Flux density vector	[T]
$Bmax$	Maximum flux density	[T]
$B_{m,n}$	Flux density magnitude for mode (m, n)	[T]
B_L	Flux density in the slot	[T]
$c(\psi)$	Parameter in interpolation function	[rad.$^{-1}$]
C	Central limb radius or central limb half width	[m]
$C1$	Circle 1 centre	
$C2$	Circle 2 centre	
$d(\psi)$	Parameter in interpolation function	
d	Distance from circle 2 to Z-plane origin	[m]
D	Outer limb width	[m]
D'	Overlap between armature and outer limb	[m]
D_i	Distance from circle 1 and circle 2 in Z-plane	[m]
$\overline{E}$	Electric field vector	[V.m^{-1}]
E	Core height	[m]
E_θ	Cylindrical coordinate of $\overline{E}$	[V.m^{-1}]
F	Core back-iron thickness	[m]
f_e	Magnetic force	[N]
F_{fluid}	Fluid forces	[N]
F_m	Magnetic force	[N]
F_{mmf}	Magneto-motive force	[N]
F_{spring}	Spring force	[N]
F_{stk}	Stack factor	
g	Air gap length	[m]
G	Air gap length	[m]
H_c	Magnetic field in the iron	[A/m]
$\overline{H_i}$	Magnetic field vector in material i	[A/m]

$Hcoil$	Winding height	[m]
H_g	Magnetic field in the air	[A/m]
H_{ij}	Magnetic field in section j at position i	[A/m]
H_L	Magnetic field in the slot	[A/m]
I	Current	[A]
I_{2i}	Current in diffusion network layer i	[A]
I_a	Current at maximum inductance position a	[A]
I_{ei}	Eddy current in diffusion network layer i	[A]
I_{Ga}	Armature and airgap current	[A]
I_{Li}	Current in diffusion network layer i	[A]
I_{max}	Maximum Current	[A]
I_N	Gauge curve	
I_{Ni}	Normalised current at position i	
I_u	Current at minimum inductance position u	[A]
$I_{\theta i}$	Eddy currents in cylindrical shell i	[A]
J_{ei}	Eddy current density in diffusion network layer i	[A/m^2]
$J_{\theta i}$	Eddy current density in cylindrical shell i	[A/m^2]
$\overline{J_s}$	Surface eddy current density vector	[A/m]
K_{si}	Local saturation coefficient	
L_1	End-winding leakage inductance	[H]
L_G,L_g	Airgap inductance (fringing+main airgaps)	[H]
L_{ij}	Length of section j at position i	[m]
L_{imbsec}	Number of limb sub-sections over coil height	[m]
L_l	Slot leakage inductance	[H]
L_{min}	Smallest length of $Lstk$ and $Astk$	[m]
$Lstk$	Stack length	[m]
m	Armature mass	[Kg]

N	Number of turns	
$N_{section}$	Number of sub-sections in P_{ai} and P_{yi}	
N_c	Number of diffusion network layers	
p	Half slot width	[m]
P_{ai}	Armature permeance of section i	[Wb/A]
P_{cl1}	Central limb iron permeance under the coil	[Wb/A]
P_{cl2}	Central limb iron permeance on the coil	[Wb/A]
P_{cl3}	Central limb iron permeance above the coil	[Wb/A]
P_{el1}	Outer limb iron permeance under the coil	[Wb/A]
P_{el2}	Outer limb iron permeance on the coil	[Wb/A]
P_{el3}	Outer limb iron permeance above the coil	[Wb/A]
P_{fe}	Outer fringing permeance	[Wb/A]
P_{fei}	Outer fringing permeance for limb i	[Wb/A]
P_{feia}	Section a of P_{fei}	[Wb/A]
P_{feib}	Section b of P_{fei}	[Wb/A]
P_{fi}	Inner fringing permeance	[Wb/A]
P_{g1}	Central limb main airgap permeance	[Wb/A]
P_{g2}	Outer limb main airgap permeance	[Wb/A]
P_{gId}	Ideal total airgap permeance	[Wb/A]
P_{gtot}	Total airgap permeance	[Wb/A]
P_L	Total leakage permeance	[Wb/A]
P_{L1}	Leakage permeance under the coil	[Wb/A]
P_{L2}	Leakage permeance on the coil height	[Wb/A]
P_{L3a}	section a of P_{L3}	[Wb/A]
P_{L3b}	section b of P_{L3}	[Wb/A]
P_{L3c}	section c of P_{L3}	[Wb/A]
P_{L3}	Leakage permeance above the winding	[Wb/A]
P_{yi}	Core yoke permeance of section i	[Wb/A]
R	Radial coordinate	[m]
r	Radial coordinate	[m]

$R1$	Coil resistance	[Ω]
$R1$	Circle 1 radius in Z-plane	[m]
$R2$	Circle 2 radius in Z-plane	[m]
$R1$	Iron resistance of the cylindrical shell 1	[Ω]
$R2$	Iron resistance of the cylindrical shell 2	[Ω]
R_{2i}	Iron resistance in diffusion network layer i	[Ω]
$r1$	Circle 1 radius in t-plane	[m]
$r2$	Circle 2 radius in t-plane	[m]
s	Steel resistivity	[Ω.m]
S	Insulation thickness	[m]
S1	Cross-section area of limb 1	[m^2]
S2	Cross-section area of limb 2	[m^2]
t	Time	[s]
T	Armature thickness	[m]
$T_{1,1}$	Time constant for mode $(1,1)$	[s]
T_e	Torque	[N.m]
Th_j	Thickness of layer j	[m]
$Uncoil$	Limb height under the winding	[m]
v	Armature speed	[m/s]
V	Voltage	[V]
V_G	Voltage drop across the armature	[V]
V_s	Source voltage	[V]
Vol_i	Closed flux tube volume	[m^3]
W	Slot width	[m]
W_c	Coenergy	[J]
W_e	Magnetic stored energy	[J]
x	Armature position	[m]

$xAstk$	Parameter proportional to $Astk$	[m]
xD	Parameter proportional to D	[m]
x_i	Intermediate armature position	[m]
X	Limb length for inner fringing flux	[m]
z	Axial coordinate	[m]
δ	Effective airgap length	[m]
δ_0	Airgap length	[m]
Δ	Limb length	[m]
Δ_i	Length of iron section i	[m]
ρ	Iron resistivity	[Ω.m]
$\rho_{m,n}$	Damping factor	[s^{-1}]
θ	Rotor position	[rad or deg]
θ_a	Rotor position at aligned position	[rad or deg]
θ_u	Rotor position at unaligned position	[rad or deg]
μ_0	Air permeability	[H/m]
μ_i	Iron permeability in the limb section i	[H/m]
μ_0	Iron permeability in the limb section 3	[H/m]
τ_i	Main airgap flux to total flux ratio of limb i	
τ_{ij}	τ_i in layer j	
ϕ	Flux	[Wb]
ϕ_{0i}	Flux in the limbs at level i	[Wb]
ϕ_G	Airgap flux	[Wb]
ϕ_{gi}	Main airgap flux of limb i	[Wb]
ϕ_L	Leakage flux	[Wb]
ϕ_{L1}	Leakage flux due to P_{L1}	[Wb]
ϕ_{L2}	Leakage flux due to P_{L2}	[Wb]
ϕ_{L3}	Leakage flux due to P_{L3}	[Wb]
ψ	Flux linkage	[V.s]

$\psi_{2,1}$	Flux linkage in diffusion network layer i	[V.s]
ψ_a	Flux linkage at maximum inductance position	[V.s]
ψ_G	Airgap flux linkage	[V.s]
ψ_{L2}	Leakage flux linkage due to P_{L2}	[V.s]
ψ_N	Normalised flux linkage	
ψ_{tube}	Flux linkage in a (closed) flux tube	[V.s]
ψ_u	Flux linkage at minimum inductance position	[V.s]

Chapter 1

Introduction

1.1 Background

Increasingly stringent U.S. and European engine noise and emission regulations have necessitated technological advances in fuel and combustion systems. Engine manufacturers have to produce products that meet these regulations but also provide the end user with improved performance, driveability, reliability and cost. Diesel fuel injection equipment has made and is set to continue to make a major contribution to reducing particulate emissions by reducing nozzle hole diameters and increasing injection pressures to mix the fuel and air in the combustion chamber more rapidly. However as injection pressures rise, improving the refinement of the engine becomes even more challenging. For example in noise reduction, refinement has been analysed to determine what contributions can be made by modification to the fuel injection equipment. Apart from minimising mechanical noise, positive contributions can be made by pilot injection and injection rate control to reduce combustion noise [2]. However initial rate of injection control becomes more difficult as the mean injection pressure increases.

Due to its advantages in terms of fuel economy and power density compared to indirect injection concept, an increasing number of passenger cars are today powered with high speed direct injection diesel engines. The increase in the application of this technology to passenger cars combined with the low emission regulations raise

the requirement for more flexible and fully electronic controlled high pressure fuel injection equipment. By controlling injection timing, injection pressure and rate of injection by multiple injection strategy, a common rail injection system is said to be capable of achieving a level of performance and driving comfort for Diesel cars similar to that for petrol powered models with significant improvements in fuel economy and low exhaust emissions [3]. An example of injector design developed by Lucas Diesel Systems for a rail system is shown in figure 1.1 . The opening of the nozzle is achieved by electrohydraulic control. When the fast-acting solenoid actuator, shown more clearly in fig. 1.2, is energised via the electronic control unit (ECU), the control valve leaves its seat and the needle control chamber pressure drops suddenly. Since the fuel pressure at the nozzle seat remains equal to the rail pressure, the needle opens and the injection begins. By stopping the electrical pulse, the actuator magnetic force starts to decay and the injection will stop when the control valve returns to its seat due to the solenoid spring force. The minimum pulse duration required to open the nozzle is a function of the coupled electric, mechanical, magnetic and hydraulic time constants corresponding to this injector assembly. Increasing the dynamic range of injection therefore involves minimising this overall injector response delay to an ECU electrical pulse.

The technical advances in fuel and combustion systems also include the replacement of the mechanical control from a camshaft of the engine exhaust and inlet valves with electrohydraulic power managed by an electronic control unit. This gives complete control over all valve motion parameters and therefore increases the fuel economy and the lower gaseous and particulate emissions [4]. Similar technological developments have also been undertaken for the petrol engines [5].

The general trend in replacing mechanical control with an equivalent electrohydraulic system will affect more and more automotive components; and the existing products already require significant refinements for dealing with competition and potential changes in exhaust and noise regulations. As the products are often destined for mass production, the design developments are usually driven by material and production costs, often with demanding requirements for compactness. The design optimisation is in itself becoming more and more difficult due to the constant increase

in dynamic requirements. The conventional design approach based on building prototypes is therefore no longer worth considering alone for optimising the strongly coupled electric, magnetic and mechanical subsystems characterising for example the dynamic response of an electrohydraulic controlled injector.

In the HEUI injector development, Caterpillar recognised the need for computer aided-design and increased the resources devoted to this analysis between a third to a half of their development program manpower [6]. For example, the complex fluid flow characteristics in the injector were studied using 3D CFD tools and the results were fed into simpler 1D analysis models which could be more easily combined with the models of the other subsystems. An unexpected result from their analysis was that the tolerances could be loosened. The overall study resulted in fewer iron/test cycles, minimised development time and reduced costs.

Because mechanical engineers were for years the only ones in charge of the design of automotive components, design optimisation was first applied to the mechanical and hydraulic subsystems. The electromechanical part was often modelled with extremely simplified linear models. However to properly design a fuel injector for use in high-speed engine, one must carefully analyse the various factors that influence its performance. Therefore the need for more accurate models of especially fast-acting solenoid actuators has appeared in the last decade.

Figure 4.22 shows an example for such a solenoid actuator developed by Lucas Varity for a heavy duty truck engine injector. Because of the requirement for power delivery and because the actuator must interface mechanically with the system being controlled, actuators are usually purpose-built and may vary significantly from one application to the another. In this case the actuator core is made of thin E-shaped laminations of grain-oriented Unisil steel. The solid iron armature contains many holes to enable the assembly of the actuator and to allow for fuel flow. The transient performance of such actuators has been carefully assessed using time stepping 3-D finite-element analysis and also through testing [7].

This approach contrasts heavily with Smith's general method for modelling the

solenoid injector dynamics [8]. In order to simulate the coupled electric, magnetic and mechanical subsystems, Smith proposes a reluctance model for the actuator. Although the entire flux path is modelled, the method can lead to a high level of inaccuracy as the BH characteristic is replaced by a hyperbola; the current in the winding is computed by means of energy consideration increasing the error sensitivity to the inaccuracy of the mechanical model. The magnetic stored energy and the magnetic force are evaluated from linearised expressions. Also iron losses are not modelled. In [9], Smith replaces the reluctance model with a transient finite-element model allowing for armature movement and eddy current generation. However this approach seriously compromises the trade-off between accuracy and computation speed in favour of the former, making it unsuitable for rapid computer-aided design.

Several authors have however pursued the analytical approach for evaluating the dynamic performance of fast-acting solenoid actuators [10], [11]. Some, such as Karidis [12], have even added a new dimension to the analysis by considering an analytical model of eddy currents. The proposed model developed for an E-core type solenoid actuator is capable of accounting for magnetic saturation, leakage, eddy currents and squeeze-film dynamic fluid effects of a fuel injector. The basis of the model is a lumped reluctance network which consists of a distributed circuit reluctances and magneto-motive forces. The leakage reactance is estimated at different gap lengths from a 2D finite-element analysis. Eddy currents are accounted for by including the so-called eddy current *inductances* in the *magnetic reluctance model.* The inductance expression derived from a time constant retrieved from a true linear analytical solution expressing the flux decay within a thin infinite flat plate due to an instantaneous field decay in the surrounding air. Only the plate's dimensions and electrical resistivity appear in their computation. This model agrees well with static and transient measurements. However it is not clear from the results whether the eddy currents, a function of the driving conditions, significantly affect the actuator performance in the given transient curves. The dynamic simulations (i.e. with armature movement) show in many cases a significant fluid damping effect.

In the last decade the advent of large computing facilities has also lead to a real

breakthrough of the general purpose numerical tools such as the 2D and 3D finite-element and boundary element methods. The success of these tools is closely linked to the level of accuracy they can provide compared to the more traditional approaches such as the magnetic equivalent circuit method, but is also due to their high level of flexibility enabling nearly any complex geometry or transient problem to be accurately analysed. These advantages are certainly outstanding for the electromagnetic analysis of fast-acting solenoid actuators considering their variety in configurations, sizes and design requirements. However their integration within a practical design environment has been and still is a major challenge of this decade. Indeed the actuators are usually fed with *DC* voltage in contrast to the numerical methods which are current driven; while the dynamic analysis requires the simultaneous computation of the mathematical model of the other subsystems, especially the mechanical system that involves a time varying gap [13], [14]. This general approach is essential to ensure an accurate evaluation of the transient magnetic phenomena such as eddy currents. The high level of accuracy obtained by such a computation is still today offset by the problem of the time required for computing the results and consequently this technique is not yet suitable for repeated design trials.

The work of Lequesne [15] is probably an attempt to remedy this problem as the author tries to combine the advantage of both analytical and numerical methods: the computation speed of the former and the accuracy of the later. In his hybrid approach the flux leakage is assessed with conventional linear lumped reluctance calculations; and the flux distribution in the iron, a function of the eddy current density, is derived from a finite-difference solution of the field equations reduced to 1-dimension corresponding to the depth of penetration. This technique, applied to a cylindrical flat-faced plunger-type and disk-type actuator agrees well with finite-elements and test data. However the comparison is only based on impact excitations. Also, to reduce the amount of equations, the actuator geometry was modified such that the iron volume is reduced to its inner cylinder portion but characterised by a length equal to the total core perimeter. This assumption may be partly justified by the fact that the transient behaviour of the actuator inner section dominates the overall actuator transients during an impact excitation (as it will be shown in chapter 5). However the eddy current distribution

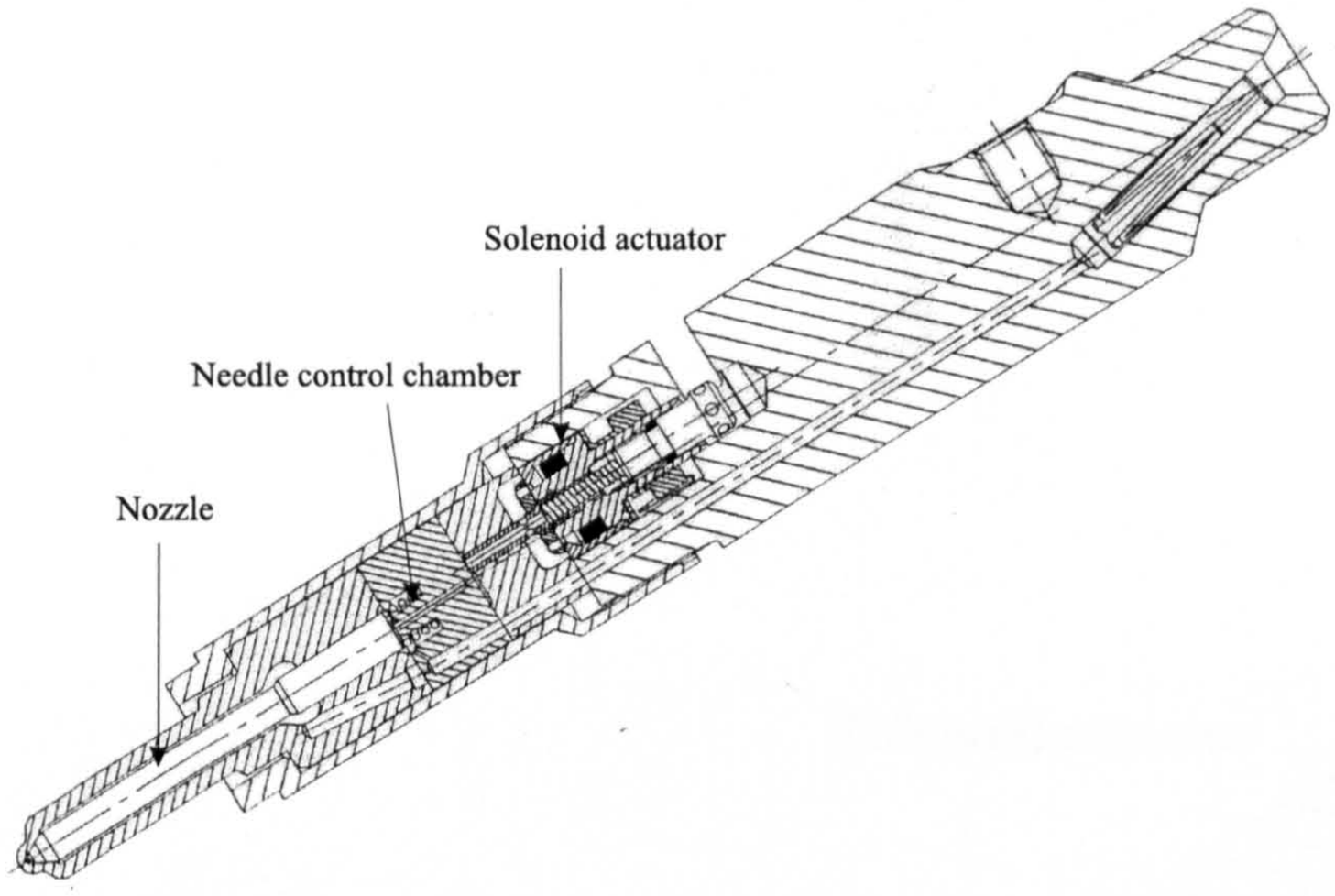

Figure 1.1: Common rail injector cross-section.

may be significantly affected by such a simplification and could lead to a difference between computed and real eddy current losses. This also reduces the potential for generalisation of the proposed approach to different electromagnetic configurations or driving conditions (i.e. switch-off transient).

Although the digital technology is evolving very quickly it is often recognise that the bottle neck in using the numerical tools for repeated design trials is mainly the limit in computing power. However it is interesting to note that the benefit of faster computers will be equally enjoyed by the analytical tools. So, for any computation speed the analytical tools will always be faster than the numerical ones. The conventional design methods may then never be replaced by the numerical techniques but will certainly be improved thanks to the rich source of electromagnetic information available from the numerical analysis and which was not available 40 years ago.

This thesis explores in depth this complementary relationship between finite-elements and the magnetic equivalent circuit method in order to improve the accuracy of the latter with the magnetic understanding acquired from the former.

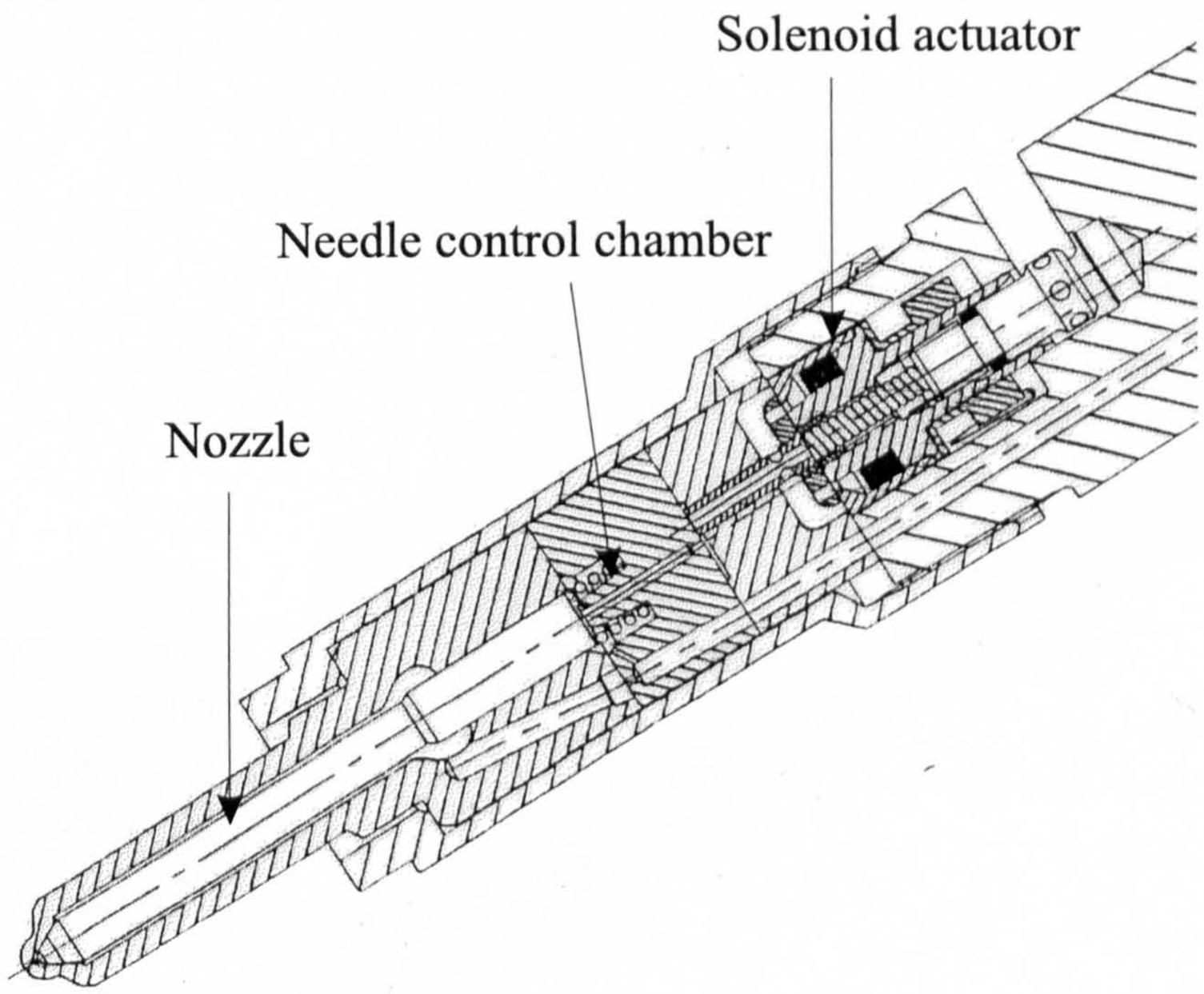

Figure 1.2: Common rail injector cross-section. Closer view of the actuator

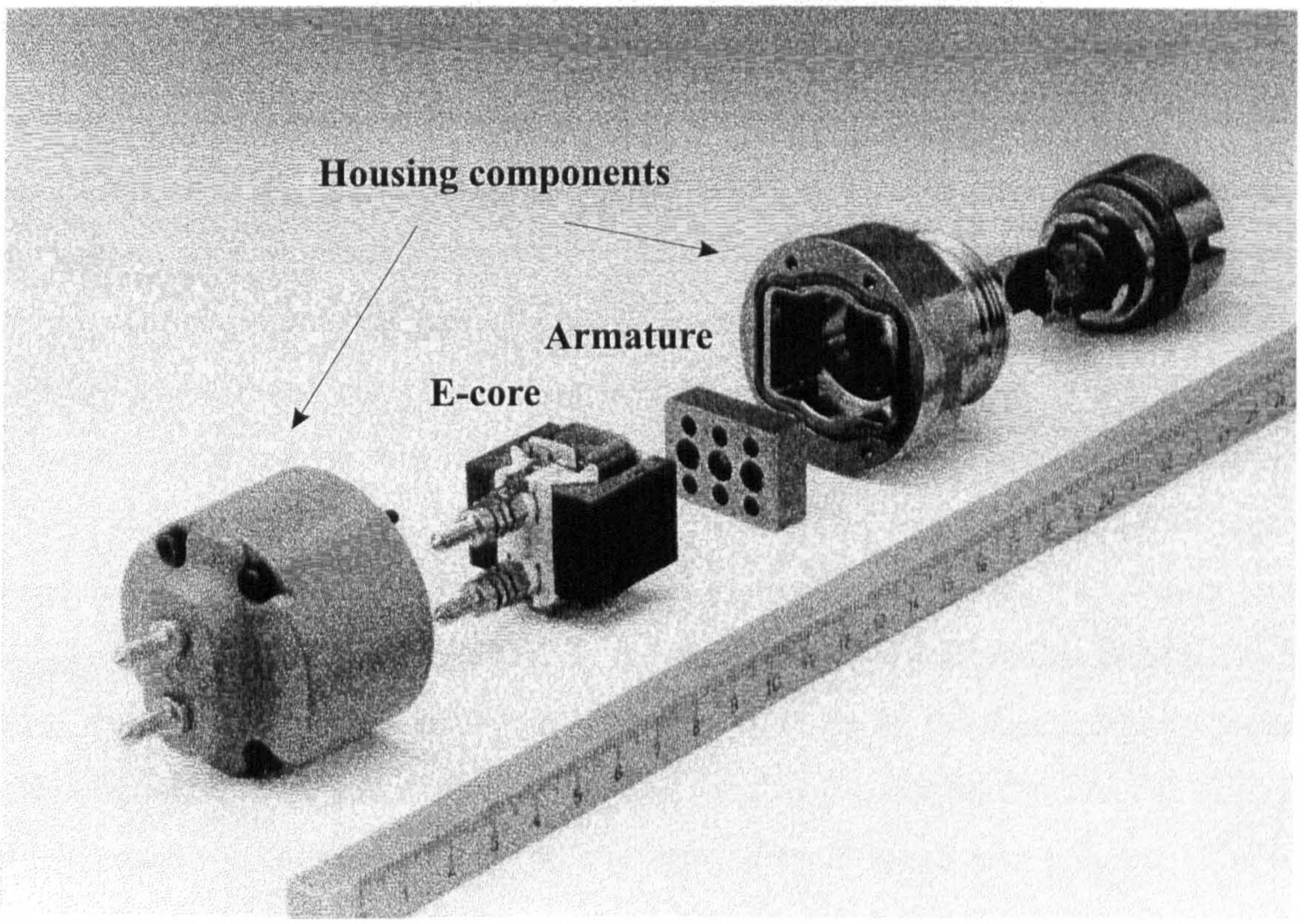

Figure 1.3: Fast-acting solenoid actuator.

1.2 Thesis Objectives and Limitations

In the development of a rapid computer-aided design tool for fast-acting solenoid actuators, an analytical method is required to assess the steady-state and transient performance of these actuators usually energised from a *DC* source. The method should therefore be relatively accurate and also very flexible to allow for different driving conditions.

In order to estimate the dynamic response of the different designs, the material nonlinearities and the magnetic delay due to eddy current generation have to be modelled with accuracy without heavily compromising the speed requirements. The effect of hysteresis on eddy current generation is not developed in this thesis. This aspect has been previously studied by Harmer [16]. However, if the hysteresis loss are significant, the proposed dynamic model can be combined with existing approaches for modelling hysteresis [17]. In general, fast-acting solenoid actuators are voltage-fed devices. if the resistance of the winding can be neglected, their flux linkage evolution is mainly fixed by the voltage waveform applied to the winding (see eq.(2.1)) and their effect are not significant on the eddy current evolution, proportional to $(\frac{dB}{dt})^2$ according to the classical calculation in thin lamination. However the voltage drop due to the winding resistance may be significant. Therefore, based on eq.(2.1), the flux transient is likely to be modified by the hysteresis loop relating the flux density (or flux) to the magnetic field strength (or current), instead of the usual normal magnetising curve. The hysteresis effects, a function of the past magnetic history of the actuator are in general very complex to analyse [18].

As the number of actuator configurations is high, the general technique will be developed and demonstrated for only two actuator types: an axisymmetric and a rectangular solenoid actuator both with a flat-faced armature (cylindrical and rectangular respectively). Some prototypes of both types of actuators are shown in figure 1.4. Both problems are characterised by different modelling challenges such that each case is relevant in order to provide a sufficient guidance for other solenoid actuator configurations.

An improvement of the existing hydraulic models is outside the scope of this thesis

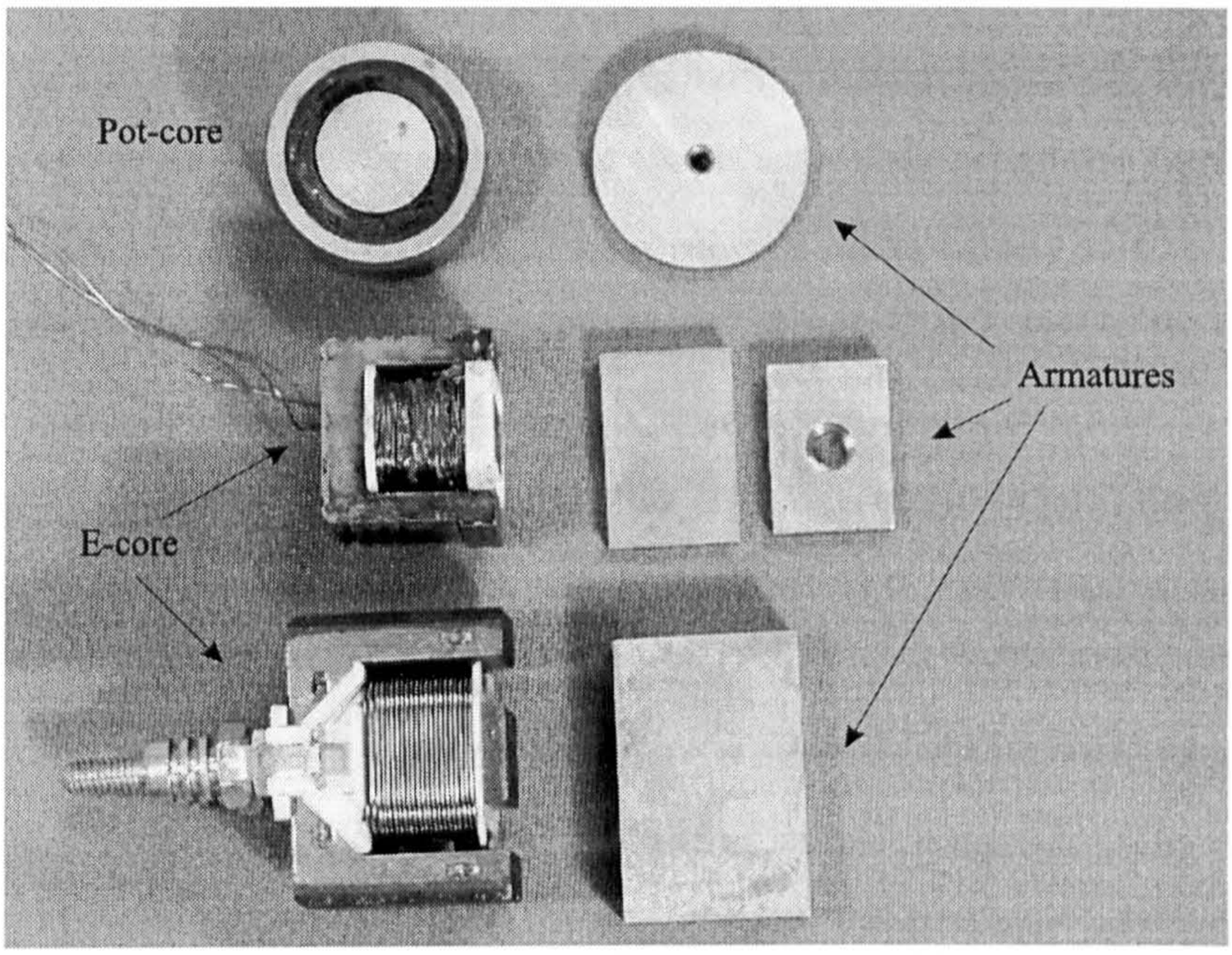

Figure 1.4: Prototypes of E-core and pot-core actuators with a flat-faced armature.

and the modelling of the fluid subsystems is not discussed further. However most of the analytical fluid force models already available in the literature (i.e. [12], [8]) could be solved simultaneously with the proposed electromagnetic model.

A software requirement is also imposed on this project. Indeed, in order to incorporate the new model with an already existing platform for switched reluctance machines [19] [20], [21], the model has to be implemented in Turbo Pascal.

1.3 Thesis Structure and Original Contributions

The thesis aims to develop techniques of electromagnetic analysis for rapid computer-aided design of fast-acting solenoid actuators. These techniques may vary greatly in terms of complexity and also computational speed depending on whether eddy currents have to be simulated. For this reason the work has been divided into two different sections.

In part I, the electromagnetic analysis focuses on the static analysis (no eddy currents) which is suitable for computing the dynamic performance of completely laminated devices or for steady-state analysis of those with high magnetic damping. Chapter 2 summarises the general approach adopted for computing, in this context, the dynamic performance of fast-acting solenoid actuators and focuses on the magnetic equivalent circuit development for both axisymmetric and rectangular devices. Based on finite-element observations, the models are completely analytical and are obtained by combining classical reluctance evaluation methods and conformal or bilinear transformations. The permeance equations involve all the main parameters characterising the geometry of the devices, ensuring therefore a sensible dimension range with good accuracy during design trials. In chapter 3, the concept of magnetic gauge curve for any type of variable reluctance machine is introduced, developed and applied to the fast-acting solenoid actuators and also to the switched reluctance motors. The advantages of this technique for rapid computer-aided design are discussed in each example. A comparison of the previous analytical developments against finite-element and test data is given in chapter 4 for different designs of axisymmetric and rectangular actuators, leading to the end of part I.

Part II summarises the dynamic analysis of solid-iron or partly solid-iron solenoid devices. In chapter 5, a nonlinear electro-magnetic equivalent circuit simulating the diffusion of the flux and eddy currents into a cylindrical solid-iron core is first developed from the field equations. Based on this analysis a first electro-magnetic equivalent network is derived for the axisymmetric solenoid actuators and compared against transient and dynamic finite-element results. The proposed model is discussed in detail and leads to a general formulation of the minimum electro-magnetic equivalent circuit configuration for solid iron axisymmetric actuators which would provide sufficient accuracy for any driving conditions and would be suitable for rapid computer aided-design . Based on this experience a similar technique is applied in chapter 6 to evaluate the dynamic performance of the partly solid-iron rectangular devices . An electro-magnetic equivalent circuit is also proposed and discussed. Finally the analytical steady-state and transient force results are compared in chapter 7 against test data for both actuator types.

The general conclusions are summarised in chapter 8.

Part I

MAGNETOSTATIC PERFORMANCE

Chapter 2

Magnetisation Characteristic Computation

2.1 Dynamic Algorithm

Solenoid actuators are variable reluctance devices i.e. made of steel and copper only. The armature is usually placed on the top of the core as shown schematically in fig. 2.1, with a constant gap left between both parts. When the actuator is energised, a tractive magnetic force is generated in the airgap existing between the core and the moving part (armature). The force rise is a function of the magnetic and electric characteristics of the device and its electronic circuit. When the force is greater than the preload of the spring attached to the armature, the latter starts moving from its seat and progressively closes the gap existing between both iron parts. In an injector, this armature movement is usually associated with the start of the injection. When the current stops flowing in the winding, the magnetic force decays progressively and the armature returns to its seat due to the spring force.

When eddy currents are not an important issue, the computation of the dynamic performance of a solenoid actuator can be assessed rapidly and with relatively good accuracy by applying a decoupled technique in which the magnetic information is evaluated prior the integration of the circuit and mechanical differential equations.

In its most generalised form, the equation of the electrical circuit describing the flux generation in the actuator is given by:

$$\frac{d\psi}{dt} = V - R1\ I, \tag{2.1}$$

where ψ is the flux linkage, V the voltage source, $R1$ the total resistance of the electrical circuit and I the current in the winding. Similarly the movement of the armature is described by the mechanical equation:

$$m\,\frac{dv}{dt} = F_m - F_{spring} - F_{fluid}, \tag{2.2}$$

where m and v are the mass and the speed of the moving assembly respectively, F_m the magnetic force, F_{spring} and F_{fluid} the forces due to the spring and to the fluid surrounding the armature. The displacement x of the moving part is then evaluated from:

$$\frac{dx}{dt} = v. \tag{2.3}$$

A solution of this system of equations is obtained by applying a finite-difference method. At each time step, the evaluation of the current I from the computed flux linkage ψ and displacement x is retrieved from a look-up table containing a set of magnetisation characteristics [1]. Similarly the magnetic force corresponding to these values of current and armature/plunger position can be retrieved either from a look-up table containing a set of force curves versus current and displacement, or directly from the magnetisation characteristics by means of coenergy evaluation [1], [18], [22]:

$$W_c(I,x) = \int_0^I \psi(I,x)\,dI, \tag{2.4}$$

where W_c is the magnetic coenergy. The magnetic force is obtained from [2]

$$F_m = \frac{\partial W_c(I,x)}{\partial x}\Big|_{I=Cst}. \tag{2.5}$$

The quality of the results obtained from this algorithm is closely related to the technique applied for computing and handling the magnetic information. Due to time

[1] Flux linkage versus current at constant armature/plunger position.

[2] This approach is only strictly valid when applied to a conservative system [1].

constraint, repeated design trials usually rely on an analytical evaluation of the magnetisation curves by means of a magnetic equivalent circuit [23]. A more accurate dynamic analysis requires a set of data from a numerical technique such as finite-elements or simply from measurements [24] [25]. Note that the force computation based on eq.(2.5) is more accurate than the evaluation based on:

$$F_m = \frac{B_n^2 \, S}{2\mu_0}, \tag{2.6}$$

where B_n^2 is the normal flux density in the main airgaps (see fig. 2.2), S the airgap cross-section and μ_0 the air permeability. Indeed the latter can be derived from the former by neglecting the presence of fringing and cross-slot leakage [18]. Also, in this context, eq. (2.6) is not a convenient approach as the normal flux density is not an explicit output from the magnetisation curves.

The computation of the current and the magnetic force at each time step also involves a 2-D interpolation technique between the points stored in the look-up table(s). Several methods have been successfully applied to the analysis of the switched-reluctance machines and include:

1. a piecewise quadratic interpolation in function of I and a piecewise linear interpolation in function of the rotor position θ [22],
2. a curve fit of the magnetisation curves based on exponential functions with a piecewise linear interpolation in function of θ [26],
3. a 2-D interpolation based only on spline functions [25].

These relatively sophisticated interpolation techniques are highly recommended when the amount of data stored in the look-up table is rather small. In the context of the thesis, the computation of the magnetisation characteristics is achieved by developing a nonlinear Magnetic Equivalent Circuit (MEC) for each type of fast-acting solenoid actuator shown in fig. 1.4. Although this approach involves a considerable development cost, it leads to a very fast computation of the magnetisation characteristics for any armature position. For this reason, the method applied for interpolating the large set of data provided by the MEC is simply a piecewise 2-D linear interpolation technique.

2.2 The Magnetic Equivalent Circuit Method

The nonlinear performance of any type of rotary and linear motion electromagnetic device can be evaluated with the magnetic equivalent circuit method [23, 18]. The key idea in creating a magnetic equivalent circuit is to generate enough elements to reflect all properties of an electromagnetic device on the one hand, and not have too many elements, on the other, as this could unnecessarily slow down the computation without a significant gain in accuracy. In the MEC method the flux paths of the machine are indeed divided into permeances, a function of the device geometry and flux distribution. Ideally a permeance is equivalent to an element of flux tube in which the flux density is assumed to be uniformly distributed over any cross-section perpendicular to the flux direction. In contrast to the finite-element method, the creation of the MEC requires a good understanding of the machine flux distribution, varying with rotor/armature position and saturation.

2.2.1 Airgap Permeances

The computation of the airgap permeances is usually obtained by dividing the airgap flux into several 'flux tube' elements, approximated with simple geometries [18, 22, 27, 28, 15] . When the machine is characterised by large airgaps, an accurate evaluation of the magnetic performance often require a more refined computation.

In the case of a doubly salient variable reluctance machine, Miller [19, 21] and Tolikas [29] proposed in the computation of the minimum inductance, a geometric and an algebraic evaluation of the dual-energy method respectively. The geometric approach is also commonly known as the tube and slice method.

In [12], Karidis proposed an hybrid lumped/ 2D finite-element model in order to estimate more accurately the airgap and cross slot leakage permeances of a flat-faced armature rectangular actuator.

Similarly, Smith [30] evaluated the magnetic performance of an axisymmetric and

rectangular actuator with a flat-faced armature by computing a reluctance network including some correction factors for the airgap permeances obtained from a 3D analysis.

In the thesis, the evaluation of the airgap permeances is obtained entirely analytically by combining conventional geometric approximations for the airgap paths and bilinear or conformal transformations.

2.2.2 Iron Section Permeances

The evaluation of the iron permeance is usually based on the iron geometry and is, in most problems, relatively straightforward. However this task becomes a lot more complicated when the given machine is also characterised by local saturation phenomena as is the case in the switched reluctance motor [28, 27]. The actuators studied in the thesis are not particularly affected by the local saturation phenomenon.

The aim of this chapter is to present the nonlinear magnetic equivalent circuits developed for both axisymmetric and rectangular solenoid actuators (fig. 1.4). In several of the following chapters, there will be regular references to the magnetic circuit permeances. So it is important to present, in some details, their evaluation and underlying assumptions.

2.3 Axisymmetric Solenoid Actuator

The dimension parameters taken into account in the magnetostatic analysis of both axisymmetric and rectangular actuator types are summarised in fig. 2.1[3]. In the cylindrical problem, the armature diameter B is kept equal to the core outer diameter A. A minimum clearance of 40 micrometer is maintained between the moving part and the core, allowing for a faster armature response during the switch-off period [12]. The subscripts '1' and '2' in the following equations (except for the cross slot leakage) refer to the central and outer limb respectively of the axisymmetric solenoid actuator, more

[3]The stack length variables *Astk* and *Lstk* are only valid for the rectangular device.

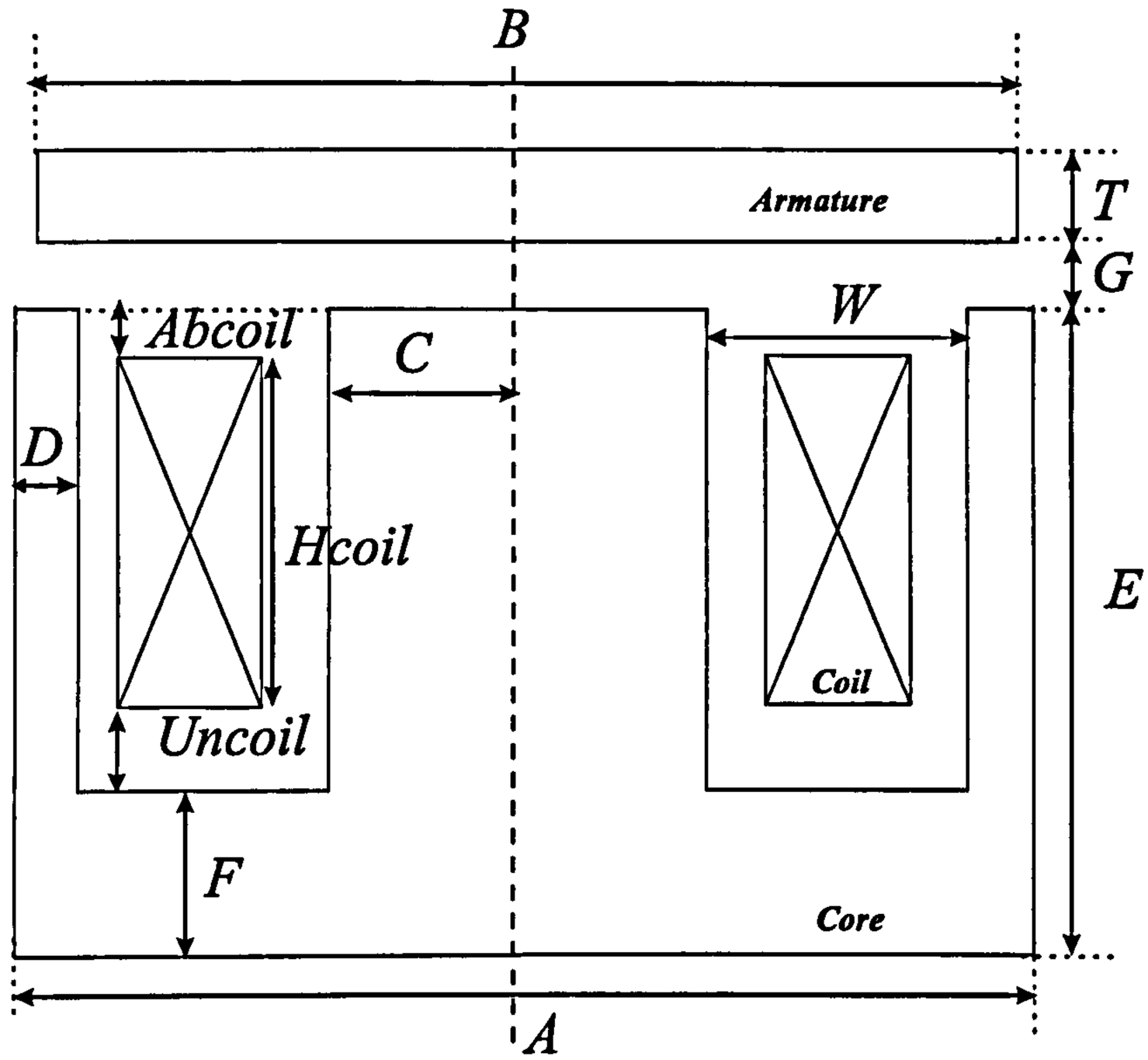

Armature stack length= Astk
Core stack length = Lstk
Number of turns = N

Figure 2.1: Actuator cross-section

commonly called pot-core solenoid . In the following development, a uniform flux density distribution is assumed over any airgap or iron 'cross-section' considered in the permeance computation.

The development of the magnetic equivalent circuit starts with the evaluation of the different airgap permeances. The circuit is then completed with a series of nonlinear permeances in order to simulate the effect of saturation in the iron sections.

2.3.1 Airgap Paths

An analytical approximation of the different airgap paths is required in the magnetic equivalent circuit for pot-core solenoids.

Figure 2.2 shows the different airgap paths associated with an axisymmetric flat-faced armature solenoid actuator. As it is shown in table 2.1, the distribution of flux between the cross slot leakage, fringing and working airgap paths computed from finite-element analysis varies significantly with armature position. At small airgap lengths (e.g. around 0.1mm) the effect of fringing and cross slot leakage can be easily neglected. However, at 0.5mm, their flux proportion is a lot more significant as both fringing and cross slot leakage paths carry about 50 percent of the total flux.

In order to ensure a relatively constant level of accuracy within the design parameter range, it is therefore compulsory to incorporate the different airgap paths within the analytical model.

Gap	Main gap G_2 (%)	Outer fringing (%)	Slot leakage (%)	Inner fringing (%)
0.15 mm, $B_{max} \approx 1T$	70	11.5	11.5	7
0.5mm, $B_{max} \approx 1T$	43	20	28.4	8.6
0.15mm, $B_{max} \approx 2T$	73	10.7	8	8.3
0.5mm, $B_{max} \approx 2T$	45.2	24	21.6	9.2

Table 2.1: Flux proportion in an axisymmetric actuator between the different airgap paths as a function of airgap length and saturation level. 2D finite-element results .

To some extend, the airgap flux distribution is also affected by magnetic saturation. Indeed it modifies the amount of MMF drop required in the flux paths 'connected in parallel', including each an airgap section and various iron sections undergoing different saturation level. An example of flux variation in the different airgap paths due to saturation is given in table 2.1. The maximum value of flux densities, given in the table, appears in the bottom part of the limbs. This phenomenon is at the origin of the major variation of flux distribution due to saturation and will be modelled in the MEC by completing the linear MEC with the nonlinear permeances of the iron sections. However another more subtle effect of saturation involves modifying the airgap path geometry (and thus permeance) and also their distribution over the iron outer surface.

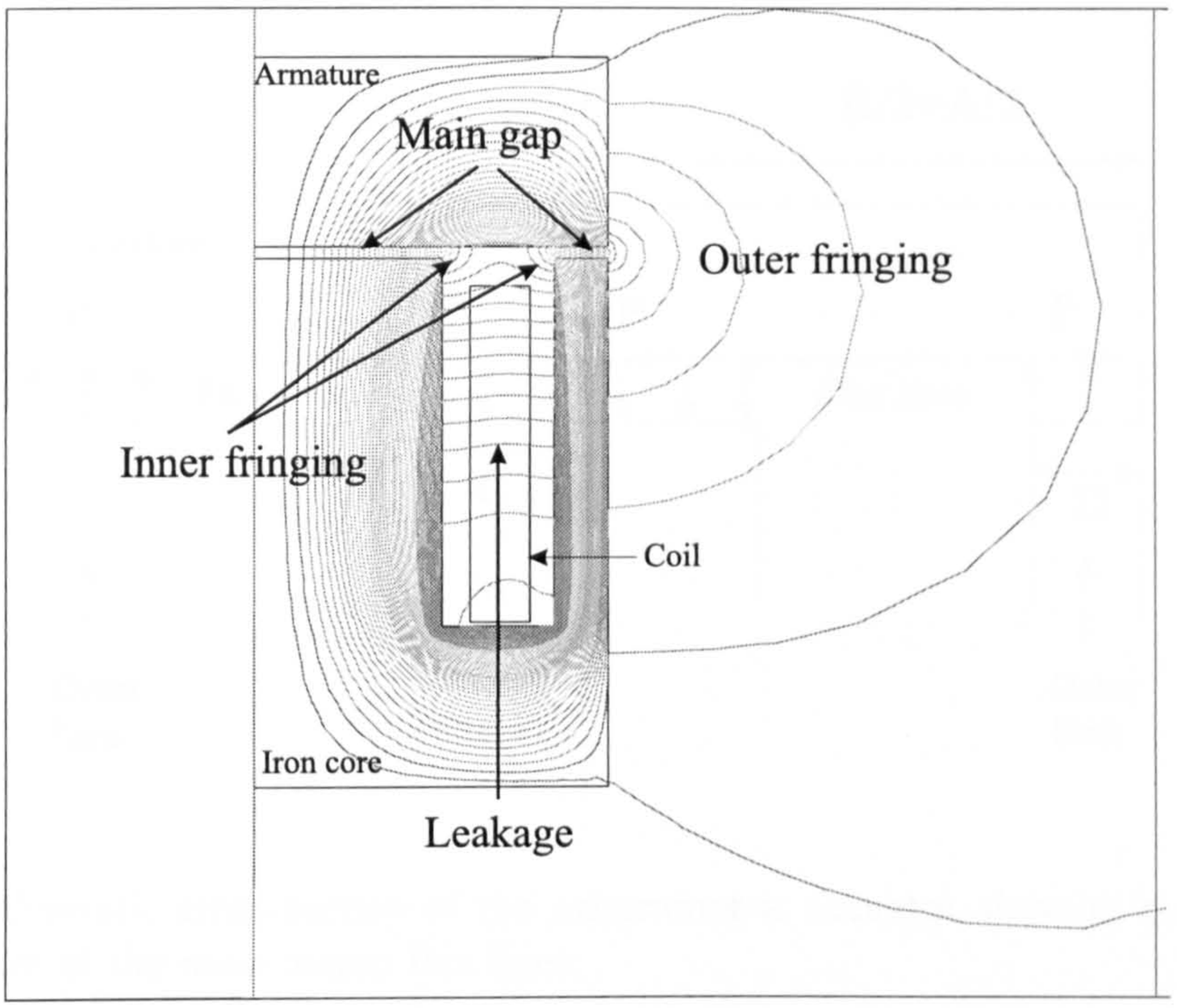

Figure 2.2: 2D finite-element flux plot of an axisymmetric solenoid actuator and definition of the different airgap paths.

This is shown in figure 2.4. With saturation increasing, this phenomenon becomes more important. However it is beyond the MEC capabilities to simulate the variation of airgap path geometry due to saturation. Therefore it is further assumed that the airgap permeances depend only on solenoid geometry and dimensions.

2.3.2 Working Airgap Permeances

In the computation of the main airgap permeances, the flux lines are assumed to cross the main airgaps in straight lines flowing from the core to the armature or vice versa as shown in fig. 2.3. The working airgap permeances Pg_1 and Pg_2 are then equal to:

$$Pg_1 = \frac{\mu_0 \pi C^2}{G}, \tag{2.7}$$

and

$$Pg_2 = \frac{\mu_0 \pi ((A/2)^2 - (A/2 - D)^2)}{G}. \tag{2.8}$$

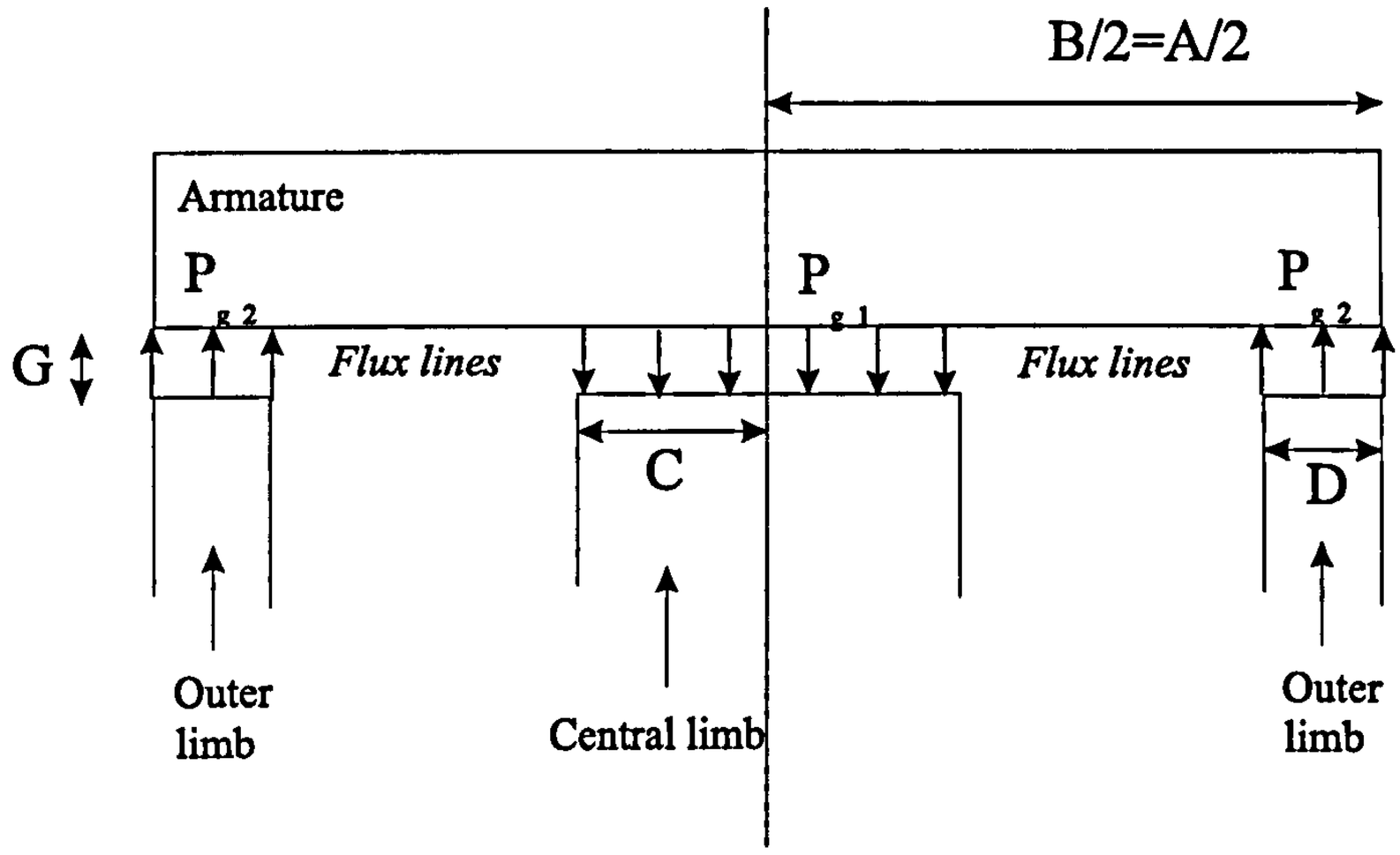

Figure 2.3: Schematic cross-section of the axisymmetric actuator showing the approximation of the main airgap flux lines.

The variables are shown in fig. 2.1

2.3.3 Cross Slot Leakage Permeances

The computation of the cross slot leakage permeance, also called slot leakage or simply leakage permeance in this thesis, depends on the distribution of the coil within the slot. For this reason, the total leakage is split into 3 regions as shown in fig 2.6. In each of them, the leakage flux is also assumed to cross the slot width in straight radial lines [18] as shown in fig. 2.5.

The leakage above the coil P_{L3} (region III in fig. 2.6), embraces the entire winding such that its permeance is equal to:

$$P_{L3} = \frac{2\pi\mu_0(abcoil - X)}{\ln \frac{A/2-D}{C}}, \tag{2.9}$$

where X corresponds to the limb length 'short-circuited' by the inner fringing path. The computation of X is presented in the fringing section.

Although this leakage does not produce any flux linkage, the computation of the

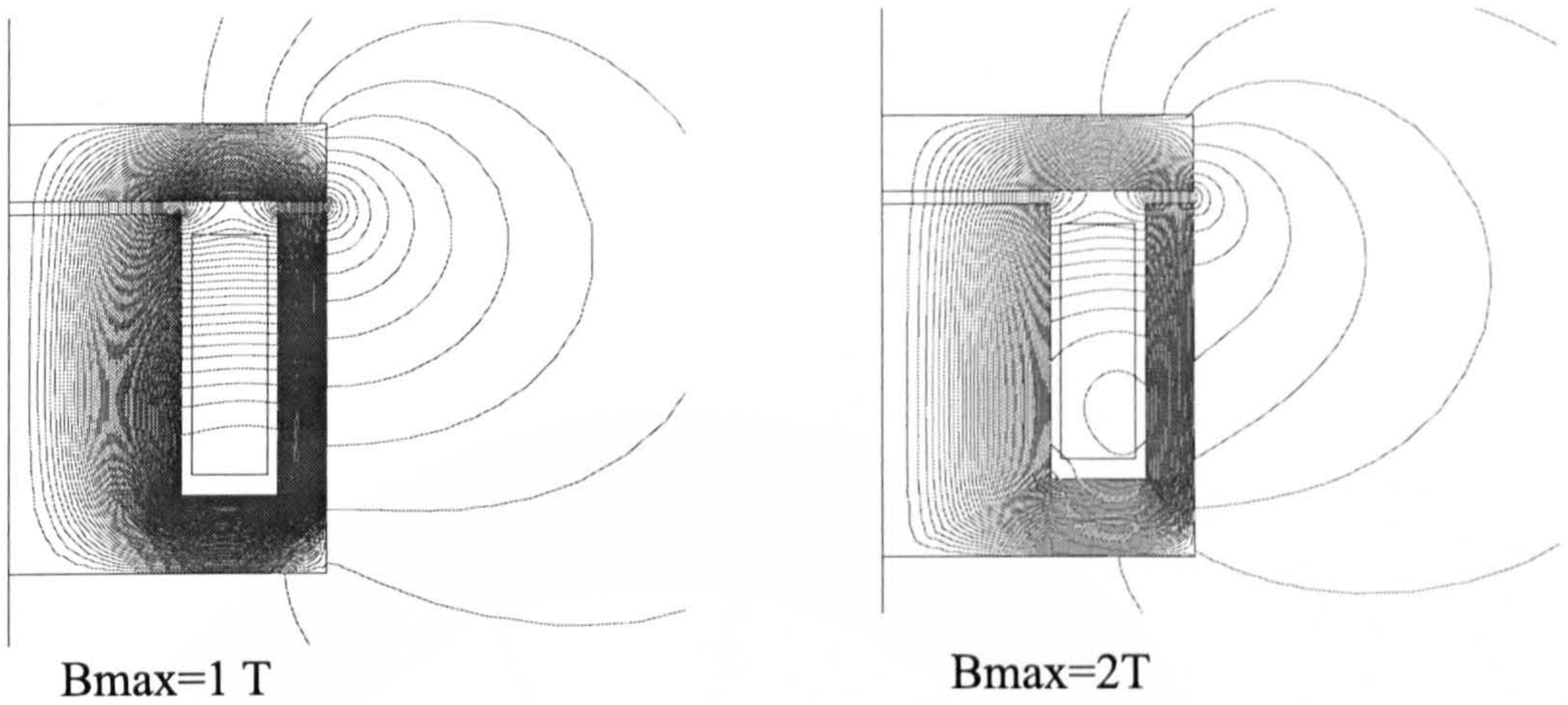

Figure 2.4: 2D finite-element flux plot of an axisymmetric actuator for an airgap length of 0.5mm and two saturation levels. In each case, the indicated maximum flux density level is reached in the bottom parts of the limbs.

leakage permeance under the winding P_{L1} (region I), is obtained in a similar way:

$$PL_1 = \frac{2\pi\mu_0 uncoil}{\ln \frac{A/2-D}{C}}. \tag{2.10}$$

In theory no leakage flux flows under the coil until saturation significantly increases in the yoke. This can be demonstrated by computing Ampere's law along the dashed contour shown in fig. 2.7. The magnetic field H_g in the slot, under the coil, is proportional to the magnetic field in the iron H_c, which remains fairly small until a large amount of saturation is generated in the yoke. Also from Ampere's law it appears that the magnetic field H_g (due to P_{L1}) flows in the same direction as H_c and short-circuits the yoke when the latter is too heavily saturated. This conclusion has however been drawn some time after the development of the proposed MEC. For this reason, the MEC used in this work will incorporate the leakage permeance P_{L1}, treated in the same way as P_{L3} [4].

The evaluation of the leakage permeance P_{L2} requires the computation of the total

[4]Although the permeance is usually very small compared to the other leakage components, this permeance can be completely removed from the magnetic equivalent circuit.

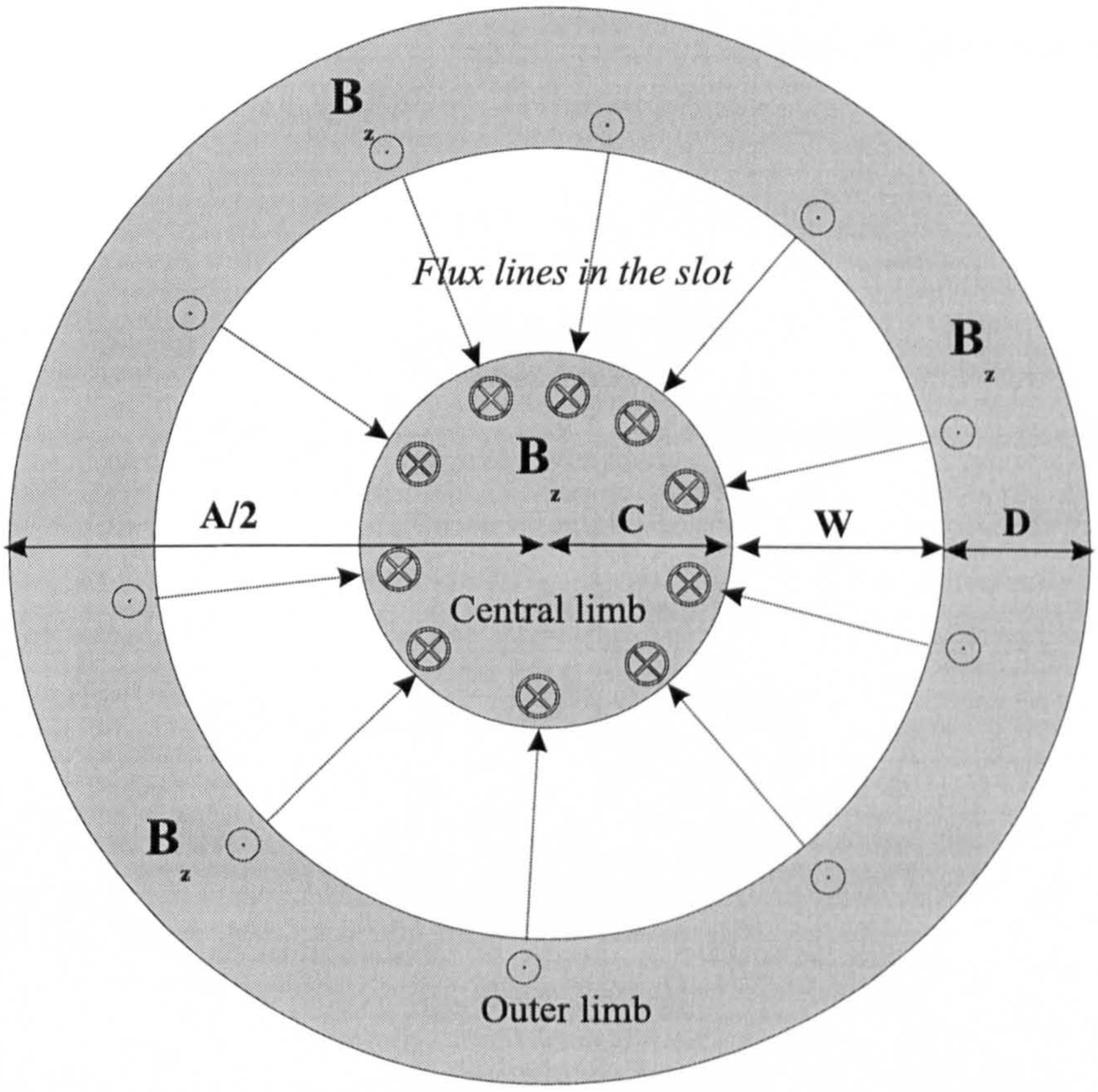

Figure 2.5: Schematic top view of the axisymmetric core showing the approximation of the slot leakage flux lines.

leakage flux comprised in region II. The iron is assumed infinitely permeable in the following development. If $B_L(R,z)$ corresponds to the flux density in the slot at (R,z), the leakage flux in region II is equal to:

$$\phi_{L2} = \int_{z_d}^{z_u} B_L(R,z) 2\pi R dz, \tag{2.11}$$

where z_d and z_u are shown in fig. 2.6.

As region II is characterised by a uniform distribution of the total current in the slot, the flux density $B_L(R,z)$ increases linearly in region II from bottom to top such that $B_L(R,z)$ can be expressed as:

$$B_L(R,z) = B_L(R)\,\frac{(z-z_d)}{z_u - z_d}, \tag{2.12}$$

where $B_L(R)$ depends only on the radial coordinate R.

By replacing $B_L(R,z))$ in eq.(2.11) with eq.(2.12) and integrating between z_d and z_u, it follows:

$$\phi_{L2} = B_L(R)\frac{hcoil}{2} 2\pi R, \tag{2.13}$$

with $hcoil = (z_u - z_d)$.

From Ampere's law, we can also write:

$$\oint H(R,z)\, dR = NI, \tag{2.14}$$

where $H(R,z)$ is the magnetic field strength along the closed contour shown in the left-hand side of fig. 2.6, embracing the entire coil cross-section.

However, if the iron is infinitely permeable, the magnetic field is very small in the iron sections, and the integration can be reduced to the contour path crossing the slot above the coil where $H(R,z) = B_L(R,z)/\mu_0$. By combining eq.(2.14) and eq.(2.13) in which ϕ_{L2} is a constant, it follows:

$$\frac{\phi_{L2}}{\mu_0 \pi\ hcoil} \oint \frac{1}{R} dR = NI. \tag{2.15}$$

Or

$$\phi_{L2} = \mu_0 \pi N I \frac{hcoil}{\ln \frac{A/2-D}{C}}. \tag{2.16}$$

The effective leakage permeance P_{L2} which would produce ϕ_{L2} such that

$$\phi_{L2} = PL_2.NI, \tag{2.17}$$

is given by:

$$P_{L2} = \mu_0 \pi \frac{hcoil}{\ln \frac{A/2-D}{C}}. \tag{2.18}$$

The expression of P_{L2} as given by eq.(2.18) corresponds to the maximum value of the leakage permeance on the coil section. Indeed, the previous computation assumes an infinite permeability in the iron when applying Ampere's law. In reality as soon as the iron in the limbs saturates , its permeability drops significantly, leading to a decrease of the effective leakage permeance with saturation increasing.

This fact can be observed in the finite-element flux plots shown in fig. 2.4: When saturation increases, the mmf required by the yoke and the limb base becomes larger, reducing the mmf available for the leakage flux at the bottom of the slot. However, at a higher limb height, the leakage flux embraces more turns; also the saturation in the limb is slightly reduced by the lower level leakage flux such that the leakage is denser at the top of the slot.

For this reason, it was chosen to only incorporate two third of the total permeance P_{L2}, as computed above, in the MEC [5].

As shown in fig. 2.8, Roters [18] assumes no space under and above the coil; his total leakage permeance P_L is then equal to:

$$P_L = \mu_0 \pi \frac{E-F-X}{\ln \frac{A/2-D}{C}}. \tag{2.19}$$

[5]The factor two-third corresponds the flux linkage produced by the leakage flux ϕ_{L2} and also corresponds to the proportion of the leakage flux ϕ_{L2} producing an mmf drop in the limbs.

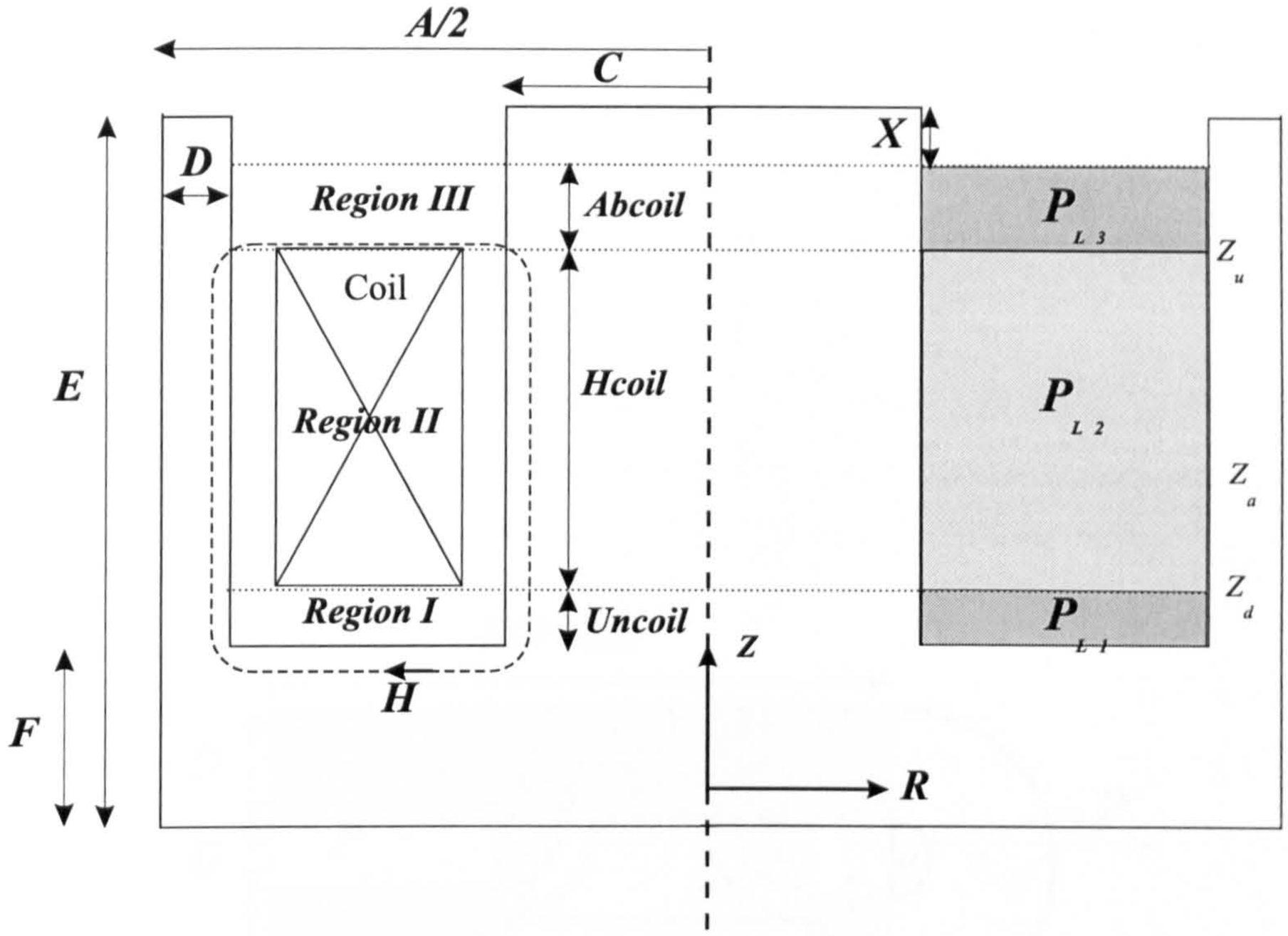

Figure 2.6: Division of the slot into three regions and associated cross slot leakage permeances.

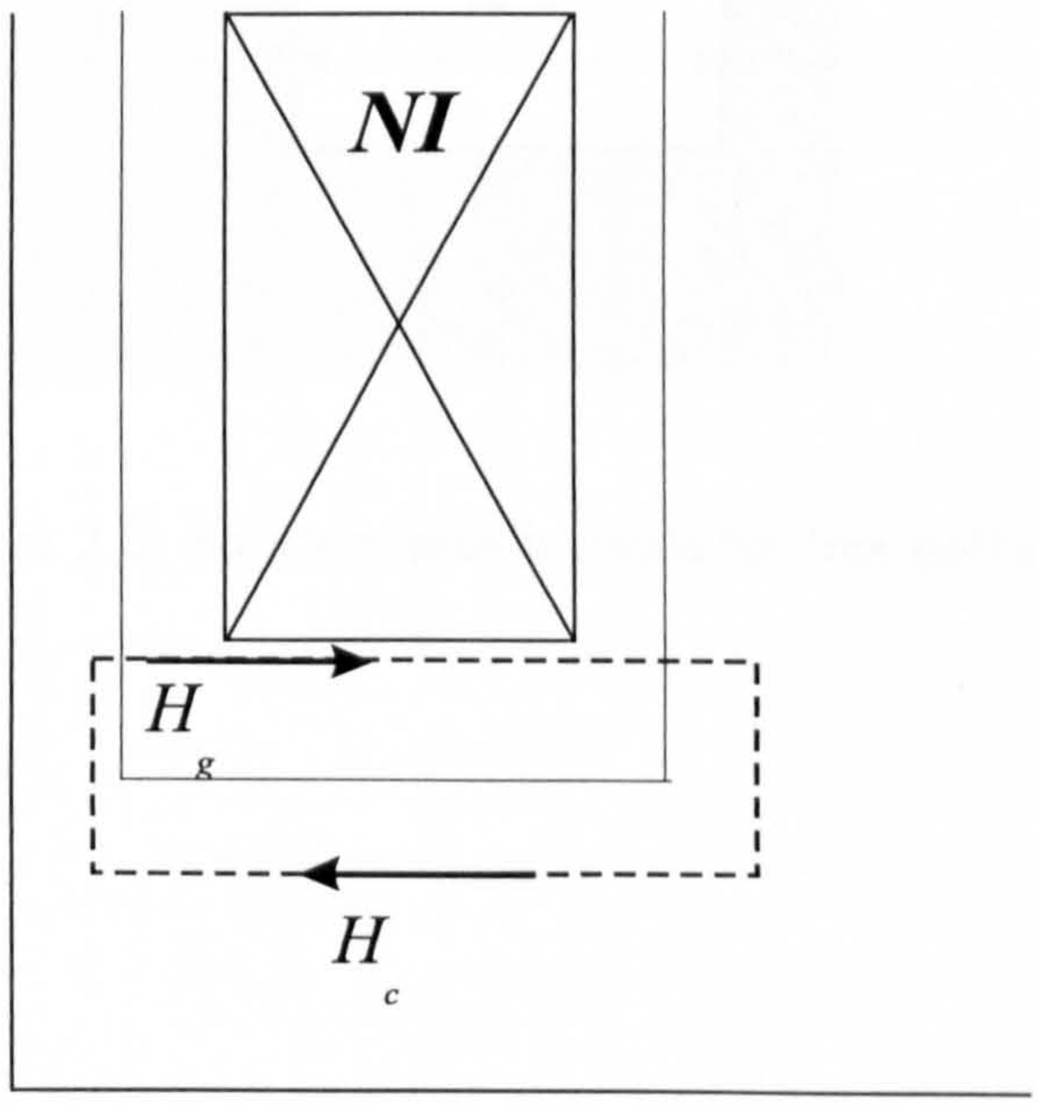

Figure 2.7: Leakage under the coil.

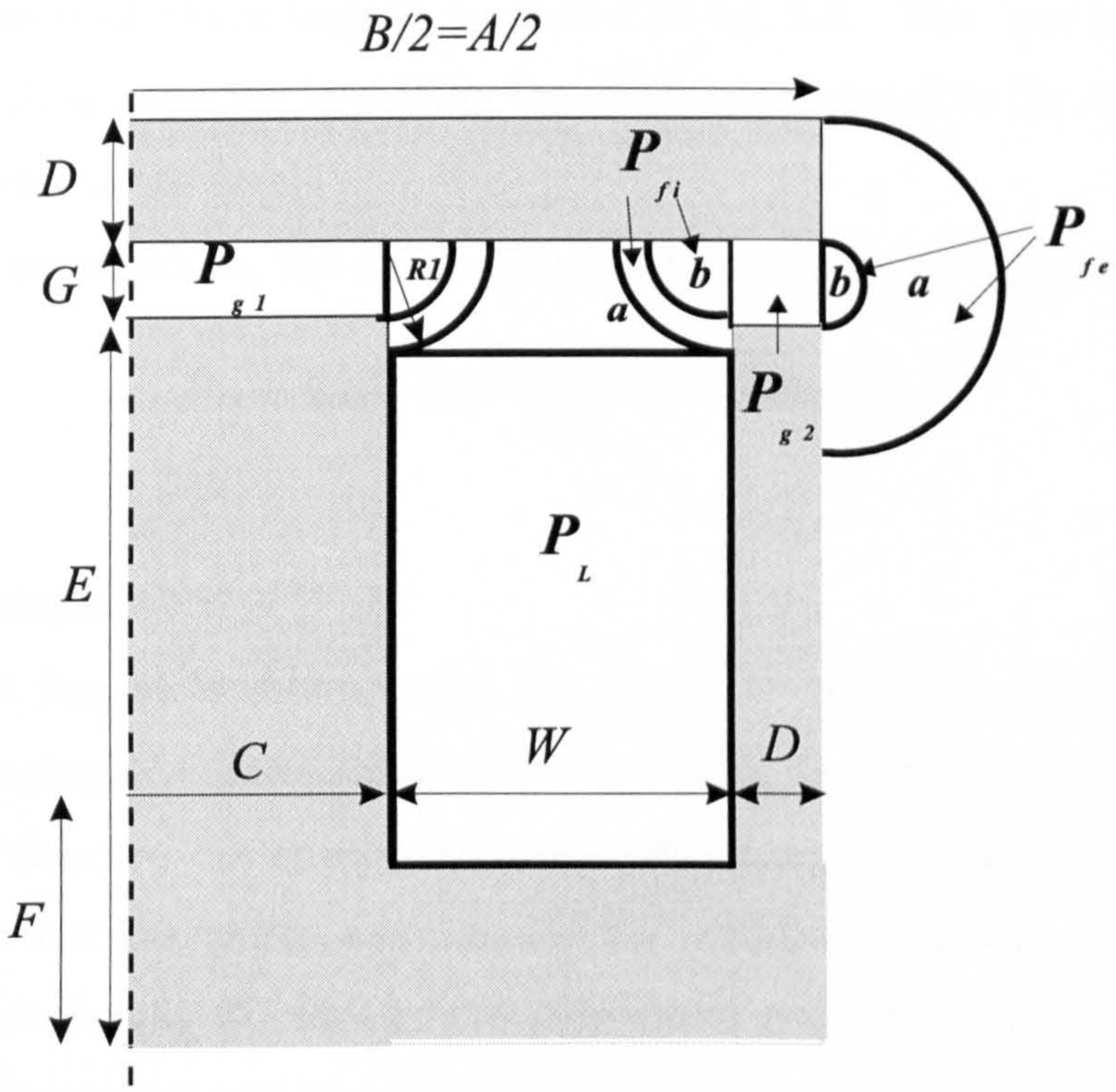

Figure 2.8: Roters'approximations for flux paths

2.3.4 Outer Fringing Permeance

a. Roter's Approach

Figure 2.8 summarises the airgap paths assumed by Roters for computing the permeances of a pot-core solenoid. The outer fringing is divided into two regions called a and b. In region a the fringing is limited by a pair of concentric circles defined by the working airgap length and the armature thickness. In region b the fringing contribution, although minor, is compared to a semicircular cylindrical volume. In each case, the computation is not truly axisymmetric. The permeances are first evaluated in the $2D$ plane, per unit of 'stack length', as shown in fig. 2.8. This 'per unit of length' computation is then corrected by setting the stack length equal to '$2\pi A/2$' where A is the outer diameter of the core.

Based on these assumptions, the computation of the outer fringing leads to [18]:

$$P_{fe} = 2\mu_0 \frac{A}{2} \ln\left(\frac{T + G/2}{G/2}\right) + 1.63\mu_0 \frac{A}{2}. \tag{2.20}$$

b. New Technique

From the FEA flux plots shown in fig. 2.4, it can be observed that the flux tubes in the outer fringing diverge significantly when flowing from the armature side to the outer surface of the core. An improved computation of this permeance should therefore incorporate this flux divergence, a function of the armature height T, airgap length G, and also the core height E. Ideally the permeance evaluation should also be truly axisymmetric. However it was found that these two requirements were not compatible analytically. For this reason, the $2D$ approach as proposed by Roters was kept in this analysis. However the $2D$ paths based on concentric circles (permeance a) were replaced by a new path defined by two non-concentric circles, a function of T, G, E. The proposed new outer fringing path is shown in fig. 2.9 and requires the support of a bilinear transformation to evaluate the corresponding permeance expression.

The technique involves mapping the non-concentric circles, as shown in fig. 2.10, to a pair of concentric ones for which the permeance equation is known (eq.(2.20)). Based on the assumptions that the boundaries (bold contours in fig. 2.10) in each map

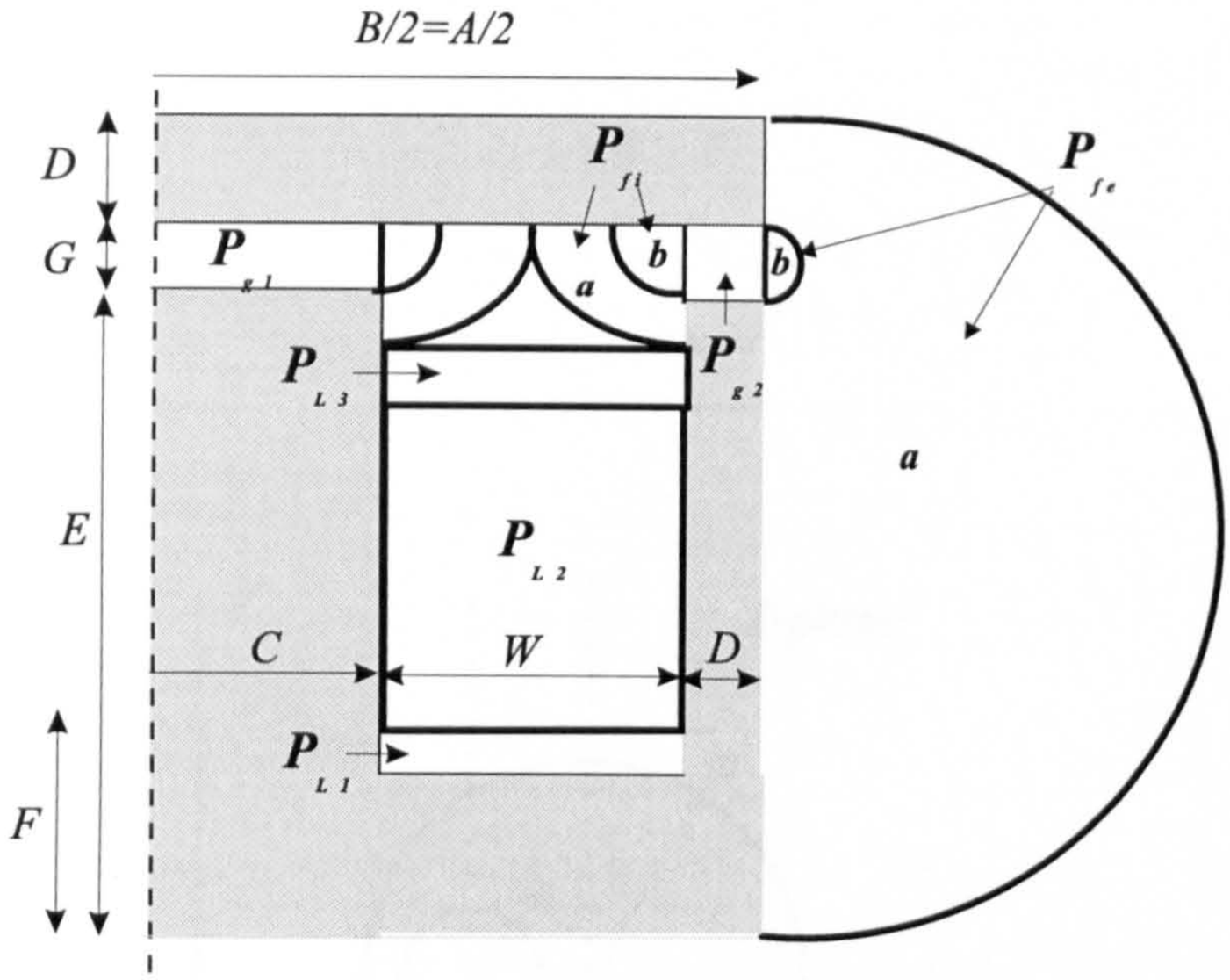

Figure 2.9: New approximations for flux paths.

are either coincident with flux lines or equipotentials (infinitely permeable), the field properties in both planes will be conserved.

The transformation between the complex planes of respective variables t and Z is given by [31]:

$$Z = \frac{1}{t}, \tag{2.21}$$

with $t = u + jv$ and $Z = X + jY$. The equation of a circle, centre $(a_i, 0)$ and radius r, in the t-plane is

$$r = |t - a_i|. \tag{2.22}$$

By replacing t in (2.22) with (2.21) and rearranging,

$$r^2 = \frac{(1 - a_i X)^2 + a_i^2 Y^2}{X^2 + Y^2}, \tag{2.23}$$

which may be rearranged again as

$$(X - \frac{a_i}{a_i^2 - r^2})^2 + Y^2 = (\frac{r}{a_i^2 - r^2})^2. \tag{2.24}$$

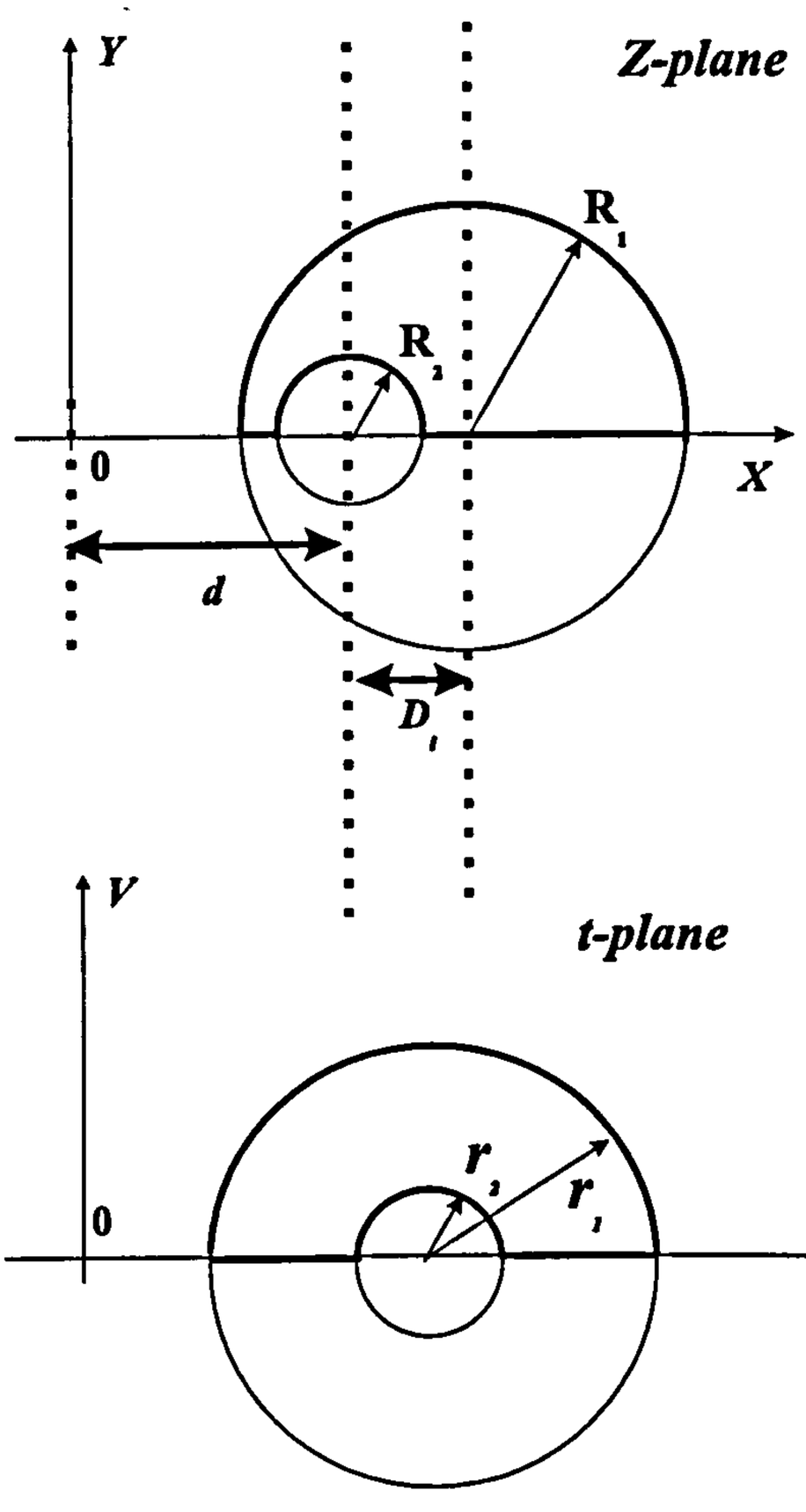

Figure 2.10: Z-plane and t-plane characterising the bilinear transformation.

This is the equation of a circle, radius $\frac{r}{a_i^2-r^2}$ and centre $(\frac{a_i}{a_i^2-r^2},0)$ in the Z-plane mapped by (2.21) from the circle , centre $(a_i,0)$ and radius r, in the t-plane.

In the case of fig. 2.10, the two non-concentric circles are in the Z-plane with a distance d between the smaller circle and the origin of the inversion. d is an unknown parameter which will be evaluated so that the mapped circles in the t-plane will be concentric. From (2.24) it appears that the smaller circle, centre $(d,0)$ and radius $R2$ transforms into a circle with centre coordinates

$$(\frac{d}{d^2-R2^2},0), \tag{2.25}$$

and radius

$$r2=\frac{R2}{d^2-R2^2}. \tag{2.26}$$

Similarly, the large circle, with radius $R1$ and centre $(d-D_i,0)$, transforms into a circle with centre

$$(\frac{d+D_i}{(d+D_i)^2-R_1^2},0), \tag{2.27}$$

and radius

$$r1=\frac{R1}{(d+D_i)^2-R1^2}, \tag{2.28}$$

where D_i is the distance between both circle centres in the Z-plane.

Then the necessary condition for having a pair of concentric circles in the t-plane is

$$\frac{d+D_i}{(d+D_i)^2-R1^2}=\frac{d}{d^2-R2^2}, \tag{2.29}$$

or

$$d=\frac{-(D_i^2+R2^2-R1^2)}{2D_i}\pm\sqrt{(\frac{D_i^2+R2^2-R1^2}{2D_i})^2-R2^2}. \tag{2.30}$$

The value of d is chosen so that $r1$ and $r2$ are positive.

Therefore the permeance between the non-concentric circles in the Z-plane is obtained by combining the equations (2.28), (2.26), (2.30) with

$$P_{fe}=2\mu_0\frac{A}{2}\ln(\frac{r1}{r2})+1.63\,\mu_0\frac{A}{2}. \tag{2.31}$$

2.3.5 Inner Fringing Permeance

a. Roter's Approach

The assumptions made by Roters [18] for computing the inner fringing on each limb are summarised on fig. 2.8. For each limb, the path is divided into two sections (a and b). For each of them, the computation is similar to the previous Roters' development for the outer fringing. As the paths are however two time shorter, the permeances are multiplied by a factor of two. The longest flux line (equal to $0.5\pi R1$) in section a is arbitrarily set equal to half of the slot width. Therefore $R1 = W/\pi$ and $X = R1 - G$. It follows:

$$P_{fi} = 4\mu_0 l \ln(\frac{W}{\pi G}) + 3.26\,\mu_0 l, \tag{2.32}$$

where l is equal to C for the central limb and to $C + W$ for the outer limb.

In this computation, the limit between fringing and cross slot leakage is thus arbitrarily fixed and does not vary with armature position. However, in the case of a rectangular slot, Carter [32] showed with the help of a conformal transformation that this limit is also a function of the airgap length and could be easily computed analytically. Therefore an equivalent conclusion is expected for the axisymmetric case. The choice of Roters' approximation, for both rectangular and axisymmetric problems is then very crude. Unfortunately the author is not aware of any work equivalent to Carter's development for the axisymmetric problem. For these reasons, the limit between fringing and cross slot leakage is computed in the thesis based on Carter's development applied to both rectangular and axisymmetric problems [6].

b. New Technique

b.1. Conformal Transformation

The computation of the field generated by a current in a slot of an electrical machine has been reported in many electromagnetic textbooks [31], [33], [32]. In fig. 2.11, the

[6] Carter's development has been widely used in the field of rotary machines, although the latter are not either a proper rectangular problem. This development led to a correction of the main airgap length in order to take the slot leakage into account.

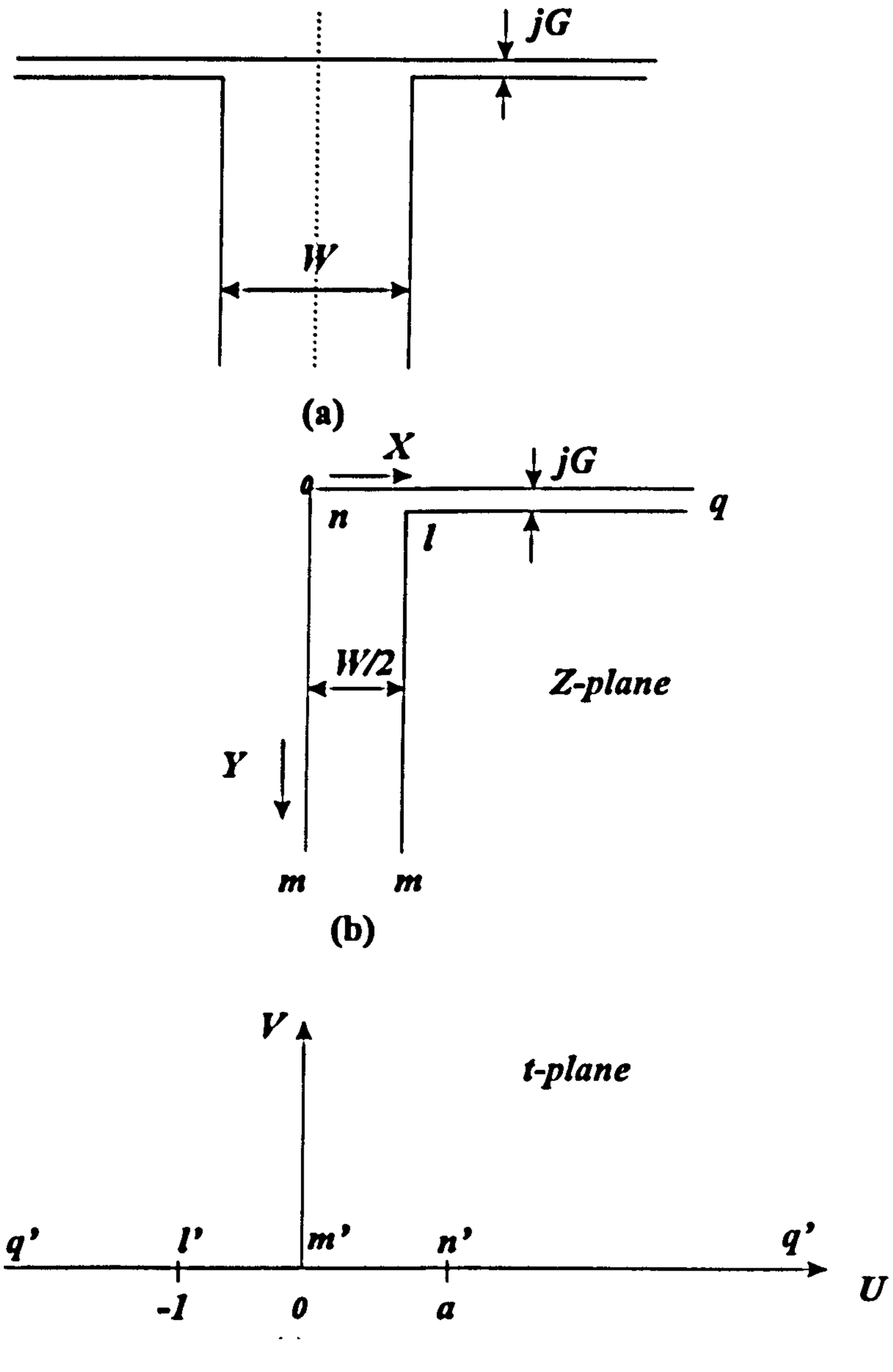

Figure 2.11: Conformal transformation for computing the field generated by a current in a slot

airgap G is assumed to be small compared with the width W of the slot. As far as the field in the airgap is concerned, the slot can be treated as infinitely deep with a current at the 'bottom' of it. For a current $2I$ the potentials of the poles (fig. 2.11.a) are I and $-I$ with respect to the plane surface at zero potential and the potential on the line of symmetry down the slot centre is also 0.

Thus, one half of fig. 2.11.a can be represented in the Z-plane as shown in fig. 2.11.b where the boundary mnq has a potential differing by I from that of the boundary mlq. The polygon has four vertices at l, m, n and q; and the limits in the t-plane,(fig. 2.11.c), are chosen to correspond to q.

Then the Schwarz-Christoffel equation, giving the transformation between the planes, is [31]:

$$\frac{dz}{dt} = S\,(t+1)^{1/2}\,t^{-1}\,(t-a)^{-1/2}, \tag{2.33}$$

with the pair of corresponding points being:

at l, $z = \frac{W}{2} + jG$ and $t = -1$,

at m, $z = j\infty$ and $t = 0$,

at n, $z = 0$ and $t = a$.

S and a are two parameters that can be evaluated by the method of residues. The origin in the Z-plane is chosen to correspond with the point $t = a$. After evaluation of all the parameters, it follows

$$z = \frac{2G}{\pi}[\frac{W}{2G}tan^{-1}\frac{Wu}{2G} + \frac{1}{2}ln\frac{1+u}{1-u}], \tag{2.34}$$

with

$$u^2 = \frac{t-a}{t+1}, \tag{2.35}$$

and

$$a = (\frac{2G}{W})^2. \tag{2.36}$$

b.2. Field Computation

To obtain the required field in the Z-plane it is necessary to have in the t-plane a potential I on the real axis between $-\infty$ and 0, and a potential 0 on the real axis between 0 and ∞. This gives a field in the t-plane described by

$$w = \frac{I}{\pi} ln t, \tag{2.37}$$

where $w = \phi + j\psi$ with ϕ the flux function, and ψ the potential function.

b.3. Evaluation of X

if $t = R e^{j\theta}$, then

$$\phi = \frac{I}{\pi} ln R. \tag{2.38}$$

The flux lines in the t-plane are concentric semi-circles with the plane origin for centre. The flux distribution in the Z-plane is more complex than the one in the t-plane. However by using the unique correspondence between points and field properties of each map, it is possible to evaluate in the Z-plane the position of the particular flux line which gives the transition between leakage and fringing. One 'extremity' of this flux line corresponds to the point n in the Z-plane on the line of symmetry, which corresponds to $t = a$ in the t-plane. Therefore the other 'extremity' is given by $t = -a$ in the t-plane. And the mapped point, in the Z-plane, is obtained by computing (2.34) with $t = -a$ and by replacing a with (2.36). Therefore it follows that X is equal to

$$X = Imz - G \tag{2.39}$$

and

$$Imz = \frac{G}{\pi}\left[\frac{W}{2G} ln\left|\frac{1+\frac{Wr}{2G}}{\frac{Wr}{2G}-1}\right| + tan^{-1}\left(\frac{2r}{1-r^2}\right)\right], \tag{2.40}$$

with

$$r = \sqrt{\left[\frac{2(W/2G)^2}{(1-(W/2G)^2)}\right]}. \tag{2.41}$$

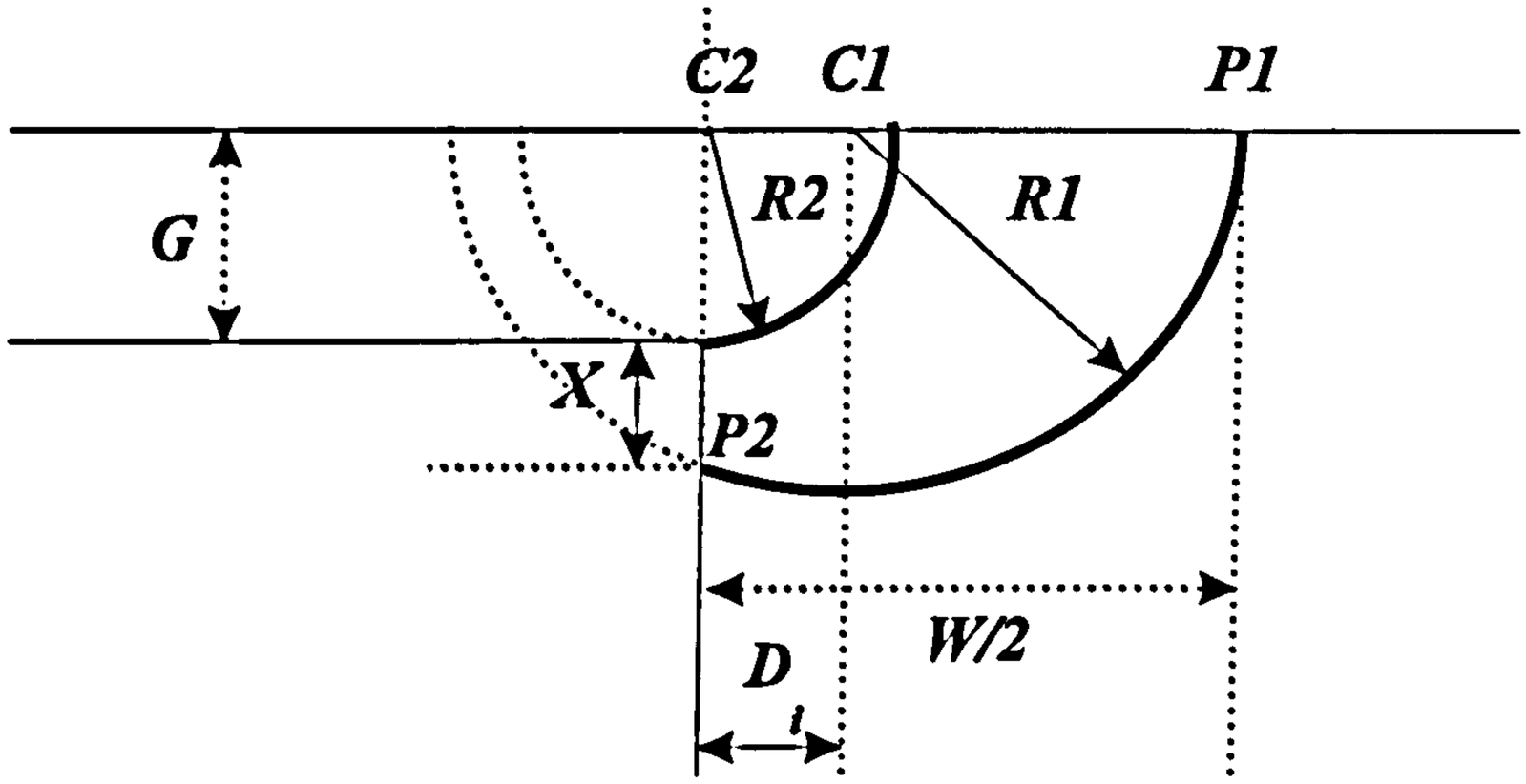

Figure 2.12: Inner fringing path in part *a*

b.4. Inner fringing permeance

The fringing permeance is divided into two parts (a and b) as shown in fig. 2.9. The permeance in part b is computed using Roters'method. Figure 2.12 summarises the geometric assumptions made for evaluating the inner fringing permeance corresponding to part a. The inner fringing flux within part a is delimited by two non-concentric circle arcs. A circle arc, centre $C1$ and radius $R1$, approximates the longest flux line such that $P1$ and $P2$ delimit the arc length. And the shorter flux line is given by a circle arc, centre $C2$ and radius $R2 = G$. Therefore, it follows

$$R1^2 = (G + X)^2 + D_i, \tag{2.42}$$

and

$$D_i = \frac{W}{2} - R1. \tag{2.43}$$

By combining eq.(2.42) and eq.(2.43), it results that

$$R1 = \frac{(\frac{W}{2})^2 + (G + X)^2}{W}, \tag{2.44}$$

and

$$D_i = \frac{(\frac{W}{2})^2 - (G + X)^2}{W}. \tag{2.45}$$

The fringing permeance of path a is then obtained by evaluating the bilinear transformation defined in the outer fringing section and by computing:

$$P_{fi} = 3.26\, l\, \mu_0 + 4\, \mu_0\, l \ln \frac{r1}{r2}, \tag{2.46}$$

where l is equal to C for the central limb and to $C + W$ for the outer limb. The values of $r1, r2, d$ are derived from equations (2.28), (2.26), (2.30) using (2.45), (2.44) and $R2 = G$.

2.3.6 Linear Equivalent Magnetic Circuit

The linear components of the magnetic equivalent circuit have been all evaluated analytically. Maximum care has been taken during their development in order to improve the accuracy compared with a more conventional approach. The apparent complexity of the resulting equations does not compromise the speed of a computer-aided design method. The choice of such a development is more about optimising the accuracy by combining several analytical techniques which may reduce the number of arbitrary assumptions and improve the dimension range of application. The complete network of airgap permeances is shown in fig. 2.13.

2.3.7 Nonlinear mmf Drop due to Leakage Flux

The leakage flux generates a certain amount of mmf drop in the limbs. The computation of this mmf requires some mathematical development due to the distribution of leakage throughout the slot. The following considerations are supported by fig 2.14, showing a schematic representation of a pot-core solenoid. The right hand-side of the solenoid includes the different airgap paths computed in the previous section. The left part shows the solenoid core divided into several sections. In particular, each limb contains three permeance elements called $Pcli$ (with i=1..3) for the central limb and $Peli$ (with i=1..3) for the outer limb. $Pcl1$ and $Pel1$ are the limb permeances defined on the same limb height as $PL1$. Similarly $Pcl2$ and $Pel2$ corresponds to $PL2$. $Pcl3$ and $Pel3$ cover the limb sections interacting with the leakage flux due to $PL3$ and the inner fringing

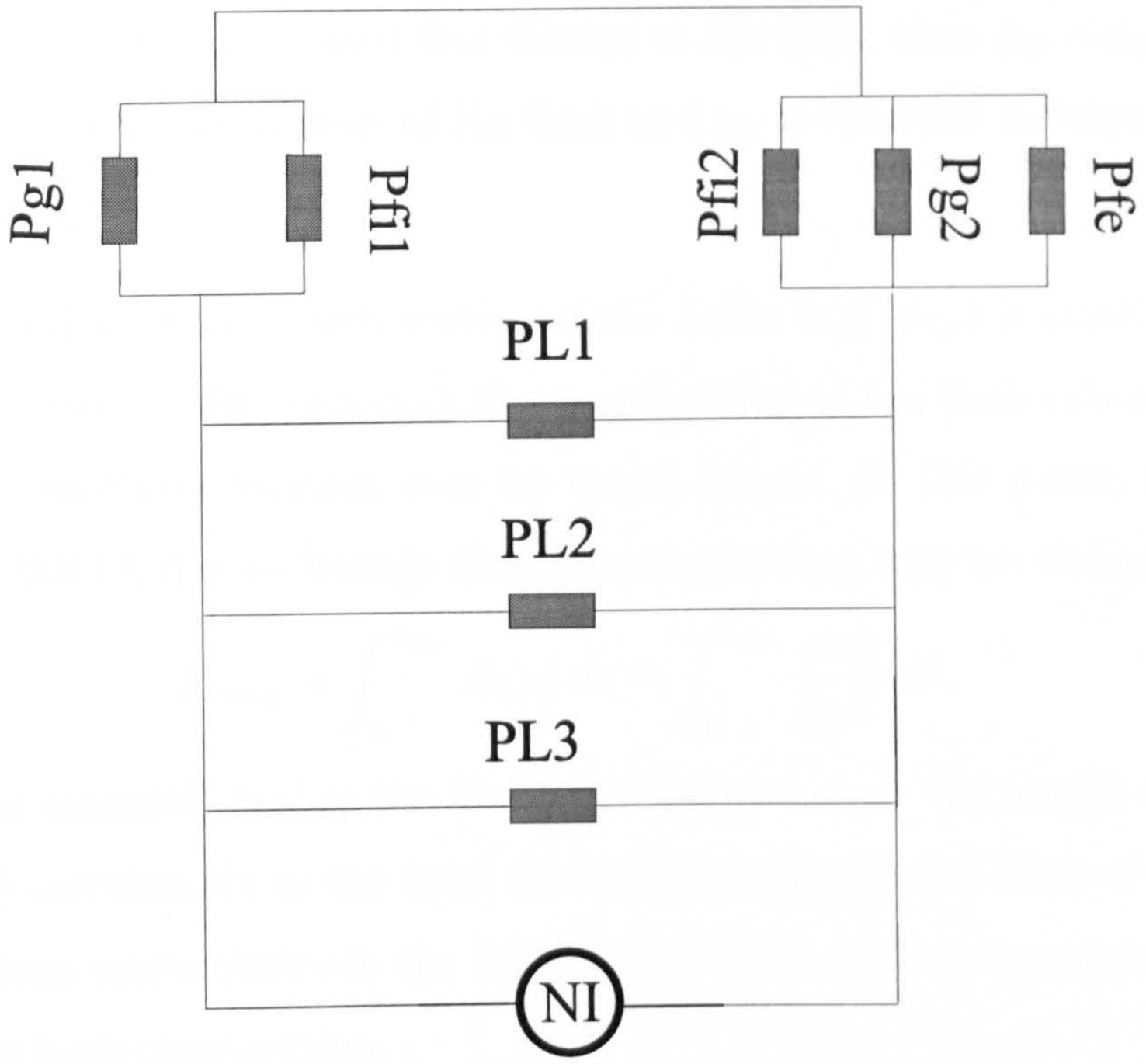

Figure 2.13: Linear magnetic equivalent circuit for axisymmetric actuator.

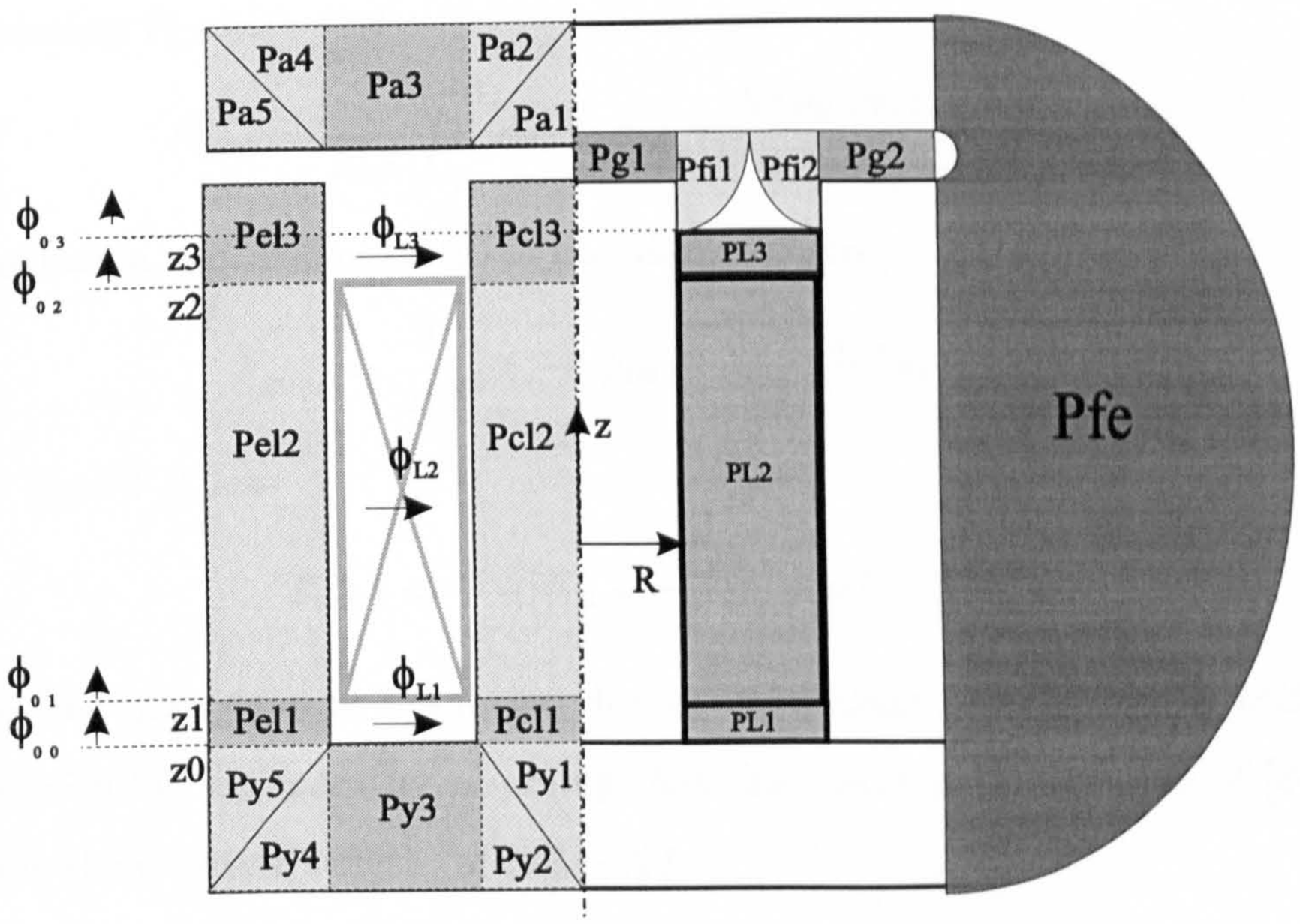

Figure 2.14: Nonlinear permeance distribution in the axisymmetric solenoid actuator

flux.

If ϕ_{03} defines the total constant flux flowing in the limb, then $\phi_{00} - \phi_{03} = \phi_L$ where ϕ_{00} is the total flux at the bottom of the limb and ϕ_L is the total leakage flux equal to $(\phi_{L1} + \phi_{L2} + \phi_{L3})$

When the leakage flux in each section of the limbs (e.g. ϕ_{L3}) is small compared to the respective constant flux (e.g.ϕ_{03}), the permeability of the limb subsection may be considered substantially constant over its entire length. In this event, the magneto-motive force (MMF), due to leakage flux over one section, may be obtained with [18]:

$$F_{mmf} = \int_{z_i}^{z_{i+1}} H(z)\, dz = \int_{z_i}^{z_{i+1}} \frac{\phi(z)}{\mu_i S}\, dz, \tag{2.47}$$

where H is the magnetic field in the limb at coordinate z, dz the length element along the limb; $\phi(z)$ corresponds to the total flux flowing through the limb at coordinate z; μ_i is the constant permeability in the limb section i due to the corresponding constant flux and S the limb cross-section.

When applied between z_2 and z_3, (2.47) changes into:

$$F_{mmf} = \frac{1}{\mu_3 S} \int_{z2}^{z3} \phi_{02} + \phi_{L3} - P_{L3}(z) N I\, dz\,. \tag{2.48}$$

Or by replacing P_{L3} with (2.9),

$$F_{mmf} = \frac{1}{\mu_3 S} \int_{z_2}^{z3} \phi_{02} + \phi_{L3} - \frac{N I \mu_0\, 2\pi (z - z_2)}{\ln \frac{A/2 - D}{C}}\, dz\,. \tag{2.49}$$

After integration, expression (2.49) is transformed into:

$$F_{mmf} = \frac{1}{\mu_3 S} [\phi_{02} + \phi_{L3} - \frac{N I P_{L3}}{2}]\ (z_3 - z_2). \tag{2.50}$$

As $\phi_{L3} = P_{L3} N I$, then

$$F_{mmf} = \frac{1}{\mu_3 S} [\phi_{02} + \frac{\phi_{L3}}{2}]\ (abcoil - X)\,. \tag{2.51}$$

Therefore, the mmf drop in the limbs, due to the leakage flux above the coil, can be estimated with fair accuracy by assuming that they carry a uniform flux of $[\phi_{02} + \frac{\phi_{L3}}{2}]$ throughout their section length $(abcoil - X)$.

As mentioned earlier in section 2.3.3, the leakage permeance P_{L1}, associated with the slot volume under the winding, generates an amount of leakage flux increasing with

the yoke saturation. The leakage permeance P_{L1} is set in this work as a permanent element of the MEC, producing an amount of mmf drop in the iron section, *uncoil*, equal to half of its total leakage flux ϕ_{L1}.

The computation of the mmf drop due to the leakage flux ϕ_{L2} requires a separate treatment due to the uniform distribution of the coil in the slot section under consideration. By applying (2.47) to one of the limb sections between z_1 and z_2, it follows:

$$F_{mmf} = \frac{1}{\mu_2.S} \int_{z_1}^{z_2} \phi_{01} + \phi_{L2} - P_{L2}(z) N(z) I \, dz \,, \tag{2.52}$$

or by expressing $P_{L2}(z)$ in (2.52),

$$F_{mmf} = \frac{1}{\mu_2.S} \int_{z_1}^{z_2} \phi_{01} + \phi_{L2} - \frac{NI\mu 0\, \pi (z - z_1)^2}{(z_2 - z_1) \ln \frac{A/2-D}{C}} \, dz \,, \tag{2.53}$$

where ϕ_{02} is in this case the constant flux flowing throughout the limbs up to the winding height. After integration, (2.53) changes into

$$F_{mmf} = \frac{1}{\mu_2 S} [(\phi_{01} + \phi_{L2}) hcoil - \frac{NI\mu_0\, \pi hcoil^2}{3 \ln \frac{A/2-D}{C}}] \,, \tag{2.54}$$

as $hcoil = (z_2 - z_1)$, or

$$F_{mmf} = \frac{1}{\mu_2 S} [(\phi_{01} + \phi_{L2})\, hcoil - \frac{NI P_{L2}\, hcoil}{3}] \,. \tag{2.55}$$

The relation between the total leakage permeance P_{L2}, as defined by eq. 2.18, and Φ_{L2} is:

$$\phi_{L2} = P_{L2} NI \,.$$

Using this expression in (2.55), it follows:

$$F_{mmf} = \frac{1}{\mu_2 S} [(\phi_{01} + \frac{2}{3}\phi_{L2})\, hcoil] \,. \tag{2.56}$$

The mmf drop in the limbs due to P_{L2} can be estimated with reasonable accuracy by assuming them to carry a uniform flux of $[\phi_{01} + \frac{2}{3}\phi_{L2}]$ throughout their length between z_1 and z_2. For the same reason, the computation of the flux linkage contribution ψ_{L2} due to P_{L2} would also lead to a factor 2/3 such that

$$\psi_{L2} = \frac{2}{3} P_{L2}\, N^2\, I. \tag{2.57}$$

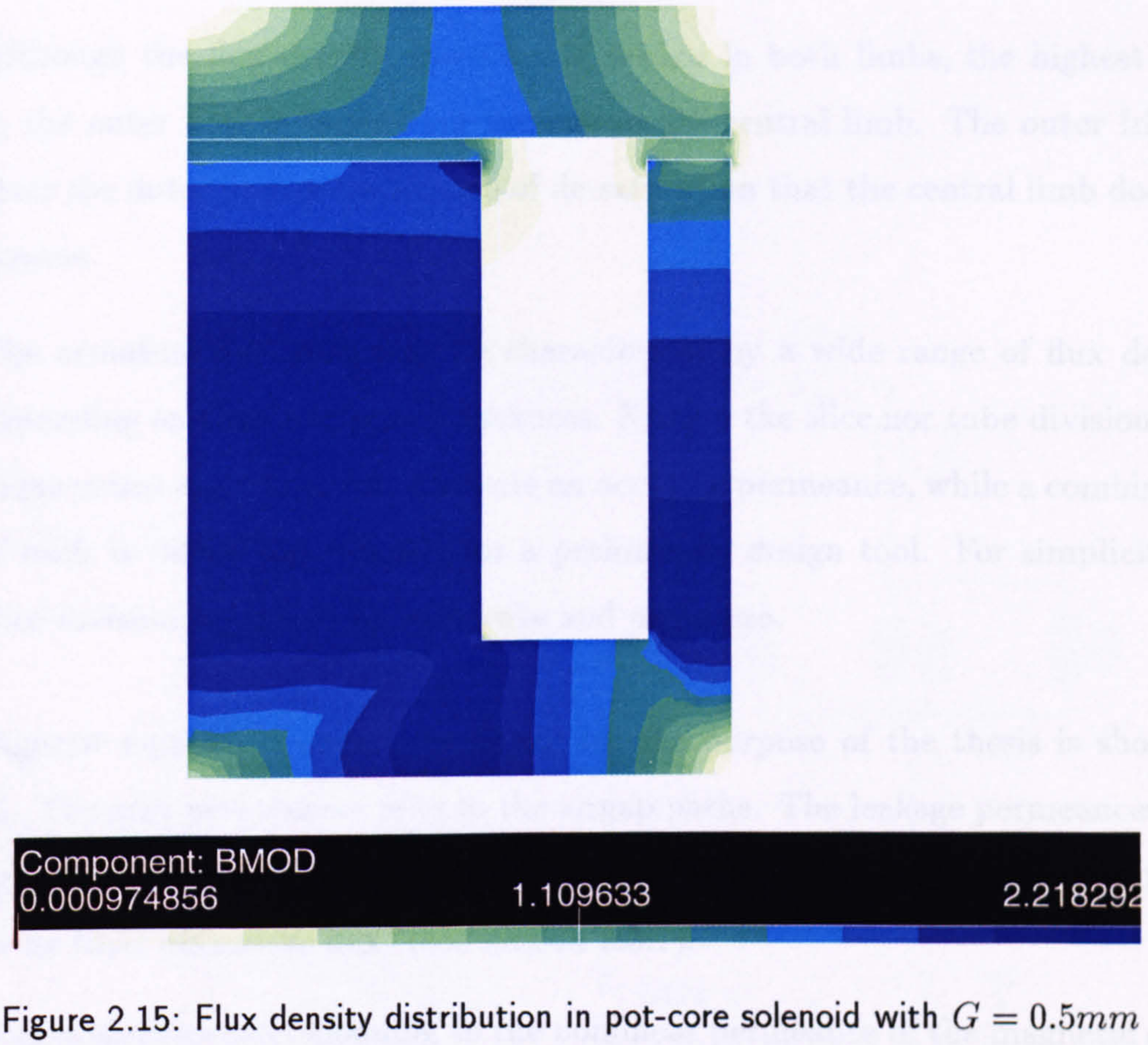

Figure 2.15: Flux density distribution in pot-core solenoid with $G = 0.5mm$

2.3.8 Configuration of the Nonlinear Magnetic Circuit

Useful information regarding the design of the nonlinear magnetic equivalent circuit can be drawn directly from the flux density plot given in fig. 2.15. The gap was set to 0.5mm and the given solenoid design is such that the cross-section area of the limbs is identical .

From this figure, it appears that:

1. The limbs are characterised by the highest values of flux density, decreasing from bottom to top. The flux density appears in most sections uniformly distributed, such that a division of the limbs in slices seems to be a sensible approximation.

2. The slot leakage is responsible for the major variation of flux density between limb slices. From this observation it follows that the evaluation of the mmf drop due to the leakage permeance P_{L2} is relatively approximate as the permeability

was assumed constant over the entire height of the winding.[7]

3. Although the flux density spectrum is similar in both limbs, the highest value in the outer limb is lower than the one in the central limb. The outer fringing gives the outer limb a mechanism of de-saturation that the central limb does not possess.

4. The armature and yoke may be characterised by a wide range of flux density, depending on their respective thickness. Neither the slice nor tube division technique seems appropriate to compute an accurate permeance, while a combination of both is rather too complex for a preliminary design tool. For simplicity the slice division is applied to both yoke and armature.

The magnetic equivalent circuit developed for the purpose of the thesis is shown in fig. 2.16. The grey permeances refer to the airgap paths. The leakage permeances have been split into two elements[8] in order to take into account the nonlinear mmf drop induced by their respective flux. (see section 2.3.7).

The core sections corresponding to the nonlinear permeance of the magnetic equivalent circuit are given in fig. 2.14. The average flux lengths and cross-section areas considered for the limb slices are summarised in table 2.2.

As shown in fig. 2.14, the armature and the yoke include a set of five permeances, which have been, each, divided into a subset of $N_{section}$. The average area and flux length used for computing the mmf drop in the ($5N_{section}$) yoke and armature sections are summarised in table 2.3. For the case of $Py1, Py2, Py4, Py5$ and $Pa1, Pa2, Pa4, Pa5$, the average area, through which the flux is flowing, is approximated by a conical surface whose area is given by:

$$Area = 2\pi \sqrt{K+1}\ (Dst\ Wth + \frac{Wth^2}{2}), \tag{2.58}$$

---

[7]This is an easy source of possible improvement that could be added on the work presented in this thesis. For high saturation an accurate network should model the limbs and slot with more than 3 subsections or 3 leakage permeances.

[8]However, only two-third of the leakage permeance P_{L2} has been used in the MEC. See discussion at section 2.3.3

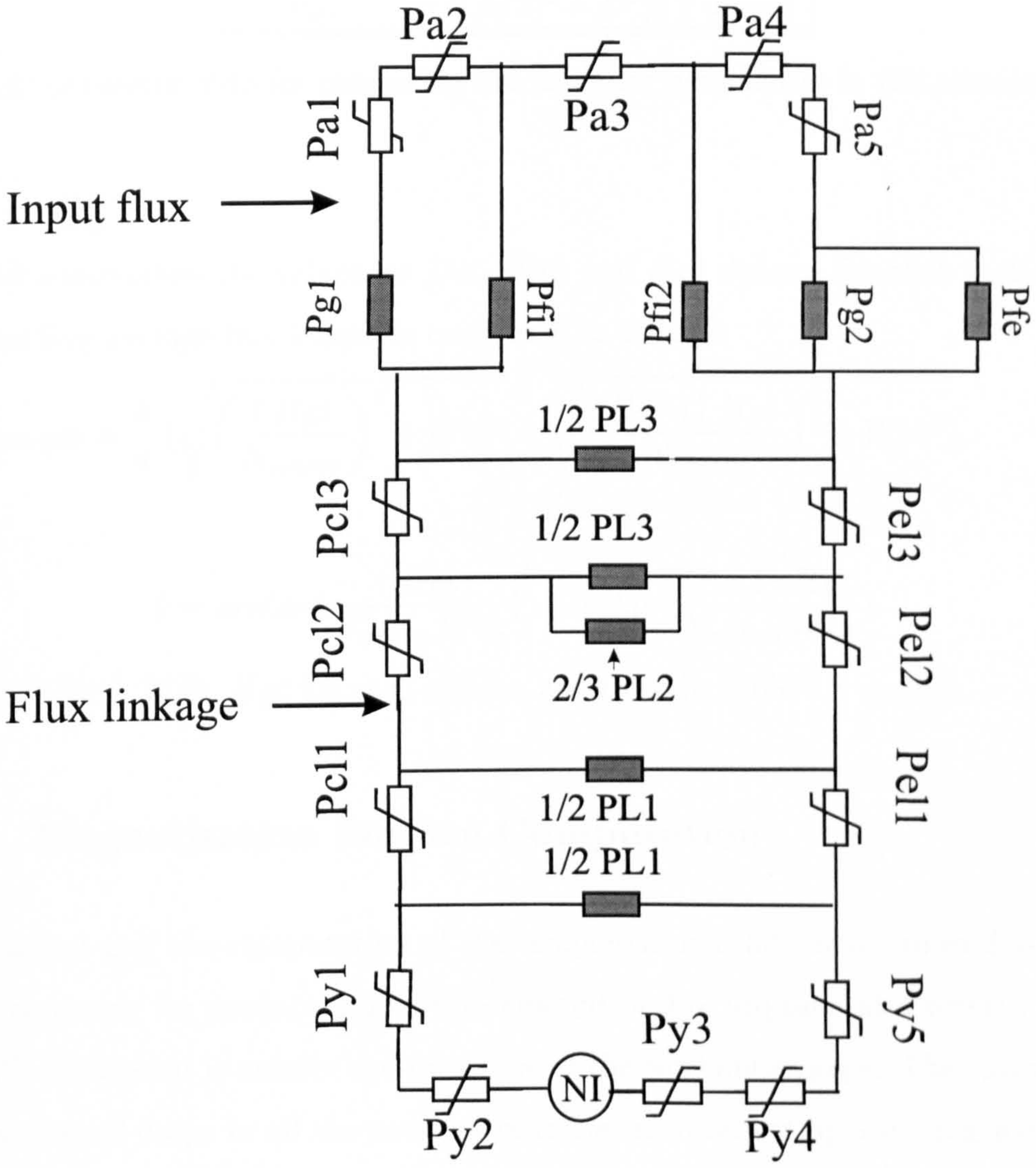

Figure 2.16: Nonlinear magnetic equivalent circuit for axisymmetric solenoid actuator

	Limb sections	
Permeance	Area	Length
P_{cl3}	πC^2	$abcoil$
P_{el3}	$\pi\left((A/2)^2 - D^2\right)$	$abcoil$
P_{cl2}	πC^2	$hcoil$
P_{el2}	$\pi\left((A/2)^2 - D^2\right)$	$hcoil$
P_{cl1}	πC^2	$uncoil$
P_{el1}	$\pi\left((A/2)^2 - D^2\right)$	$uncoil$

Table 2.2: Geometric data for computing the nonlinear permeances in the actuator limbs

with $K = (\frac{Hgt}{Wth})^2$.

Table 2.3 summarises the values for Dst, Wth and Hgt defined for each section. The corresponding average flux length is computed as follows:

$$Length = \frac{\theta}{4}\left(\sqrt{\left(\frac{l\ Hgt}{N_{section}}\right)^2 + Wth^2} + \sqrt{\left(\frac{(l-1)\ Hgt}{N_{section}}\right)^2 + Wth^2}\right), \tag{2.59}$$

with

$$\theta = arctan(\frac{l\ Hgt}{N_{section}\ Wth}) - arctan(\frac{(l-1)\ Hgt}{N_{section}\ Wth}). \tag{2.60}$$

The values for l, Wth, Hgt for each section are given in table 2.3 as well.

2.3.9 Magnetisation Surface Computation

At a constant gap the computation of the magnetisation data involves evaluating the current necessary for producing a certain amount of flux imposed at a certain point in the MEC. This point is usually chosen as one of the working airgaps. The computation of flux and mmf drops in all the network branches is obtained by applying Kirchhoff's Laws and Ampere's law which requires also the BH characteristic of the core steel.

With the network configuration as shown in fig. 2.16, only one simple iterative process is required in the overall nonlinear computation (between the permeance P_{fi2} and the group of permeances (P_{g2}, P_{fe}, P_{a5}, P_{a4})).

As shown in fig. 2.16, the flux linkage corresponds to the flux computed in the limb sections defined by P_{cl2} and P_{el2}. The total mmf drop obtained at the bottom of the

	Yoke sections	
Permeance	**Area**	**Length**
Py1	Eq. (2.58) with $Wth = \frac{Fj}{N_{section}}, Hgt = C, Dst = 0$	Eq.(2.59) with $l = j, Wth = F, Hgt = C$
Py2	Eq. (2.58) with $Wth = F, Hgt = \frac{C(N_{section}-j)}{N_{section}}, Dst = \frac{Cj}{N_{section}}$	Eq.(2.59) with $Wth = C, Hgt = F,$ $l = N_{section} + 1 - j,$
Py3	$2\pi F(C + Wj/N_{section})$	$W/N_{section}$
Py4	Eq. (2.58) with $Wth = F, Hgt = \frac{Dj}{N_{section}}, Dst = C + W$	Eq.(2.59) with $l = j, Wth = F, Hgt = C$
Py5	Eq. (2.58) with $Wth = \frac{F(N_{section}-j)}{N_{section}}, Hgt = D, Dst = C + W$	Eq.(2.59) with $Wth = F, Hgt = D,$ $l = N_{section} + 1 - j$
	Armature sections	
Permeance	**Area**	**Length**
Pa1	Eq. (2.58) with $Wth = \frac{Tj}{N_{section}}, Hgt = C, Dst = 0$	Eq.(2.59) with $l = j, Wth = T, IIgt = C$
Pa2	Eq. (2.58) with $Wth = T, Hgt = \frac{C(N_{section}-j)}{N_{section}}, Dst = \frac{Cj}{N_{section}}$	Eq.(2.59) with $Wth = C, IIgt = T,$ $l = N_{section} + 1 - j$
Pa3	$2\pi F(C + Wj/N_{section})$	$W/N_{section}$
Pa4	Eq. (2.58) with $Wth = T, Hgt = \frac{Dj}{N_{section}}, Dst = C + W$	Eq.(2.59) with $l = j, Wth = T, IIgt = C$
Pa5	Eq. (2.58) with $Wth = \frac{T(N_{section}-j)}{N_{section}}, Hgt = D, Dst = C + W$	Eq.(2.59) with $Wth = T, IIgt = D,$ $l = N_{section} + 1 - j$

Table 2.3: Geometric data for computing the nonlinear permeances in the yoke and armature.

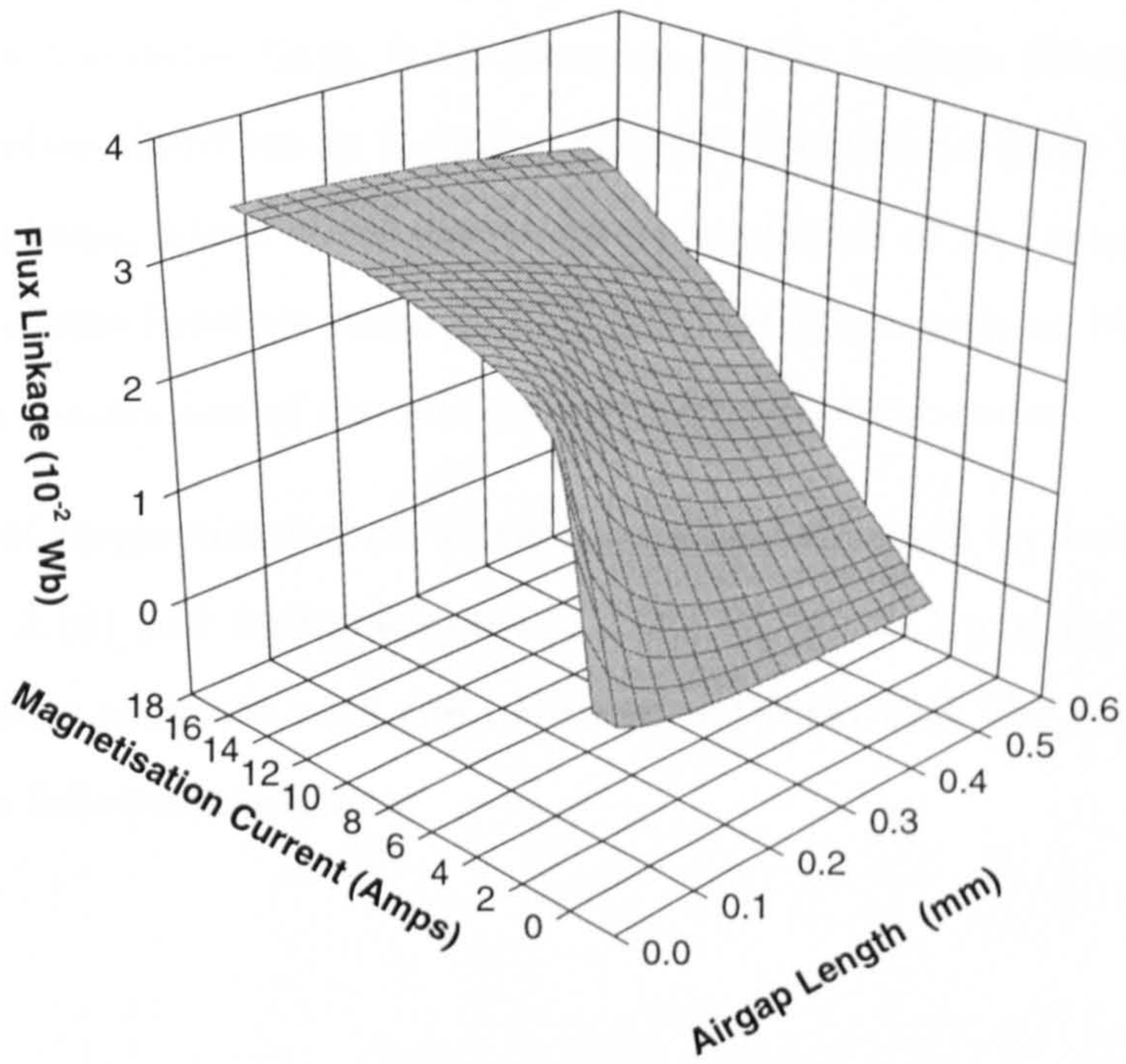

Figure 2.17: Magnetisation surface

MEC gives approximately the necessary amount of ampere-turns required to generate the imposed flux in one of the working airgaps.

By repeating the overall algorithm for a set of flux inputs and strokes, the complete magnetisation surface is rapidly generated. An example of such a surface is given in fig. 2.17.

2.3.10 Topology for High Current Level

The MEC configuration for high current level should take into account the mechanism of desaturation of the outer limb provided by the outer fringing permeance. An example of a better circuit topology is given in fig. 2.18 where the outer fringing permeance short-circuits most of the outer limb, reducing therefore the amount of mmf drop within the outer limb.

Such a configuration requires however a more tedious computation algorithm as the

amount of mmf drop on the outer fringing permeance is a function of the nonlinear mmf drop within the outer limb, itself function of the leakage fluxes. The network computation involves therefore an iteration process, including a large part of the magnetic circuit equations, which slows down the computation of the magnetisation data. If the iterative scheme involves some partial differentiation such as Newton-Raphson, an analytical approximation of the BH curves is also recommended.

An example of magnetisation curve computation, obtained by both networks (see fig. 2.16 and fig. 2.18) and finite-elements is given in fig. 4.11 and fig. 4.12. Although the results are more accurate with the modified network, only the simpler network is considered in the following chapters.

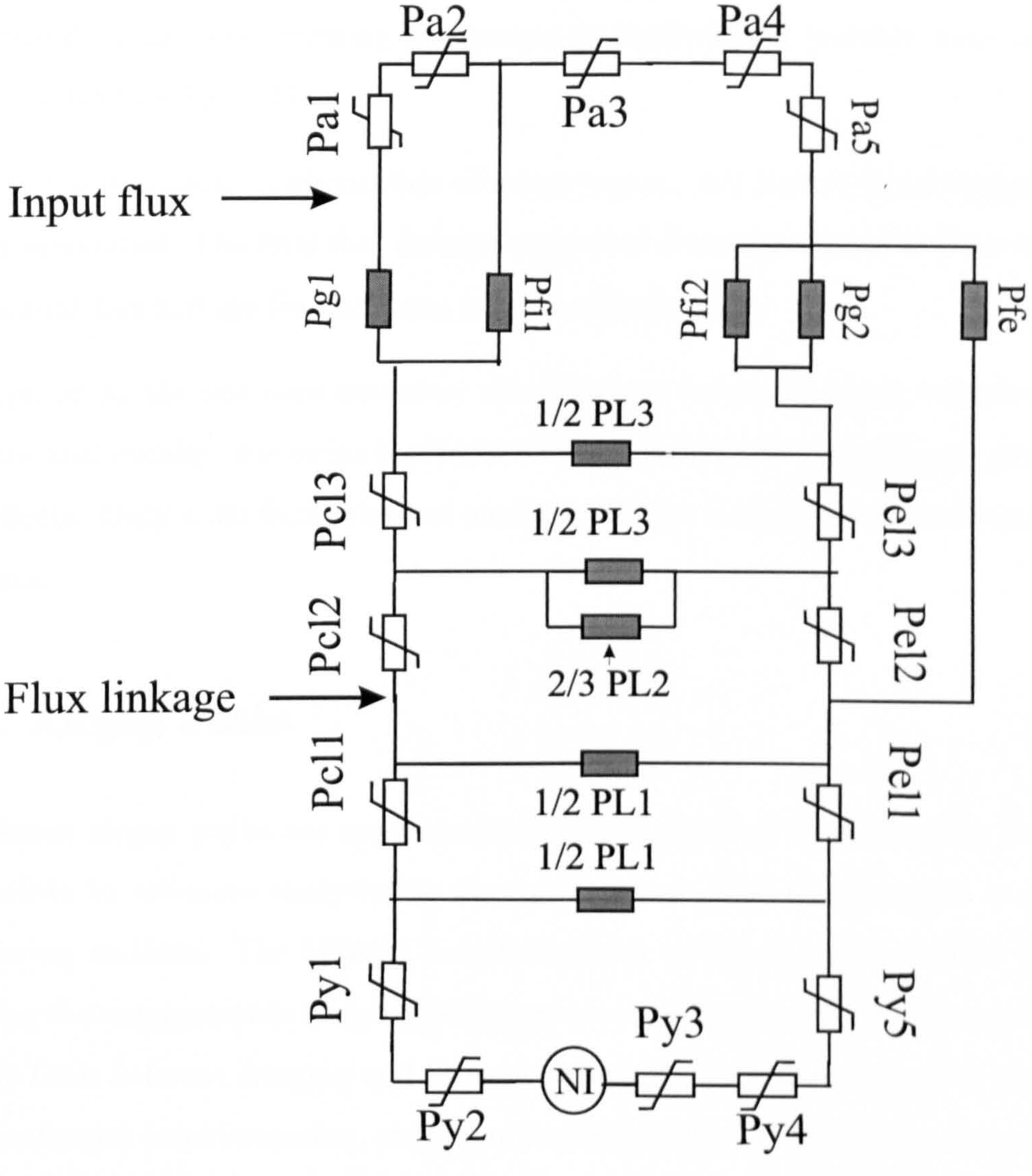

Figure 2.18: Modified magnetic equivalent circuit for high current simulation

2.4 Rectangular Solenoid Actuator

The magnetic equivalent circuit developed for the rectangular device is derived by analogy with the axisymmetric problem. For this reason, the general topology of the nonlinear network for E-core actuator is similar to the one obtained for the pot-core solenoid (fig. 2.16). However the central limb is also, in the rectangular case, characterised by an outer fringing permeance (end-effects) in parallel with the main gap permeance (see fig. 2.24).

Due to the symmetric configuration of this actuator, only half of the actual magnetic circuit is simulated. The final flux linkage computed from the circuit is then only half on the actual flux linkage for the same current consumption.

Compared to the pot-core actuator, the E-core is relatively more complex to approximate analytically, due to its short stack length leading to a significant proportion of end-effects. Only a 3D finite element analysis enables a complete evaluation of these end-effects.

2.4.1 Airgap Paths

The different airgap paths are approximated with a series of 2D flux paths for which it is possible to estimate analytically the permeances. The development is given in the following sections. The bilinear transformation, as developed in section 2.3.4 for computing the axisymmetric fringing permeances , is also applied for the E-core fringing flux. The limit between fringing and leakage on the slot side of each limb is also based on the conformal transformation, explained in section 2.3.5. Figure 2.1 supports again the following developments.

Working Airgap Permeance

The working airgap permeances P_{g1} and P_{g2} are evaluated as follows:

$$P_{g1} = \frac{\mu_0 \, L_{min} \, C}{G}, \tag{2.61}$$

and

$$P_{g2} = \frac{\mu_0 \, L_{min} \, (D - \frac{A-B}{2})}{G}, \tag{2.62}$$

where L_{min} is equal to the smallest value between $Astk$ and $Lstk$. The subscripts 1 and 2 refer to the central and outer limbs respectively.

Leakage Permeances

The computation of the permeances for leakage flux is based on the same general assumptions as the ones developed for the axisymmetric actuator (section 2.3.3). Therefore the leakage flux is divided into three sections: above (P_{L3}), on (P_{L2}) and under (P_{L1}) the coil. For simplification, the leakage permeance under the coil is computed in a similar way as above the coil. However compared to the axisymmetric case, the leakage permeances include several 2D paths labelled a, b, c as shown in fig. 2.19.

- For P_{L3}, it follows that

Section a

$$P_{L3a} = \frac{\mu_0 \, Lstk \, (abcoil - X)}{W} \tag{2.63}$$

.

Section b

In section b, the flux path is compared to a semicircular cylindrical volume of radius $W/2$, for which Roters computed the permeance as

$$P_{L3b} = 0.26 \, \mu_0 l, \tag{2.64}$$

where l is equal in this context to $(abcoil - X)$. In this computation, the mean length of the flux path is assumed to be equal to the line at midway between the diameter and the semicircunference (leading to $1.22W$). And the mean area is computed as the total volume divided by the mean flux length (leading to $\frac{\pi \, W^2}{8 \, 1.22 \, W}$). With the previous assumptions, it follows that the permeance in section b does not vary with the slot width. This permeance has to be counted twice for each side of the core.

Section *c*

The computation of section *c* involves two steps:

1. The flux is first assumed to flow between two concentric circles of radius $r1$ and $r2$ with $r1 > r2$ such that

$$P_{L3c} = \frac{\mu_0 \, (abcoil - X)}{\pi} \ln \frac{r1}{r2} \tag{2.65}$$

This permeance has to be counted twice for each side of the core.

2. In reality the circles are non-concentric such that $r1$ and $r2$ are computed with the equation of the bilinear transformation in which

$$R1 = \frac{C + D + W}{2}, \tag{2.66}$$

$$R2 = \frac{W}{2}, \tag{2.67}$$

$$D_i = \frac{|C - D|}{2}. \tag{2.68}$$

- Similarly the leakage permeance under the coil P_{L1} is evaluated by computing the three previous 2D flux paths in which the length of the limb section $(abcoil - X)$ should be replaced by *uncoil*. However another small leakage contribution has been also added to this permeance which takes into account the so-called 'corner to corner' leakage [18]. It is approximated with a spherical quadrant delimited by surface 1 and 2 shown in fig 2.20 for which Roters computed the permeance as being equal to $0.077\,\mu_0\,l$ where l is set to W in this context. This permeance has to be counted twice for each side of the core.

- The effective contribution of the leakage along the coil section (P_{L2}) is obtained by following the same procedure as the one developed for the axisymmetric actuator. From this calculation, it can be shown again that:

1. Only half of this permeance is actually producing a leakage flux which would link the total number of ampere-turns. This evaluation is based on the assumption that the iron is characterised by an infinite permeability.

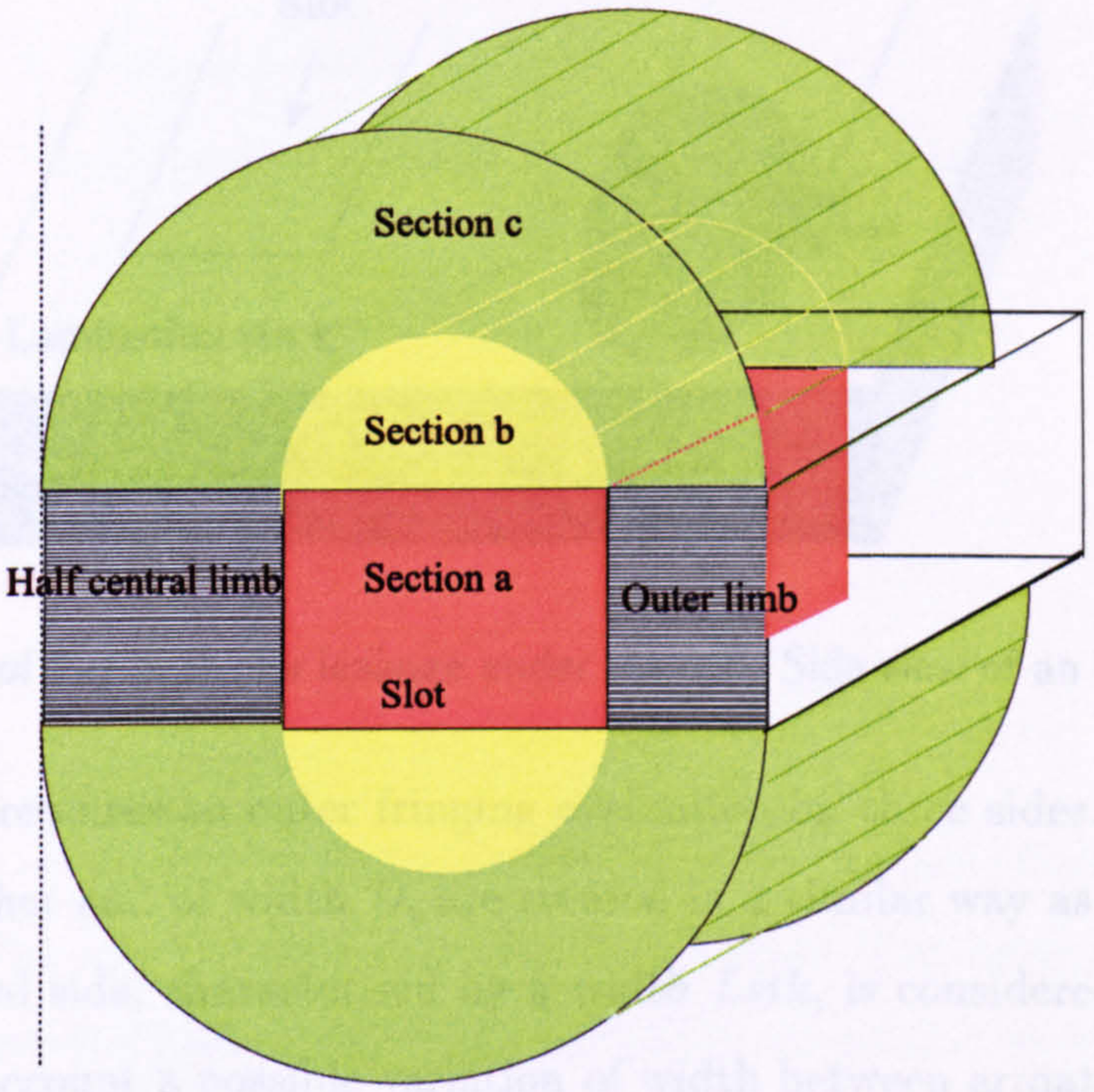

Figure 2.19: Top view of an E-core with approximated leakage flux paths.

2. A third only of the total leakage permeance is actually producing a flux linkage and only this part of the effective leakage permeance is taken into account in the magnetic equivalent circuit. (see discussion in section 2.3.3). The considered leakage permeance P_{L2} is then equal to one-third of the total permeance corresponding to the three 2D flux paths computed for P_{L3} (section a, b, c) in which $(abcoil - X)$ is however replaced by $hcoil$. It follows:

$$P_{L2} = \frac{\mu_0\ hcoil}{3}\left(\frac{Lstk}{W} + 0.52\ + \frac{2}{\pi}\ \ln\frac{r1}{r2}\right) \tag{2.69}$$

.

Outer Fringing Permeances

The E-core actuator requires the computation of an outer fringing permeance for each limb. The end-effects on the central limb involves only two sides of the limb, opposite to each other and characterised by a width C. The computation is supported by figure 2.21.

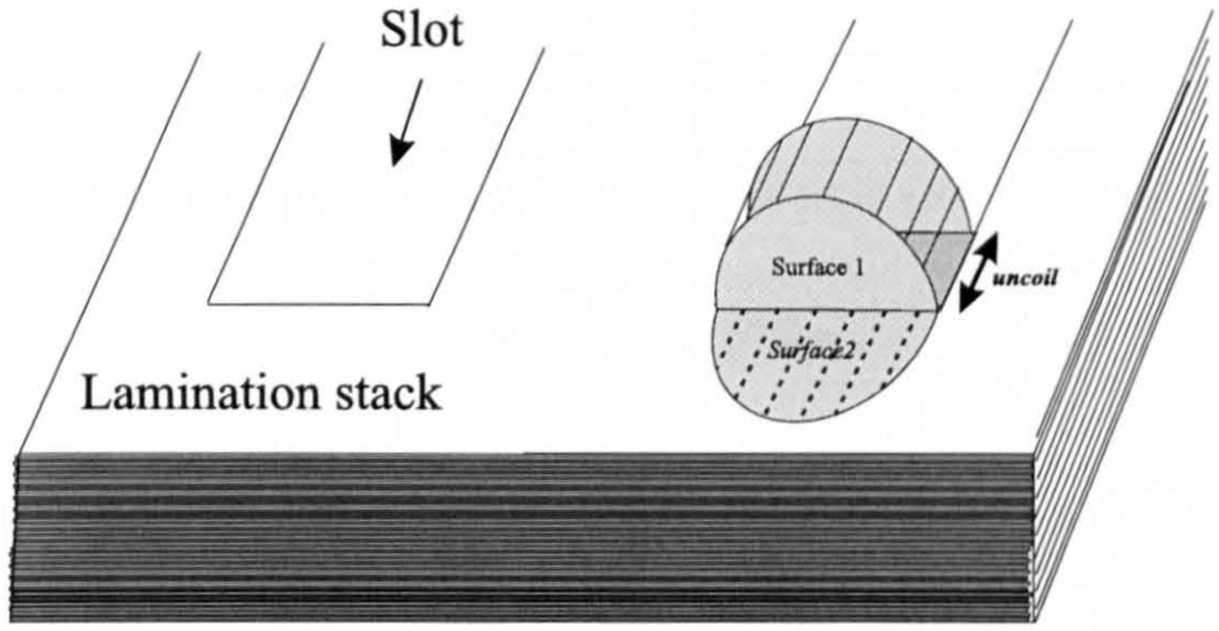

Figure 2.20: Details of flux paths for leakage under the coil. Side view of an E-core actuator.

The outer limb requires an outer fringing evaluation on three sides. Two of them, opposite to each other and of width D, are treated in a similar way as for the central limb case. The third side, characterised by a width $Lstk$, is considered separately in order to take into account a possible variation of width between armature and core [9]. This development is supported by fig. 2.22. In the event where there is a significant variation between the stack length of the core and the armature, a similar change in the fringing evaluation has to be added for the two previous sides of the outer limb and the two mentioned sides of the central limb.

- **Central Limb**

  For simplification the outer fringing for this limb is approximated by only two types of 2D flux paths called a and b in fig. 2.21.

  For section a, the computation requires once more the combination of:

$$P_{fe1a} = \frac{\mu_0 C}{\pi} \ln \frac{r1}{r2}, \tag{2.70}$$

  and the bilinear transformation given in section 2.3.4 with

$$R2 = \frac{G}{2}, \tag{2.71}$$

$$R1 = \frac{E + G + T}{2}, \tag{2.72}$$

[9] This is the case in practice due to the housing configuration in which the core and armature are placed within the fuel injector

$$D_i = \frac{E - T}{2}. \tag{2.73}$$

This permeance is counted twice.

For section b, the computation is given by eq. (2.64) where $l = C$:

$$P_{fe1b} = 0.26\,\mu_0\,C. \tag{2.74}$$

This permeance has also to be counted twice. Then

$$P_{fe1} = 2\,(P_{fe1a} + P_{fe1b}). \tag{2.75}$$

.

- **Outer Limb**

  As mentioned above the two first sides of this outer limb are affected by a similar end-effect as the one computed for the central limb. The same approximations are thus applied and lead to eq. (2.74) and (2.70) where C is replaced by D. The parameters for the bilinear transformation are also given by eq. (2.71), (2.72), (2.73).

The outer fringing flux on the third side has been divided into three 2D flux sections (a, b, c) as shown in fig. 2.22.

1. In section a, the airgap permeance is computed with eq. (2.74). However the mean flux length is here two time shorter, therefore:

$$P_{fe2a} = 0.52\,\mu_0\,Lstk. \tag{2.76}$$

2. In section b, the computation is straightforward and leads to:

$$P_{fe2b} = \frac{2\,\mu_0\,Lstk}{\pi}\,\ln\frac{A - B}{2\,G}. \tag{2.77}$$

3. In section c, the outer fringing flux is assumed to flow between two non-concentric circles by considering an imaginary E-core characterised with a same width for the armature and the core. The radius of the smaller circle is arbitrarily set to $(A - B)/4$ such that the parameters for the bilinear transformation given in section 2.3.4 are:

$$R2 = \frac{(A - B)}{4}, \tag{2.78}$$

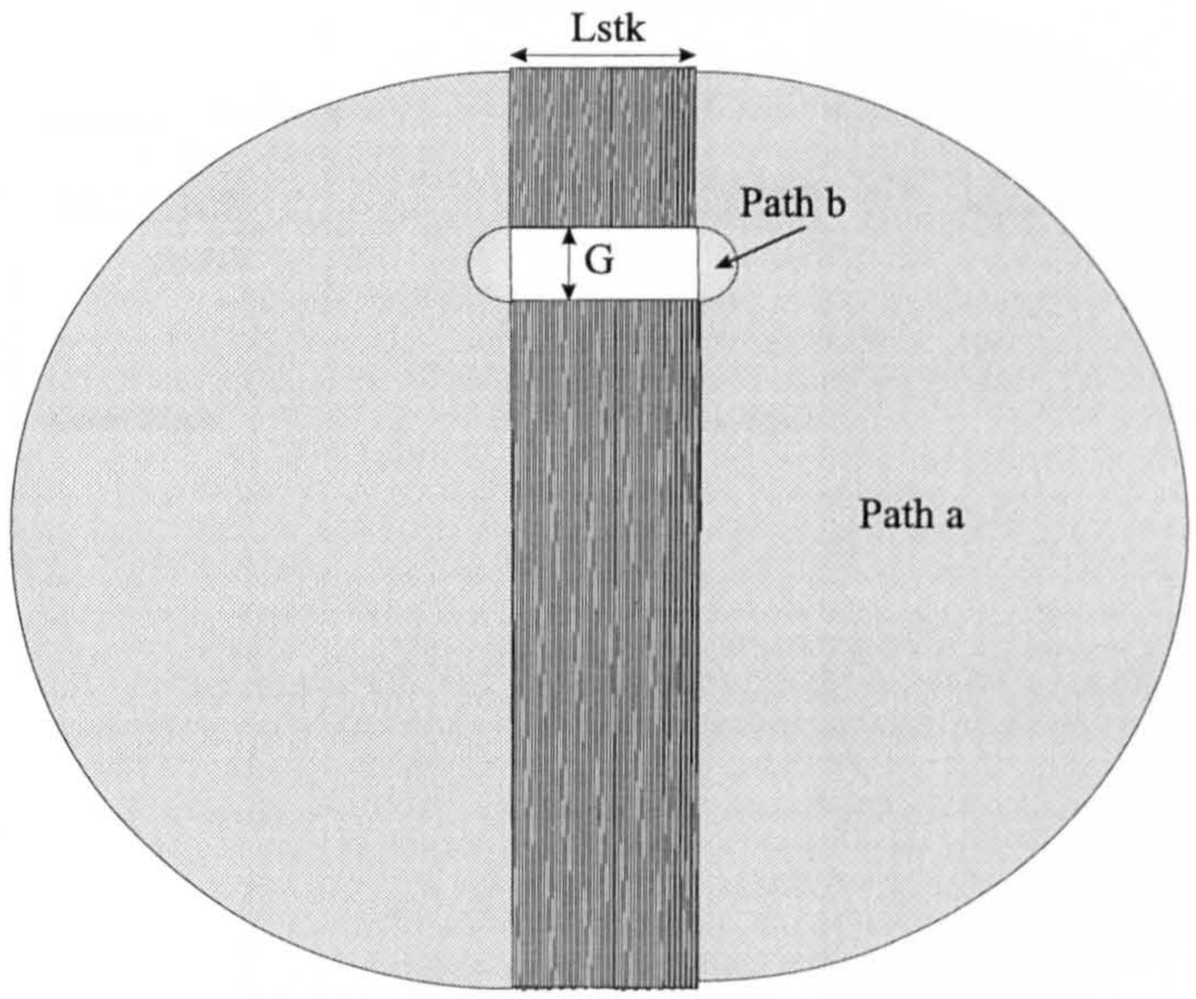

Figure 2.21: Approximation of the end-effects on the central limb for E-core actuator.

$$R1 = \frac{E + G + T}{2}, \tag{2.79}$$

$$D_i = \frac{E - T}{2}. \tag{2.80}$$

The total permeance P_{fe2} for the outer limb is obtained by adding the permeance of the five given 2D flux paths. More fringing flux coming from the corners [18] could be also considered in the computation of P_{fe2} .

Inner Fringing Permeances

The inner fringing flux (P_{fi}) is divided into two parts called a, b as shown in fig. 2.9. In each section, the permeance computation follows the same technique as the one developed for the axisymmetric actuator.

1. **Path** b

   For this section, the permeance is computed with eq. (2.76).

2. **Path** a

   The computation of section a is supported by fig. 2.12. The limit between fringing

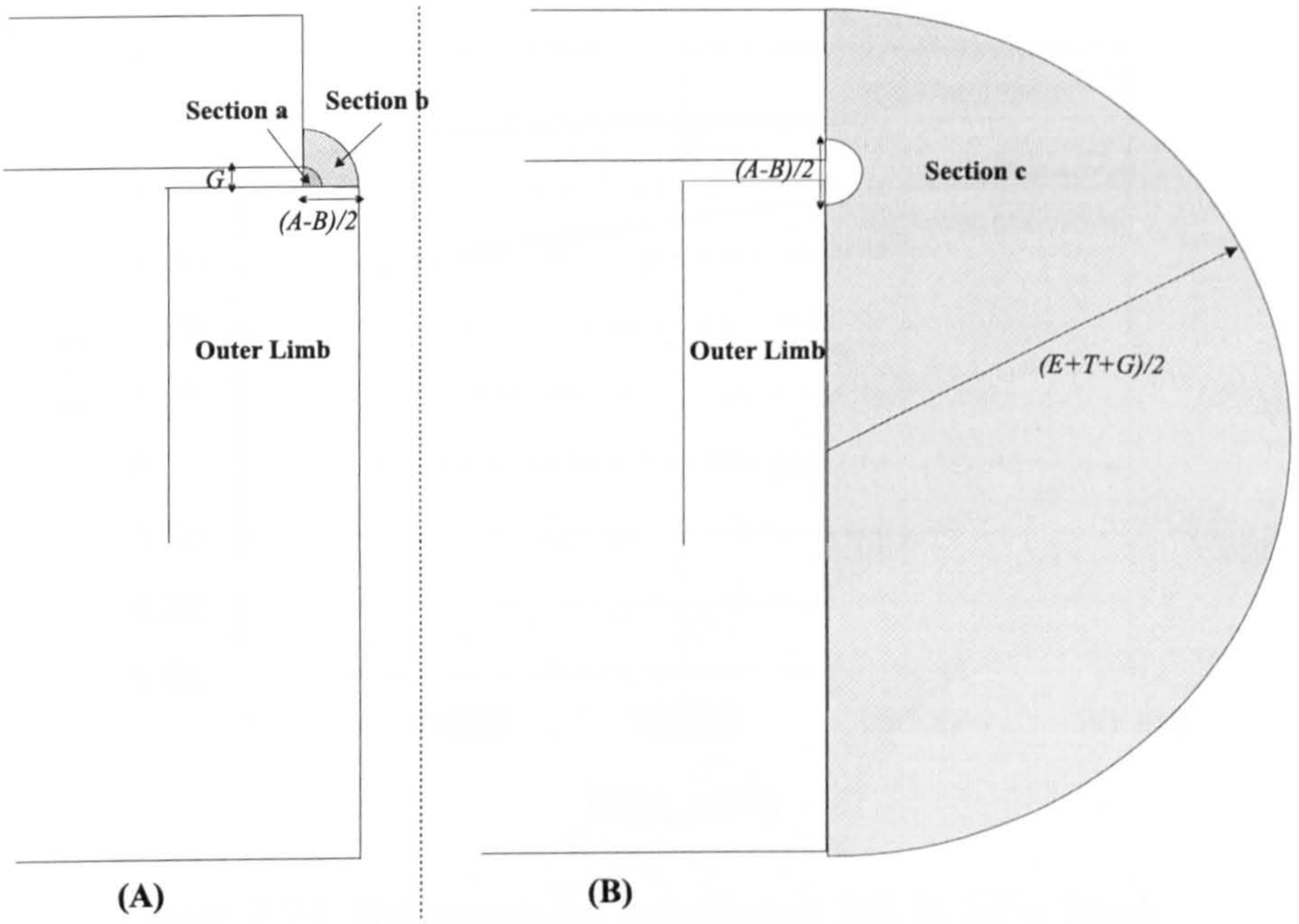

Figure 2.22: Approximation of the end-effects on one side of the outer limb.

and leakage (leading to the computation of X) is obtained from eq. (2.39) and eq. (2.40). The points $P1$ and $P2$ are computed respectively with eq. (2.43) and eq. (2.42). However the permeance between the two concentric circle arcs in a rectangular problem is equal to:

$$P_{fi} = \frac{2\mu_0 Lstk}{\pi} \ln \frac{r1}{r2}, \tag{2.81}$$

where $r1, r2$ are given by eq. (2.28) and (2.26). $R1, D_i$ are respectively evaluated from eq. (2.44), (2.45) and $R2 = G$.

2.4.2 Nonlinear Magnetic Equivalent Circuit

The nonlinear equivalent circuit for the rectangular device has been designed by analogy with the axisymmetric actuator and is given in fig. 2.24 in solid lines . The E-core iron is divided into the same number of sections as for the pot-core shown in fig. 2.14. The computation of the cross-section and mean flux length for each iron permeance is relatively straightforward and is not further discussed.

At the point of view of the dynamic performance, the rectangular device presents

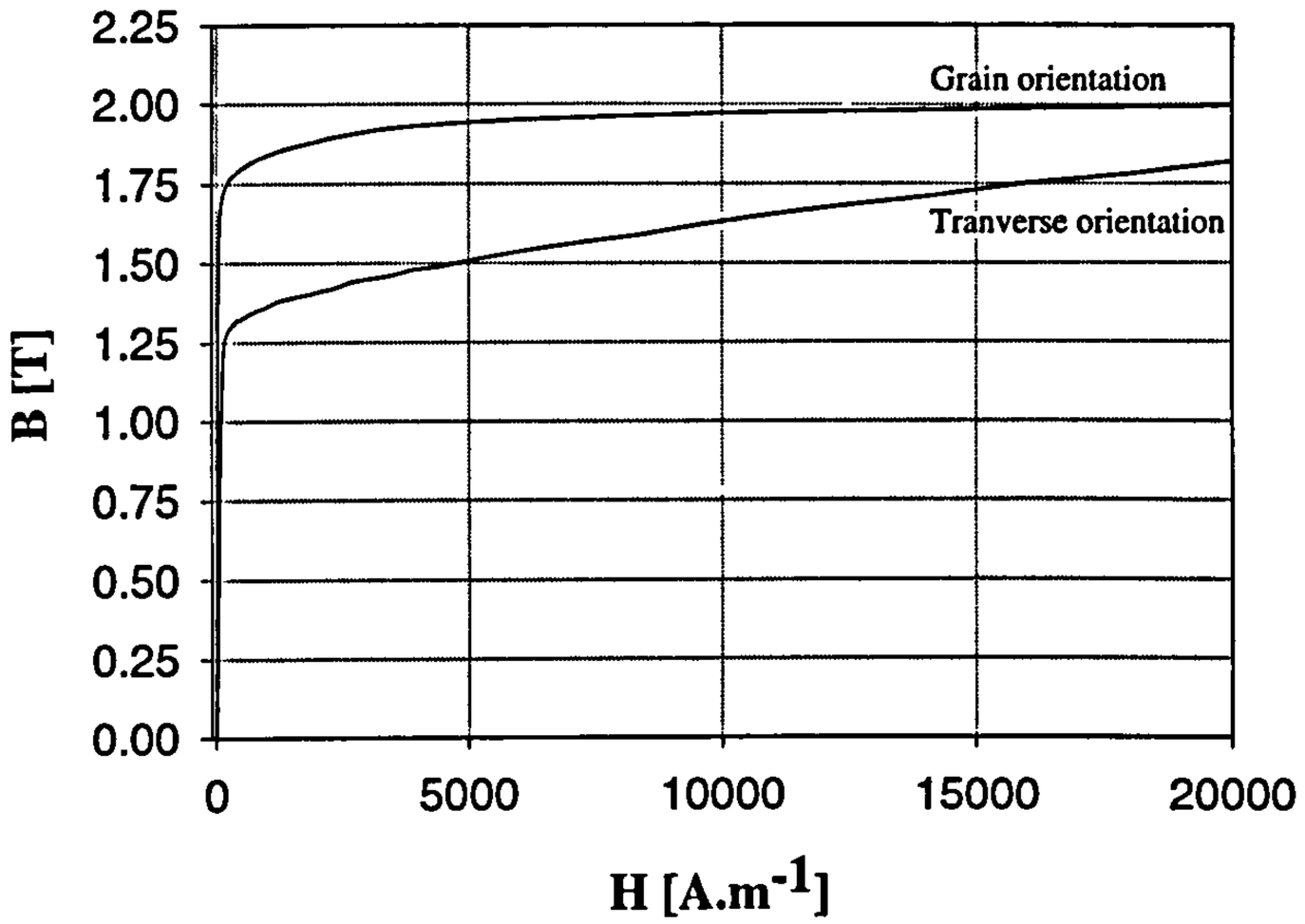

Figure 2.23: BH curves for anisotropic 2.5 % SiFe Steel.

a serious advantage compared to the pot-core. Indeed, the eddy current can be significantly reduced by laminating the core without affecting the cost. Therefore a stack factor (typically $0.95 < Fstk < 1$) should also be taken into account when computing the flux density in the iron section. The laminations are usually made of grain-oriented (anisotropic) steel such that the computation of the magnetisation curves for the E-core requires three different BH curves: two for the core and one for the solid iron armature. The first core BH curve, measured in the grain orientation, is applied for computing the mmf drop in both limbs and also in the yoke sections defined by $Py1$ and $Py5$ in fig. 2.14. The second BH curve is measured in the transverse direction of the grain orientation and is applied to the remainder sections of the yoke. The same approach has been considered in the finite-element analysis. Figure 2.23 shows the two measured BH curves corresponding to the anisotropic steel used in the E-core simulations. The E-core BH characteristics for the armature is given in fig. 4.2 and corresponds to the same steel as for the pot-core.

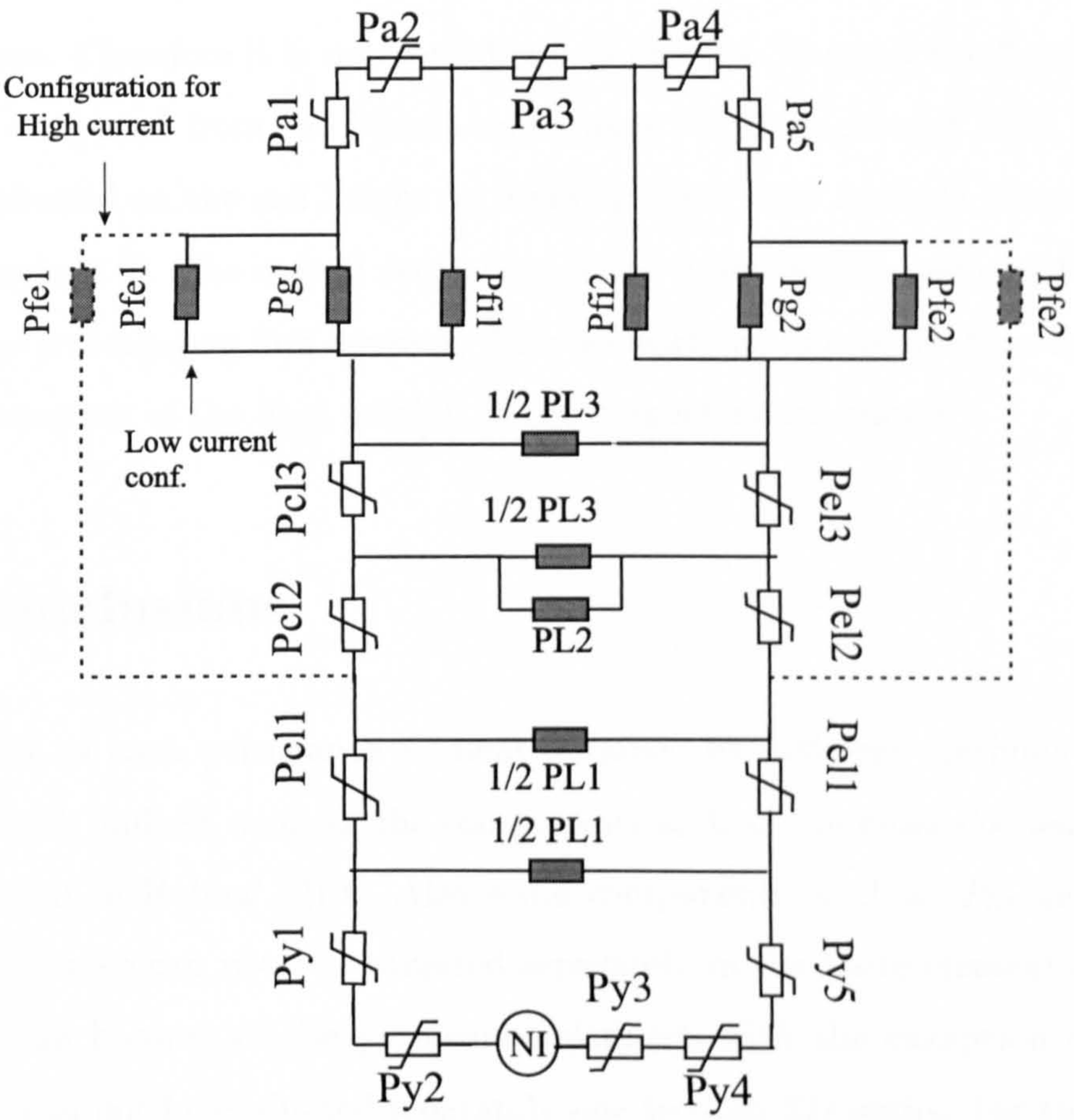

Figure 2.24: Magnetic equivalent circuit for the rectangular actuator.

2.4.3 Topology at High Current Level

The E-core magnetic equivalent network, as presented in solid lines in fig. 2.24 will not perform greatly at high saturation. The natural mechanism of de-saturation of the limbs, played by the outer fringing flux is not properly simulated in the network. A better circuit configuration could be the one shown in fig. 2.24 where the outer fringing permeances on both limbs are moved to the dashed line position. However such configuration requires a relatively complex iterative process and thus more computation time. Therefore it is not considered in practice. Instead the flux leakage ϕ_{L2} (fig. 2.14), computed from the branch containing $P_{L3}/2$ in parallel with P_{L2}, is uniformly distributed on the coil height by dividing these limb sections into a number of equal subsections [10]. The overall saturation of the limbs is then reduced for the same total leakage and fringing flux amount. This is clearly an approximation that modifies only the saturation of the final portion of the magnetisation curves.

2.5 Conclusions

A comparison of each permeance element obtained by different methods is not very straightforward. Indeed, some of the components such as the cross slot leakage P_{L1} or P_{L3} do not exit in Roters' MEC. Also some components, such as P_{L3} and the inner fringing permeance can not be evaluated separately in the finite-element analysis. In the case of the E-core, all the permeance elements with the exception of the main airgap ones, can not be evaluated separately due to their $3D$ paths. For these reasons, a comparison of the airgap elements is limited to the pot-core actuator and is performed when possible with a linear finite-element analysis and Roters'method.

The elimination of some of the airgap elements during the finite element analysis is obtained by setting a very low permeability (10^{-14}) in their region compared to the air permeability. The flux is therefore less willing to flow in these areas and concentrated within the regions under study. For a current level I and a number of turns N, the

[10] The number of subsections is given by the variable *Limbsec* in the program source code.

total flux ϕ, linking the coil, is computed over the winding cross-sections and the total permeance is obtained from :

$$P_{tot} = \frac{\phi}{NI}. \tag{2.82}$$

The equivalent computation of the total permeance *Ptot* with Roters'method or based on the analysis given in this chapter, depends on the airgap regions under study. The following analysis have been carried out:

1. The first study includes the main airgaps (P_{G1}, P_{G2}) and also the inner permeances called P_{fib}[11].

2. The second analysis includes the airgap components of the previous analysis and the outer fringing permeance (P_{fe}).

3. The third analysis contains the main airgap permeances , the inner fringing permeances (P_{fi}) for both limbs and the cross slot leakage permeance P_{L3} as they can not be separated. These is no equivalence for Roters'analysis in this case.

4. The last study includes all the previous airgap elements with also P_{L2} and P_{L1} .

The results of these analyses are summarised in table 2.4 and table 2.5 for two airgap lengths. The dimensions of the actuator are summarised in table 4.1. The permeances are given in (Wb/A) and the error between the analytical approaches and finite-elements is given between brackets for each study.

A comparison of the total airgap permeance has been also evaluated for a different pot-core for which A was set equal to 36 mm, E to 30 mm and D to 3 mm and a larger gap of 0.3mm. The *other* dimensions are summarised in table 4.1. The results are given in table 2.6.

In summary, the thesis development for the pot-core actuator performs better than Roters' approach for large gaps or more unusual designs (e.g large slot, long length).

[11]Although the inner fringing region was set up with very low permeability, the inner fringing elements ($Pfib$) could still be visible in the finite-element flux plots and has therefore be included in the analytical evaluation

Study number $G = 0.045mm$	FEA	Roters	New technique
1 (10^{-6} Wb/A)	3.025	2.995 (0.98%)	2.995 (0.98%)
2 (10^{-6} Wb/A)	3.092	3.054 (1.24%)	3.066 (0.85%)
3 (10^{-6} Wb/A)	3.128	-	3.110 (0.57%)
4 (10^{-6} Wb/A)	3.304	3.316 (0.34%)	3.267 (1.13%)

Table 2.4: Airgap permeance evaluation. Comparison between 2D finite-elements, Roters'method and the thesis approach.

Study number $G = 0.195mm$	FEA	Roters	New technique
1 (10^{-7} Wb/A)	7.185	7.080 (1.46%)	7.080 (1.46%)
2 (10^{-7} Wb/A)	7.453	7.494 (0.5%)	7.589 (1.82%)
3 (10^{-7} Wb/A)	7.744	-	7.770 (0.33%)
4 (10^{-7} Wb/A)	9.127	9.420 (3.2%)	9.144 (0.18%)

Table 2.5: Airgap permeance evaluation. Comparison between 2D finite-elements, Roters'method and the thesis approach.

However both methods reach a good level of accuracy, under 10 % error with finite-elements.

A comparison between the presented analytical approach, $2D$ and $3D$ finite-elements is also given in chapter 4 for the rectangular actuator, based on the computation of the magnetisation characteristics. The slope of the linear section of these curves depends greatly on the total airgap permeance computed at a fixed armature position.

From this chapter, it can already be concluded that:

- A magnetic equivalent circuit is a relatively flexible analytical method for analysing any type of electromagnetic device. The level of accuracy and the computational time are, to some extend, a function of the level of refinement.

- This method requires a relatively high development cost. The mathematic involved can be tedious and any new geometry or device requires in general to start the network design from scratch.

Study number $G = 0.3mm$	FEA	Roters	New technique
4 $(10^{-7}\ Wb/A)$	7.058	7.566 (7.185%)	7.127 (0.97%)

Table 2.6: Total airgap permeance evaluation. Comparison between 2D finite-elements, Roters'method and the thesis approach.

- A better network design requires a high level of understanding of the magnetic phenomena occurring in the actuator under consideration, a function of the device geometry, dimensions, armature position and also saturation level. For this reason, the support of a finite-element analysis, for observing and quantifying these phenomena is an invaluable advantage compared to 40 years ago.

- For a given machine, many different types of circuit may be considered. However the most difficult aspect remains an accurate estimation of the linear and non-linear permeances specific to each network. And unfortunately this aspect has not been widely covered in the literature and even less the notion of optimised magnetic circuit configuration.

Chapter 3

Magnetic Gauge Curve

3.1 Introduction

A computer-based modelling of a variable reluctance (VR) electromagnetic device is often required for conducting an optimisation routine or for testing some specific control scheme. Within such a process, the electromagnetic behavior of the given device is usually obtained by interpolating a set of test- or FE-data which relates the variation of flux linkage to the magnetisation current I and rotor position x. There are clearly some disadvantages associated with such a technique; a good level of accuracy requires a large amount of data to be evaluated and stored; the computational speed is decreased by the search process within the look-up table and the 2D interpolation; the evaluation of co-energy and magnetic force has to be numerically-based which reduces again the computational speed and overall accuracy

For switched reluctance or stepping motors, several techniques have been proposed over the years e.g. [22, 26, 25] considered respectively quadratic, exponential and cubic-spline functions fitted to measured magnetisation curves. [34] used a complete analytical model of the magnetisation curves allowing the direct evaluation of flux linkage for any current or rotor position. Newer approaches involved ANN or fuzzy logic trained on a set of test- or FE-data [35, 36].

The aim of this chapter is to introduce, develop and discuss a different technique for computing and handling the electromagnetic information of any type of variable reluctance device. This concept was inspired by the work carried out by Miller [37], who developed an interpolation function between the magnetisation characteristics corresponding to the aligned and unaligned positions of a switched reluctance machine (SRM). In this paper, the gauge curve technique has been re-defined and enlarged to include any type of VR device. It shows that the gauge curve is not only a mathematical tool but involves useful design information. The general technique for evaluating the interpolation function is first developed and then demonstrated on two different examples: the flat-faced linear actuator and the doubly salient rotary machine more commonly known as the switched reluctance machine.

3.1.1 General Theory

A gauge curve is defined in the thesis as an interpolation function between the magnetisation curves $\psi(I)$ corresponding to the minimum and maximum inductance positions of any type of variable-reluctance electromagnetic device.

The general expression of the gauge curve for VR machines is obtained by computing, for any intermediate rotor position i, a normalised current $I_N(x_i, \psi)$ at constant flux linkage :

$$I_N(x_i, \psi) = \frac{I(x_i, \psi) - I_a(\psi)}{I_u(\psi) - I_a(\psi)}, \tag{3.1}$$

with $\psi = Cst$ and where $I_a(\psi) = I(\psi, x_a)$ and $I_u(\psi) = I(\psi, x_u)$.
The subscripts a and u refer respectively in all equations to the maximum and minimum inductance position for any type of VR machines. The subscript i refers to the current position.

This operation can be analytically expressed by applying Ampere's law

$$N\,I(x_i, \phi) = \frac{\phi}{P_{gtot}(x_i)} + \sum_j H_{ij}(\phi)\, l_{ij}, \tag{3.2}$$

at the different rotor positions (a, u, i) and at constant flux linkage ($\psi = Cst$).
In eq. (3.2), $NI(x_i, \phi)$ is the total number of Ampere-turns and $P_{gtot}(x_i)$ is the total

airgap permeance at position x_i (including fringing and cross slot leakage). ϕ is the flux computed as the ratio of flux linkage ψ with the number of turns. The second term on the right-hand side represents the total mmf drop within the iron for the flux linkage under consideration.

By combining (3.1) with (3.2), it follows

$$I_N(x_i,\phi) = \frac{\frac{1}{P_{gtot}(x_i)} - \frac{1}{P_{gtot}(x_a)} + \left(\sum_j H_{ij}\, l_{ij} - \sum_j H_{aj}\, l_{aj}\right)/\phi}{\frac{1}{P_{gtot}(x_u)} - \frac{1}{P_{gtot}(x_a)} + \left(\sum_j H_{uj}\, l_{uj} - \sum_j H_{aj}\, l_{aj}\right)/\phi}, \tag{3.3}$$

This is the general equation of the gauge curve from which the final expression for each type of electromagnetic device can be derived by making appropriate assumptions.

In general, the interpolation function varies with flux and rotor position and corresponds to a set of curves defined, each, at constant flux linkage. If the airgap permeances are assumed to be independent of the flux level, the contribution due to flux and to airgap length appears in separate terms. Therefore when saturation is still negligible compared to the mmf drop in the gaps, a good approximation of the gauge curve may be derived from the knowledge of the total airgap permeance only.

The gauge curve model, based on a normalised current technique as presented here, is relatively new. An interpolation function has already been applied by Miller [37] between the aligned and unaligned magnetisation characteristics of a switched reluctance motor. But his approach took another direction and involved modelling the gauge curve with a set of piecewise functions, describing the variation of a normalised flux linkage $\psi_N(\theta)$ with rotor position θ. At any intermediate position, the relation between the normalised value of flux linkage, constant at any current level, and the actual flux linkage was given by :

$$\psi(I,\theta) = \psi_N(\theta)(\psi(I,\theta_a) - \psi(I,\theta_u)) + \psi(I,\theta_u). \tag{3.4}$$

The choice, in the thesis of a normalised current model, instead of a normalised flux linkage model, resulted from a comparison of both model performances.

Model 1	Model 2
$\psi(x)$ with $I = Cst$	$I(x)$ with $\psi = Cst$
$\psi_N(x, I) = \frac{\psi(x,I)-\psi_u(I)}{\psi_a(I)-\psi_u(I)}$	$I_N(x, \psi) = \frac{I(x,\psi)-I_a(\psi)}{I_u(\psi)-I_a(\psi)}$

Table 3.1: Normalisation Equations

3.1.2 Comparison of Model Performance

The two possible gauge curve models for generating the intermediate magnetisation curves of any electromagnetic devices are summarised in table 3.1. Although their performance may vary significantly with the type of machines, their main characteristics (or differences) may appear already clearly by applying both techniques on a set of magnetisation data.

Each model is based on a different sub-set of functions, derived from the magnetisation data. For example, if the magnetisation surface, given in fig. 2.17 and corresponding to a axisymmetric flat faced actuator, is taken as the basis of this discussion, it follows from table 3.1 that:

Model 1 is based on the sub-set of curves $\psi(x)$ defined at constant current levels.

Figure 3.1 shows the sub-set retrieved from fig. 2.17.

Model 2 is derived from the sub-set of curves $I(x)$ defined at constant flux linkage.

Figure 3.2 shows this sub-set retrieved from fig. 2.17.

The gauge curve equations (ψ_{Ni} for model 1 and I_{Ni} for model 2), given in table 3.1, are then applied to their respective set of curves and aim to remove the magnetic information which is already contained in the magnetisation curves corresponding to the minimum and maximum inductance positions.

The result of this operation is shown in fig 3.3 and 3.4 and is discussed below:

Normalised flux Model

In fig. 3.1 the shape of the curves $\psi(x)$ varies significantly with the current level. Indeed at high currents, saturation dominates the actuator magnetic behaviour at any armature position. This gives a relative 'linear shape' to the curves $\psi(x)$. At very low currents, the curves are, however, a function of the nonlinear variation of airgap permeances with rotor position (inversely proportional). At middle current level, both effects (current and armature position) play an important role and modify simultaneously the curve characteristics. The result of the normalisation, shown in fig. 3.3, then follows: the curves ψ_{Ni} are strongly dependent on both armature position and current level. The normalisation does not lead to major simplifications.

Similarly to the normalised current model (see section 3.1.1) , an analytical equation of this model $\psi_N(x_i, I)$ is deduced by combining Ampere's law (3.2) and (3.4):

$$\psi_N(x_i, I) = \frac{P_{gtot}(x_i) - P_{gtot}(x_u) + (P_{gtot}(x_i) \sum H_i\, l_i - P_{gtot}(x_u) \sum H_u\, l_u)\,/NI}{P_{gtot}(x_a) - P_{gtot}(x_u) + (P_{gtot} x_a \sum H_a\, l_a - P_{gtot}(x_u) \sum H_u\, l_u)\,/NI}. \quad (3.5)$$

At the opposite of eq. (3.1), eq. (3.5) includes nonlinear contribution of armature position and current (saturation) such that the resulting expression does not easily allow any simplification.

Normalised current Model

In figure 3.2 the shape of the curves $I(x)$ is relatively independent of the flux linkage level. Indeed, at constant flux linkage, each curve in fig 3.2 operates on a very small portion of the nonlinear BH characteristic of the actuator material. Thus the saturation uniformly affects each point of a same curve $I(x)$ and 'disappears' in major part with the normalisation technique. Therefore it follows that the normalised functions I_{Ni} are gathered in a very dense set as shown fig 3.4 in solid lines, which can be approximated by a single interpolation curve, a function only of the armature position.

The nonlinear content has been minimised in this model allowing a simpler analytical expression of the gauge curve. In general the gauge curve associated with other types of electromagnetic device is not as simple as the one developed here for the flat-faced armature actuators; but it is still the most efficient model as the nonlinear

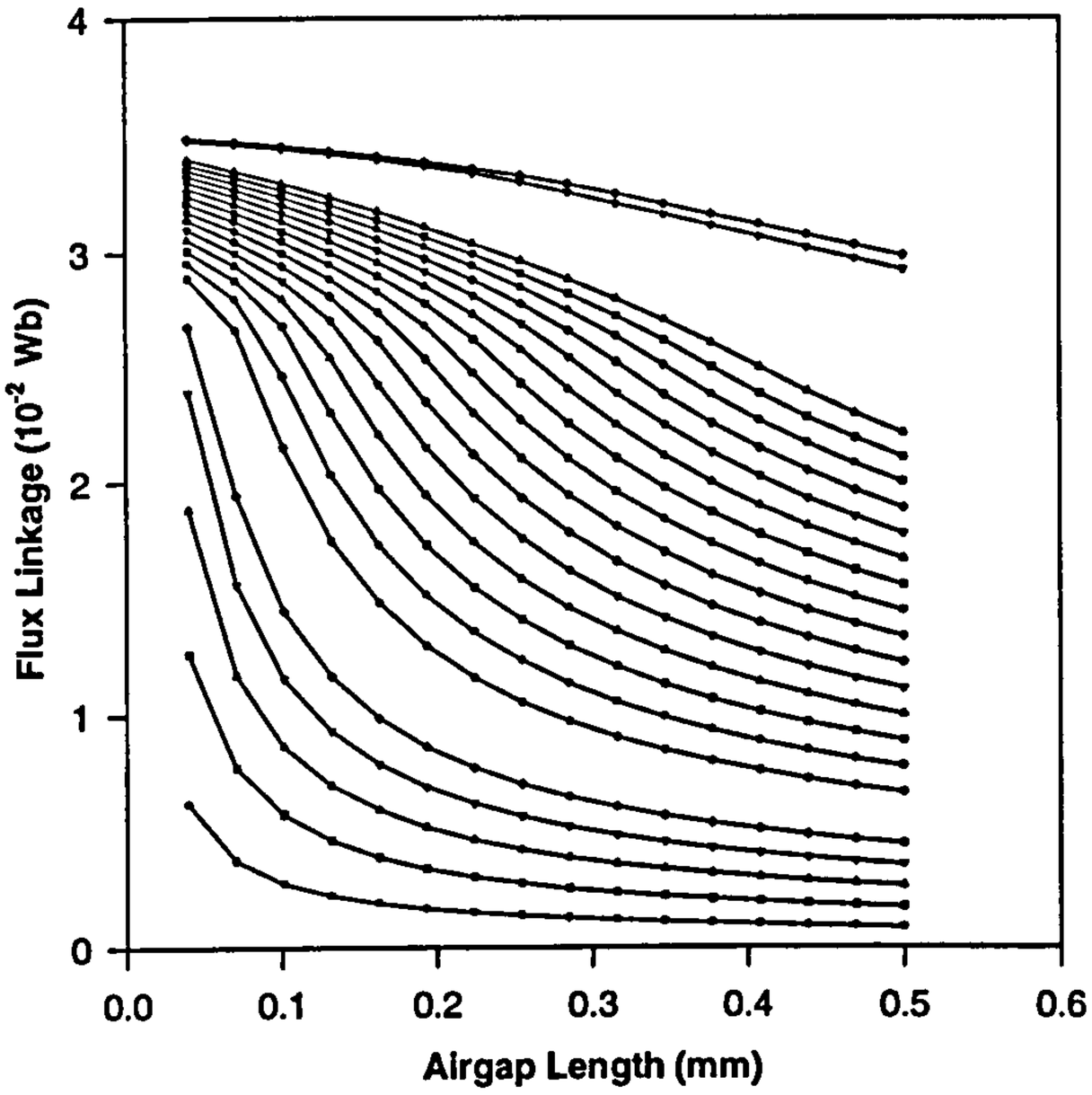

Figure 3.1: Flux linkage versus position at $I = cst$.

content of the gauge curve will be reduced to the contribution specific to the intermediate positions (e.g. local saturation). The bulk saturation, common to every position at a constant flux linkage is already included in the magnetisation characteristics corresponding to the minimum and maximum inductance positions and is removed from the gauge curve content through the normalisation method (see eq. (3.1)).

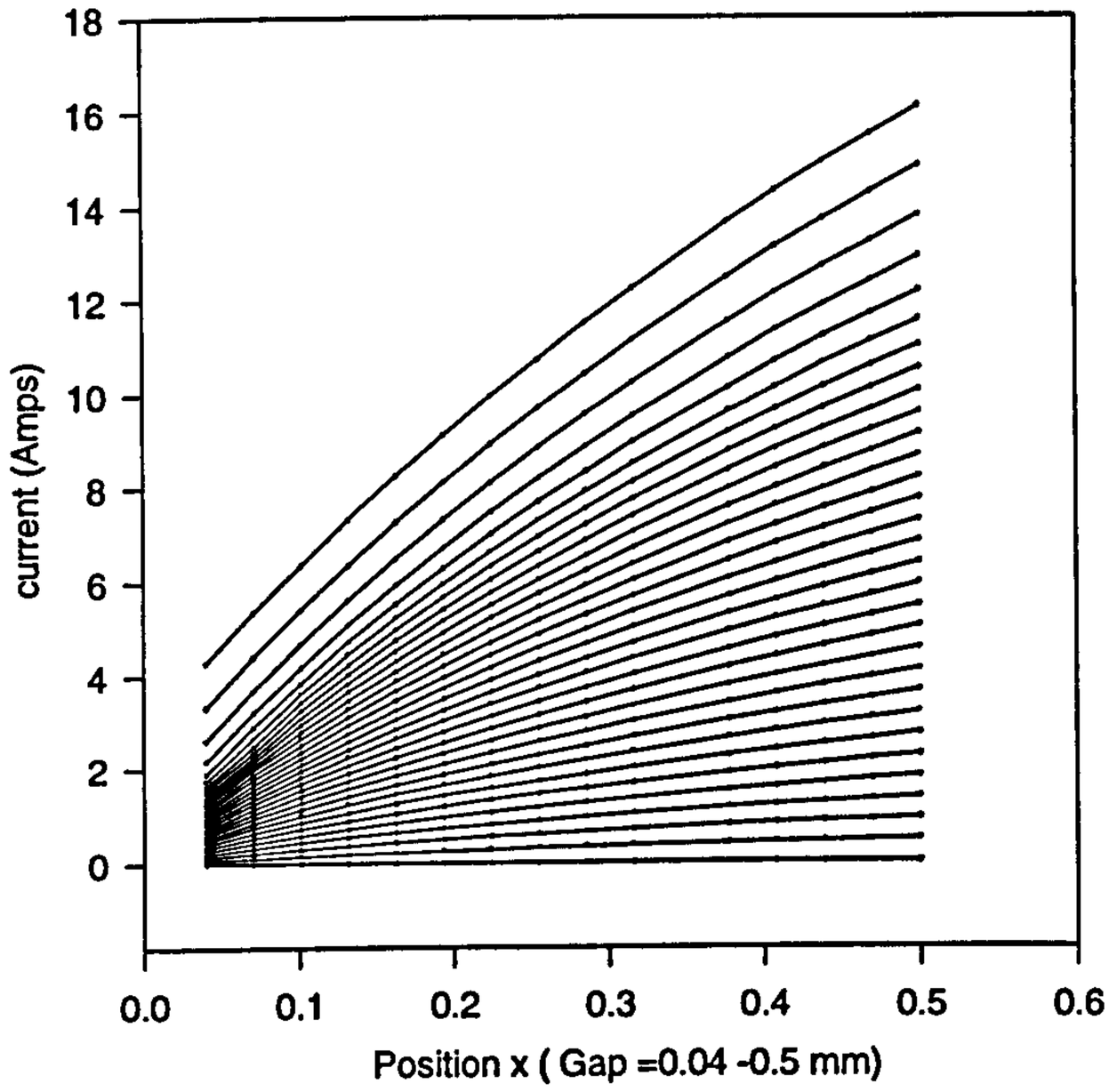

Figure 3.2: Magnetisation current versus position at $\Psi = cst.$

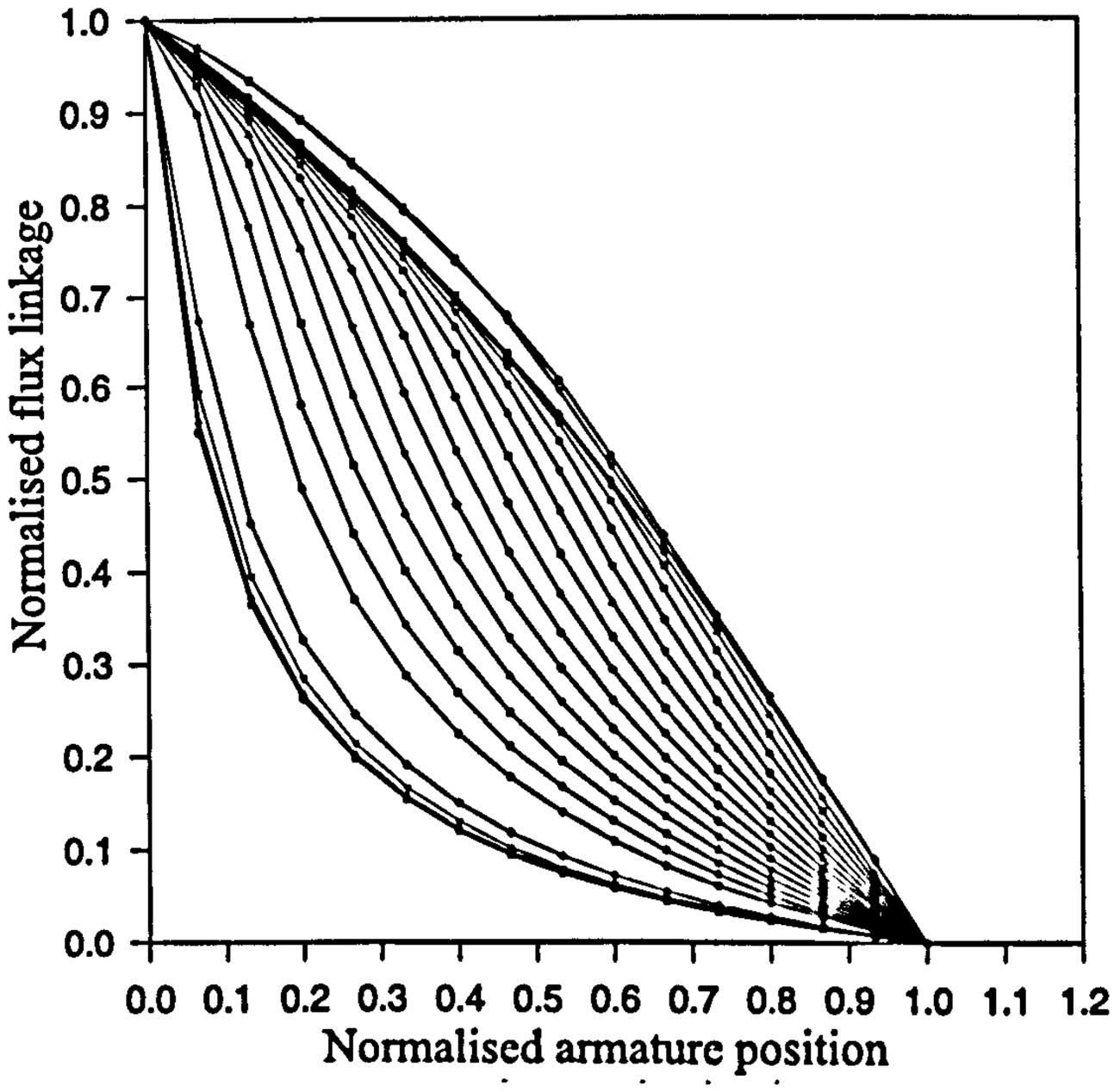

Figure 3.3: Normalised flux linkage versus normalised position, $I = cst.$

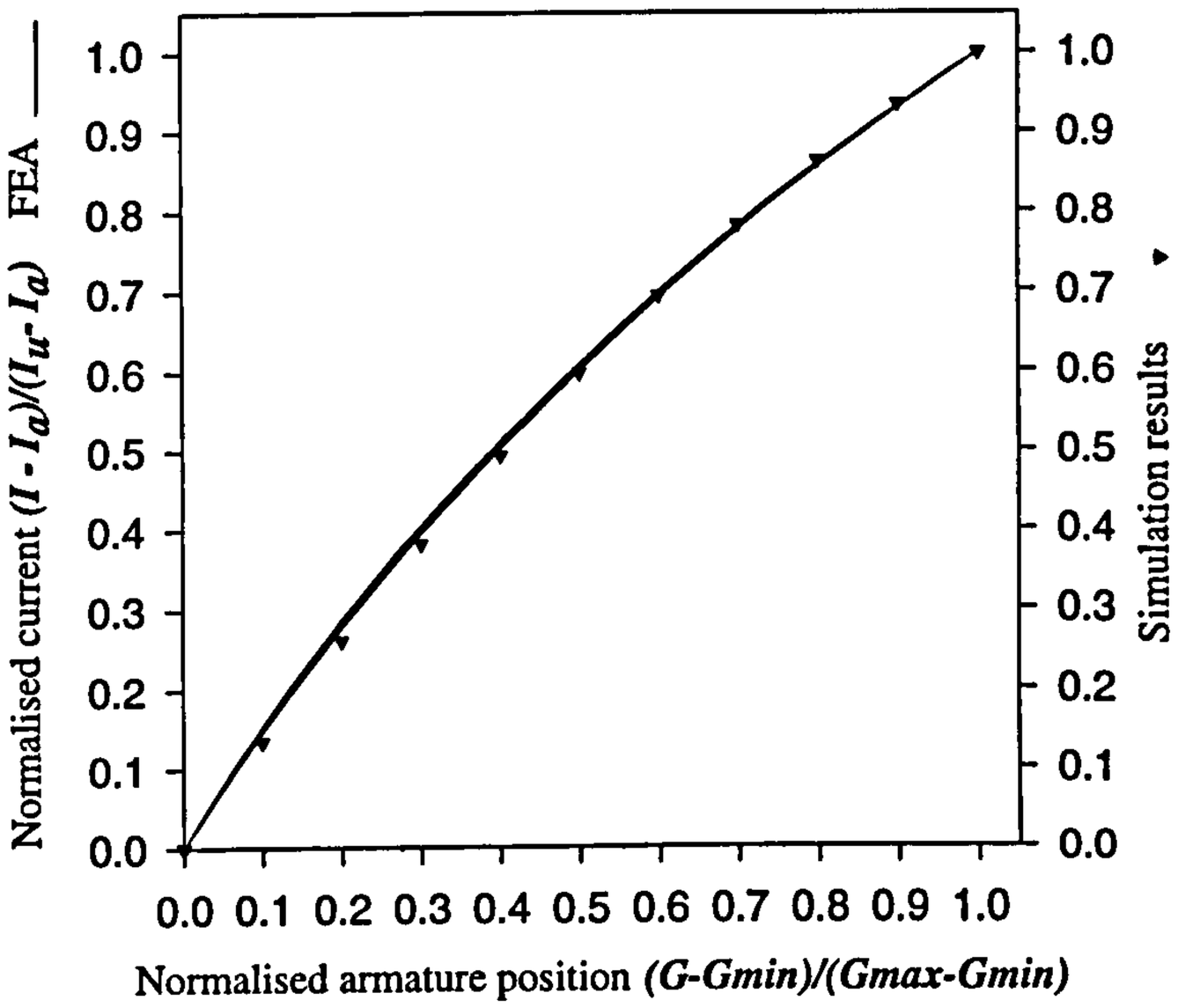

Figure 3.4: Normalised magnetisation current versus normalised position, $\Psi = cst$.

3.2 Solenoid Actuators

The general equation for the gauge curve given by eq. (3.3) may be significantly simplified depending on the type of actuator being considered. The section is dedicated to the flat-faced armature solenoid actuators and establishes the analytical expression associated with such devices (rectangular and axisymmetric). The computation of the magnetisation data is then demonstrated, based only on the knowledge of the gauge curve and two magnetisation characteristics (at x_a and x_u) . Finally a third section explores the possibility and advantages of computing the magnetostatic force based on the same three curves.

3.2.1 Analytical Expression

The flux paths within the iron as shown in fig. 2.2 or fig. 2.4 are not really affected by the armature movement. The flat-faced configuration of the armature is the main reason for this phenomenon so that, at constant flux linkage, the mmf drop within the

iron is quasi-equal for any armature position [1]. Therefore it follows from (3.2) that :

$$\sum_j H_{ij}(\phi)\, l_{ij} \;=\; \sum_j H_{aj}(\phi)\, l_{aj} \;=\; \sum_j H_{uj}(\phi)\, l_{uj}, \tag{3.6}$$

at constant flux linkage.

If this last result is combined with eq.(3.3), then the gauge curve expression is transformed into:

$$I_N(x_i) = \frac{\frac{1}{P_{gtot}(x_i)} - \frac{1}{P_{gtot}(x_a)}}{\frac{1}{P_{gtot}(x_u)} - \frac{1}{P_{gtot}(x_a)}}, \tag{3.7}$$

where P_{gtot} is the total airgap permeance (including working gaps, fringing, leakage).

Equation (3.7) is thus the analytical expression of the function obtained in fig. 3.4 which is the gauge curve associated with this particular type of actuator. It shows that the nonlinear information included in the magnetisation characteristics $I(\psi, x_a)$ and $I(\psi, x_u)$ is sufficient to re-construct the magnetisation curves $I(\psi, x_i)$ at any intermediate position.

Based on the material developed in the previous chapter, the total airgap permeances in (3.7) may be written as a function of the different permeance expressions.

Ideal Case First by considering the 'ideal' case where there is no fringing or cross slot leakage, it follows that:

$$P_{gtot}(x) = P_{gId}(x) = \frac{P_{g1} P_{g2}}{P_{g1} + P_{g2}} = \frac{\mu_0\, S_1\, S_2}{(S_1 + S_2)\, x}, \tag{3.8}$$

where the subscripts 1 and 2 correspond to the central and outer limbs respectively. S_i is the total cross-section area of the main airgap i whose total permeance is given by P_{gi}.

It follows from (3.7) and (3.8) that the gauge curve of an 'ideal' linear flat-faced device is given by:

$$I_N(x) = \frac{x - x_a}{x_u - x_a} = X_N, \tag{3.9}$$

[1] At high current levels, the variation of cross slot leakage and outer fringing flux with armature position will however generate some local differences of saturation level which may slightly modify the average operating point on the BH characteristic as a function of armature position.

where X_N is the normalised armature position. The 'ideal' gauge curve corresponds to a straight line with a slope of 45 degrees in the plane I_N versus X_N.

Real Case The total airgap permeance for an axisymmetric actuator is given by :

$$P_{gtot} = \frac{(P_{g1} + P_{fi1})(P_{g2} + P_{fi2} + P_{fe})}{(P_{g1} + P_{fi1} + P_{g2} + P_{fi2} + P_{fe})} + P_L \tag{3.10}$$

where P_L is equal to the total cross slot leakage permeance, P_{fi} and P_{fe} are the inner and outer fringing components.

Figure 3.4 also shows the result of the gauge curve computed with eq.(3.7) and (3.10) in which the different airgap permeances are evaluated with their analytical expressions developed in the previous chapter.

At the maximum inductance position the fringing and slot leakage contribution may be neglected such that the total airgap permeance at this position is reduced to

$$P_g(x_a) = \frac{\mu_0 \, S1 \, S2}{(S1 + S2)\, x_a}. \tag{3.11}$$

If the fringing permeances are also negligible compared to the working airgap permeances, it follows that at any armature position:

$$I_N(x) = \frac{\frac{1}{(P_{gId}+P_L)_x} - \frac{1}{(P_{ga})}}{\frac{1}{(P_{gId}+P_L)_{x_u}} - \frac{1}{(P_{ga})}}; \tag{3.12}$$

or by combining eq.(3.12) with (3.11) and (3.8), it results that:

$$I_N(x) = \frac{\frac{x}{(1+f_{lkg}(x))} - x_a}{\frac{x_u}{(1+f_{lkg}(x_u))} - x_a}, \tag{3.13}$$

where the leakage factor $f_{lkg}(x) = P_L(x)/P_{gId}(x)$.
Equation (3.12) shows clearly that the gauge curve bending is thus a direct measure of the amount of leakage (and also in general fringing) existing in this particular type of linear actuator.

The results obtained in this section are valid to some extent for both axisymmetric and rectangular flat-faced linear actuators. As mentioned earlier, the accuracy of the gauge curve based on equation (3.7) will deteriorate when current increases. As the

E-core device is more sensitive to fringing and cross slot leakage, it is clear that the range of relatively good accuracy for computing the magnetisation data from the gauge curve is less for this type of actuator than for the axisymmetric one. Also the accuracy given by the gauge curve method, based on analytical permeance equations, is limited by the accuracy of the corresponding magnetic equivalent circuit. Higher precision could however be reached by computing both gauge curve and magnetisation curves $\psi(I, x_a)$ and $\psi(I, x_u)$ using a finite-element analysis. Figures 4.17 and 4.24 show two examples of magnetisation curves computed for 2 different E-core designs for which the dimensions are summarised in tables 4.3 and 4.4 respectively.

3.2.2 Magnetisation Curve Computation

The algorithm for computing the magnetisation data is relatively straightforward.

1. First of all the magnetisation characteristics ($\psi(I, x_a)$ and $\psi(I, x_b)$) corresponding to the minimum and maximum inductance positions are computed. This is done either with the MEC or with a finite element analysis. If the number of points is rather large, a linear interpolation is convenient between two successive points. An analytical interpolation is also possible [22]. The curves require to be stored or interpolated in such a way that the current is the output parameter (i.e. $\psi(I)$ is transformed into $I(\psi)$).

2. The gauge curve $I_N(x)$ is also evaluated by replacing $P_{gtot}(x)$ with eq. (3.10) into eq.(3.7). This computation requires either the linear MEC elements or a linear finite element analysis. Again if the number of points is large, a linear interpolation between successive points is sufficient. A second-order polynomial interpolation may also be applied.

3. The repetitive algorithm then starts:

   At the current armature position x_j and for a series of flux linkage levels ψ_j (with j=1..N),

(a) The normalised current $I_N(x_j)$ is computed from the gauge curve equation $I_N(x)$

(b) $I_a(\psi_j)$ and $I_u(\psi_j)$ are retrieved from the computed magnetisation curves.

(c) From eq.(3.1), it follows that

$$I(x_j, \psi_j) = I_N(x_j)(I_u(\psi_j) - I_a(\psi_j)) + I_a(\psi_j), \tag{3.14}$$

leading to the evaluation of a complete intermediate magnetisation curve.

4. By repeating the previous algorithm (step 3.) for several armature positions, the complete magnetisation surface (see fig. 2.17) is rapidly computed.

Figures 3.5 and 4.23 gives two examples of magnetisation curves computed for an axisymmetric device with the gauge curve method and compared with the MEC or with measurements.

3.2.3 Magnetostatic Force Computation

When the magnetic information is stored in a magnetisation curve format ($\psi(I, x)$), the magnetostatic force or torque usually derives from the evaluation of the coenergy, which is then numerically differentiated with position x [1, 22, 28].

Based on the interpolation function $\psi_N(x)$, Miller [37] developed an analytical expression of the torque for switched reluctance motors, based also on the coenergy formulation. Regarding the development of a preliminary design tool for solenoid actuators, the analytical computation of the magnetostatic force would be certainly a great advantage that should be investigated with the new gauge curve definition.

As it is shown in table 3.2, the coenergy formulation (as used by the previous authors), implicitly makes the assumption that I and x are the independent variables of this problem and ψ the dependent one. This approach is not suitable for the gauge curve $I_N(x)$, for which the independent variables are the flux linkage ψ and the rotor/armature position x. This difficulty is however easily overcome by computing the

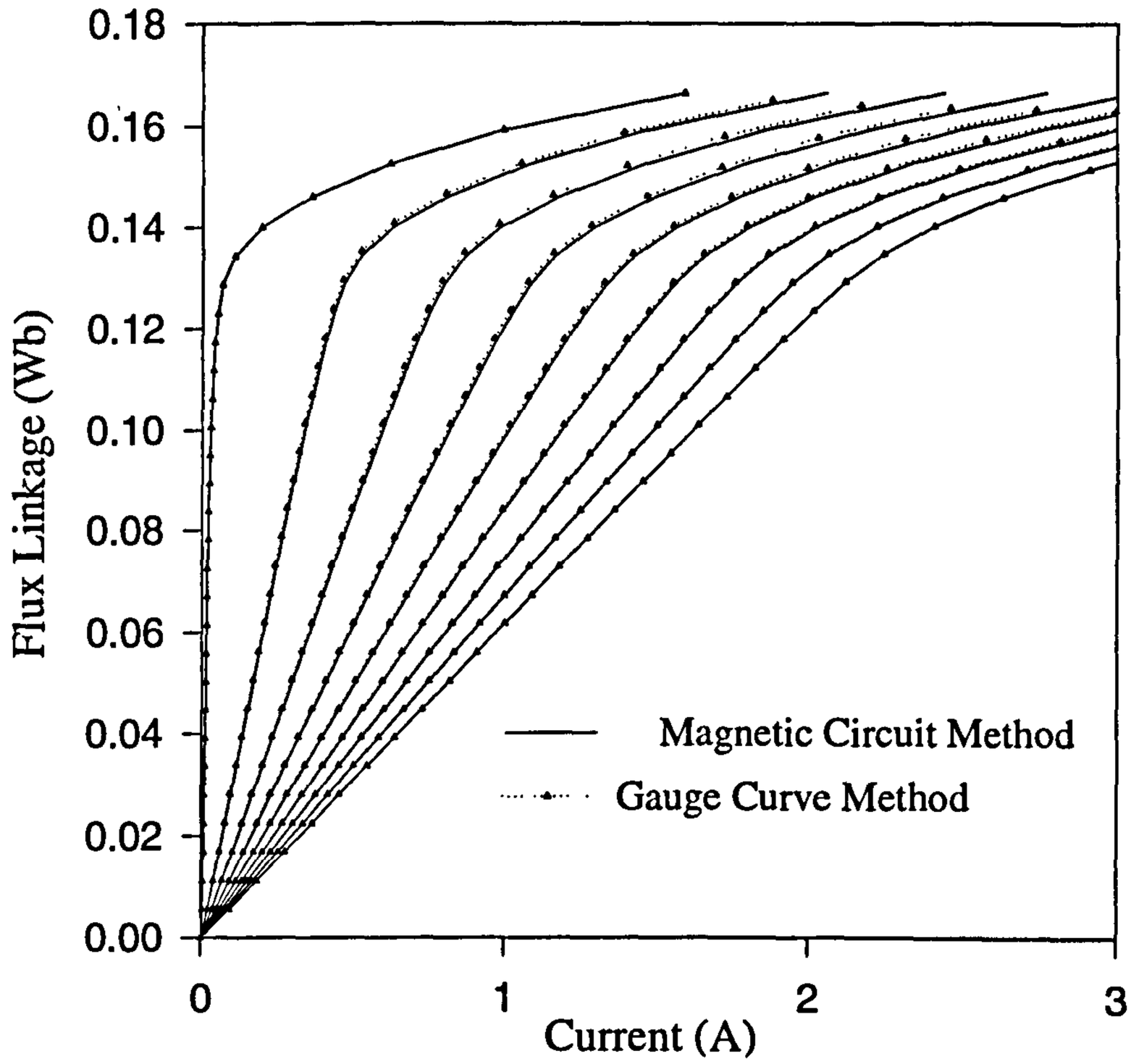

Figure 3.5: Magnetisation curves computed with the MEC and the gauge curve method.

Independent Variables	I, x	ψ, x
	Coenergy formulation (W_c) $W_c = \int_0^I \psi(I,x)\, dI$	Energy formulation (W_e) $W_e = \int_0^\psi I(\psi,x)\, d\psi$
Magnetostatic force computed from stored energy	$f_e = -\frac{\partial W_c}{\partial x} + I\,\frac{\partial \psi}{\partial x}$	$f_e = -\frac{\partial W_e}{\partial x}$
Magnetostatic Force computed from Coenergy	$f_e = \frac{\partial W_c}{\partial x}$	$f_e = \frac{\partial W_c}{\partial x} - \psi\,\frac{\partial I}{\partial x}$

Table 3.2: Formulation of magnetostatic force computation [1].

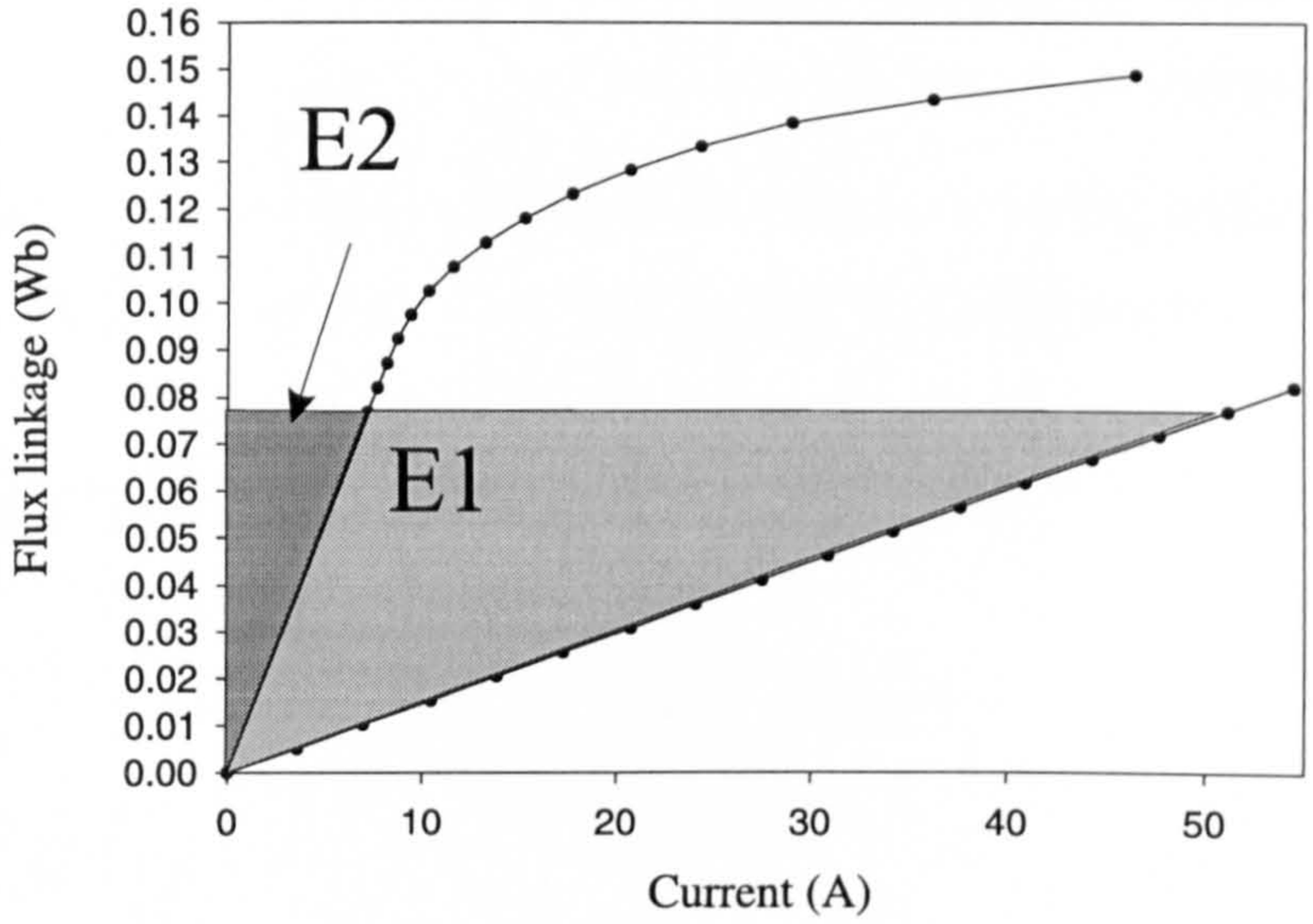

Figure 3.6: Areas $E1$ and $E2$ for magnetostatic force computation.

magnetostatic force f_e based on the energy formulation:

$$f_e = -\frac{\partial}{\partial x}\int_0^{\psi} I(\psi, x)\, d\psi. \tag{3.15}$$

The current I is expressed with eq. (3.1) into eq.(3.15):

$$f_e = -\frac{\partial}{\partial x}\int_0^{\psi} \left[I_N(x)\left(I_u(\psi) - I_a(\psi)\right) + I_a(\psi)\right]\, d\psi. \tag{3.16}$$

Therefore it follows:

$$f_e = -\frac{\partial I_N(x)}{\partial x}\int_0^{\psi} \left(I_u(\psi) - I_a(\psi)\right) d\psi; \tag{3.17}$$

Or written in a different way:

$$f_e = -\frac{\partial I_N(x)}{\partial x} E1, \tag{3.18}$$

where $E1 = \int_0^{\psi}(I_u(\psi) - I_a(\psi))\, d\psi$ is graphically represented in fig. 3.6.

The speed for computing the magnetostatic force is greatly improved based on this technique compared to the conventional numerical approach explained in section 2.1. However the accuracy of eq. (3.18) is a function of the technique chosen for evaluating the differentiation of the normalised current. It is not recommended, in this context, to

interpolate the gauge curve based only on three points. A more robust method involves implementing a first-order difference method with a larger set of computed points.

The computation of the magnetostatic force based on eq. (3.18) is therefore straightforward. At the current position x_j and flux linkage ψ_j, it follows that:

1. If the gauge curve is evaluated at position $x1 = (x_{j-1} + x_j)/2$ and $x2 = (x_j + x_{j+1})/2$, its approximated derivate is given by

$$\frac{\partial I_N}{\partial x} = \frac{I_N(x2) - I_N(x1)}{\Delta x}, \tag{3.19}$$

with $\Delta x = x2 - x1$.

2. The stored energy for a flux linkage ψ_j at the minimum and maximum inductance positions is obtained numerically [2] by considering a linear interpolation between two successive points.

Using this approach, the computation of stored energy E2, as shown in fig. 3.6, is equal to:

$$E2 = \int_0^{\psi_j} I_a(\psi)\, d\psi = \sum_{i=1..j} \frac{a1}{2}\,(\psi_i^2 - \psi_{i-1}^2) + a2\,(\psi_i - \psi_{i-1}), \tag{3.20}$$

with $a1 = \frac{I_i - I_{i-1}}{\psi_i - \psi_{i-1}}$ and $a2 = I_i - a1\,\psi_i$.

By replacing $I_a(\psi)$ in eq.(3.20) with $I_u(\psi)$ and set the result to Eu, it follows:

$$E1 = Eu - E2. \tag{3.21}$$

3. The force is then obtained by computing (3.18) with (3.21), (3.20) and (3.19) .

Fig. 3.7 and 3.8 show two examples of this computation for an axisymmetric and a rectangular actuator respectively. For the axisymmetric actuator, the results with finite-elements are computed from the integration of the Maxwell stress on a closed surface surrounding the armature. In the case of the rectangular device, the magnetostatic force derives from the coenergy formulation computed with 3D finite-element analysis. The results based on the magnetic equivalent circuit (MEC) involves

[2] An analytical interpolation of each magnetisation curve could be also considered

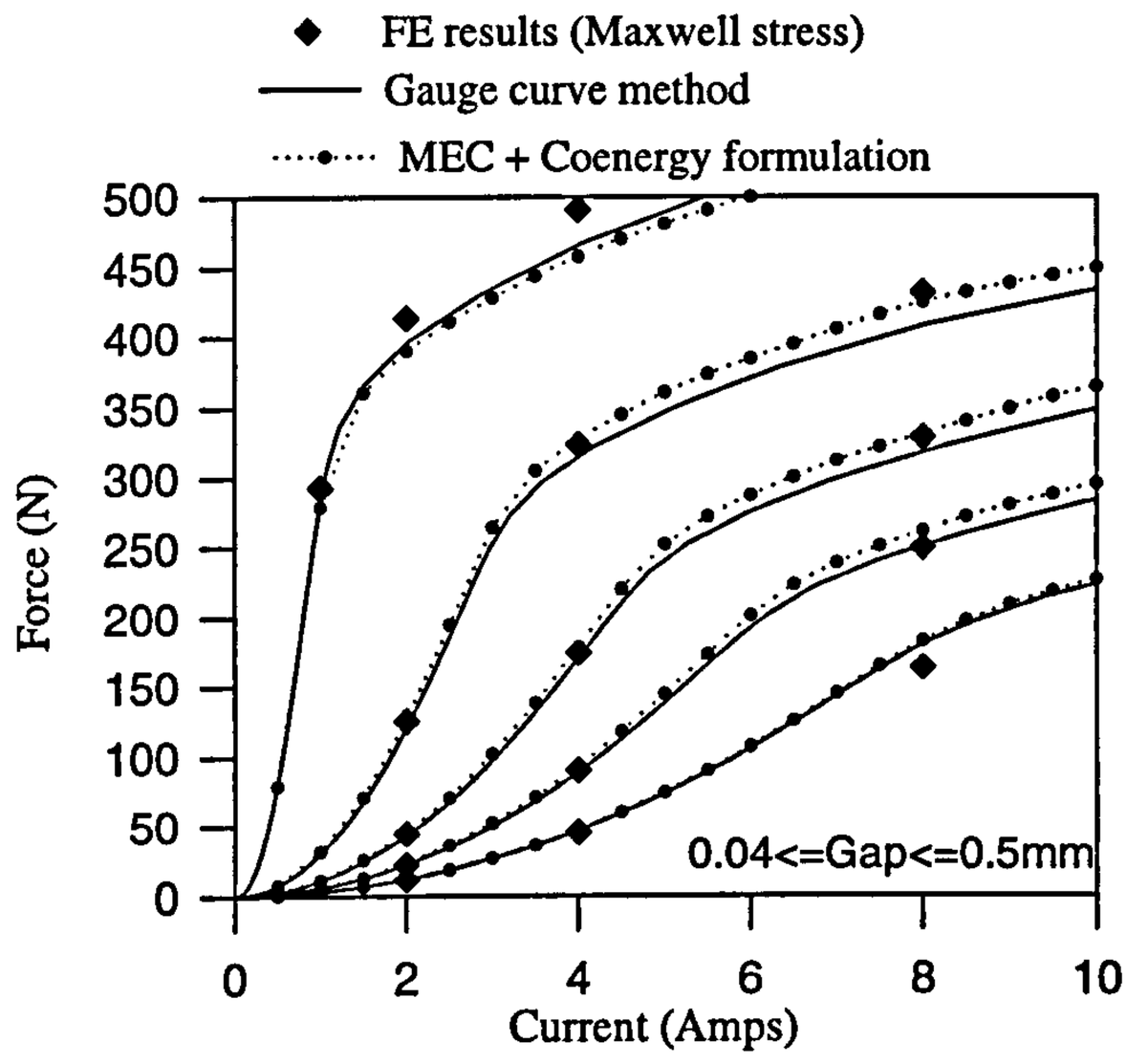

Figure 3.7: Magnetostatic force for axisymmetric actuator.

the evaluation of the coenergy from the magnetisation curves interpolated with cubic splines functions [20].

For both types of actuators, the gauge curve technique shows a good agreement with the MEC method. The computational time is however significantly reduced with this new approach. The discrepancy between finite-elements and the MEC are attributed to the approximations made in the MEC for simulating the 3D end-effects.

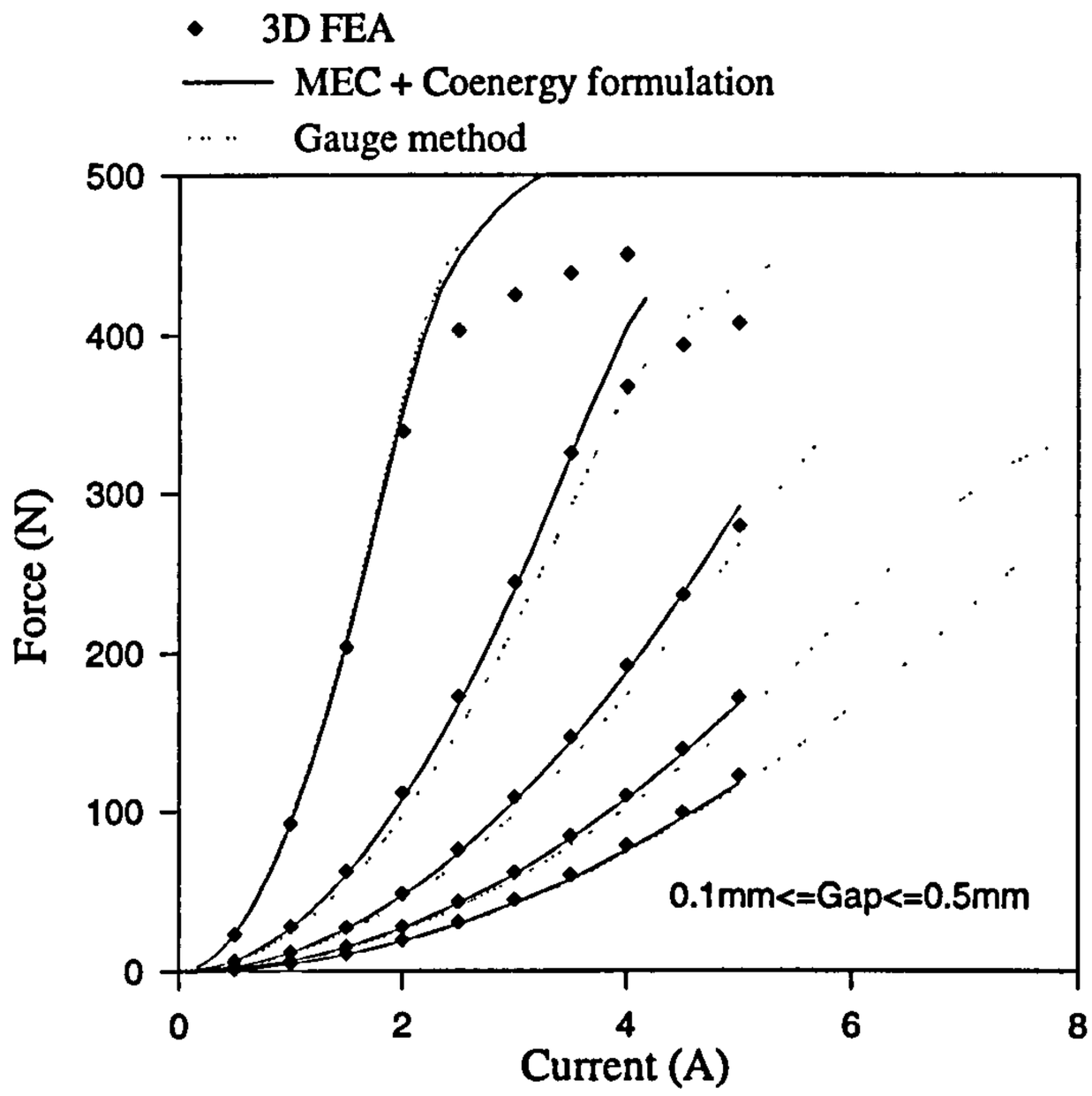

Figure 3.8: Magnetostatic force for rectangular actuator.

3.3 Double Salient Rotary Machine

A gauge curve analysis for the SR machine is also given in annexe A. In this case, the gauge curve is a function of both flux linkage and rotor position. It is shown that the nonlinear content of the gauge curve (i.e. dependence on flux linkage) is due to the local saturation occurring at the pole tips during partial overlap. Although it is not entirely developed, this approach could also lead to a fast torque computation compared to more conventional approaches (e.g. see section 2.1), and could have some computational advantages for real time application requiring large magnetic data storage [38].

3.4 Conclusions

A general model of gauge curve has been derived from Ampere's law for any type of variable reluctance electromagnetic device. The model applied to a given machine

leads to an analytical expression whose complexity reflects the variation of magnetic behaviour between the intermediate positions and the maximum inductance position. This approach is more efficient than the conventional methods as it minimises the amount of stored data and decreases the computational time without compromising significantly the level of accuracy.

In the case of the flat-faced solenoid actuators, the gauge curve technique works particularly well due to the 'constant iron geometry' seen by the flux over the stroke. At constant flux linkage, the nonlinear content of the magnetisation is then relatively constant and therefore disappears completely from the gauge curve expression. This approach includes another advantage which is a rapid and relatively accurate magnetostatic force computation.

A similar development was also undertaken for the switched reluctance machine and showed that, in this case, the gauge curve depends significantly on both rotor position and flux linkage. This is due to local saturations occurring in the pole tips during partial overlap. This phenomenon, highly nonlinear, is also strongly dependent on armature position and is therefore kept within the gauge curve expression. Although this has not been completely demontrated, it is believed the gauge curve technique could also lead to other computational advantages for torque calculation or rotor position detection.

Chapter 4

Magnetisation Curve Validation

4.1 Validation With Finite Elements

4.1.1 The Axisymmetric Solenoid Actuator

A numerical model of the axisymmetric actuator has been implemented in PC-OPERA and solved with the magnetostatic solver using the modified rA potential [39]. The mesh generated for this application is shown in fig. 4.1 and consists of about 4000 nodes. The BH curve required for the nonlinear computation is given in fig. 4.2 and corresponds to a 2.5% SiFe steel.

Design 1

Fig. 4.3 shows a flux plot of the first axisymmetric actuator considered for validation. The important dimensions, supported by fig. 2.1, are summarised in table 4.1. In this design, the armature and yoke sections are relatively thick compared to the limb cross-section areas such that the saturation affects primarily the limbs. The magnetisation characteristics evaluated with both methods (MEC and finite-elements) are given in fig. 4.4 and correspond to an airgap length of 0.5 and 0.04 mm.

At low currents, the magnetisation curves, characterised by a linear portion, are

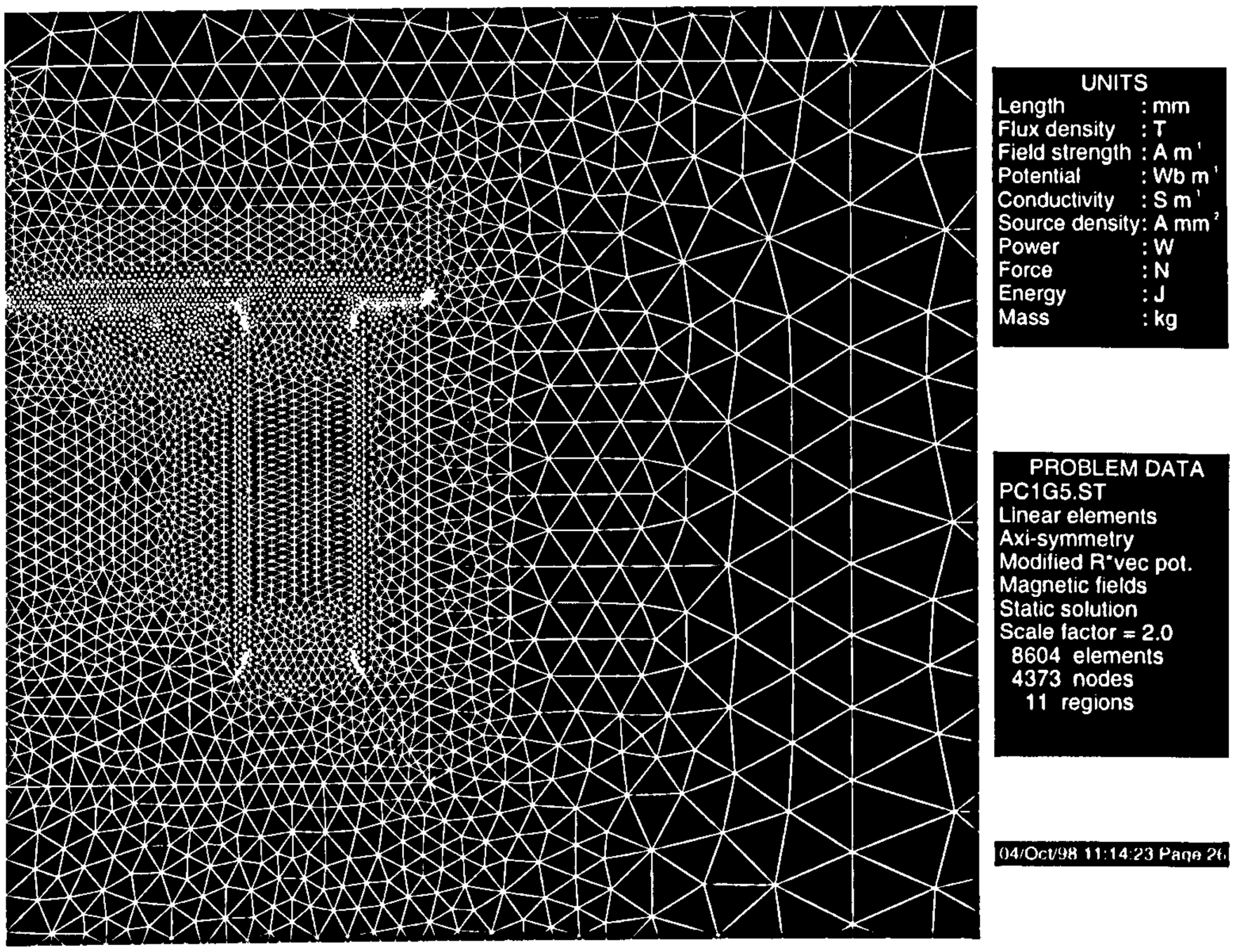

Figure 4.1: Details of the finite-element mesh computed for the magnetostatic field analysis using Vector Field Software.

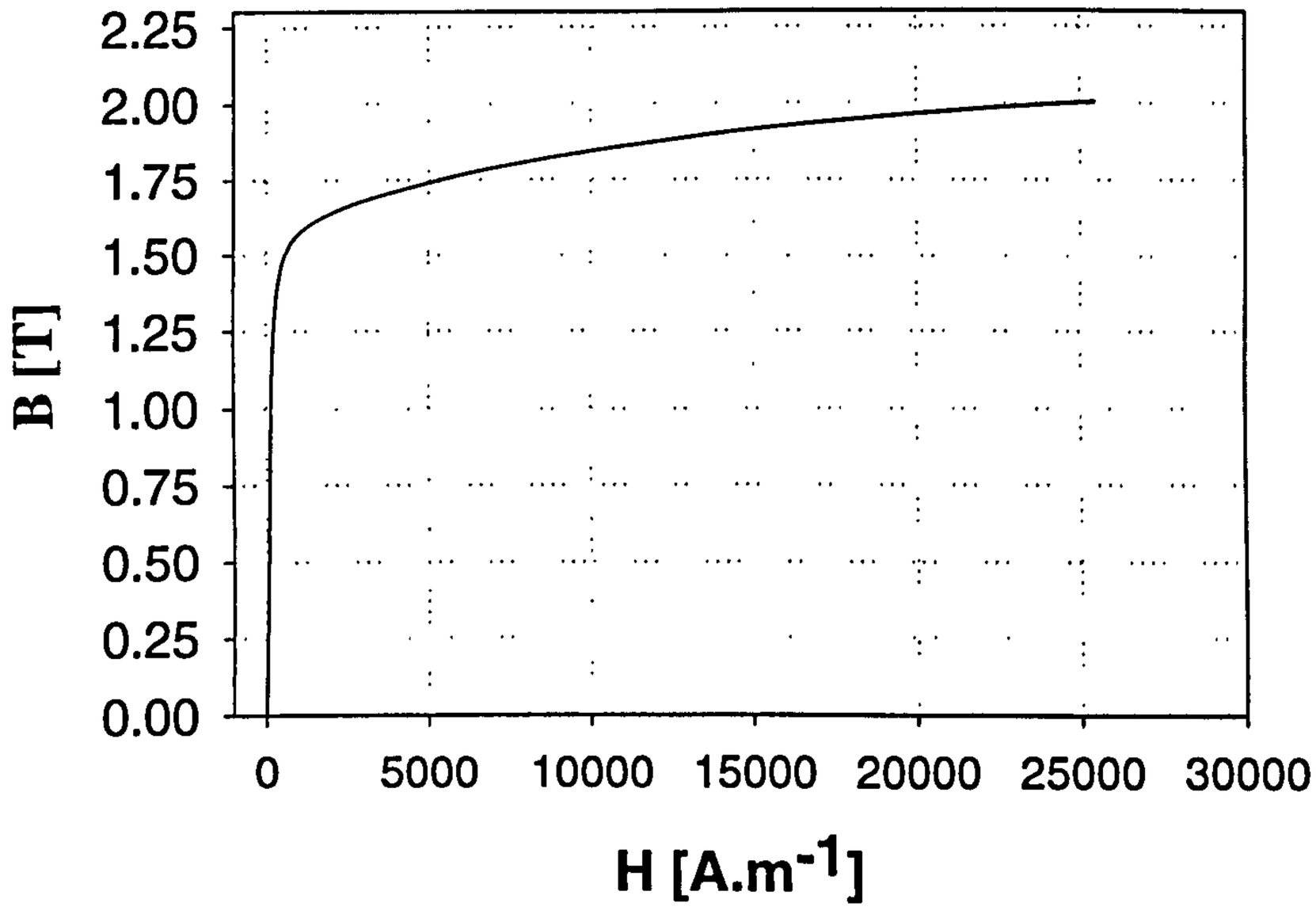

Figure 4.2: BH characteristic for the pot-core actuators and E-core armatures. Resistivity $\rho = 42.910^{-8}\Omega\, m$

A, B	31
C	8.23
D	2.37
T	8.23
F	7
E	23
$abcoil$	1.8
$uncoil$	0.49
N	60
$Steel$	2.5 % SiFe

Table 4.1: Axisymmetric actuator. Dimensions for design 1.

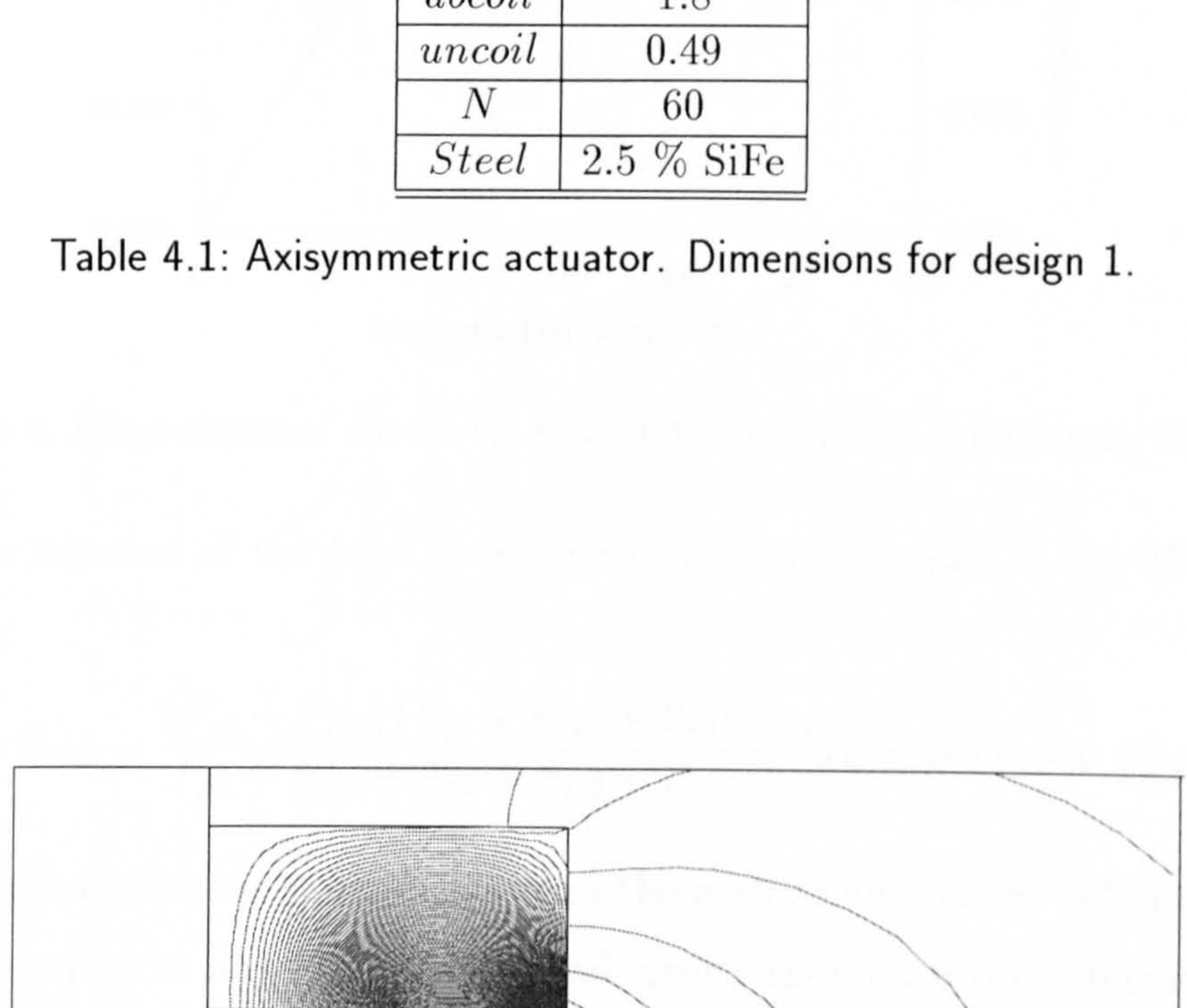

Figure 4.3: Static flux plot for the axisymmetric actuator. Design 1. I=30 A.

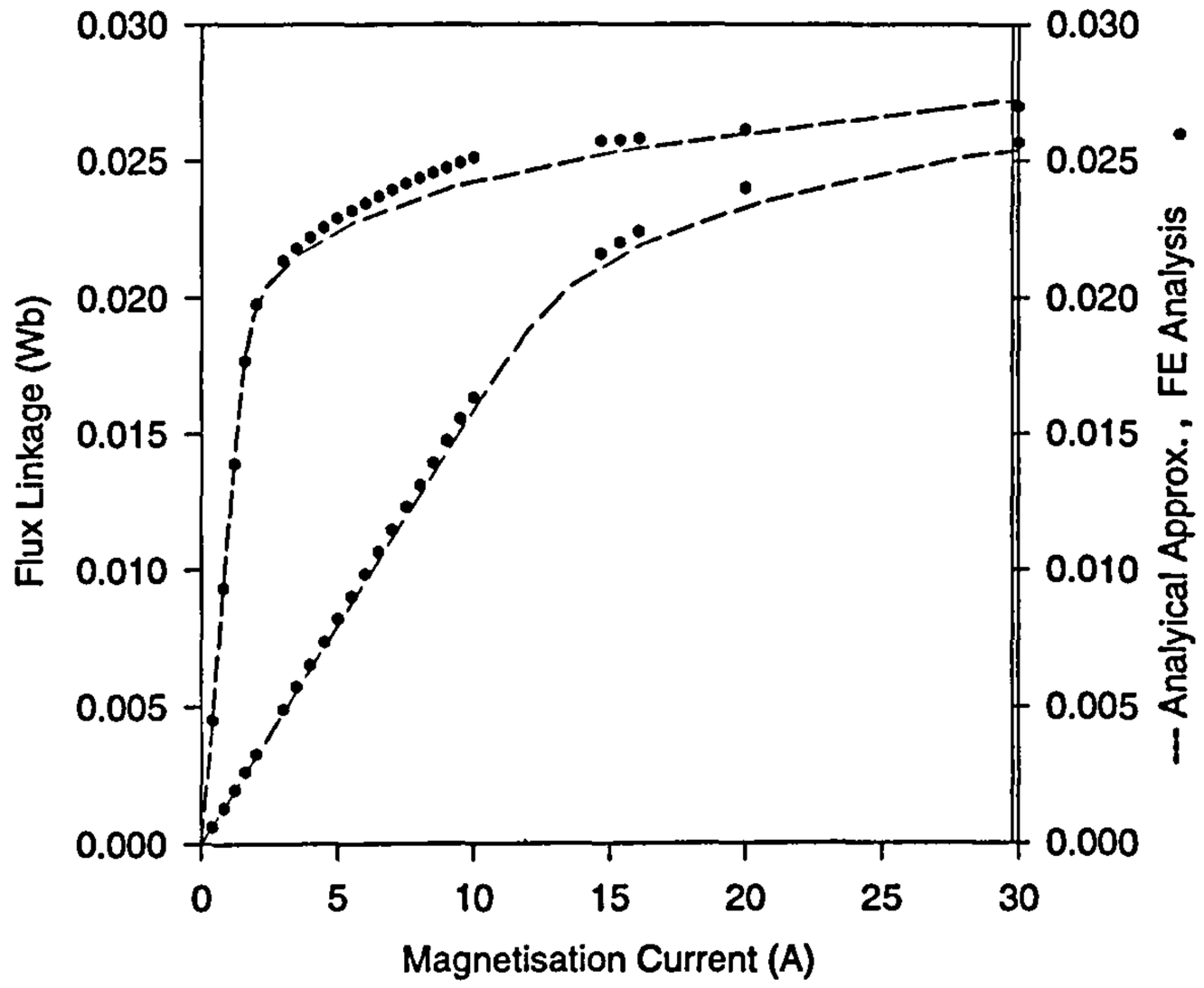

Figure 4.4: Magnetisation curves for $G = 0.04mm$ and $G = 0.05mm$. Design 1.

essentially a function of the total airgap permeance P_{gtot}, equal in the MEC shown in fig. 2.16 to :

$$P_{gtot} = \frac{(P_{g1} + P_{fi1})(P_{g2} + P_{fi2} + P_{fe})}{P_{g1} + P_{fi1} + P_{g2} + P_{fi2} + P_{fe}} + P_{L1} + 2/3\, P_{L2} + P_{L3}. \qquad (4.1)$$

At higher currents, the saturation affects the performance of the actuator. The total mmf drop required at any flux linkage level results then from the interaction between the airgap and iron flux paths and is a function of the nonlinear BH characteristic of the steel. At 30 A, the flux density is greater than 2T in some parts of the limbs. The results obtained by finite elements and by the MEC give a relatively good agreement for both curve sections (i.e. linear and nonlinear) and both airgap lengths.

Design 2

In order to test the sensitivity of the permeance and magnetic circuit model to leakage and fringing variation, the actuator chosen for design 2 (fig. 4.5) is relatively similar to design 1. However the limb length E has been increased from 23 to 30 mm. This actuator is therefore characterised by a higher cross slot leakage and also a higher mmf drop in the limb at high currents for no better magnetic performance. In this case, the

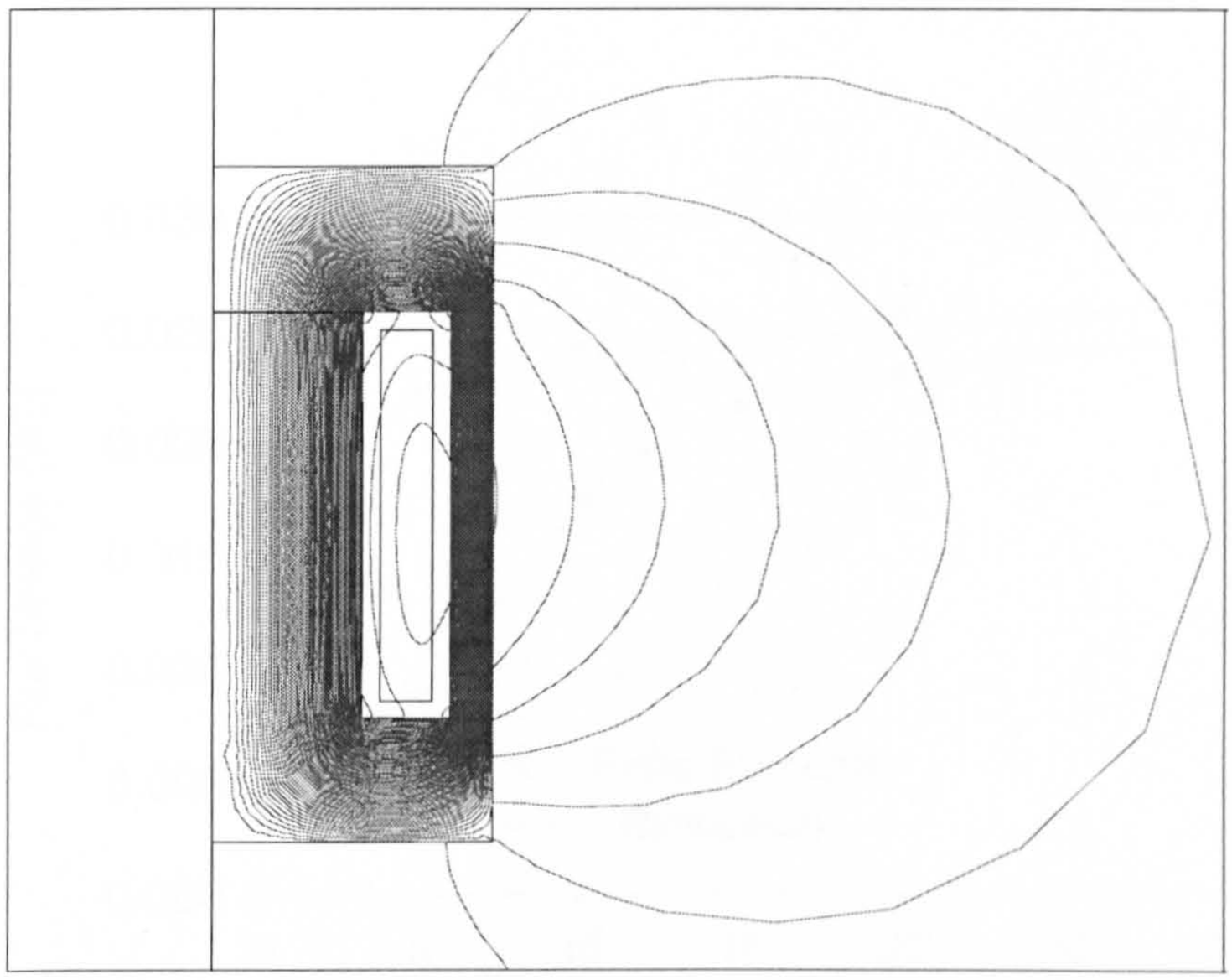

Figure 4.5: Static flux plot for the axisymmetric actuator. Design 2. I=30 A

magnetisation curves computed with the MEC present a satisfactory agreement with finite-elements as shown in fig. 4.6.

Design 3

The third actuator has been chosen with a large slot width as shown in fig. 4.7. The outer limb thickness has also been modified in order to keep a sensible cross-section area as in the first design. Table 4.2 summarises the dimensions of this new actuator. At low currents, the large slot width of this actuator tends to reduce the amount of slot leakage, as shown in fig. 4.8, compared to the two previous designs. However, at higher currents, some armature flux short-circuits entirely the saturated outer limb by crossing directly the slot from top to bottom. Although this phenomenon also appears in the last two other cases, it seems to be amplified in this design due to the relatively lower leakage permeance. As this mechanism of de-saturation is not included in the MEC, the results of the latter tends to produce less flux than with finite-elements.

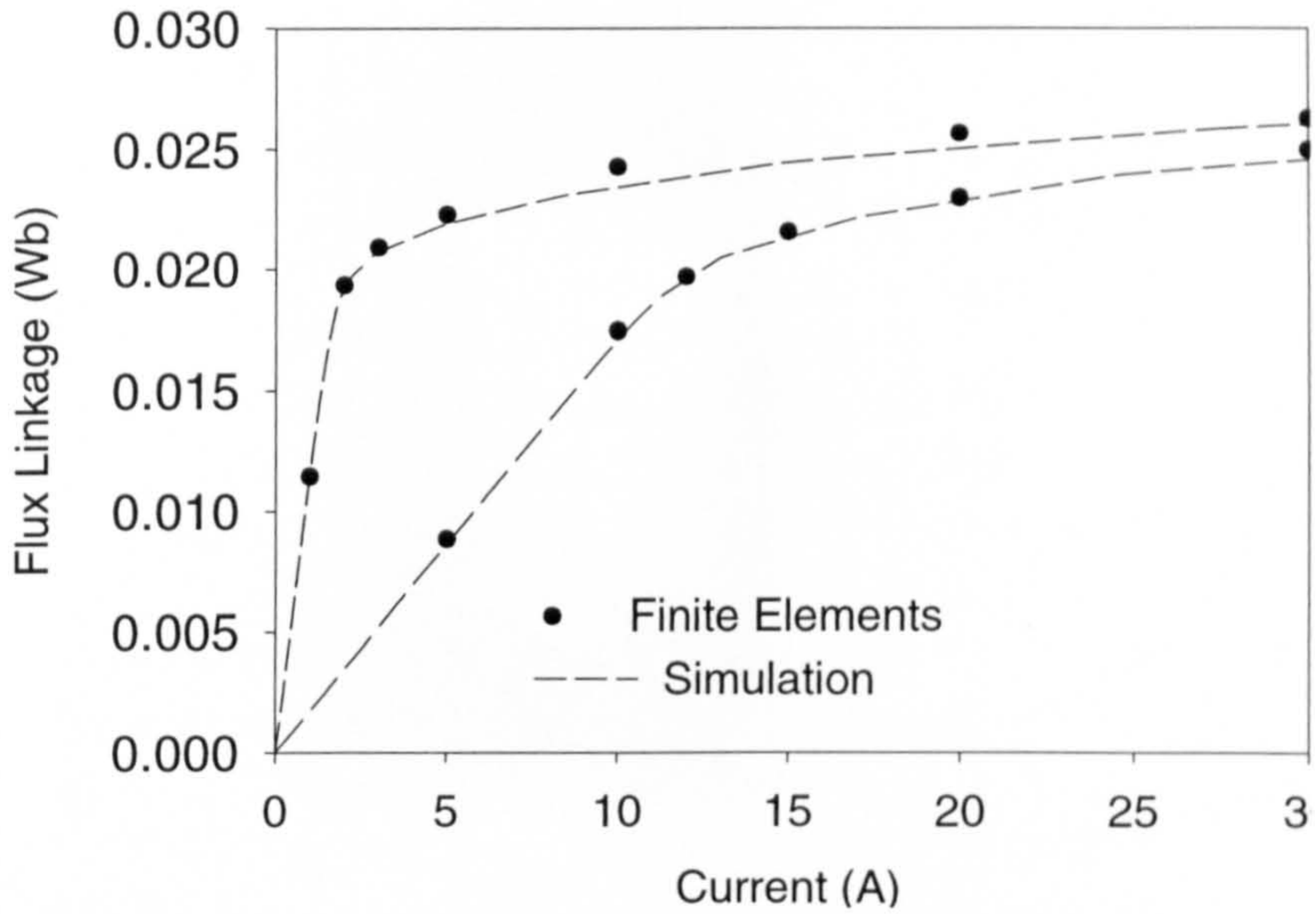

Figure 4.6: Magnetisation curves for $G = 0.04mm$ and $G = 0.05mm$. Finite-element and MEC results. Design 2

A, B	40
C	8.23
D	1.77
T	8.23
F	7
E	23
$abcoil$	1.8
$uncoil$	0.49
N	60
$Steel$	2.5 % SiFe

Table 4.2: Axisymmetric actuator. Dimensions for design 3.

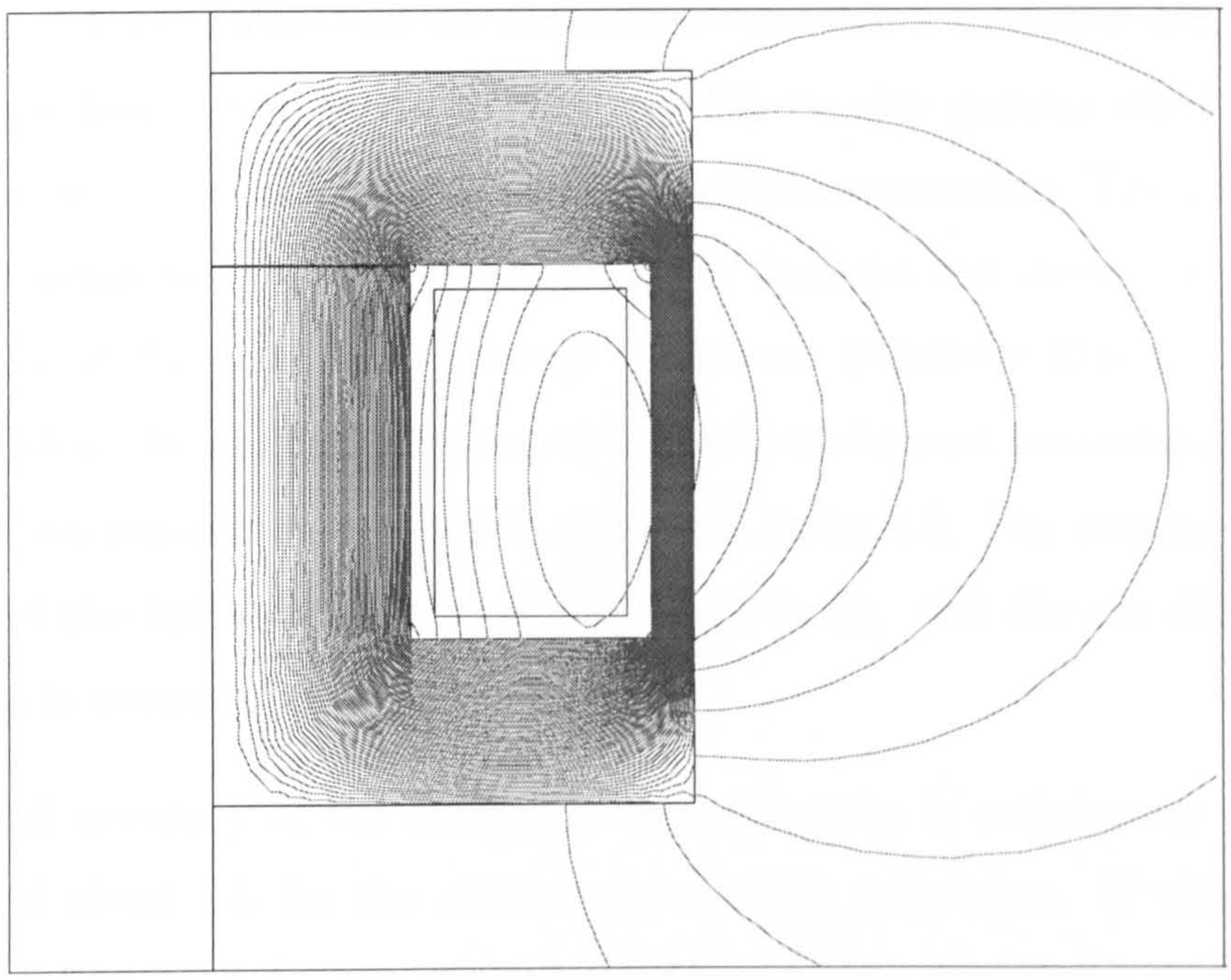

Figure 4.7: Static flux plot for the axisymmetric actuator. Design 3. I=30 A.

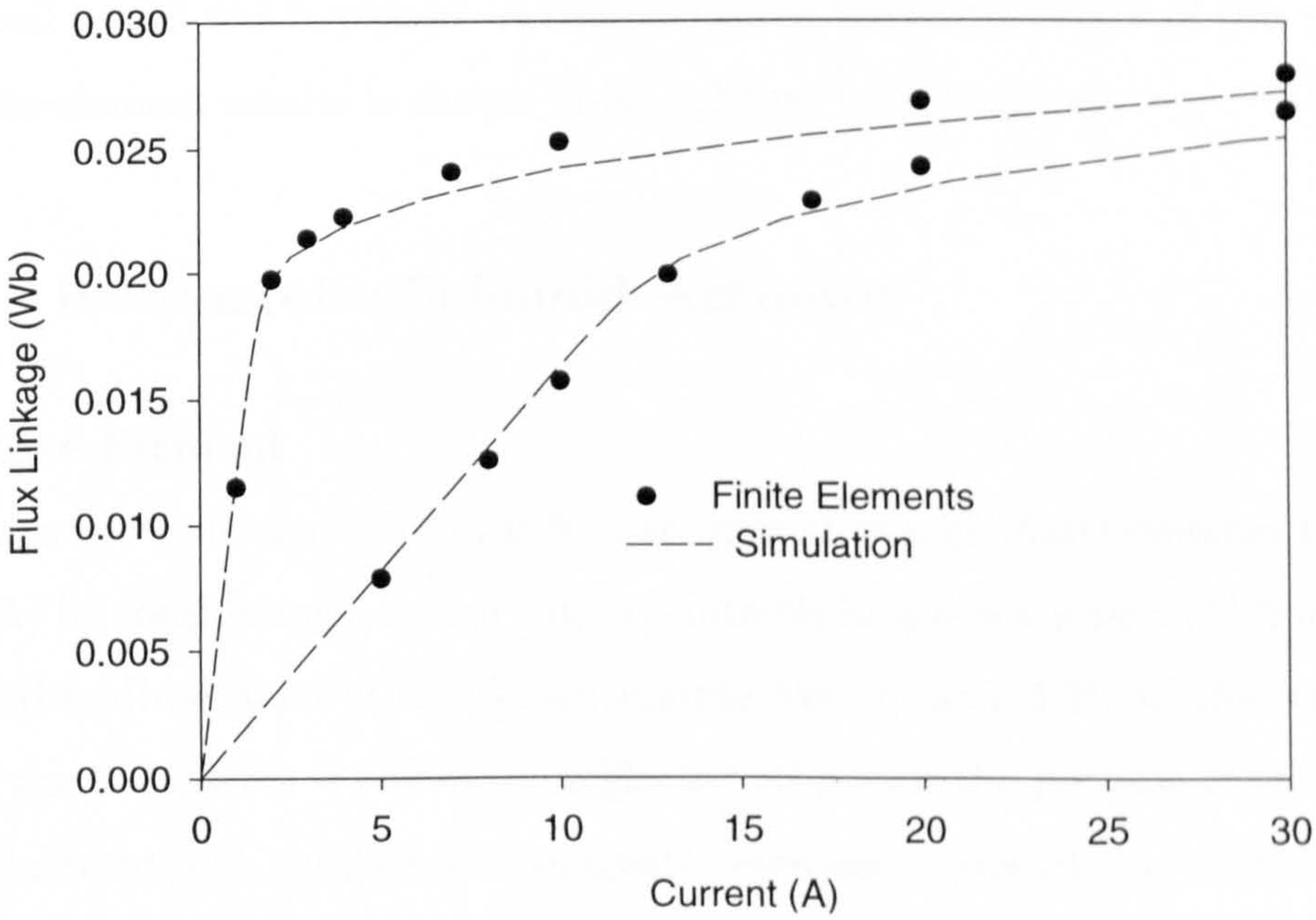

Figure 4.8: Magnetisation curves $G = 0.04mm$ and $G = 0.05mm$. Finite-element and MEC results. Design 3.

Design 4

This actuator, whose dimensions are summarised in table 5.1 column $D2$, corresponds to a prototype designed by Lucas Electric and Electronics systems which is also considered in the next section for static and transient measurements. The coil was hand-wound. The overall design is significantly smaller than the last three ones with a more realistic choice of the yoke and armature thickness. It follows that the spectrum of saturation is also different and stretches to the yoke and armature sections as shown in fig. 4.10. The corresponding flux plot is also given in fig. 4.9. The comparison between the MEC and the finite element results is shown in fig. 4.11 for six different airgap length chosen between 0.5 and 0.05 mm.

The overall accuracy of the analytical approximation is satisfactory with a maximum error of about 5% for the smaller gap at high saturation. If this comparison should extend beyond 4 A , the error at 8A for example, gets down to less than 3%. A higher accuracy could even be reached by considering the other magnetic equivalent circuit, shown in fig. 2.18, which reduces slightly the mmf drop in the outer limb by by-passing some of the limb flux into the outer fringing path. In this simulation, 60% of the coil height was bypassed. A comparison of the performance of this network with the finite-element results is shown in fig. 4.12 up to 8 Amperes.

4.1.2 Rectangular Solenoid Actuator

2D Finite-Element

The magnetic equivalent circuit is first compared to a 2D finite-element analysis (PC-OPERA) by considering a design with a relatively long stack length (150mm) compared to the other dimensions of the E-core summarised in table 4.3[1]. In this way the major part of the end-effects is obviously neglected. However the purpose of this comparison is to illustrate and validate the magnetic equivalent circuit for an E-core actuator characterised with a shorter armature (see fig. 2.22). This rectangular device actually corresponds to an existing design for a track fuel injector (see fig. 4.22).

[1]The stack length defined in the table is the one used for the 3D analysis.

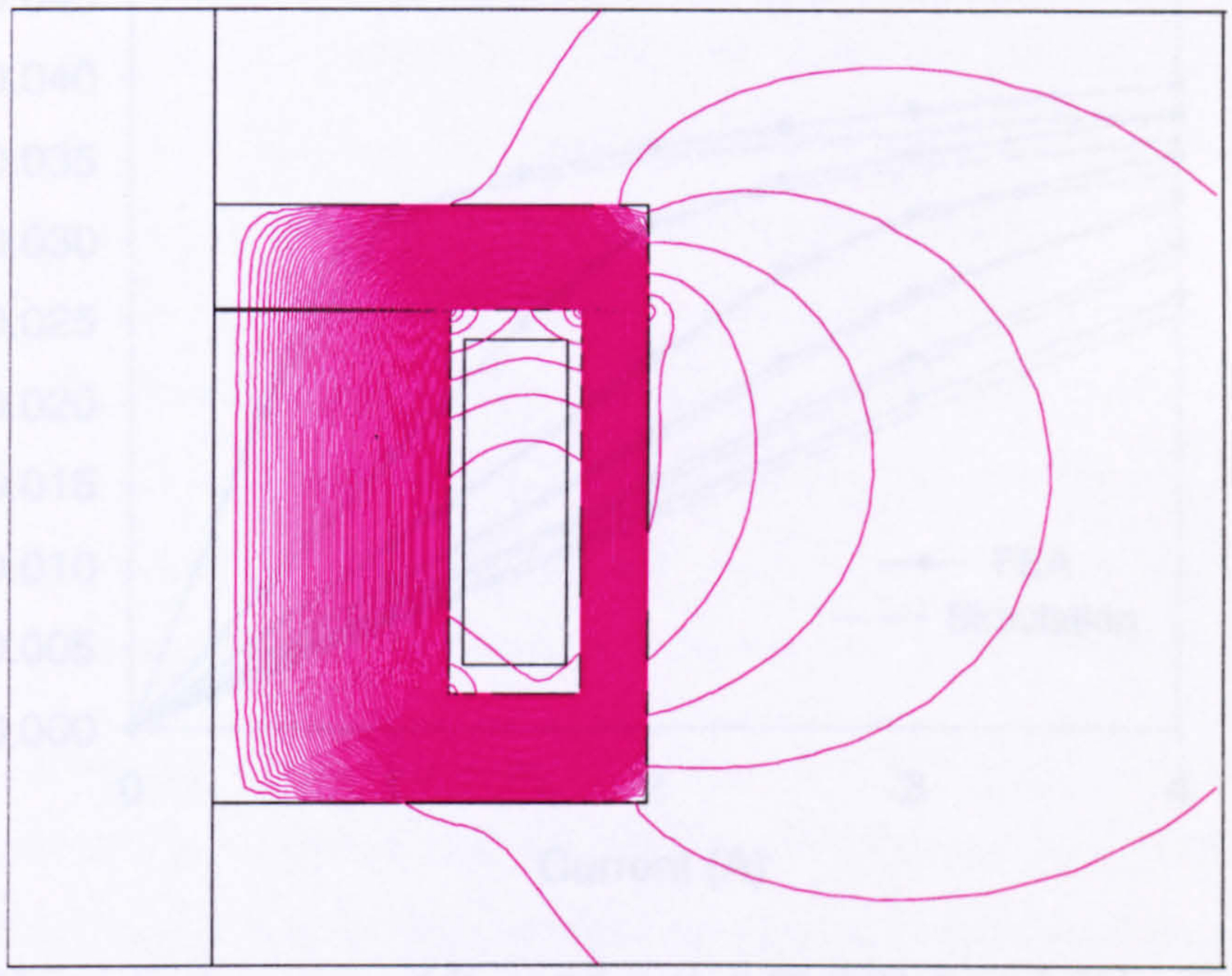

Figure 4.9: Static flux plot for the axisymmetric actuator. Design 4. $I = 3.5A$.

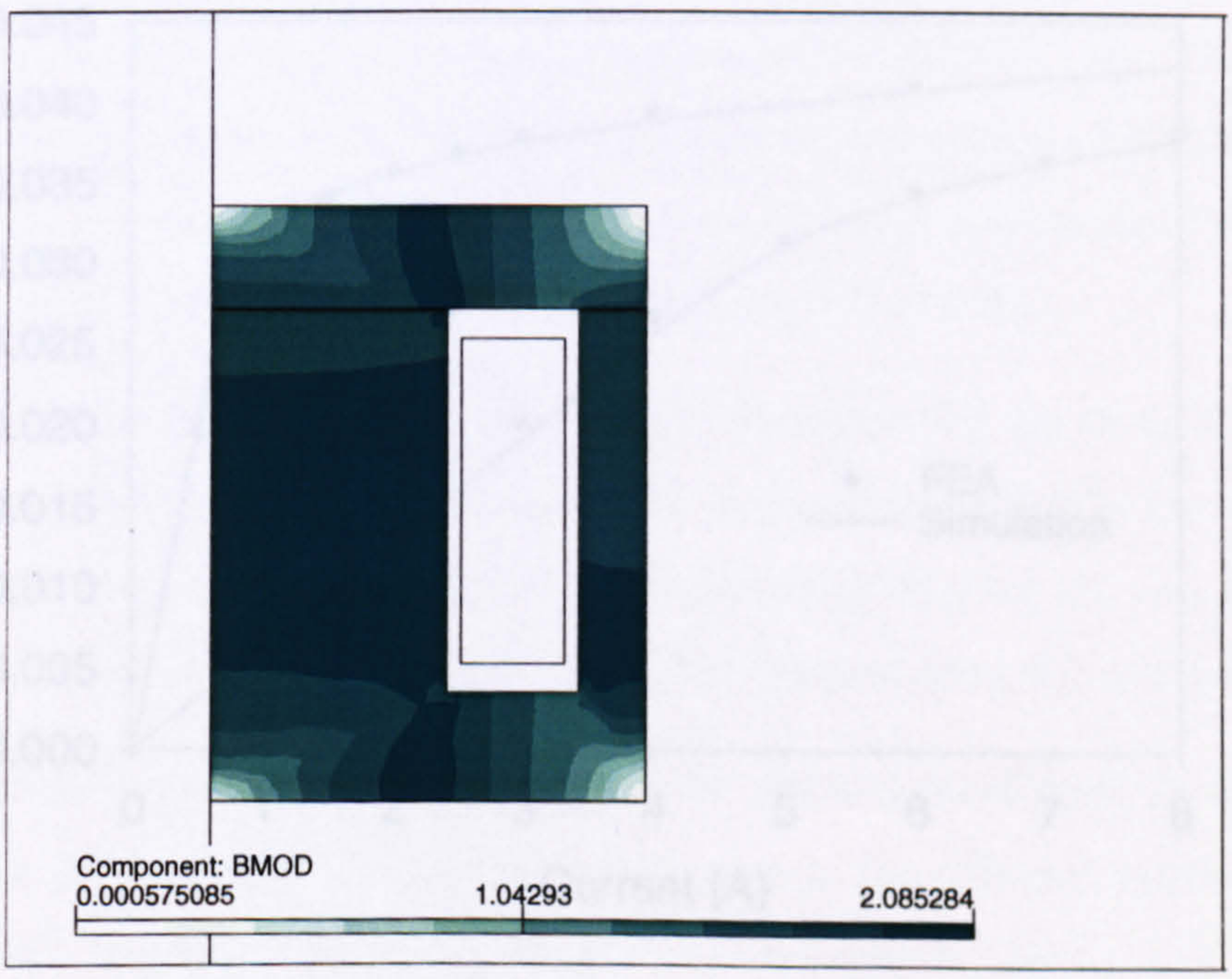

Figure 4.10: Static flux density plot for the axisymmetric actuator. Design 4. $G = 0.05mm$ and $I = 3.5A$

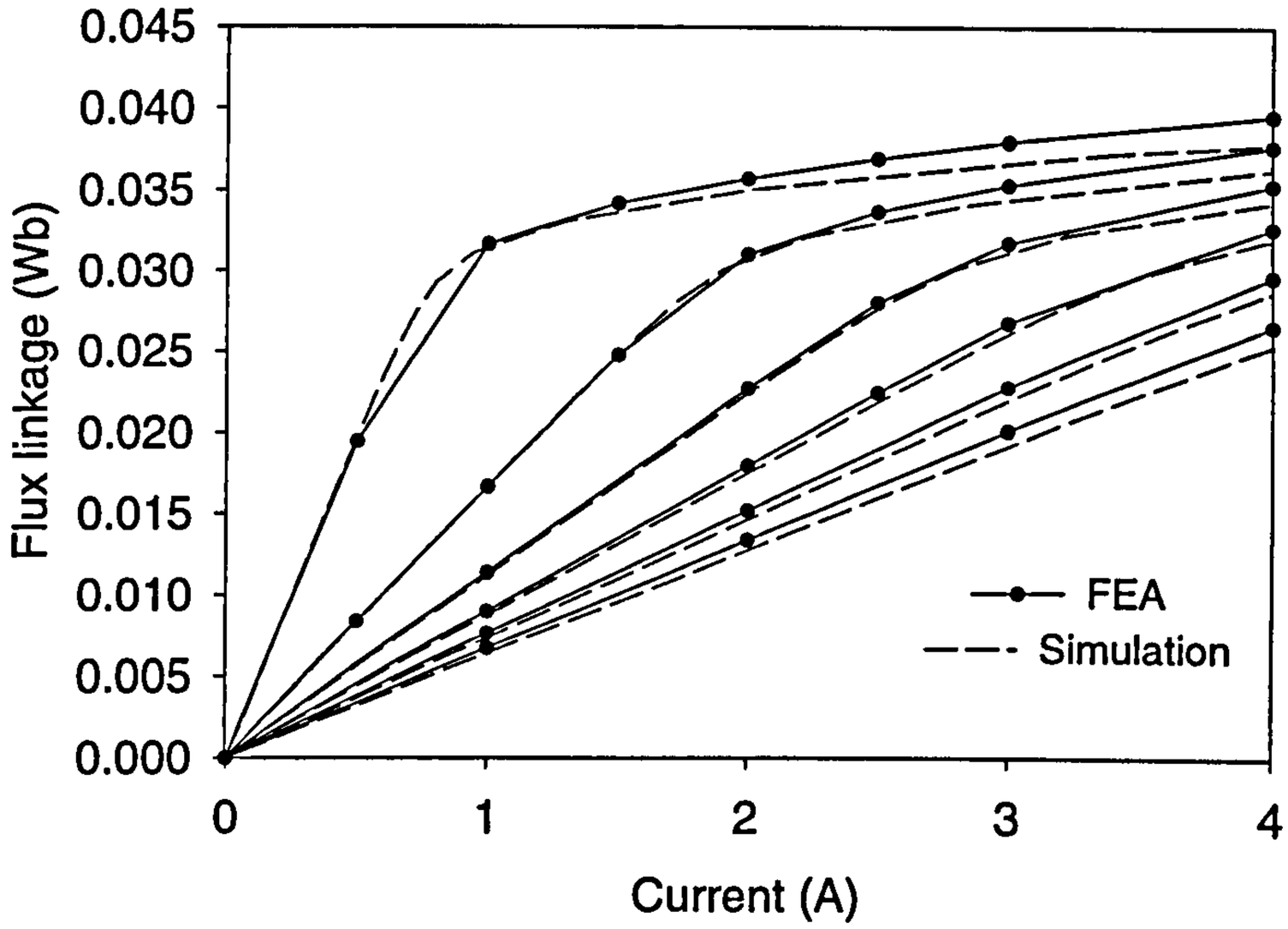

Figure 4.11: Magnetisation curves ($G = 0.5, 0.41, 0.32, 0.23, 0.14, 0.05$). Finite-element and MEC results. Design 4.

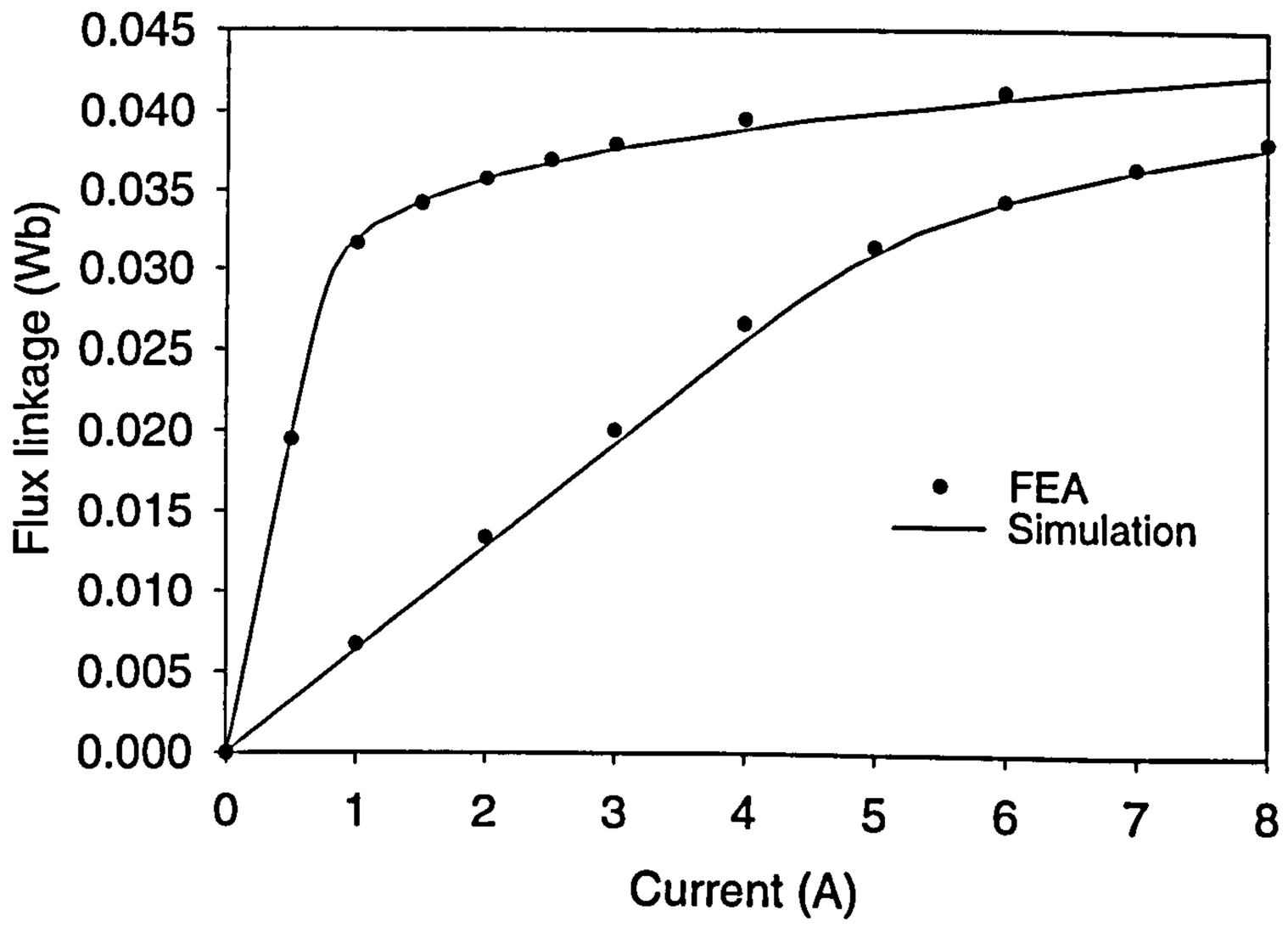

Figure 4.12: Magnetisation curves ($G = 0.5, 0.05$) for design 4, obtained with the MEC shown in fig. 2.18.

The following results have been computed for a gap=0.5mm which corresponds to the maximum airgap length for this actuator. This stroke is therefore the most sensitive to the width difference between armature and core. First, the effect of width variation is captured in fig. 4.13 showing two magnetisation characteristics derived from 2D FEA for which a stack length of 150mm has been chosen. The values for A and B are summarised in table. 4.3. The design for $B = A$ gives obviously a higher flux linkage for the same magnetisation current. The difference between both widths is kept small as it is in practice. Indeed, this variation is only due to a mechanical constraint and is not really a desired feature. Figures 4.14 and 4.15 show a comparison between one of the 2D FEA magnetisation curve and its respective analytical computation.

By reducing the stack length by a factor of ten ($Lstk = 15mm$), a large discrepancy is expected between the 2D FEA and the MEC as shown in fig. 4.16. Then it appears clearly that the analysis of a rectangular electromagnetic device based on the 2D finite element analysis requires a correction factor for end-effects.

3D Finite-Element

The complete validation of the analytical solution is based on a 3D finite element analysis. The previous E-core design has been implemented in MEGA [40]. This numerical analysis was developed at Lucas Electrical and Electronics systems for a different purpose and was run again for validation of this thesis. Two cross-sections of the 3D mesh are shown in fig. 6.4 and 6.5 and are commented in section 6.3.1.

In fig. 4.17 a comparison between the 3D finite-elements and the analytical approach is given for five different airgap lengths and with *limbsect* set to 8. The results obtained with the gauge curve method developed in the previous chapter are also shown. The minimum and maximum gaps chosen for this last method were 0.1 and 0.5 mm.

The computation of the flux linkage in the 3D finite-element analysis was obtained by computing the coenergy over the complete system for different currents and gap lengths. Indeed, the flux linkage is related to the coenergy W_c by:

$$W_c = \int \psi \, di. \tag{4.2}$$

Therefore by applying a first-order difference method, it follows:

$$\psi(\frac{i_k + i_{k+1}}{2}) = \frac{W_c(i_{k+1}) - W_c(i_k)}{i_{k+1} - i_k}. \tag{4.3}$$

As expected, the performance of the analytical method are not as good as in the axisymmetric case. The results are within 10 percent agreement. However , in the context of developing a preliminary design tool, there is still a great potential in applying the MEC approach instead of the slow 3D FEA. The results obtained with the gauge curve method are in excellent agreement with the MEC. As the gauge was computed from the linear elements of the magnetic circuit as well as the magnetisation curves corresponding to the minimum and maximum gaps (0.1 and 0.5 mm), this is a relatively expected conclusion. Although this is not demonstrated here, the computation of any intermediate magnetisation curves based on the same data but computed with 3D FEA instead of the MEC would give a better agreement with the finite-element results.

In the previous results, the variable *limbsec* creates an artificial de-saturation in the limbs that slightly compensates for the circuit simplicity. Figure 4.18 shows the MEC results obtained with and without ($limbsec = 1$) this parameter. Figure 4.19 confirms the importance of simulating the end-effects in the rectangular actuator and also shows that the MEC leads to more accurate results than a 2D FEA.

Variables	3D FEA
A	30.96
B	28.48
C	5.225
D	5.355
T	8.225
F	7
E	23.02
$Lstk$, $Astk$	20.25
$abcoil$	3.02
$uncoil$	1
N_t	131
$R1$	1.15 Ω
$Lamination\ material$	Unisil 35 M7
$Armature\ material$	2.5 % SiFe

Table 4.3: E-core prototype. Dimensions for design 1.

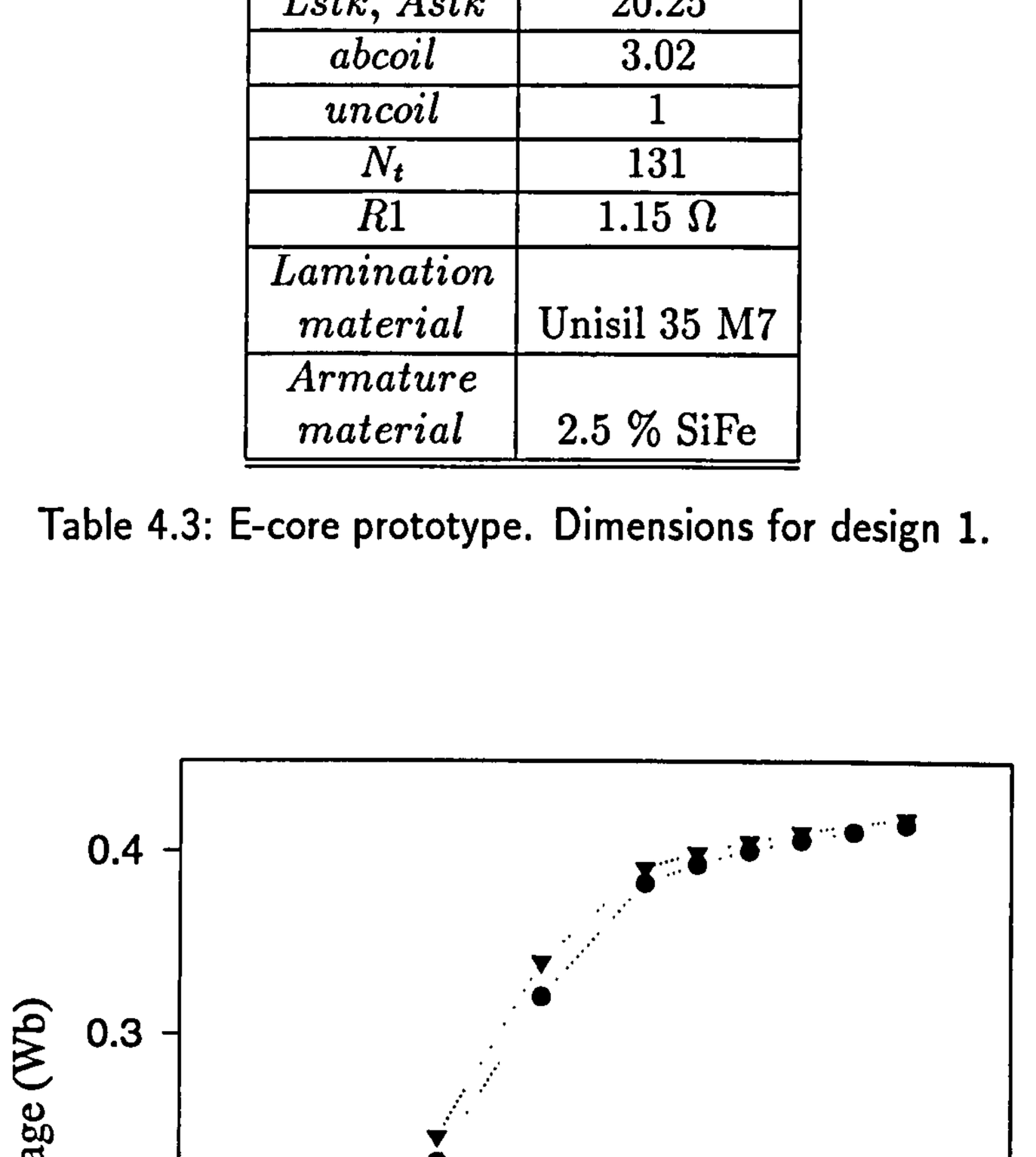

Figure 4.13: 2D finite-element analysis for $A = B$ and $A > B$ at $G = 0.5mm$. See table 4.3.

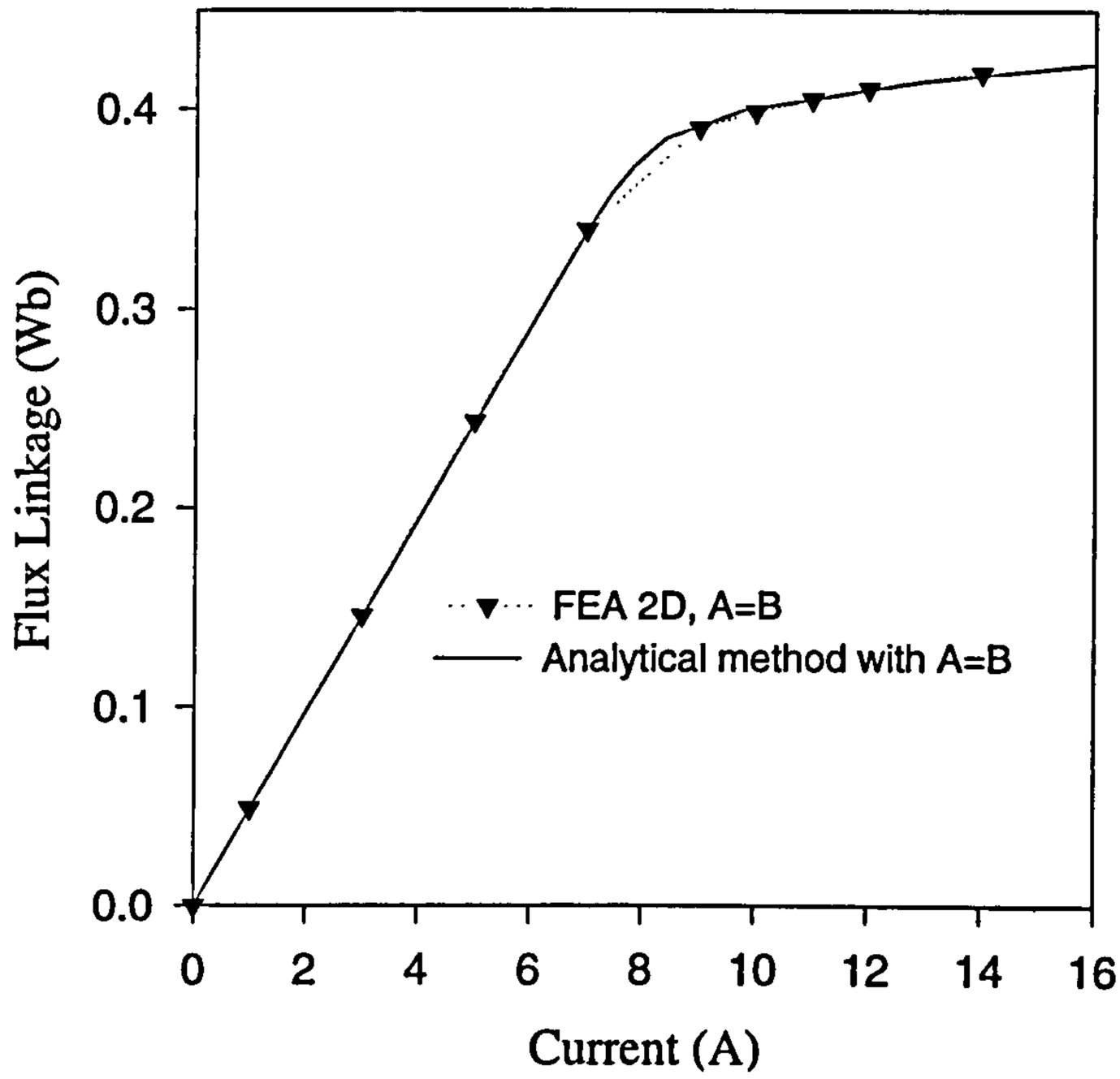

Figure 4.14: Magnetisation curve at G=0.5mm, with $Lstk = 150mm$ and $A = B$. $2D$ FEA and MEC results. E-core design (see table 4.3).

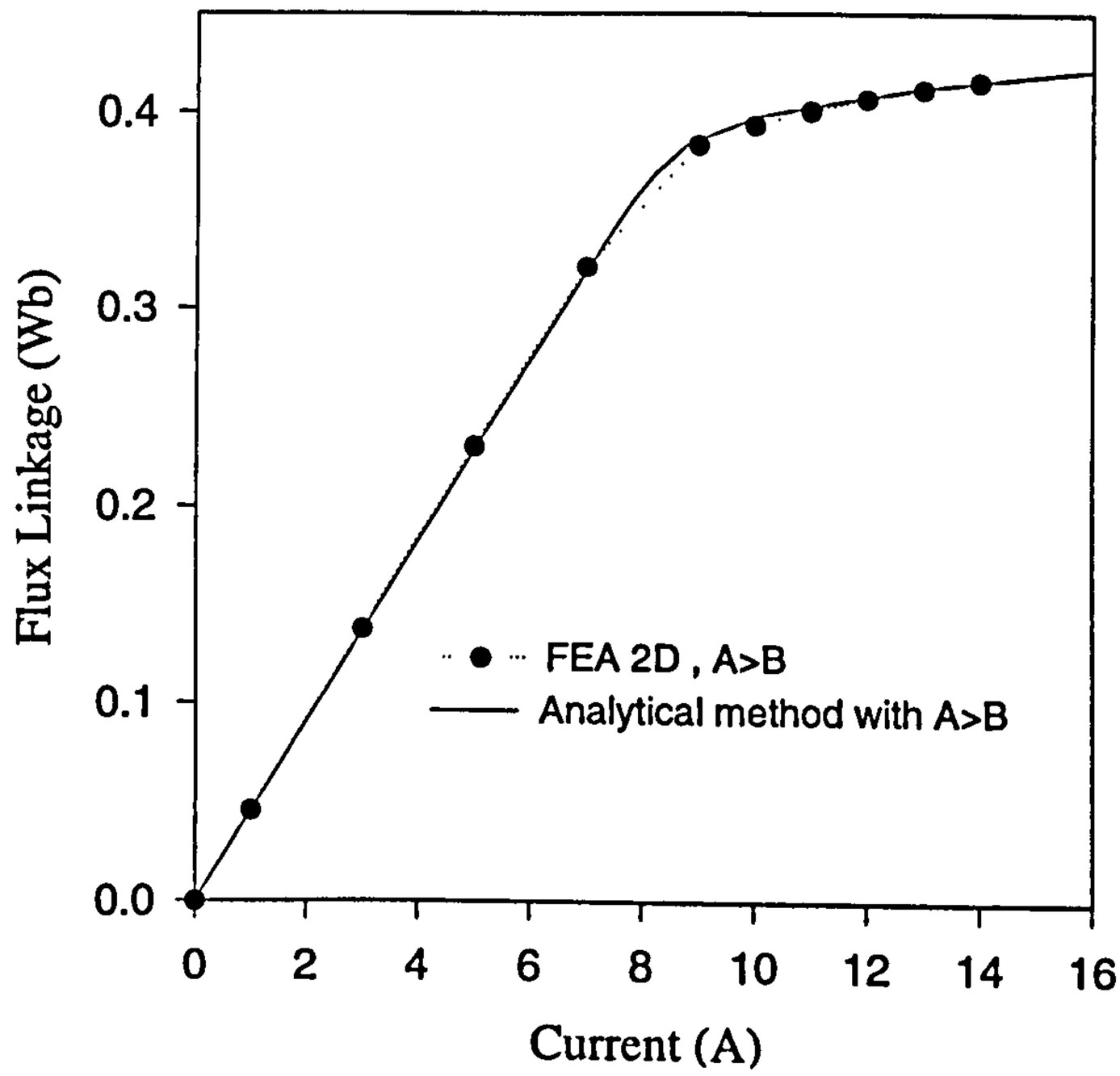

Figure 4.15: Magnetisation curve at G=0.5mm, $Lstk = 150mm$ and $A > B$. $2D$ FEA and MEC results. E-core design (see table 4.3).

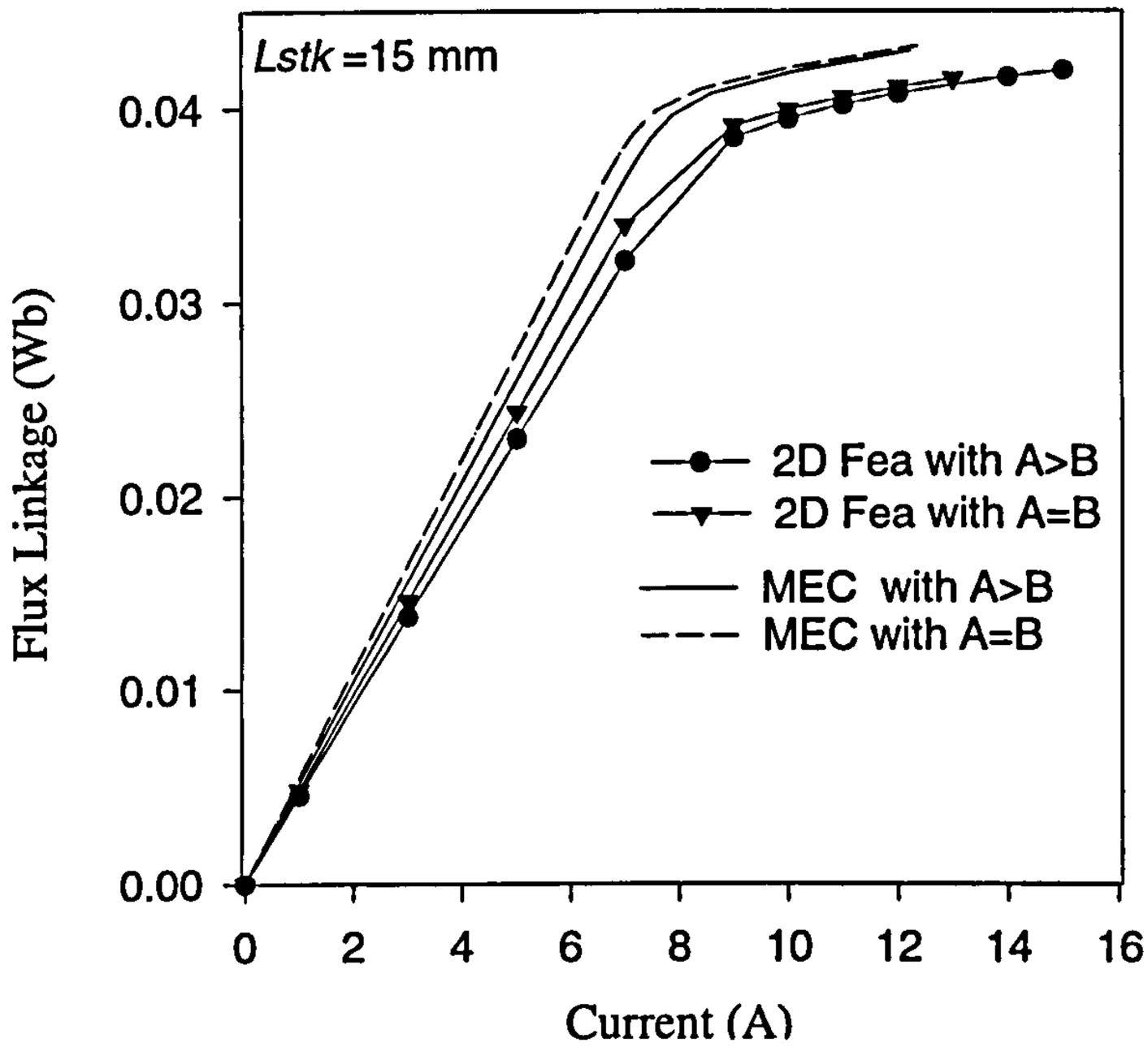

Figure 4.16: Magnetisation curve at $G = 0.5mm$ at $Lstk = 15mm$ with $A \geq B$. E-core design (see table 4.3).

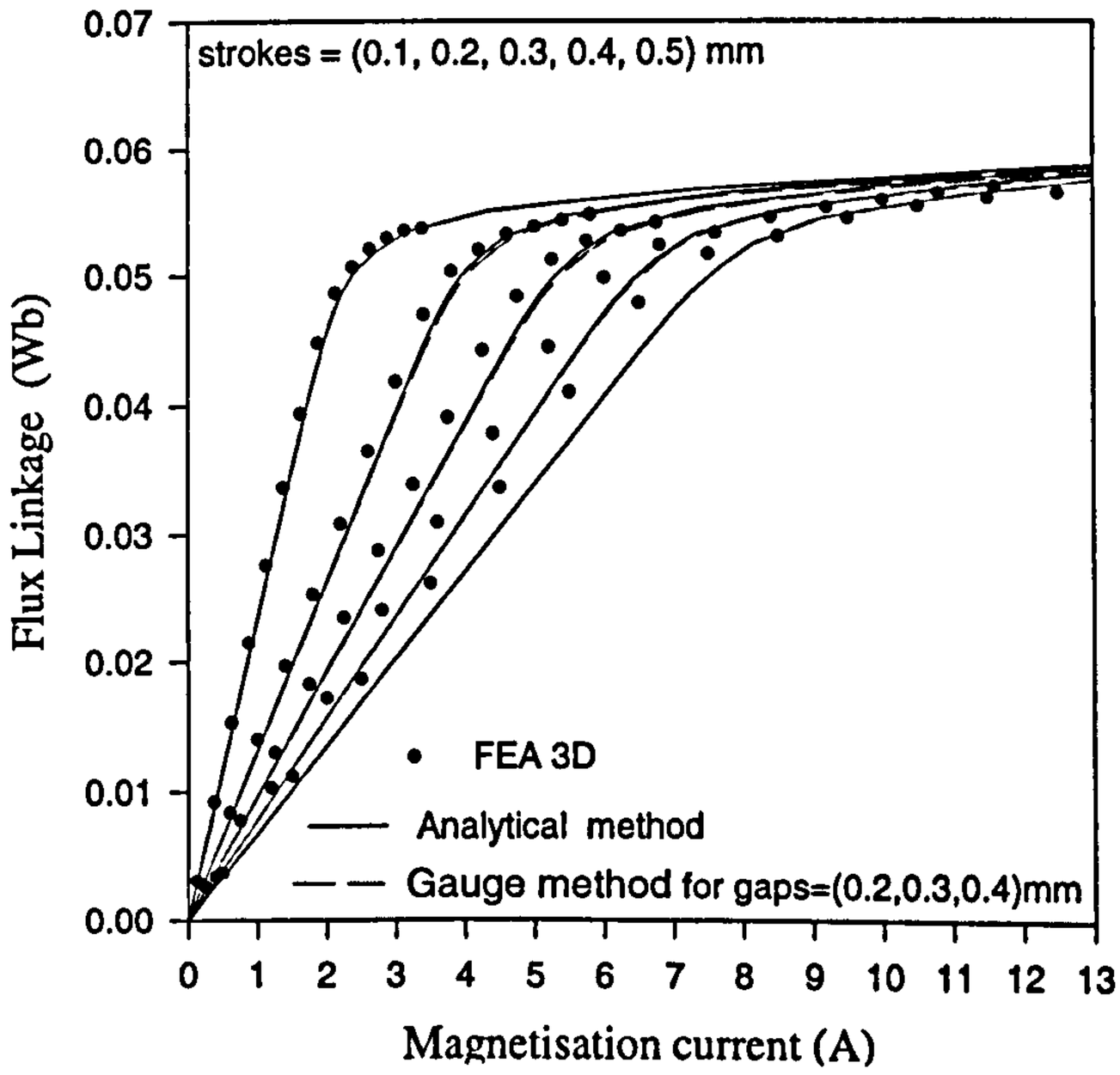

Figure 4.17: Magnetisation curves. Comparison between MEC, gauge curve and 3D FEA.

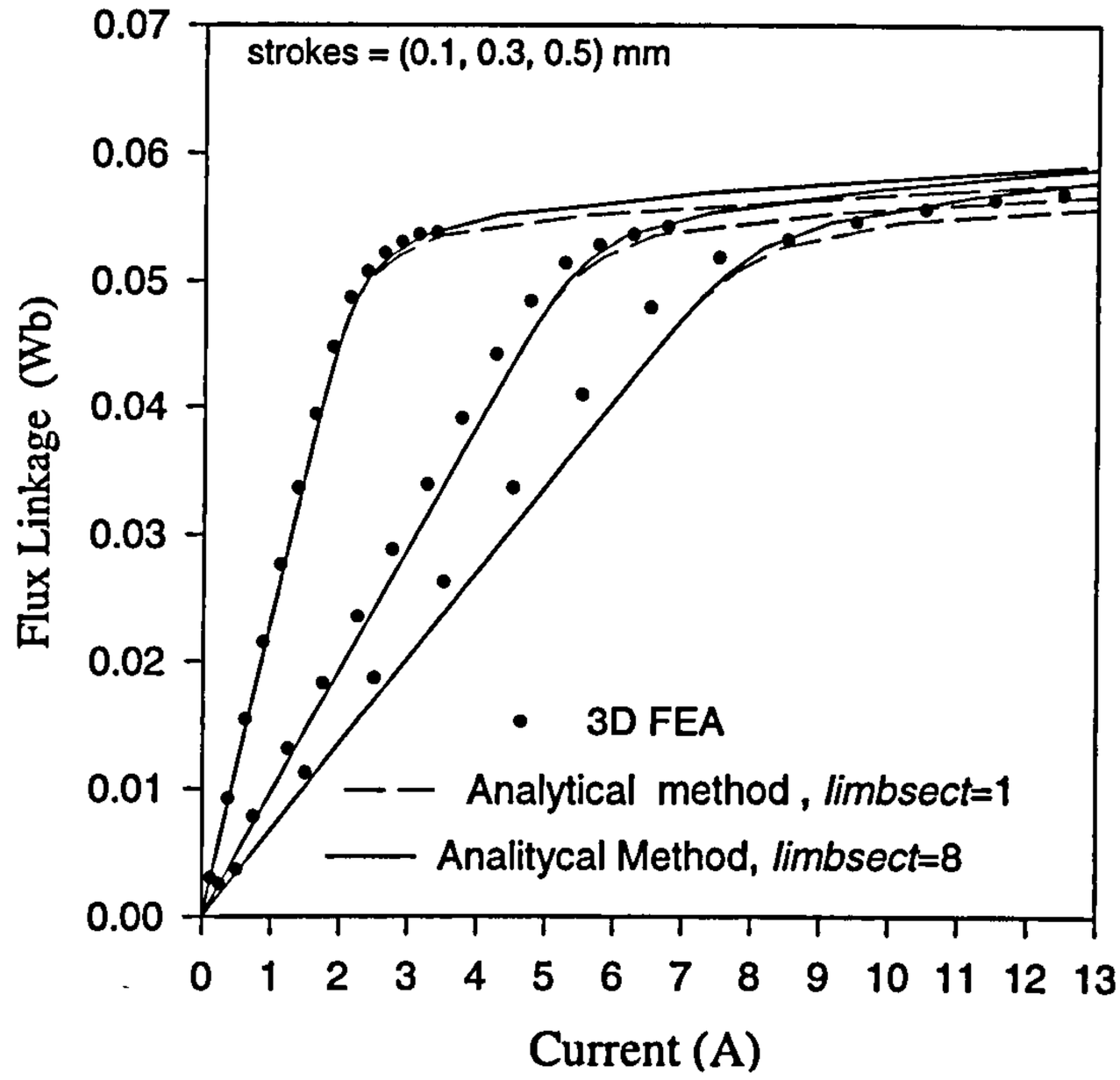

Figure 4.18: Magnetisation curves. Effect of variable $Limbsect$ on MEC results. $3D$ FEA and MEC results.

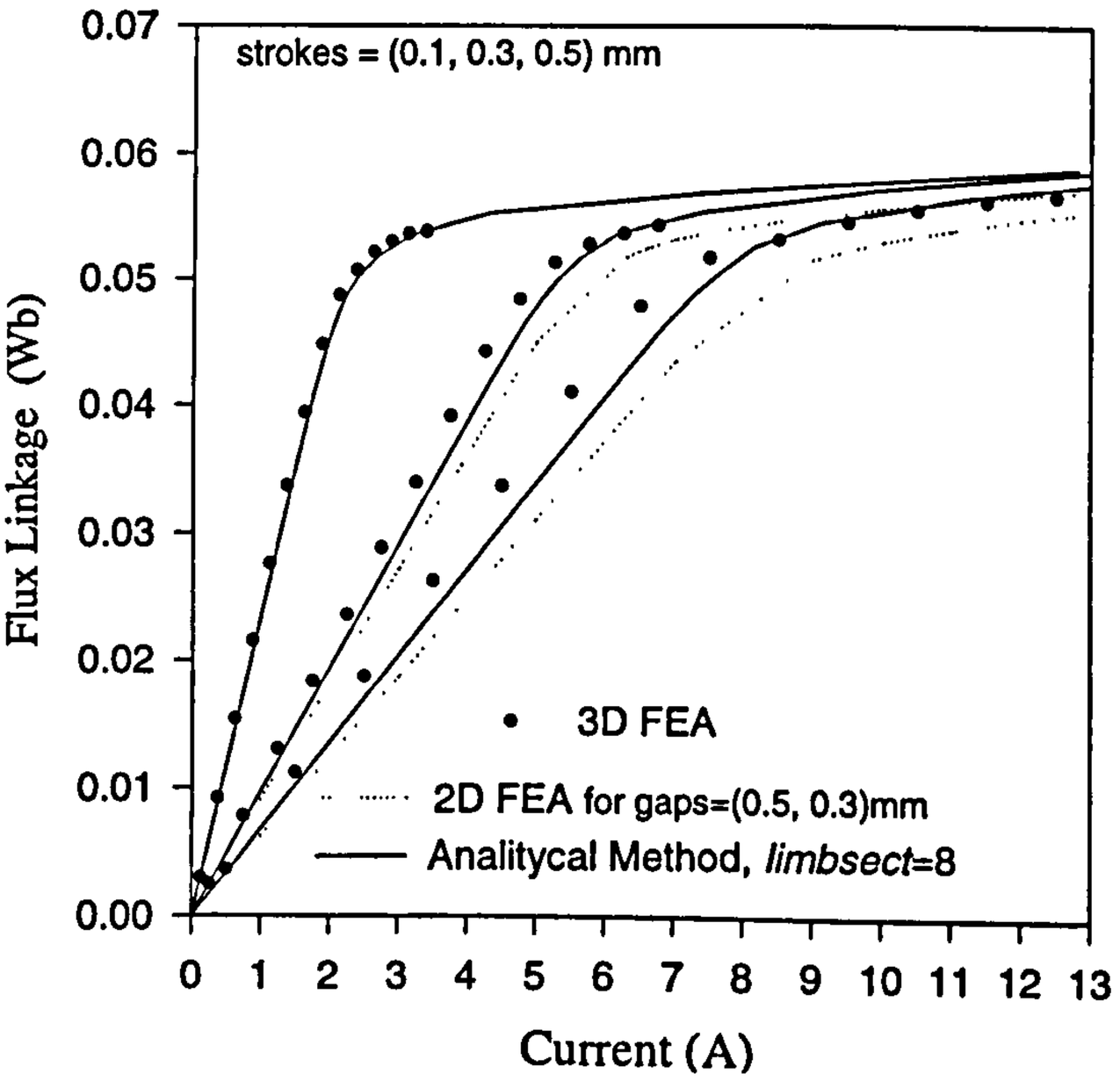

Figure 4.19: Magnetisation curves. Comparison between MEC, 2D and 3D FEA.

4.2 Validation With Measurements

Flux linkage Measurement

A simple test-rig was conceived in Glasgow in order to measure the magnetisation characteristics of an E-core and a pot-core prototype and to compare the results with the analytical predictions. The static and transient force measurements have been obtained from another test rig built by Lucas Diesel for their own purpose. The principles of this second rig are summarised in chapter 7.

The evaluation of the magnetisation curves involves the measurement of the flux linked by the coil, at constant gaps and for several current values.
A conventional technique for such a task involves integrating the induced voltage from the energizing coil such that:

$$\psi = \int V(t) - R1\, I(t)\, dt, \tag{4.4}$$

where $R1$ is the winding resistance, ψ the flux linkage, $V(t)$ the instantaneous voltage on the winding and $I(t)$ the instantaneous winding current.
This method has been successfully applied for the magnetisation curve measurement of the switched reluctance machine. The technique is relatively fast and consists mainly of applying a pulse of voltage on a phase such that the phase current increases from zero to I_{max} at a rate determined by the time constant of the motor winding. The instantaneous voltage $V(t)$ and current waveforms $I(t)$ are recorded for computing eq. (4.4). This operation assumes that the resistance of the winding is also known. However by adding to the previous test a freewheel operation, it is possible to compute on line the winding resistance as well [41].

It is not obvious that this technique is directly applicable to solenoid actuators. Indeed the method presented in [41] for measuring the magnetisation characteristics is based on a ramp type variation of the coil current increasing from zero to a I_{max}. Such a test would generate a considerable amount of eddy current in a solid or partly solid iron core. The resulting computation of flux linkage from eq. (4.4) would then give an overestimated value of current due to the surplus of mmf required by the eddy currents.

It follows that only one point of a magnetisation curve can be measured at a time and is obtained by measuring the steady state current and flux linkage corresponding to a step voltage. This operation is repeated at several step voltage magnitudes in order to evaluate the complete magnetisation curve.

Also in order to avoid any problem such as a winding resistance change due to temperature rise, the flux linkage is measured from a search coil wound with the winding.

Test-Rig Equipment

Figure 4.20 schematises the test-rig set up in Glasgow. The instruments include

1. an oscilloscope Le Croy 9414 for current and voltage measurement,
2. a current amplifier TEK AM503 and a current probe,
3. a variable frequency squarewave generator,
4. a DC power supply,
5. a IF02 integrating fluxmeter,
6. a power phase leg (see fig. 4.21).

The IF02 integrating fluxmeter measures the magnetic flux by electronically integrating the output from the search coil. An inherent problem with the integrating circuit is the drift. It is therefore important to reset the output of the integrator to zero before each measurement and to take the measurement as soon as possible after steady-state has been reached.

In order to keep a constant gap, the actuator was clamped between two solid plastic plates joined together with two non permeable screws. The core and armature were separated with the plastic shim of known thickness. The core and armature surface have been finely grounded in order to improve their flatness and reduce the amount of residual gap. Another difficulty with this rig was to provide a perfect alignment between the armature and the core, which was adjusted by hand.

A	20.4
B	21.6
C	3.45
D	3.9
T	3.3
F	4.7
E	18.8
$Lstk$	14.1
$Astk$	14.46
N_t	140
$abcoil$	2.9
$uncoil$	1.8
$Fstk$	0.95
$R1$	1.4 Ω
$Lamination\ material$	Unisil 35 M7
$Armature\ material$	2.5 % SiFe

Table 4.4: E-core prototype. Dimensions for design 2.

The dimensions of the potcore prototype are given in table 5.1. The number of turns of the search coils was 100. The results of these measurements of flux linkage versus current for several gaps are given in fig. 4.23.

Similarly an E-core prototype from Lucas was tested on the rig. Its dimensions are summarised in table 4.4. The coil was again hand-wound with 140 turns. The search coil was made with 120 turns. The results of these measurements are compared with the MEC in fig. 4.24. The minimum specified value for the stack factor (0.95) was chosen when running the MEC. The variable *limbsec* was set to 1. For comparison, figure 1.4 shows the two rectangular actuators used for validation either by finite-elements or measurements as well as the pot-core solenoid actuator.

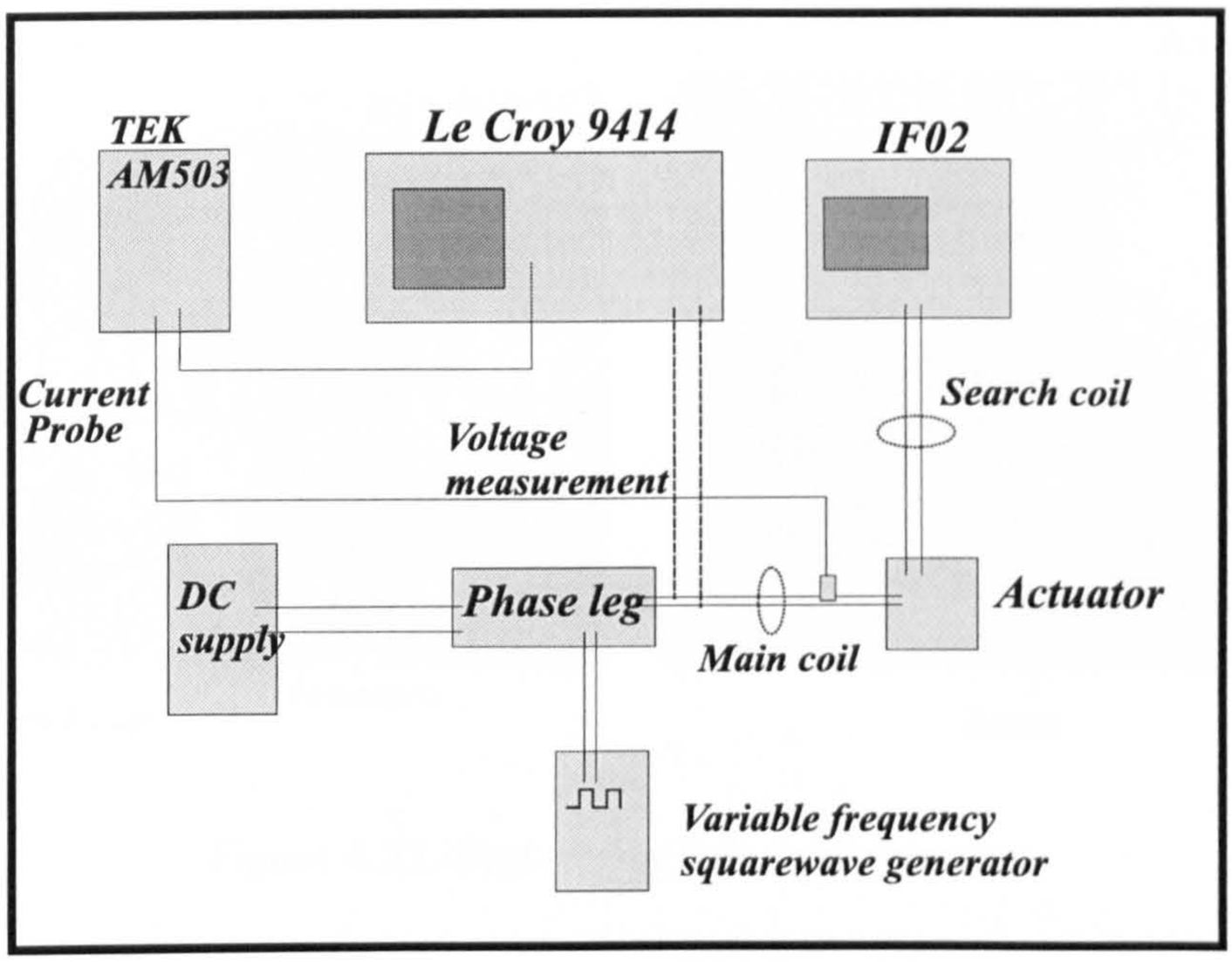

Figure 4.20: Test-rig set up for magnetisation characteristics measurements.

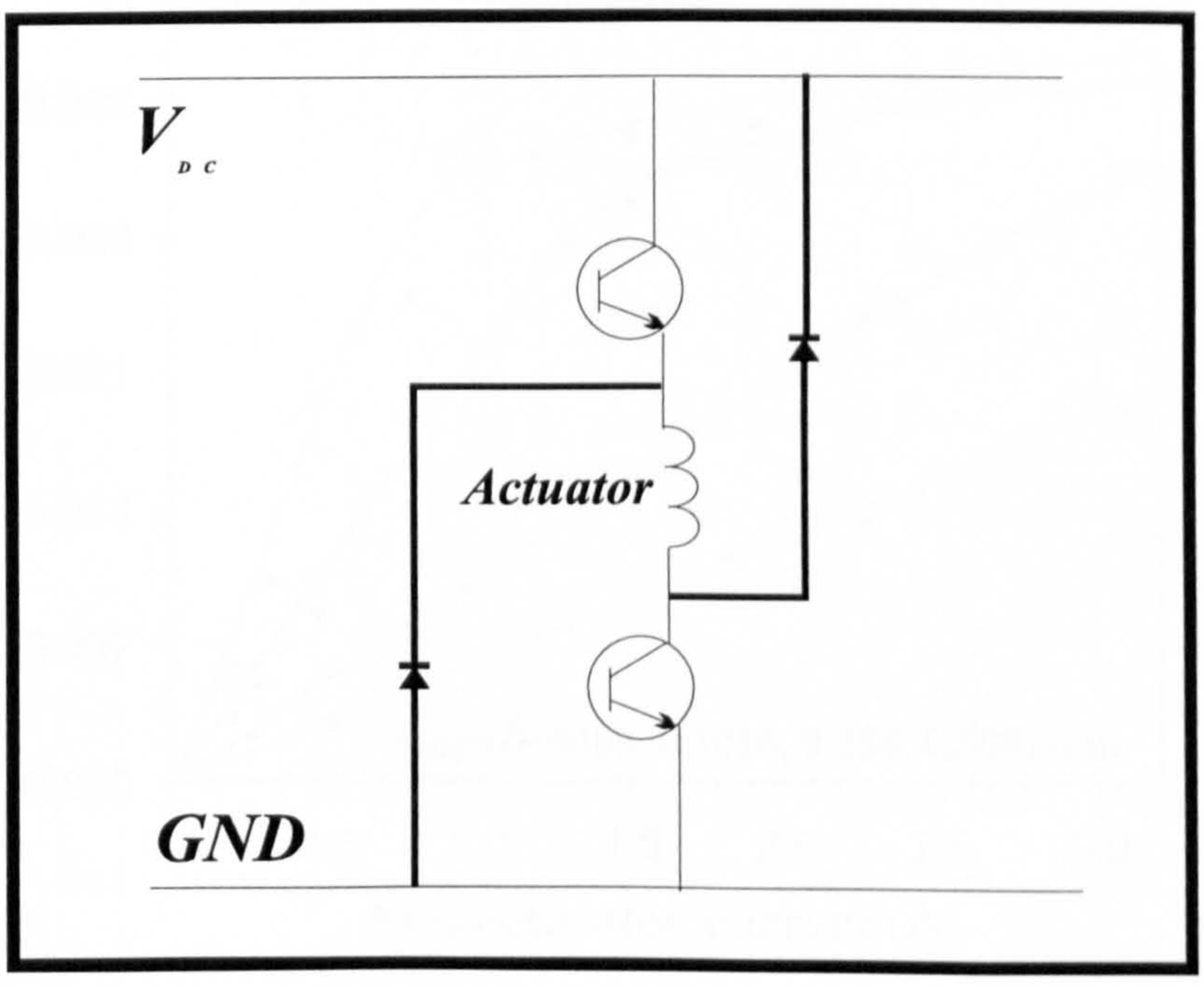

Figure 4.21: Driving circuit for static measurements.

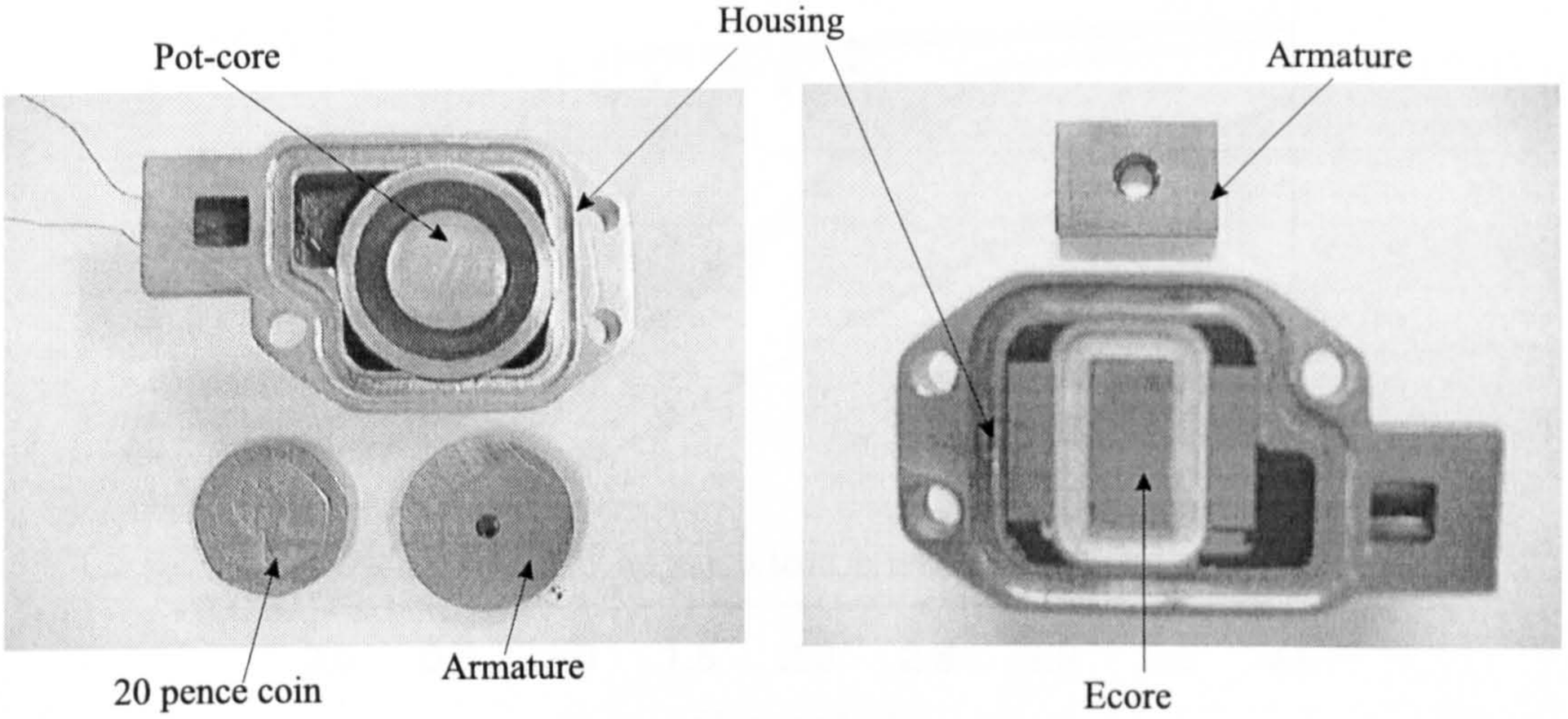

Figure 4.22: Fast-acting solenoid actuator.

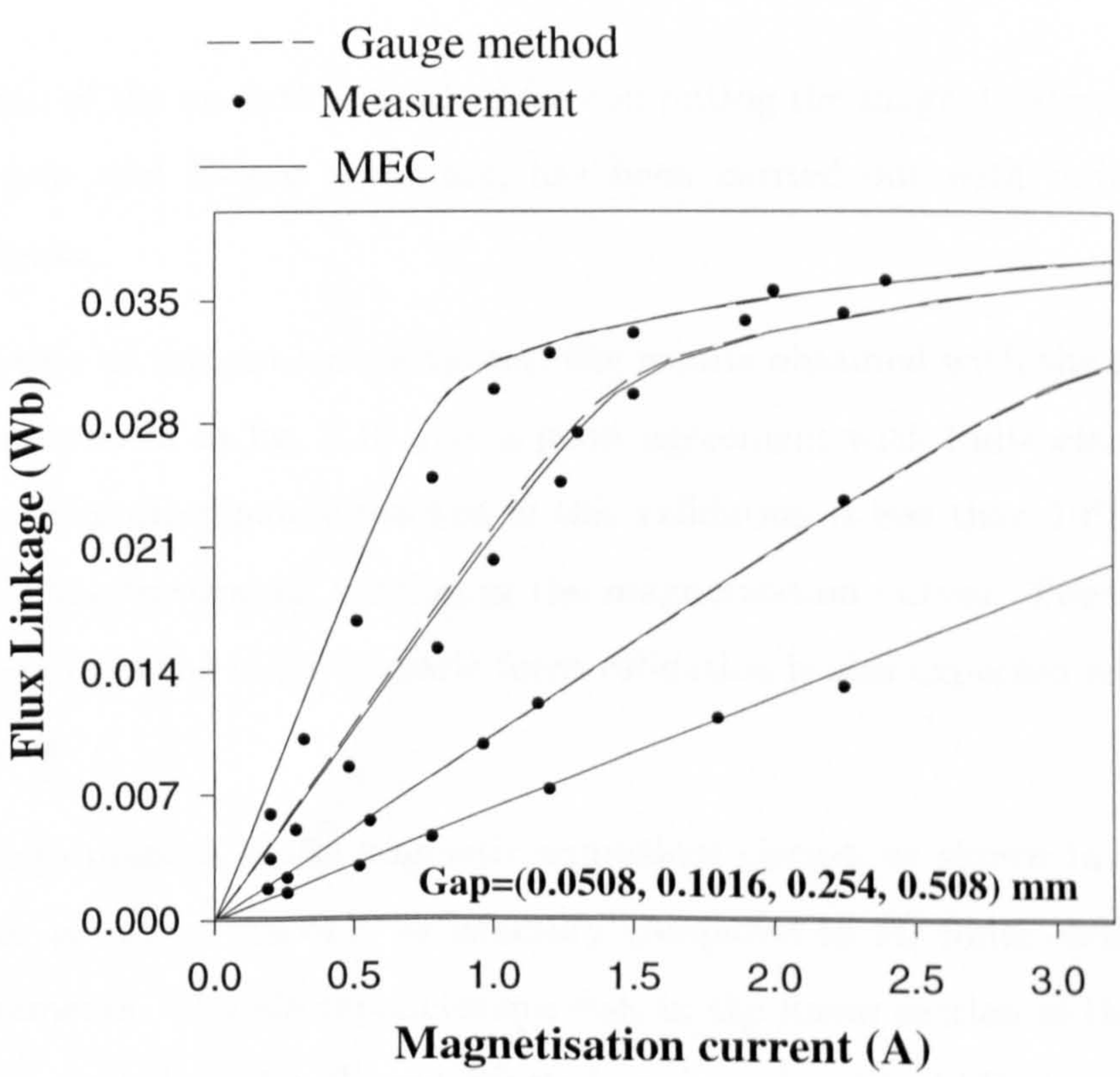

Figure 4.23: Magnetisation characteristics for a Pot-core actuator. MEC, gauge curve and measurement results. Design 4

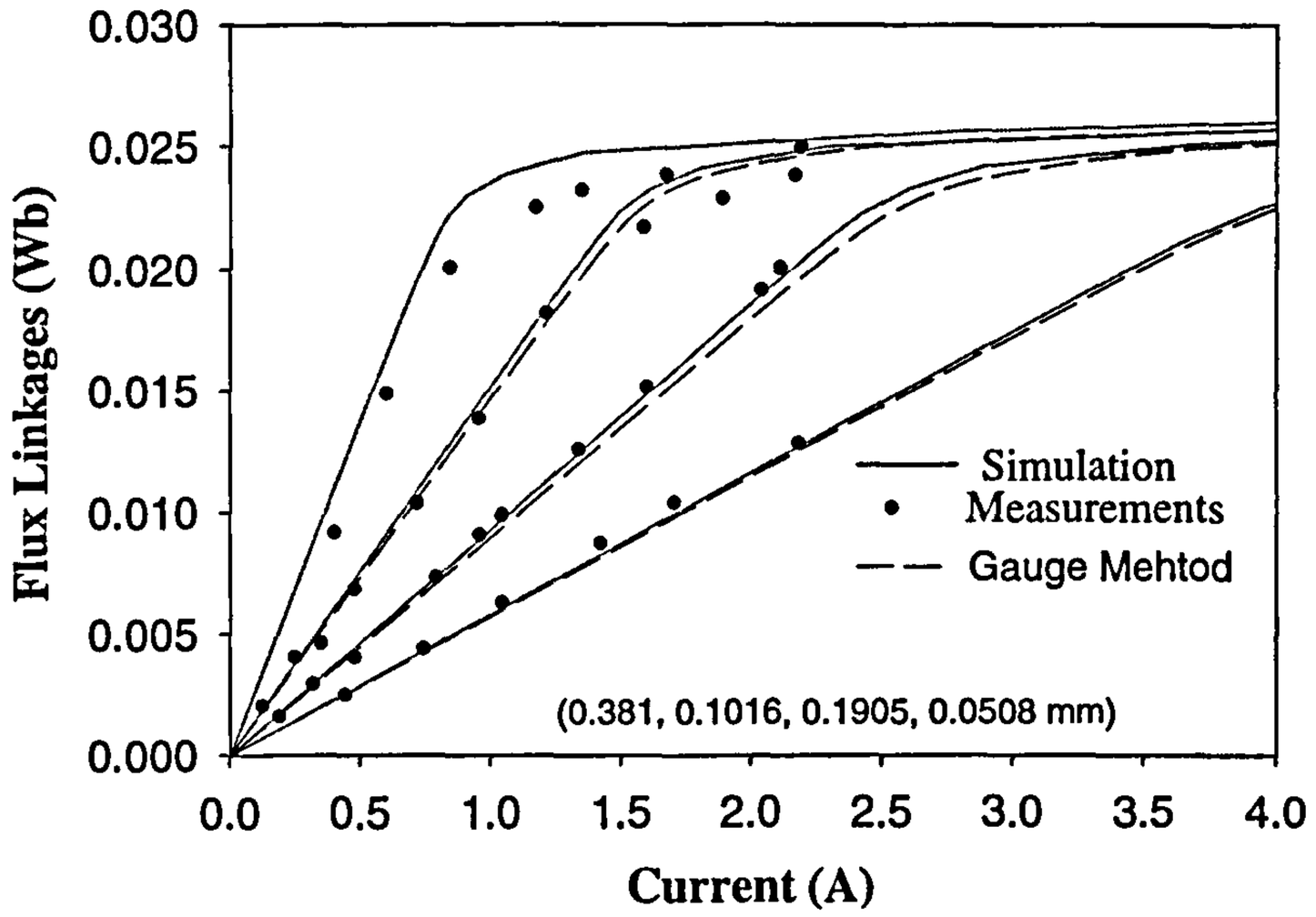

Figure 4.24: Magnetisation characteristics for an E-core actuator. MEC, gauge curve and measurement results.

4.3 Conclusions

A validation of the analytical method for computing the magnetisation characteristics, for both pot- and E-core actuators, has been carried out with finite-elements and measurements.

In the case of the pot-core actuator, the results obtained with the magnetic equivalent circuit shown in fig. 2.16 give a good agreement with finite-elements and measurements. The discrepancy reached in this validation is less than 10% (design 4) and affects only the 'saturated' portion of the magnetisation curves. Therefore a satisfactory agreement in the magnetostatic force validation is also expected with this network configuration.

The performances of the magnetic equivalent circuit, as shown in fig. 2.24 for the rectangular actuator, are only satisfactory compared to 3D finite-element analysis or to measurements. The discrepancies are due, in the linear section of the curves, to the difficulty in modelling the 3D end-effects based on simplified 2D shapes of flux paths. Above the knee point in the magnetisation characteristics, their origin may be due to a high interaction between the fringing, slot leakage flux and the flux within the iron,

changing the overall requirement in Ampere-turns; or it could also be linked to the modelling of the nonlinear anisotropic steel in the iron. The 3D finite element analysis was based on a fitted polynomial expression while the simulation uses directly the BH data interpolated linearly. In general, the analytical results are however better than the ones retrieved from a 2D finite-element analysis, confirming the 3D 'nature' of this problem.

The gauge curve method has also been applied to different pot-core and E-core designs and has shown a very good agreement with the MEC approach.

Although the geometry of the devices studied in the thesis are relatively simple, these previous results show the difficulty in simulating highly nonlinear devices using a magnetic equivalent circuit. The finite-element is certainly a great help in building the analytical model for axisymmetric devices such as the pot-core actuator. However, this approach is nearly impossible for the E-core actuator due to its 3D flux paths. In this case, the model of the end-effects is unfortunately a very crude approximation of the real paths. The magnetic equivalent circuit does not allow easily the modification of the actuator geometry. If the changes 'disturb' the original flux paths in the airgap, a new evaluation of the airgap permeance expression is most probably required.

Part II

DYNAMIC PERFORMANCE

Chapter 5

Axisymmetric Solenoid Actuators

5.1 Introduction

In the previous chapters a general method has been established for computing the magnetostatic performance of solenoid actuators. This has involved designing a magnetic equivalent circuit for each type of actuator, from which a set of magnetisation characteristics is rapidly evaluated. Although this magnetic data is the only information required for evaluating the general dynamic performance of a conventional switched reluctance machine [21], this approach would induce large discrepancies in the case of the axisymmetric solenoid actuators. Indeed the solid-iron structure of such devices involves a significant generation of eddy currents during their operating time. Their dynamic performances are easily delayed by several tenths of a ms. However some applications such as diesel injection may require an actuator time response in less than a ms [3]. The magnetic delay can, to some extent, be minimised by applying appropriate control schemes [10]. The actuator requires indeed a certain amount of energy to diffuse the eddy currents and the flux through the entire iron cross section. Therefore any control approach capable of providing quickly a boost of energy during a few tenths of a ms will lead to a faster actuator response. Although the eddy current generation can not be avoided, a careful magnetic design (e.g. steel choice, geometry, dimensions) may also help in reducing the overall time response.

The account of eddy currents, when studying the dynamic performance of solid or partly solid iron machines, is then definitely a requirement. However the analysis of eddy currents based on the finite-element method still remains a challenge [42, 13, 43, 44]. Real engineering problems, involving any specific control approach, requires a time-stepping technique, which slows down significantly the overall numerical analysis. However the optimisation of the control strategy for a particular prototype in a new application does not require such a sophisticated analysis, nor does the choice of the number of turns or the general dimensions of the actuator. Although the finite-element method is important at a certain stage in the design process , it is not however compulsory until the latest one when the effect of small design features, such as holes in the armature, has to be quantified on the dynamic performance. Therefore the general objective of this chapter is to develop an analytical method for a rapid computer-aided design tool, which will include the nonlinear effects of eddy currents on the dynamic performance of axisymmetric actuators without any constraint on the control strategy.

5.2 Eddy Current Analysis

5.2.1 Literature Survey

The literature review includes a series of papers in which the eddy current analysis is not strictly numerical and therefore may be relevant in this context. The laminated problem is not well covered in this review as the author considers it as being less general than the solid iron case.

In 1948, Pohl [45] proposed a method for computing the transient flux in a solid iron core in which the actual core was replaced by a laminated one with a short-circuited secondary winding and 100% coupling. In his development, the conductance and inductance of this damping ring were evaluated from first principles by assuming a linear rise with time of the magnetising field within the solid iron circuit of various cross-sections. In the case of a partly solid iron machine or in the presence of airgaps within the magnetic circuit, Pohl proposed replacing the permeability of the solid iron core

by a resultant one, much reduced by the reluctance of the remaining path. Although he did not reach a satisfactory agreement when compared with measurements, Pohl's paper had an important impact on other authors' works as he introduced the analogy between the eddy currents and a secondary damping winding, suitable for any *DC* or *AC* systems.

In '*Transient Performance of Electric Power systems*' written in 1950, Rüdenberg [46] proposed two different approaches regarding the analysis of the eddy current in an iron core. The first one was similar to Pohl's technique as the effects of eddy currents were compared to a secondary damping winding. However Rüdenberg's objective was to study their effects on a saturated magnetic circuit. In his analysis, the leakage flux between the primary and secondary winding was neglected as well as any presence of airgaps within the magnetic path. The resistance of the damping winding was not explicitly computed; instead it was replaced by defining a fictitious time constant. His development concluded that, under the joint effect of the current and the induced currents, the magnetic flux performs as if the the total current was carried by the primary winding and was characterised by a time constant equal to the sum of both circuit time constants. Although Rüdenberg also gave an experimental method for evaluating the fictious time constants for both winding, his method is of limited interest as the time constants in a nonlinear problem are no longer a function of the circuit components but a function of the steady state flux and induced voltage.

More importantly Rüdenberg studied the eddy current formation within a U-shaped electromagnet with rectangular solid steel limbs of length Δ. A second part of the magnetic circuit consisted of airgaps of length δ_0 and a third part, the yokes, contained laminated-steel sheets in which eddy currents were neglected. Rüdenberg started his analysis by the following statements which have had a large influence on the direction of this thesis:

'If a D-C magnet is switched on or off, the solid-steel core of which has a substantial cross-sectional area, every change of the flux induces secondary currents in the iron circulating in eddies around the magnetic flux. Such eddy currents effect transient phenomena very much as currents in secondary winding do. However, since they do not follow any particular paths as in wires but are distributed over the solid-steel core in

various directions with various density , it is not possible to correlate from the outset a definite resistance or a definite self inductance to the eddy currents. Rather we must determine the electromagnetic linkage of every elementary path of current and must develop a differential law of the phenomena in order to derive the performance of the eddy currents in space and time. '

By applying the first principles (Faraday's and Ampere's laws) on an elementary closed 3D flux tube and combining the resulting equations, the author derived a second-order partial differential equation. A finite solution was obtained by assuming an instantaneous switch-off in the winding leading to the instantaneous decay of the flux density ($B = 0$) within the surface layer of the limbs. The complete flux density distribution in a rectangular core during natural decay is then given by :

$$B(x,y,t) = B_{n,m}\, cos(n\pi\frac{x}{a})\, cos(m\pi\frac{y}{b})\, e^{-\rho_{n,m}\, t}, \tag{5.1}$$

where n, m are odd integers defining each an infinite series of modes; the variables $a\ (x-direction)$, $b\ (y-direction)$ are the side lengths of the limb cross-section. $B_{n,m}$ gives the amplitude of the (n,m) mode as equal to:

$$|B_{n,m}| = \frac{4}{\pi}\,\frac{B_0}{n\,m}, \tag{5.2}$$

where B_0 is the constant flux density uniformly distributed over the entire cross-section before the field interruption. And the damping factor $\rho_{m,n}$ is given by:

$$\rho_{n,m} = \frac{s\,\delta}{4\pi\,\Delta}[(n\pi\frac{x}{a})^2 + (m\pi\frac{y}{b})^2], \tag{5.3}$$

where s is the steel resistivity and $\delta = \delta_0 + \Delta/\mu_r$ with μ_r being the relative permeability of the iron.

This solution has only a limited practical interest due to the assumption of material linearity and to the restricted and ideal 'driving conditions'. However, with this formulation, the decay of the flux due to the eddy currents in an iron core is a function of an infinite number of modes, each characterised by a particular time constant. The high harmonic waves decay very rapidly due to the quadratic influence of the mode

numbers n and m in eq. (5.3). Therefore the fundamental time constant is the longest and is given by :

$$T_{1,1} = \frac{4\,\Delta}{\pi\, s\, \delta} \frac{ab}{(a/b + b/a)}. \tag{5.4}$$

The time decay is then proportional to the cross-sectional area of the steel core, to the steel conductivity and also to the limb length. It is also affected by the presence of airgaps within the magnetic path. By reducing the results to a 1-dimensional problem e.g. $a >> b$, it results that $T_{1,1} \propto b^2$ as found by Polh [45] for the time constant of the fictious damping winding.

Kesavamurthy proposed two different methods for the analysis of eddy currents in solid iron core. In [47] he studied the rise of flux due to impact excitation. Based on a 'limiting nonlinear theory' the author compared the rise of flux in the core to the propagation of a ' magnetic field wave' from the surface to the centre of the cross-section. For a rectangular section, the eddy currents were explicitly assumed to follow closed rectangular paths. This original treatment fails however to take into account the real electro-magnet configuration (e.g. airgaps, armature movement). In [48] Kesavamurthy computed analytically the rise of flux under the effects of eddy current by solving simultaneously Poisson's equation and the complete electrical circuit equation (including the winding resistance). A finite solution for the current and flux rise is only available for the limited case where the width/depth ratio of the rectangular cross-section is large. The author extended his treatment to the finite rectangular cross-section by making different assumptions:

1. on the eddy current paths (rectangular or rhombic configuration) in order to reduce the 2-dimensional problem to a 1-dimensional case only.

2. on the fact that the eddy current density within one elementary closed path is due to the flux embraced by this path or is what it would be for an infinitely wide rectangular block (1D problem).

Then the author extended his analysis to the flux decay for which a comparison can be done with the known analytical solution [46]. For a wide range of width/depth

ratio, the best results were obtained by assuming rectangular paths and an eddy current density function of the flux embraced by the path under consideration. Based on the previous results, Kesavamurthy also defined an electric equivalent circuit by computing the impedance function between the induce voltage and the magnetic field at the core surface. The resulting circuit topology is equivalent to a ladder network having its inductances and resistances a function of the roots of two computed functions. Although the method can be extended to take partly into account the presence of airgaps and saturation, the author admitted that this would also assume a transient uniform distribution of the flux density across the core section. In the conclusions he added that the extension of the equivalent circuit representation to take the non-linearity into account, without introducing physical contradictions, would be interesting and useful.

This is probably the way that Brailsford chose in 1962 to built his analogue of a steel lamination for studying the flux density waveform distortion within a silicon-iron lamination due to a magnetising field at 50c/s [49]. However no information is given on the origin of the chosen magnetic circuit, nor on the formulae for computing the inductances and resistances shown in the model. Therefore the paper is not very useful in this context.

In 1962 Roberts [50] presented another analogue model for simulating the eddy current and magnetic flux penetration in saturated iron. His approach was very different from Kesavamurthy as he deduced the general shape of the equivalent network from first principles. However Roberts failed to associate a physical interpretation to his network and designed it on a RC line model by setting arbitrarily the value of the resistance elements as a function of permeability. The saturation is then modelled by replacing the resistance elements with a more complex model based on a biased bridge-rectifier circuit.

More conventional is certainly the work carried out by Subba Rao. In 1964, he presented a method for predetermining the eddy current losses in a rectangular solid-iron core due to an alternating magnetic field under saturation [51]. More importantly he also developed an equivalent magnetic circuit of the rectangular solid iron core

for impact excitation problems [52]. The basis for obtaining the circuit is the eddy current expression under an alternating magnetisation for a solid-iron core of large width/depth ratio, obtained from Maxwell equations. The equivalent circuit consisted of a secondary resistance and a leakage reactance, which depend on the shape of the section and the electrical and magnetic characteristics of the material. The circuit was obtained at constant permeability and then extended for use under nonlinear conditions. Although the correlation obtained by Subba Rao was satisfactory, it is not correct to solve a nonlinear problem on the basis of an analytical solution obtained from a linear problem as it introduces some physical contradictions [48]. The effect of airgaps within the magnetic path was also neglected.

Another important paper is the one presented in 1965 by Silvester [53]. His analysis was based on the analytical solution obtained from Maxwell equations, describing the natural flux decay in a linear rectangular bar [46]. The magnetic field and the eddy current density were given by an expression similar to eq. (5.1), a function of an infinite numbers of mode (m, n). All these modes are assumed to coexist in the bar, superimposed on one another. Therefore the author described them as being characteristic of the rectangular bars. Indeed Silvester considered that the spatial distribution of the field and eddy currents was dictated by the shape of the iron boundary while the nature of the time functions (see eq. (5.1)) must reflect the way the coil current varies. Each mode was then replaced in a magnetic equivalent circuit by a different short-circuit secondary winding, uncoupled from each other and characterised by a leakage inductance, a resistance and a coupling coefficient with the energizing coil. The evaluation of these elements was based on the computation of the dissipated power and the stored energy as well as of the total current of each mode flowing in the bar [1]. The transient waveforms of flux and current in the resulting magnetic equivalent circuit were then retrieved from the evaluation of the external-coil terminal admittance function. In practice the infinite sequence of circuits had to be truncated, creating a shift of all the admittance poles, which also lead to an error in the slowest and dominant time

[1]This computation is difficult as the currents are circulating in loops spread in different parts of the section, a function of the value given at m and n. Unfortunately the current computation per mode is not fully explained in the article.

constant. Two other problems were the fact that saturation was not being accounted for and this method did not provide any answer when the solid iron part was only a part of a larger problem.

More recently (1988), Lequesne [15] described an original approach for computing the dynamic performance of a plunger-type axisymmetric actuator. Lesquesne's method is a mixture of both analytical and numerical (FE) techniques in order to combine the advantages of both methods which are speed and accuracy respectively. The dynamic model includes the electrical equation of the circuit, the mechanical equation for the armature movement and also Ampere's law applied on an average flux path. The total transient flux linkage and mmf drop are approximately computed by finite elements by dividing the device in layers equivalent to closed flux tubes such that the problem is reduced to a 1-dimension case. This method showed a good agreement with conventional finite-elements and measurements, but was only tested on impact excitation.

In 1993, Zhu [17] proposed a simple electromagnetic equivalent circuit for computing the iron losses in any magnetic core with a special attention for thin laminations. The model involved an inductor including the hysteresis loop and the core nonlinearity, in parallel with two resistances for the eddy current and the so-called anomalous loss. The hysteresis loop is derived from Preisach model. The eddy current and anomalous resistances are deduced from classical and empirical formula already known for the instantaneous eddy current and anomalous loss computation. The method has been applied to an annular laminated ring inductor. The proposed method showed a good agreement with measurements under a very low sinewave and square wave voltage excitation ($100Hz$ frequency).

Several of the previous methods have been reported in [54]. The literature contains many more papers on the subject of eddy current analysis.

However most of the earlier ones had a great contribution to this thesis, either by giving a better understanding of the eddy current generation, or by developing ideas which have inspired the following analysis.

5.2.2 Theoretical Developments

Introduction

The literature review has clearly shown the limits of an analytical approach for computing the effects of eddy currents. A direct solution of Maxwell equations is only available in a linear magnetic domain and under restricted energizing conditions. On the other hand several authors have proposed an equivalent electromagnetic network. This idea has a tremendous potential in *DC* problems as it would remove the constraints on the driving conditions. However none of the earliest attempts has been completely successful. The proposed network configuration for the same problem varies depending on the analytical problem the authors considered for retrieving their equivalent network and also on their associated assumptions e.g. the network configuration . None of them found a proper way for taking saturation into account.

As it has been shown in Part I of the thesis, the development of a proper electromagnetic equivalent network only goes through a physical understanding of the phenomena that we are trying to simulate. For this reason the nonlinear eddy current generation is so complex that it cannot be properly simulated with a network configuration extrapolated from an analogy with a linear analytical solution related to a specific and already simplified problem. The eddy current generation is a nonlinear diffusion problem and the electromagnetic equivalent network should reflect the particular nature of this phenomenon.

Layer distribution

A physical understanding of the transient electromagnetic effects is possible nowadays by the development of numerical analysis such as finite-elements. Figures 5.1 to 5.6 show the diffusion of eddy currents and flux within a flat-faced axisymmetric actuator at three different times before steady state. Just after switching on, the flux and eddy currents start their diffusion within the iron from the surface layer next to the coil to the centre part of the core. The flux density as well as the eddy current density appear

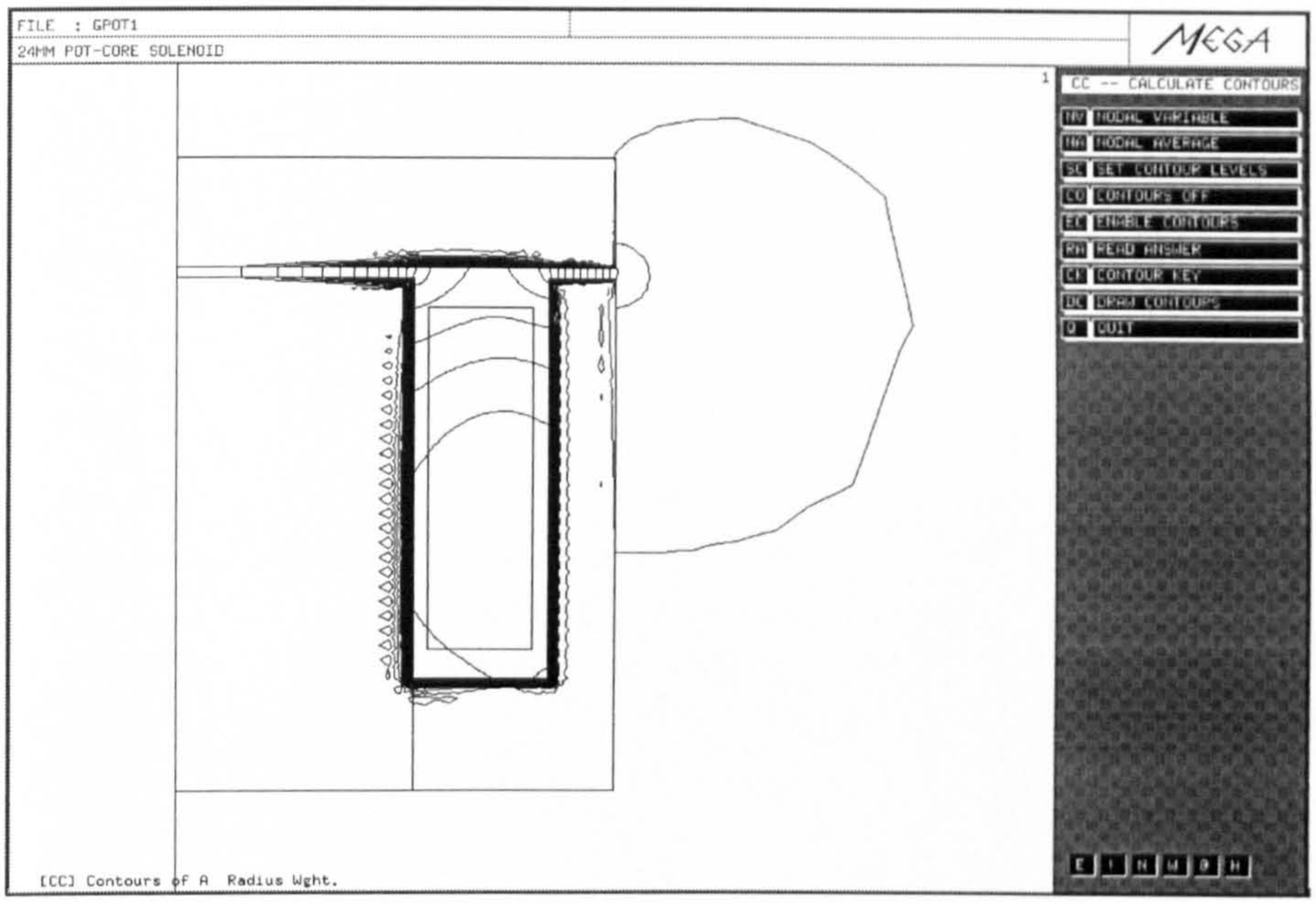

Figure 5.1: Transient flux distribution at $t = 0.5ms$ in an axisymmetric actuator. $0.3mm$ airgap, $90V$ step voltage.

to vary in time and space . Indeed the eddy current density in the central limb is higher than nearly anywhere else at any time.

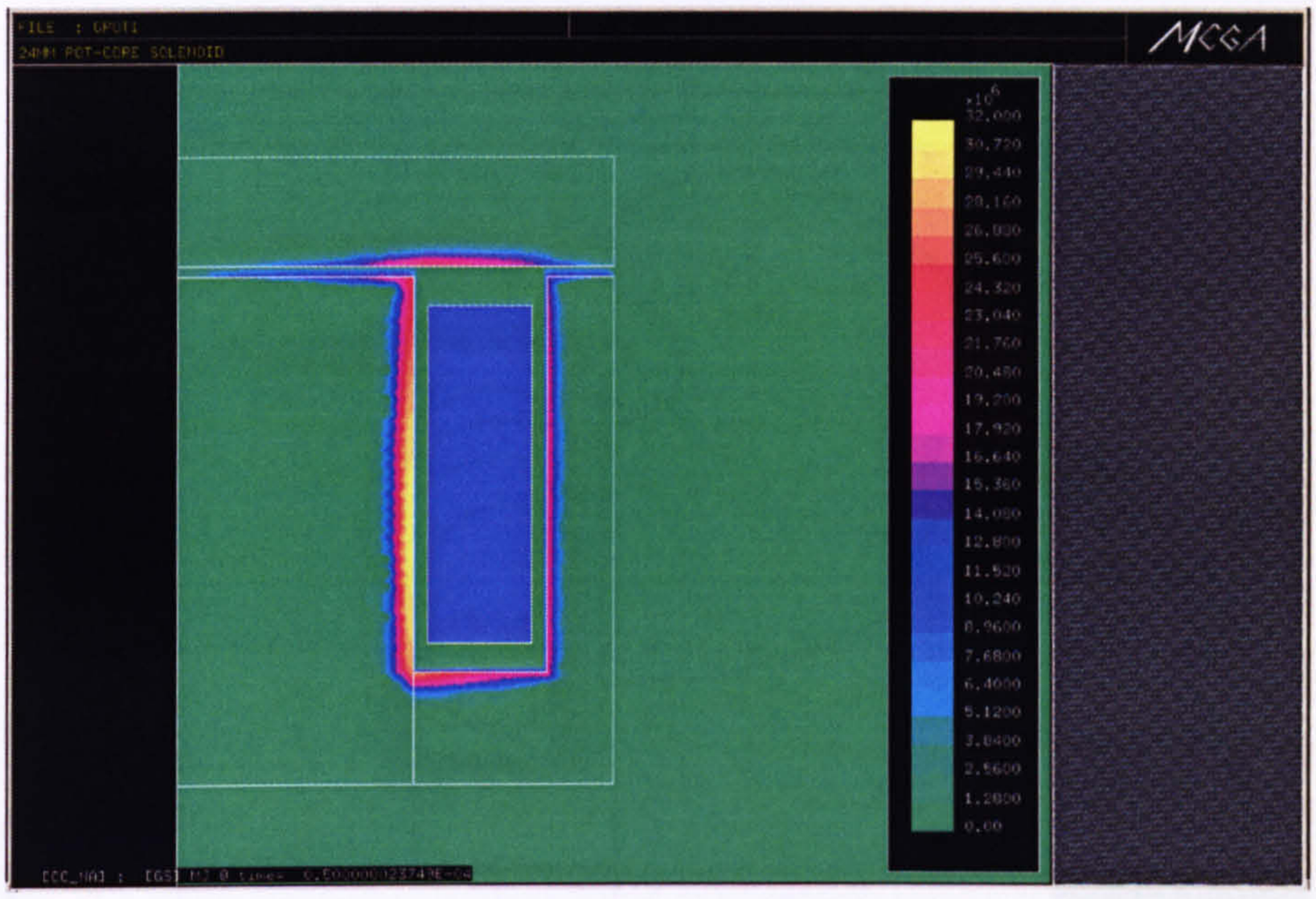

Figure 5.2: Transient eddy current distribution at $t = 0.5ms$ in an axisymmetric actuator. $0.3mm$ airgap, $90V$ step voltage.

From the previous observations, it seems then appropriate to divide the actuator into a series of closed flux tubes whose cross-sections are shown in fig. 5.7. Each closed tube has an axisymmetric configuration in which eddy currents can flow in a perpendicular direction to the page. Closed flux tube means, in this context, a flux tube that goes through the different sections of the solenoid i.e. central limb, main airgap, armature, main airgap again, outer limb, and yoke such that the cross-section area of a tube in a particular section is proportional to the total cross-section area of this actuator section. The comparative thickness of all closed tubes should reflect the way the eddy currents and the flux propagate within the iron.

Obviously this simplified flux tube distribution neglects the influence of fringing and leakage on the transient process. Also, due to this division into closed flux tubes, it is implicitly assumed that the same amount of time is required to reach steady-state in every section of the actuator, including the airgaps. This is clearly an approximation. However, given this assumption, the analysis of flux and eddy current diffusion can be limited to the case of the central limb section in the first stage .

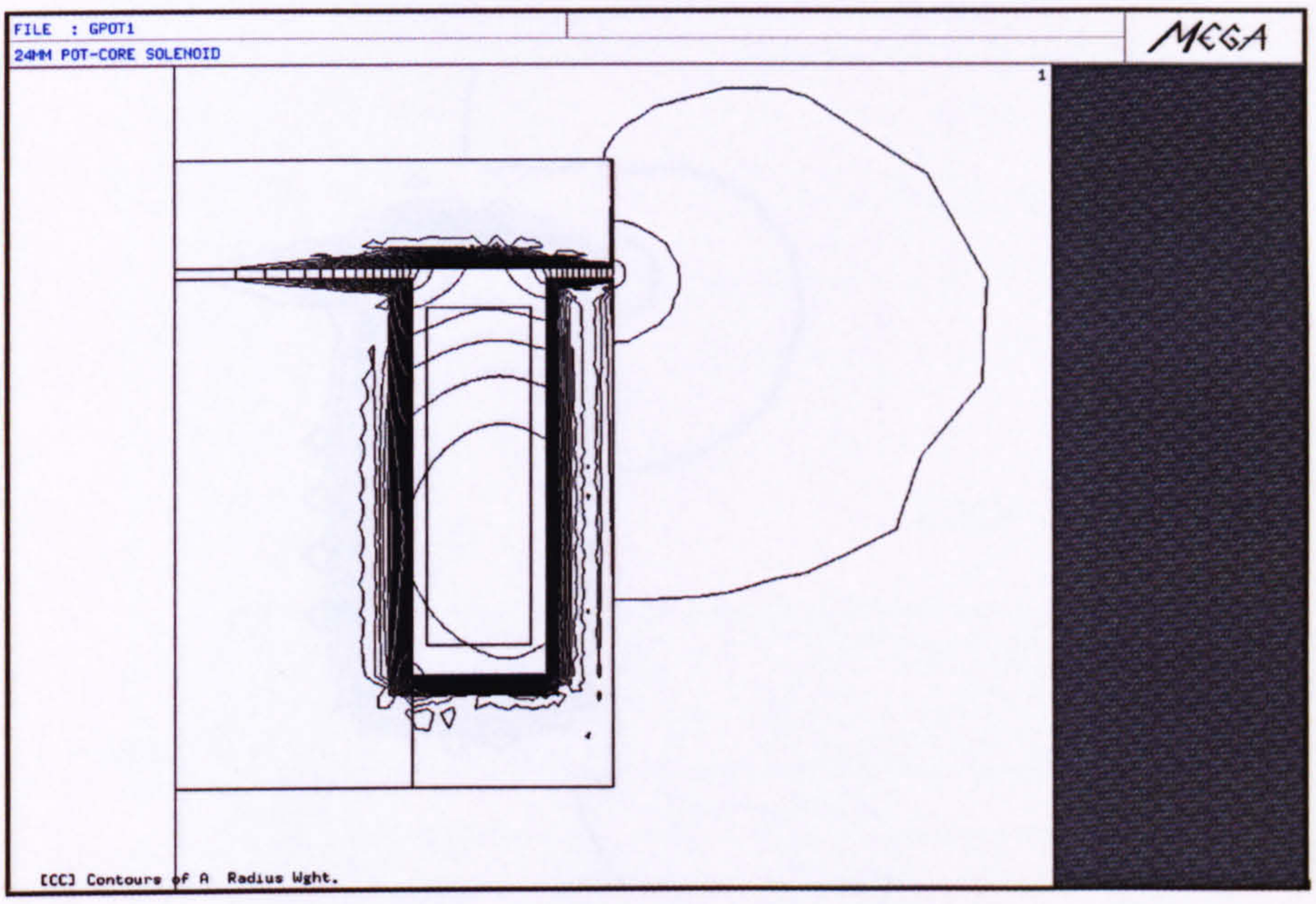

Figure 5.3: Transient flux distribution at $t = 1ms$ in an axisymmetric actuator. $0.3mm$ airgap, $90V$ step voltage.

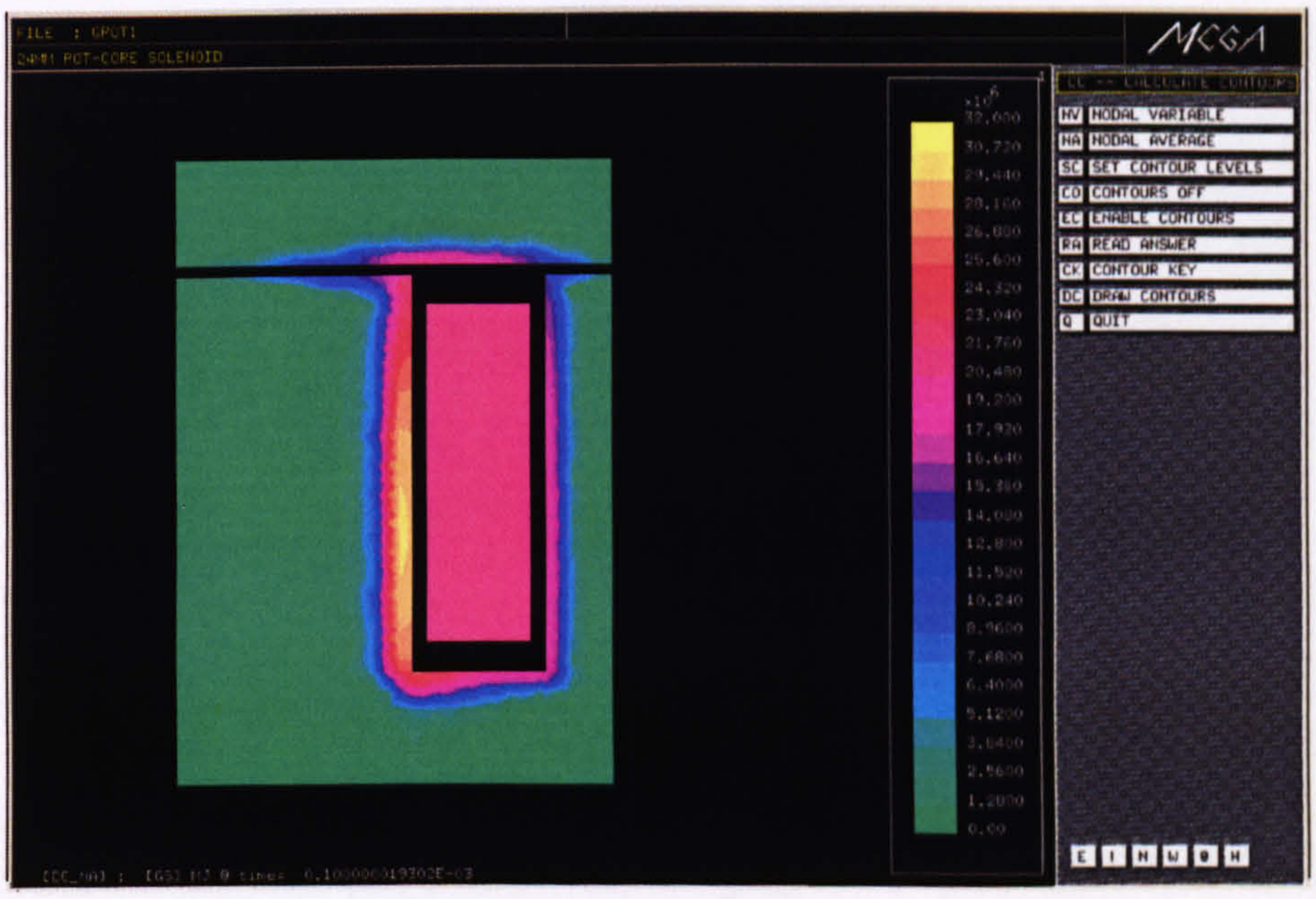

Figure 5.4: Transient eddy current distribution at $t = 1ms$ in an axisymmetric actuator. $0.3mm$ airgap, $90V$ step voltage.

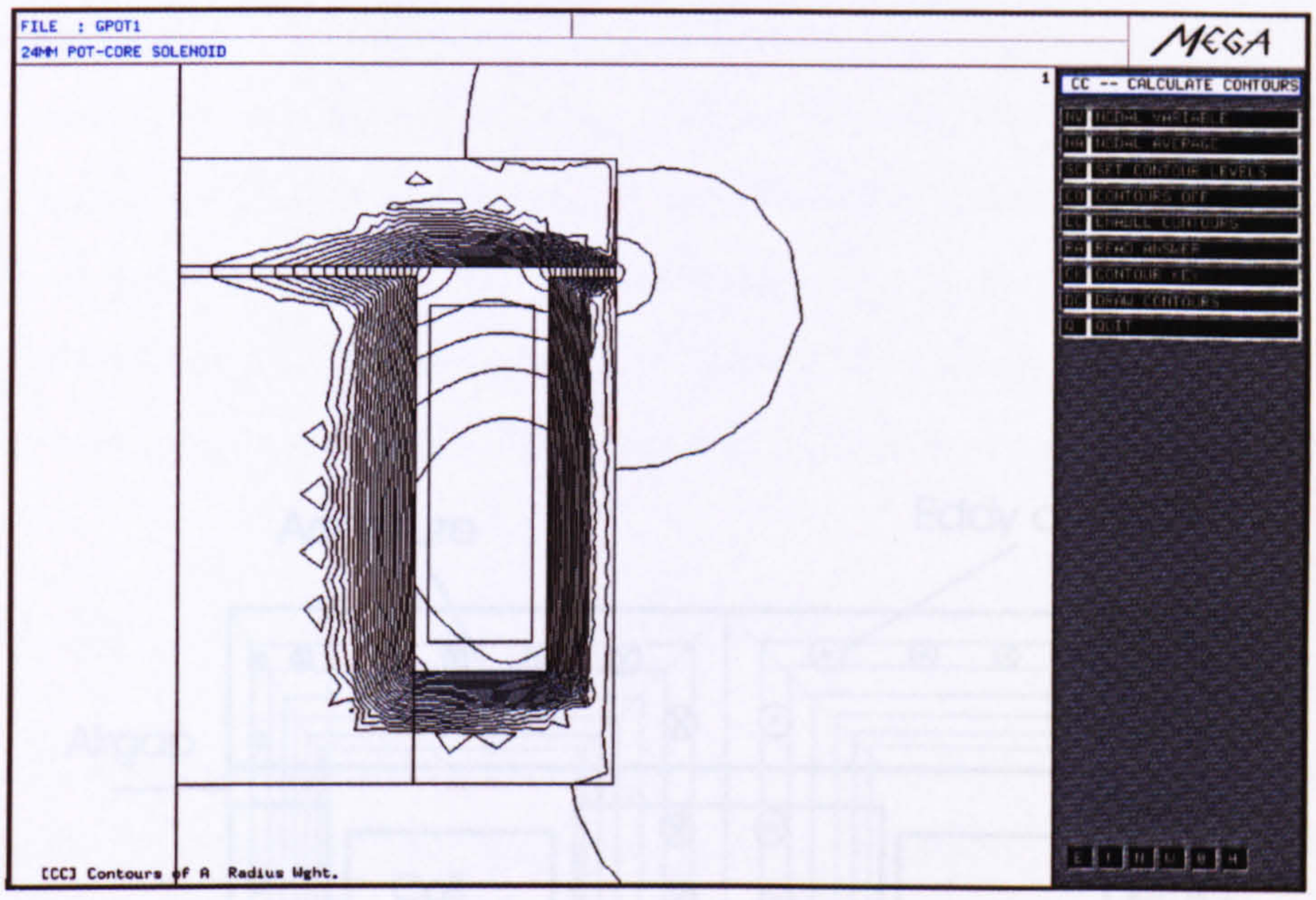

Figure 5.5: Transient flux distribution at $t = 3ms$ in an axisymmetric actuator. $0.3mm$ airgap, $90V$ step voltage.

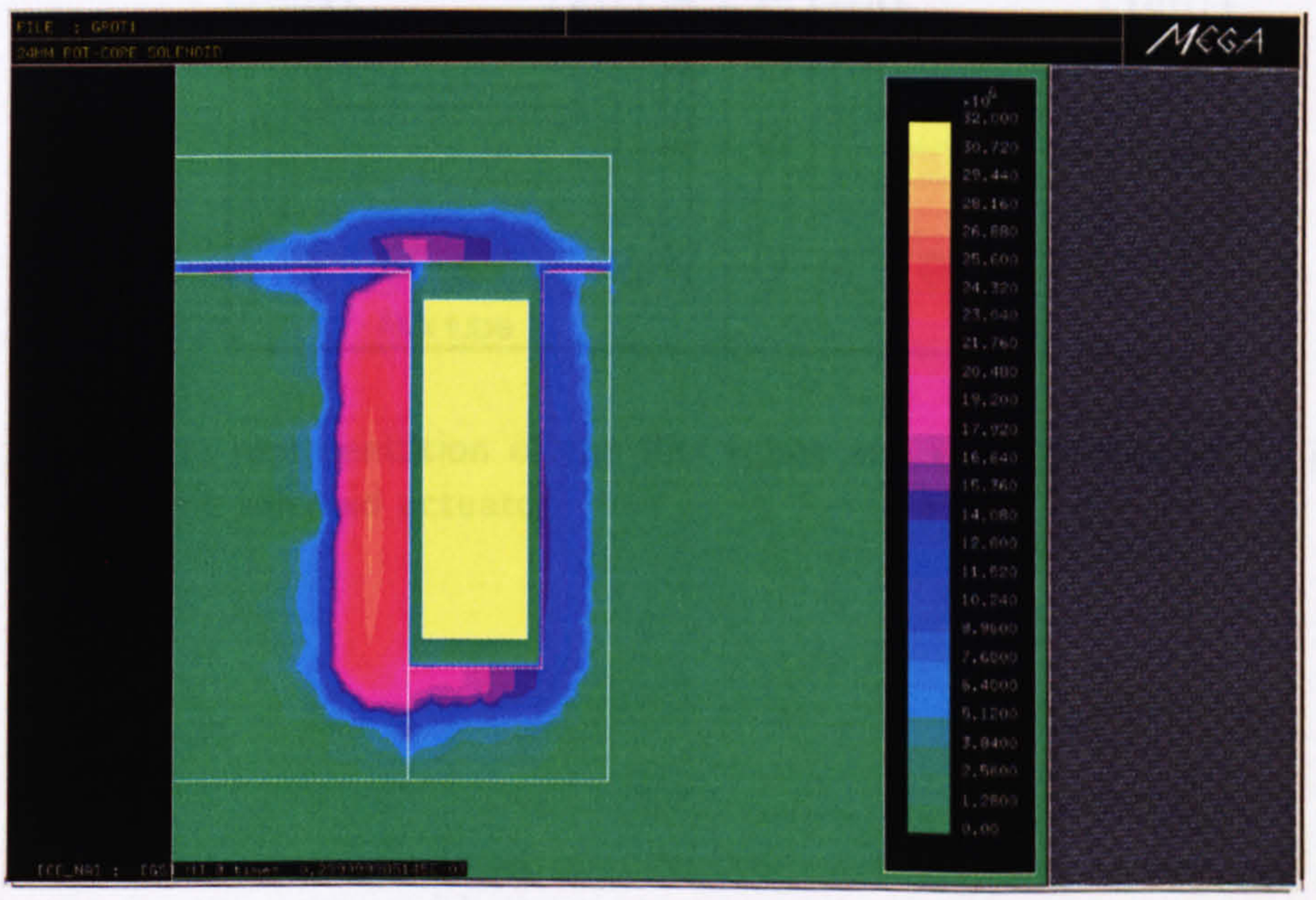

Figure 5.6: Transient eddy current distribution at $t = 3ms$ in an axisymmetric actuator. $0.3mm$ airgap, $90V$ step voltage.

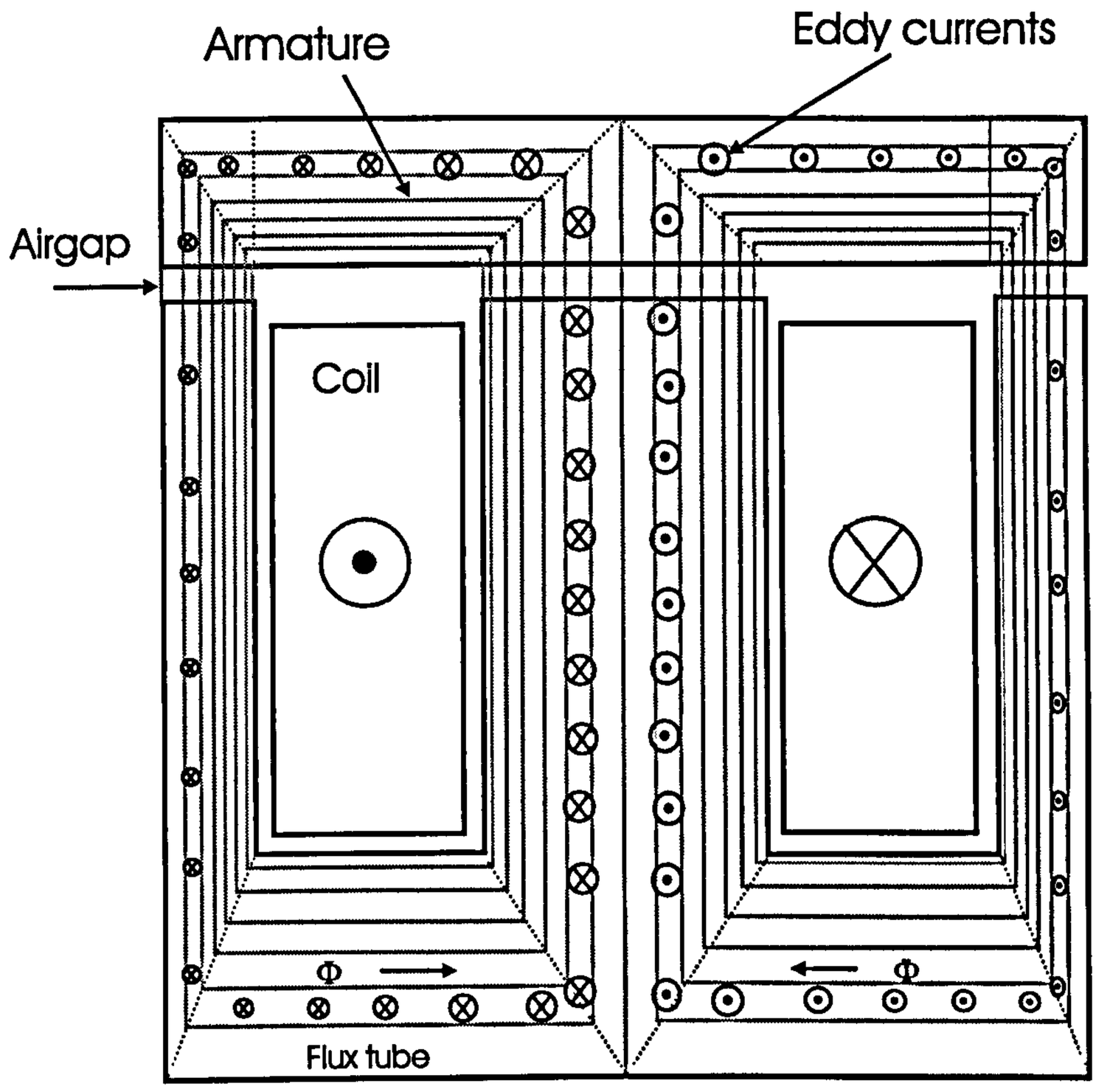

Figure 5.7: Schematic representation of the flux tubes and eddy current paths in an axisymmetric solenoid actuator

Diffusion Between Two Successive Layers

The following analysis is supported by fig. 5.8 showing a central limb cross-section. For clarity, only two successive flux tubes, defined between the radii $r0$, $r1$ and $r1$, $r2$ have been drawn on this cross-section. A uniform eddy current density distribution is assumed in each flux tube. An approximation of the diffusion law requires the evaluation of the magnetic linkage of each of these eddy current loops per unit of axial length. For example, at a radius r, the magnetic linkage is given by writing Faraday's law :

$$\oint \vec{E}(r,t)\,\vec{dl}(r) = -\frac{d\phi(r,t)}{dt}, \tag{5.5}$$

where $\vec{E}(r,t)$ is the electric field along the loop of elementary length dl and of radius r (e.g. $r1$); $\phi(r,t)$ is the magnetic flux embraced by this loop.

Similarly the voltage drop at a radius $r + dr$ is given by:

$$\oint \vec{E}(r+dr,t)\,\vec{dl}(r+dr) = -\frac{d\phi(r+dr,t)}{dt}, \tag{5.6}$$

The electric field $\vec{E}$ does not depend on θ-coordinate due to the axisymmetric configuration and therefore it is constant along the contour. Also its positive direction is given by the eddy current density direction (J_θ) such that

$$\oint \vec{E}(r,t)\,\vec{dl}(r) = -E_\theta(r,t)\,2\pi\,r. \tag{5.7}$$

By replacing $\vec{E}(r+dr,t)$ in eq.(5.6) with a first-order expansion, it follows that

$$-[E_\theta(r,t) + \frac{\partial E_\theta(r,t)}{\partial r}\,dr]\,2\pi\,(r+dr) = -\frac{d\phi(r+dr,t)}{dt}. \tag{5.8}$$

And subtracting eq.(5.5) from eq.(5.8), it follows:

$$[E_\theta(r,t)\,dr + \frac{\partial E_\theta(r,t)}{\partial r}\,r\,dr + \frac{\partial E_\theta(r,t)}{\partial r}\,dr^2]\,2\pi = \frac{d(\phi(r+dr,t) - \phi(r,t))}{dt}. \tag{5.9}$$

By dividing the actuator in many flux tubes such that their thickness (dr) is kept small, the second-order term in the left-hand side of eq.(5.9) can be neglected. The right-hand side of eq.(5.9) corresponds to the time variation of the flux $\Delta\phi$ embraced by the elementary flux tube defined between r and $r + dr$.

If $\vec{B}$ is assumed to be uniformly distributed within each flux tube, it follows that :

$$2\pi \frac{\partial(r\,E_\theta(r,t))}{\partial r}\,dr = 2\pi\, r\, dr \frac{dB_z}{dt}. \tag{5.10}$$

The relation between the electric field E_θ and the eddy current density J_θ is given by

$$E_\theta = \rho\, J_\theta, \tag{5.11}$$

where ρ is the iron resistivity.

By integrating eq. (5.10) between $r1$ and $r2$, as shown in fig. 5.8 and taking eq. (5.11) into account, it follows:

$$2\pi\,\rho\,(r_2\,J_{\theta\,2} - r_1\,J_{\theta\,1}) = \frac{d\phi_{12}}{dt}, \tag{5.12}$$

where

$$\frac{d\phi_{12}}{dt} = \pi\,(r_2^2 - r_1^2)\,\frac{dB_z}{dt}. \tag{5.13}$$

As the eddy current density has been assumed uniform on each flux tube, it results that the total eddy current flowing per unit of axial length between $r0$, $r1$ is given by:

$$I_{\theta 1} = \Delta r_{01}\, J_{\theta 1}, \tag{5.14}$$

where $\Delta r_{01} = (r_1 - r_0)$. The corresponding iron resistance per unit of axial length is approximated with:

$$R_1 = \frac{2\pi\,\rho\, r1}{\Delta r_{01}}. \tag{5.15}$$

Similarly between $r1$, $r2$, it follows that the total eddy current is equal to:

$$I_{\theta 2} = \Delta r_{12}\, J_{\theta 2}, \tag{5.16}$$

where $\Delta r_{12} = (r_2 - r_1)$ while the iron resistance is given per unit of axial length by:

$$R_2 = \frac{2\pi\,\rho\, r2}{\Delta r_{12}}. \tag{5.17}$$

By combining eq.(5.14), (5.15), (5.16), (5.17) with eq.(5.12), a first-order approximation of the flux and eddy current diffusion within the iron between two successive flux tubes is expressed by :

$$R_2\, I_{\theta\,2} = \frac{d\phi_{12}}{dt} + R_1\, I_{\theta\,1}. \tag{5.18}$$

This equation is easily translated into an electric equivalent circuit shown in solid lines in fig. 5.9. The actuator cross-section however includes more than two flux tubes and therefore this network should be repeated for each pair of successive flux tubes as shown on the same figure in dashed lines.

By taking into account the division of the actuator into a series of closed flux tubes, the computation of the network elements could be approximated as follows:

- The iron resistance of one layer within the electric equivalent network is evaluated by computing the eddy current paths associated with the corresponding closed flux tube. In each network layer, the total iron resistance is then equal to the sum of the iron resistance of each actuator section put in parallel. The central limb is characterised by the smallest iron resistance. Therefore it is expected that the simulated eddy current density within the central limb will be higher than in any other actuator section. This conclusion has been confirmed by finite-element analysis and can be observed in fig. 5.2, 5.4, 5.6.

- With the previous assumptions, the element $\frac{d\phi}{dt}$ of each layer would then correspond to the voltage drop within the corresponding closed tube due to flux variation in both iron and main gaps.

External Conditions

In the previous section a first-order approximation of the diffusion law of the eddy currents and flux within the iron has been established. New assumptions have then been added in order to associate the elements (resistance, nonlinear inductances) of the resulting network to the complete actuator configuration. However no information has

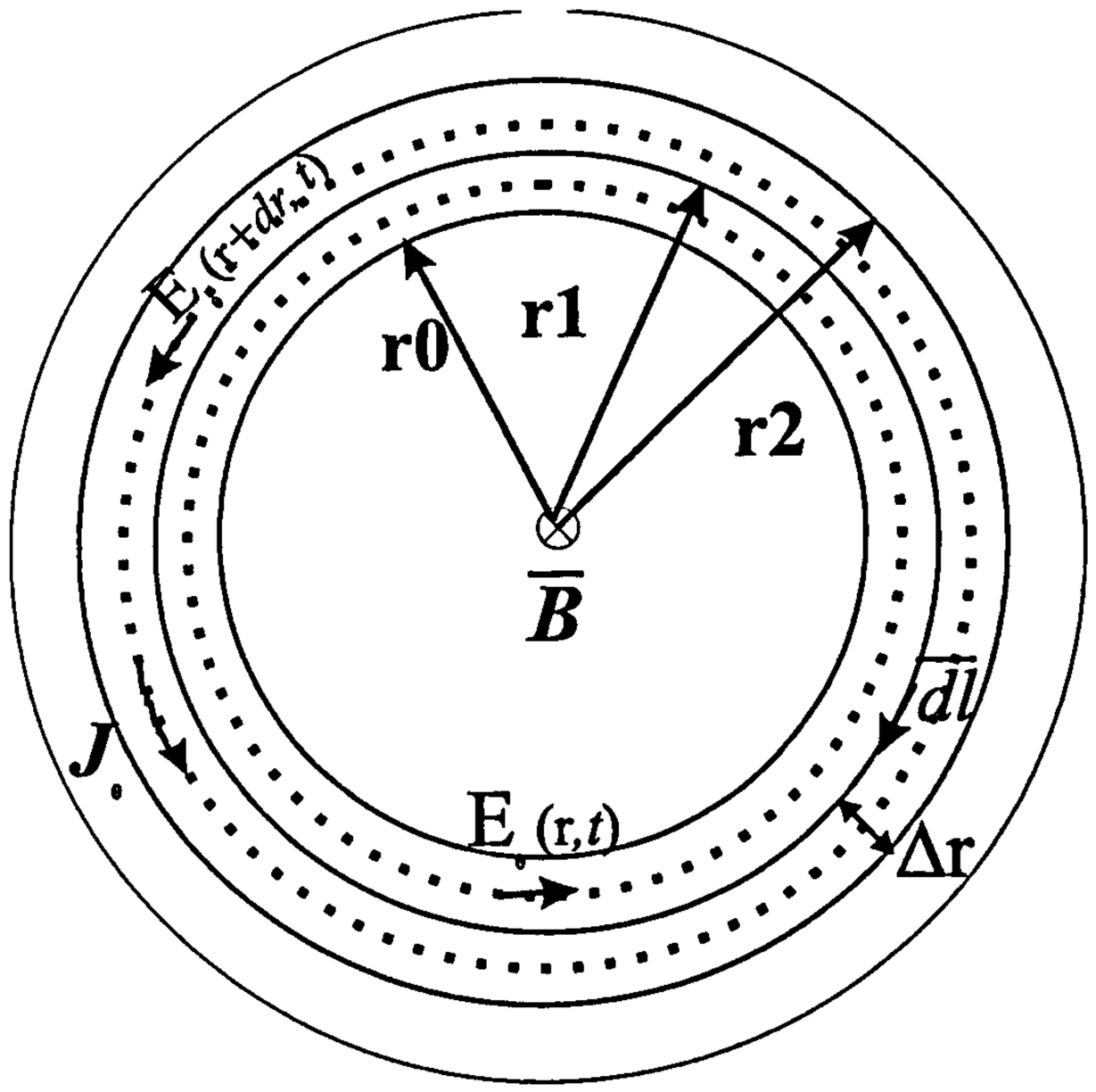

Figure 5.8: Schematic representation of the flux tubes and eddy current paths in an axisymmetric solenoid actuator

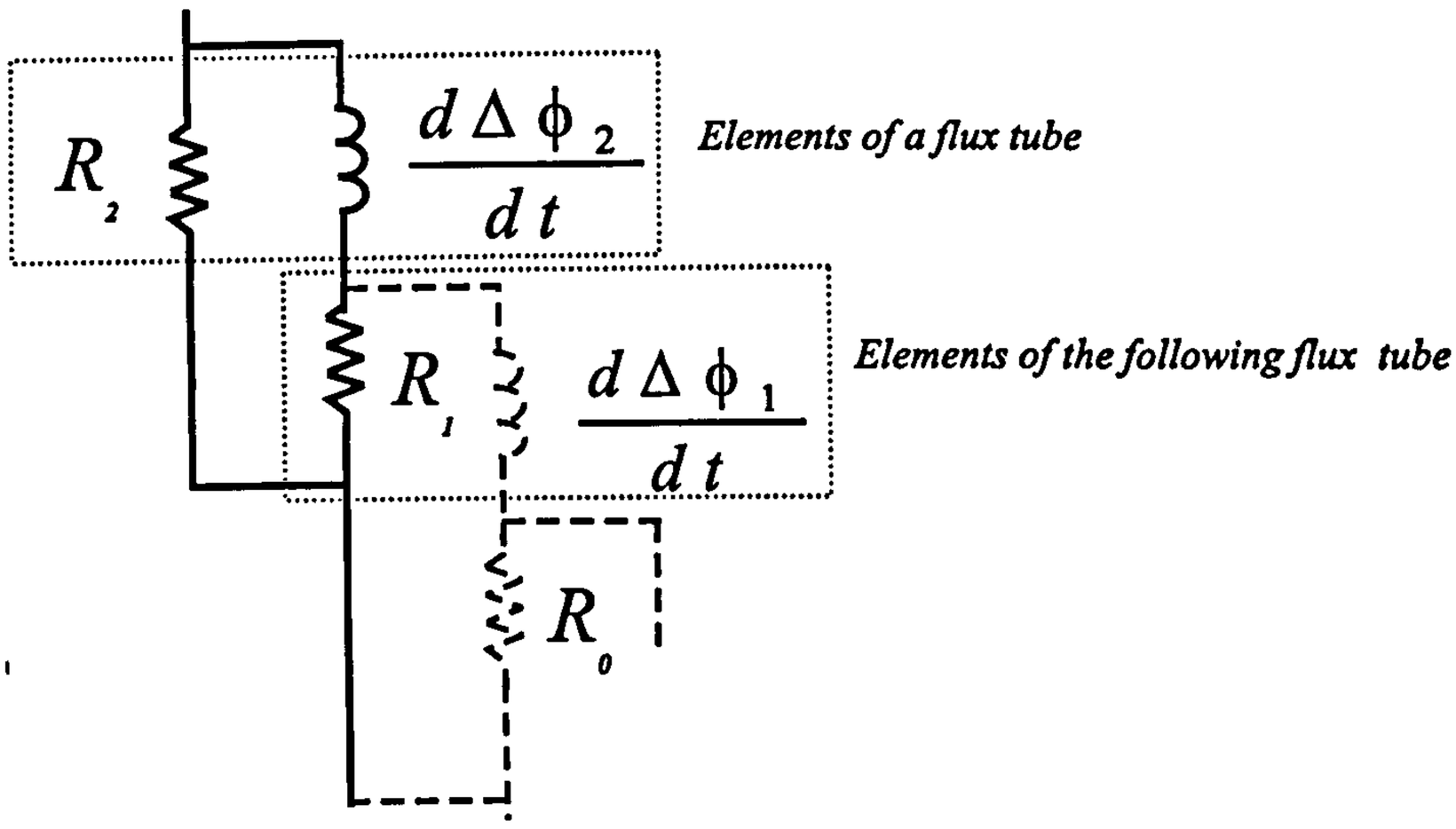

Figure 5.9: Electric equivalent network for first-order approximation of the flux and eddy current diffusion in solid iron.

yet been provided about the way this network should be connected to the energizing winding. This particular aspect of the problem is discussed in this section.

Previous authors [46, 53, 48, 52] have compared the transient phenomena due to eddy currents to the effect of a damping winding coupled to the energizing winding. Therefore the diffusion network should be related to the energizing winding by following the same laws as for a transformer whose primary is characterised by N turns (the energizing winding) and secondary by only one turn (the diffusion network) [55].

If there is nothing to demonstrate on this subject, it is however very important to understand why the generation of eddy currents occurs and to establish from it a simple law to approximately evaluate their quantity throughout the transient process. The following developments are supported by fig. 5.10. However, for simplicity, it is first assumed there is no airgap between the armature and the core. ($\delta_1 = 0$ and $\delta_2 = 0$).

The generation of eddy currents within the iron can be explained by the fundamental laws of Maxwell on field continuity at an interface between two different materials (e.g. air and iron). The laws related to a magnetic fields are :

1.

$$B_{n1} = B_{n2} \tag{5.19}$$

where B_{n1}, B_{n2} are the normal component of the flux density at the interface between two materials 1 and 2, within 1 and 2 respectively. There is then no discontinuity of the normal component of the flux density field at the interface between the air and the iron.

2.

$$\vec{a}_n \otimes [\vec{H}_1 - \vec{H}_2] = \vec{J}_s, \tag{5.20}$$

where $\vec{H}_1, \vec{H}_2$ are the magnetic field strength vectors in material 1 and 2; $\vec{a}_n$ is the positive unit vector, normal to this interface and $\otimes$ is the vector product. The discontinuity of the magnetic field strength at the interface between air and iron creates a surface current density J_s (A/m) in the iron whose intensity is given

by the difference of the tangential component of magnetic field strength on both sides of the interface.

From this law, it appears then that the generation of eddy currents is due to a discontinuity of the tangential component of the magnetic field in the iron surface and in the surrounding air. Therefore by applying Ampere's law on the two contours shown in fig 5.10 (lying on each side of the interface, very close to each other) and by evaluating their difference. It leads to :

$$\oint_{air} \vec{H}\,\vec{dl} - \oint_{iron} \vec{H}\,\vec{dl} = \sum \Delta_i\, J_{si}, \tag{5.21}$$

where Δ_i defines the contour length in the actuator iron section i; J_{si} is the magnitude of surface eddy current density per unit of contour length.

However, just after switching on, it is assumed that the magnetic field strength in the iron is very small compared to its value in the surrounding air such that:

$$\oint_{iron} \vec{H}\,\vec{dl} \approx 0, \tag{5.22}$$

While

$$\oint_{air} \vec{H}\,\vec{dl} = NI, \tag{5.23}$$

where N is the total number of turns of the energizing winding in which a current I is flowing.

And by combining eq. (5.21), (5.22) with eq. (5.23), the total amount of eddy current I_e just after switching on is equal to the total amount of Ampere-turns:

$$I_e = \sum \Delta_i\, J_{si} = NI \tag{5.24}$$

This would indeed be the current generated in a transformer short-circuited secondary winding with only one turn.

It can be shown that the previous relation is not only valid just after switching on but at any time during the transient period for which it is still possible to define in

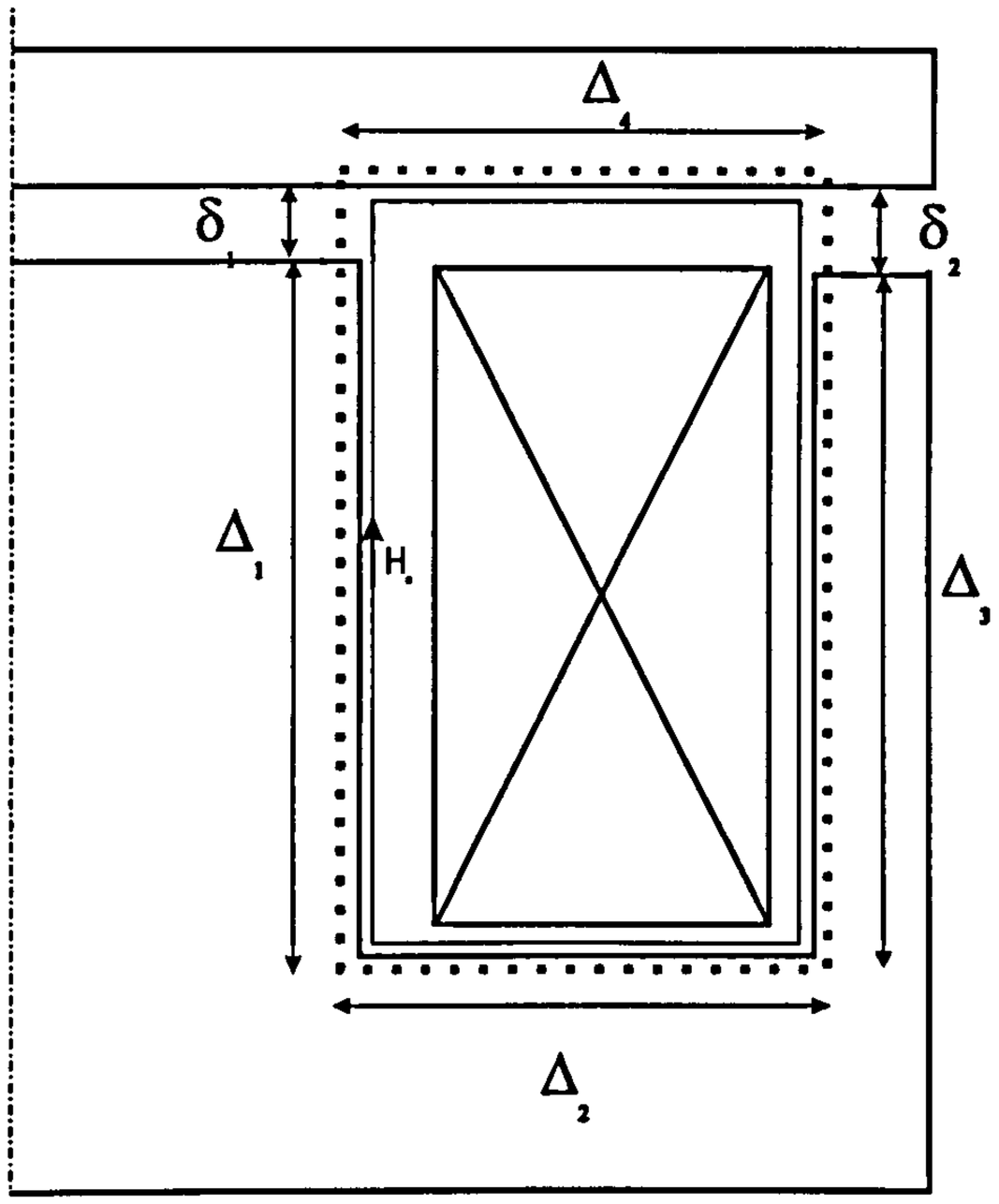

Figure 5.10: Contours chosen for computing the eddy currents at the air-iron interface just after switching on.

the iron a contour along which the magnetic field strength is still very small. In other words, the total eddy current is equal to the total amount of ampere-turns until the flux has not yet reached the centre of the iron core cross-section.

In the presence of airgaps, the total amount of ampere-turns available for magnetising the iron is reduced by the amount of ampere-turns required for the gaps. Therefore the total amount of eddy current in the actuator is approximatively equal to :

$$I_e = \sum \Delta_i \, J_{si} = NI - \int_{\delta_1+\delta_2} \vec{H} \, \vec{dl} \tag{5.25}$$

where δ_1 and δ_2 are the airgap lengths on the central and outer limbs respectively. Again this expression is only valid during the transient process when it is still possible to define a contour in the iron on which the magnetising flux is very small.

Simple Electromagnetic Equivalent Network for Axisymmetric Solid Iron Actuator.

By following the same rules as for a transformer, the complete electromagnetic equivalent circuit of the flat-faced solenoid actuator is given in fig. 5.11. The equivalent circuit has been related to the 'primary' such that the iron resistances are in this network multiplied by the squared value of the number of turns N and the flux is now replaced by the flux linkage $\psi = N\,\phi$.

However it can already be observed that this network is not compatible with equation (5.25). Indeed the total amount of eddy current computed from this network will be equal to the total amount of ampere-turns although the flux paths include the two main airgaps[2]. The amount of eddy currents predicted by this network is then somewhat higher than the real amount.

Computational Advantages of the Electromagnetic Network.

The simplicity of this network has many computational advantages:

- First of all its computation does not require any iterative procedure nor any matrix handling. Its computation is straightforward due to the fact that the actuator is entirely made of solid iron[3].
- The total number of equations for solving this network is rather small ($Nc + 1$), a function only of the number of layers into which the actuator has been divided. These equations are:

1. The general electric equation of the energizing winding:

$$V = R_1\, I_1 + L_1 \frac{dI_1}{dt} + N^2\, R_{21}(I_1 - I_{21}), \tag{5.26}$$

where R_1 is the winding resistance, I_1 is the energizing winding, L_1 the winding leakage inductance and R_{2i} and I_{Li} the resistance and current of

[2]This problem is discussed in a following section.

[3]The rectangular actuator, made of solid iron and also laminations, requires a more complex algorithm as it will be demonstrated in the next chapter.

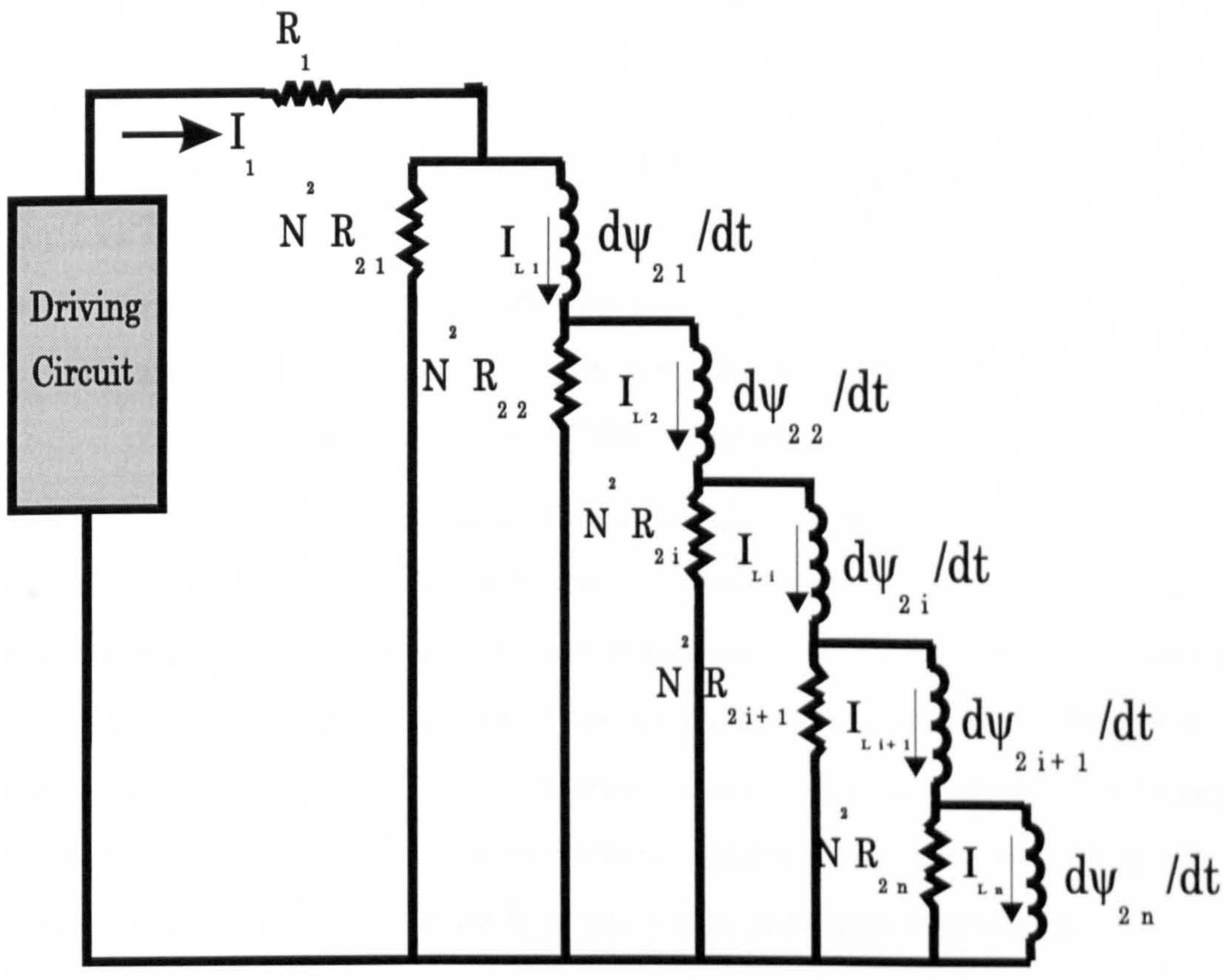

Figure 5.11: Electromagnetic equivalent circuit for an axisymmetric solenoid actuator

layer i in the diffusion network (see fig. 5.11).

2. And the Nc equations of the diffusion network :

$$\frac{d\psi_{21}}{dt} = N^2 R_{21} (I_1 - I_{L1}) - N^2 R_{22} (I_{L1} - I_{L2}), \tag{5.27}$$

for the first layer.

$$\frac{d\psi_{2i}}{dt} = N^2 R_{2i} (I_{Li-1} - I_{Li}) - N^2 R_{2i+1} (I_{Li} - I_{Li+1}), \tag{5.28}$$

for $i = 2...Nc$ where $\frac{d\psi_{2i}}{dt}$ is the flux linkage in layer i.

- Each layer of this network corresponds to a *closed* flux tube. Therefore the computation of the current I_{Li} required for magnetising each flux tube in this network can be directly computed from the magnetostatic characteristics of the actuator. Indeed, at a given magnetising current, the flux quantities produced in a closed tube and in the total actuator are related by the ratio of their respective cross-section area (in any section of the actuator).

  In order to increase the computational speed , a complete set of magnetisation curves is not directly computed (and interpolated). Instead only two of them corresponding to the minimum and maximum gap length are computed from the magnetostatic MEC as well as the gauge curve presented in chapter 3. The magnetising current at any intermediate position and for a given flux linkage in a closed flux tube is then retrieved from equation 3.1 by first scaling the flux linkage value in order to relate it to the entire actuator dimensions.

  A direct consequence of this procedure is that the static effects of fringing and slot leakage are spread over each flux tube such that the steady-state performance of the static (fig. 2.16) and the dynamic (fig. 5.11) networks will be exactly the same.

Transient Magnetic Force Computation.

In theory the transient magnetic force could be computed using the gauge curve approach. This approach has not however been tested. Instead the transient force is

approximately evaluated with:

$$F_{mag} = \frac{\phi_{g1}^2}{2\,\mu_0\,S_1} + \frac{\phi_{g2}^2}{2\,\mu_0\,S_2}, \tag{5.29}$$

where ϕ_{g1}^2 and ϕ_{g2}^2 are the total flux flowing in the central and outer limb main airgaps respectively. S_1 and S_2 are the cross-section areas of the central and outer limb main airgaps respectively.

An extra computation is then required in order to evaluate the flux in both main airgaps as this knowledge is not available from the magnetisation curves.

A first possibility would be to pre-compute and interpolate two sets of curves giving each the total flux in one airgap as a function of armature position and magnetising current (or flux linkage). This option would however significantly slow down the speed of the overall algorithm while the amount of data to be pre-computed would be also greatly increased. For these reasons, this approach has not been considered.

A more subtle technique consists of computing the main airgap flux to total flux ratio τ versus flux linkage. An example of computation of this ratio is given in fig. 5.12. At constant gap, this ratio is constant under low saturation level and can be derived analytically by only considering the linear elements of the MEC. For the central limb, this ratio is given by:

$$\tau_1 = \frac{P_{g1}\,(1 - \frac{P_L}{P_{tot}})}{P_{g1} + P_{fi1}}, \tag{5.30}$$

where P_{tot} is the total airgap permeance:

$$P_{tot} = \frac{(P_{g1} + P_{fi1})(P_{g2} + P_{fi2} + P_{fe})}{P_{g1} + P_{fi1} + P_{g2} + P_{fi2} + P_{fe}} + P_L, \tag{5.31}$$

and

P_{g1} is the main airgap permeance of the central limb,

P_{fi1} is the inner fringing permeance of the cental limb,

P_L is is the total effective slot leakage permeance,

P_{g2} is the main airgap permeance of the outer limb ,

P_{fi2} is the inner fringing permeance of the outer limb,

P_{fe} is the outer fringing permeance of the outer limb.

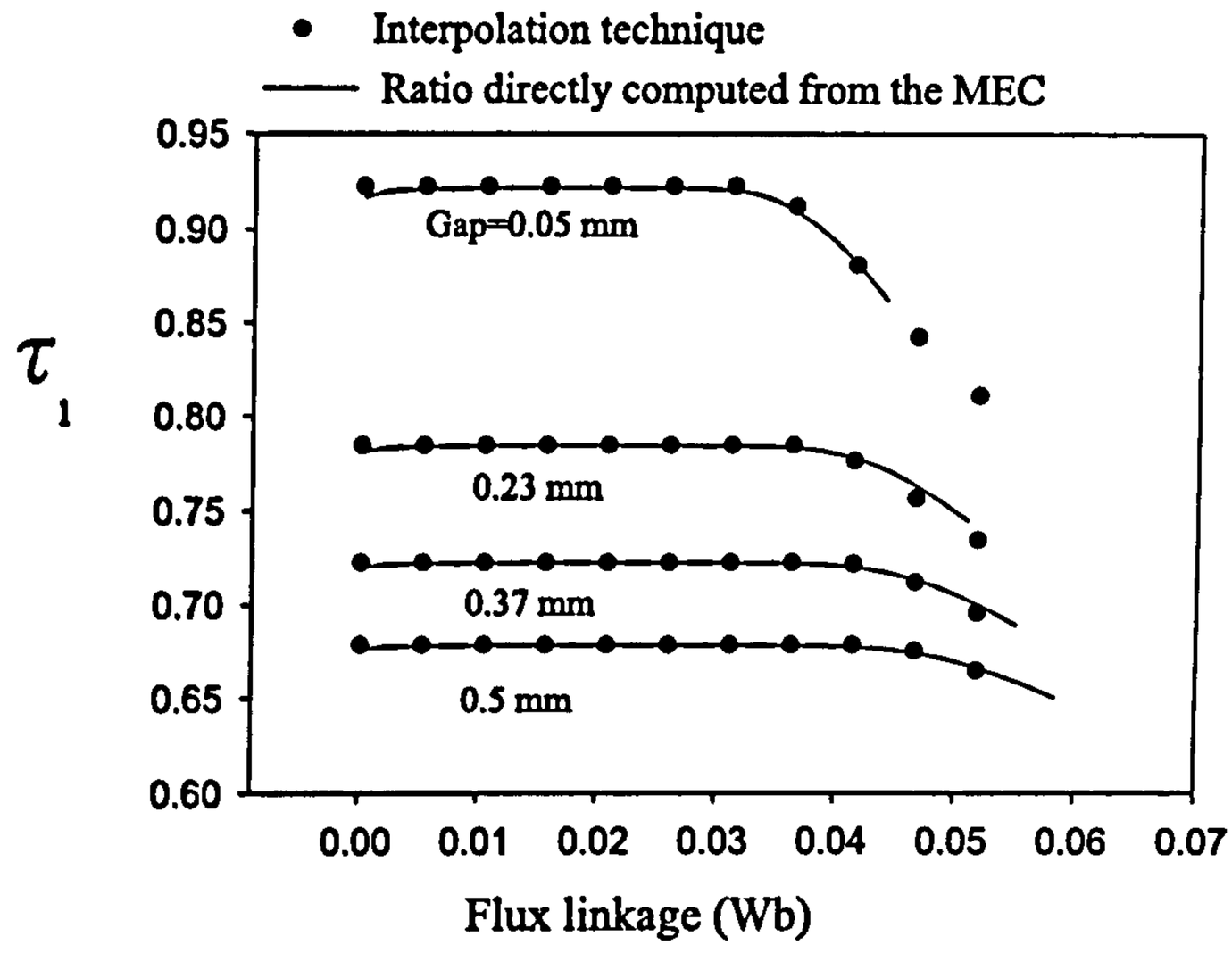

Figure 5.12: Gap flux to total flux ratio versus flux linkage

Similarly for the outer limb, the ratio is computed with:

$$\tau_2 = \frac{P_{g2}\,(1 - \frac{P_L}{P_{tot}})}{P_{g2} + P_{fi2} + P_{fe}}. \tag{5.32}$$

When saturation increases, the leakage flux increases, progressively reducing the the proportion of flux going through the main gaps. This information is stored for a series of gap lengths using the following technique.

At constant gap length, the ratio τ and its slope $\frac{d\tau}{d\psi}$ are evaluated at three different values of flux linkages ψ_a, ψ_b, ψ_c, each being a function of the armature position and of the main airgap flux in the central limb (the input flux parameter in the MEC) :

- ψ_c is the flux linkage computed for the maximum value of the main airgap flux in the central limb considered in the analysis [4] ($\phi_{g1\,max}$).

- ψ_a is, at minimum gap length, the maximum flux linkage for which τ_1 is still given with good accuracy by eq. (5.30). The corresponding value of the main

[4]This is usually the maximum value of airgap flux considered in the magnetisation curve computation for minimum and maximum gap lengths.

airgap flux $\phi_{g1\,min}$ is used for computing ψ_a at any other gap length.

- ψ_b is the flux linkage computed at a constant central limb airgap flux set arbitrarily equal to $(\phi_{g1\,min} + \phi_{g1\,max})/2$.

At a given gap and a given flux linkage ψ_{tube} in a closed flux tube, it follows that the ratio $\tau 1$ is obtained :

1. by computing the flux linkage ψ in the entire actuator which would correspond to the flux linkage ψ_{tube} in the closed flux tube (using a scaling factor),

2. by checking at the given gap whether $\psi < \psi_a$. If yes , the ratio τ_1 is given by equation (5.30).

3. if not, by computing τ_1 from a third-order polynomial interpolation performed between ψ_a, ψ_b or ψ_b, ψ_c depending on whether $\psi <= \psi_b$ or not respectively. For example between ψ_b, ψ_c, the ratio τ_1 is equal to:

$$\tau = a\,\psi^3 + b\,\psi^2 + c\,\psi + d, \tag{5.33}$$

where a, b, c, d are defined as a function of $\tau_1(\psi_b)$, $(\frac{d\tau_1}{d\psi})_{\psi_b}$, $\tau_1(\psi_c)$, $(\frac{d\tau_1}{d\psi})_{\psi_c}$ computed at the given gap length.

An example of the results obtained with such a technique is given in fig. 5.12 compared to the direct computation of the ratio τ from the MEC presented in fig. 2.16. The ratio τ_2 for the outer limb can be computed by following the same algorithm.

Then by taking into account the last development, the magnetic force equation (eq. 5.29) can be expressed as :

$$F_{mag} = \frac{(\sum_1^{Nc} \tau_{1i}\,\frac{\psi_i}{N})^2}{2\,\mu_0\,S_1} + \frac{(\sum_1^{Nc} \tau_{2i}\,\frac{\psi_i}{N})^2}{2\,\mu_0\,S_2}, \tag{5.34}$$

where ψ_i is the flux linkage of the closed flux tube i.

5.3 Transient Analysis

The previous method has been implemented and compared with time-stepping finite elements and measurements. In this context, 'transient analysis' means that the gap was kept constant. Similarly 'dynamic analysis' refers in this thesis to a problem including armature movement. The actuator dimensions considered in the following simulations are summarised in table 5.1, in which column $D1$ gives the actuator characteristics for the comparison with transient finite-element analysis and column $D2$ with the transient measurements and dynamic FEA. A step voltage was applied to the actuator for this comparison.

Variables	D1	D2
A, B	24	24
C	6.49	6.5
E	14	14
D	1.78	1.85
F	3	3.1
T	3	3
$abcoil$	0.2	0.8
$uncoil$	0.2	0.8
$turn$	130	152
$steel$	2.5% SiFe	2.5% SiFe
$R1$	0.92Ω	3.8Ω

Table 5.1: Axisymmetric actuator dimensions for transient FE (D1), measurement (D2) and dynamic FE (D2) comparison.

5.3.1 Layer Distribution and Iron Resistance Computation

The minimum number of layers required in the simulation can be approximately evaluated by comparing the performance of the network for different values of Nc. Fig. 5.13 and 5.14 show the results of the transient current and force due to a step voltage of $10V$, obtained with a quadratic distribution of the layers and for $Nc = 3, 7, 15, 30$. From this test, it can be observed that for a very low number of layers, the effect of

layer division is clearly visible, inducing an undulation pattern in the current waveform, due probably to the great variation of iron resistance and inductance between successive layers. Also a low number of layers implies a lower iron resistance for the first layer and therefore a higher jump in the current waveform. Above $Nc > 7$, the electromagnetic equivalent network starts performing reasonably well. In practice the number of layers Nc was set to 15.

The second test involved using a quadratic and a uniform distribution of the layers with Nc set to 15. The 'quadratic' distribution is such that the thinner layer is situated next to the coil.

In both cases, each layer is characterised by four variables corresponding to the radial coordinate of the layer extremities in both central and outer limb. Based on the knowledge of these coordinates called xc_1, xc_2 with $xc_1 > xc_2$ for the central limb, xe_1, xe_2 with $xe_2 > xe_1$ for the outer limb and the actuator dimensions, the iron resistance of each layer can be computed in the different actuator sections. The formulae developed for the iron resistance per layer and per section are summarised in table 5.2 and the different sections are shown in fig. 5.16.

A comparison of the transient current obtained with the two types of layer distribution is given in fig. 5.15. The transient force waveform was in this case exactly identical for both distributions. As the uniform layer distribution leads to smaller values of resistance in the first layers, a higher jump of the current can be observed in this case just after switching on. However the initial eddy current density given by eq. (5.20) is equivalent to a surface current density sheet such that it seems more appropriate to use a very thin layer thickness for the first layer. The quadratic layer distribution was therefore preferred to the uniform one.

In a more general context, the number and the distribution of layers is, to some extend, comparable to designing a proper mesh in a finite element analysis. Therefore the number of layers is in general:

1. an increasing function of the thickness of each actuator section,

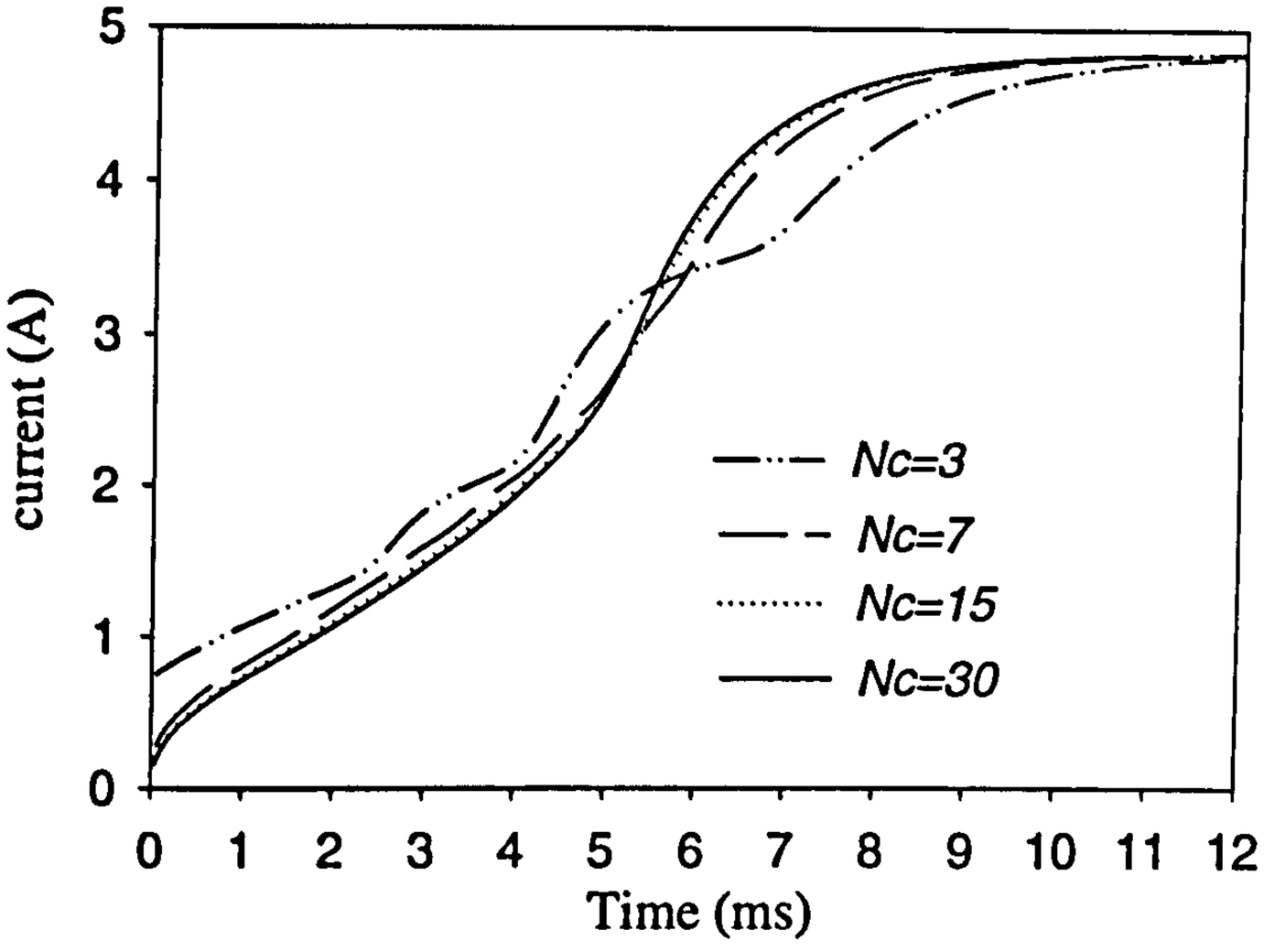

Figure 5.13: Transient current versus number of layers Nc. Step voltage of $10V$, $R1 = 2\Omega$, $G = 0.1mm$

2. a function of the chosen layer distribution, depending on the driving conditions (e.g. *ac* or *dc* conditions).

5.3.2 Comparison with Measurements and Finite-Elements

A comparison of transient current, force and induced voltage waveforms[5] has been carried out at different fixed gap lengths. The results obtained with the test rig presented in chapter 4 are reported in this section and correspond to a set of transient currents and induced voltages measured at two different gaps. The transient force measurements, requiring a different test-rig, are summarised in Chapter 7 as well as the test-rig used for that purpose.

The results of the comparison between measurements and simulations are given in fig. 5.17, 5.18. for a gap length of 0.0508 and 0.1016 respectively. The measurements were obtained at very low frequency to ensure the decay of the eddy current between two impacts and also with relatively low step voltages. A major problem was therefore

[5]This induced voltage was obtained from the search coil

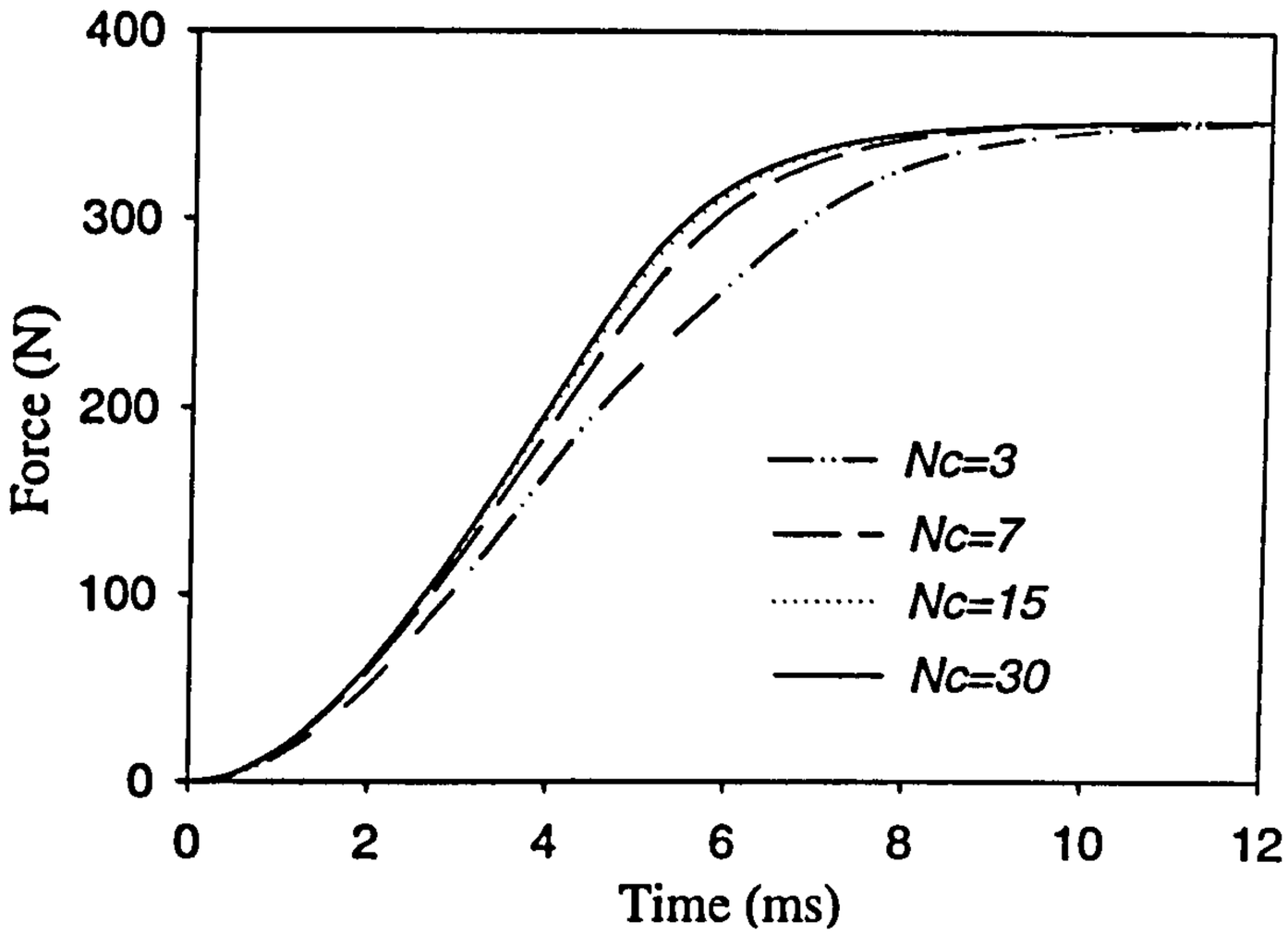

Figure 5.14: Transient force versus number of layers Nc. Step voltage of $10V$, $R1 = 2\Omega$, $G = 0.1mm$

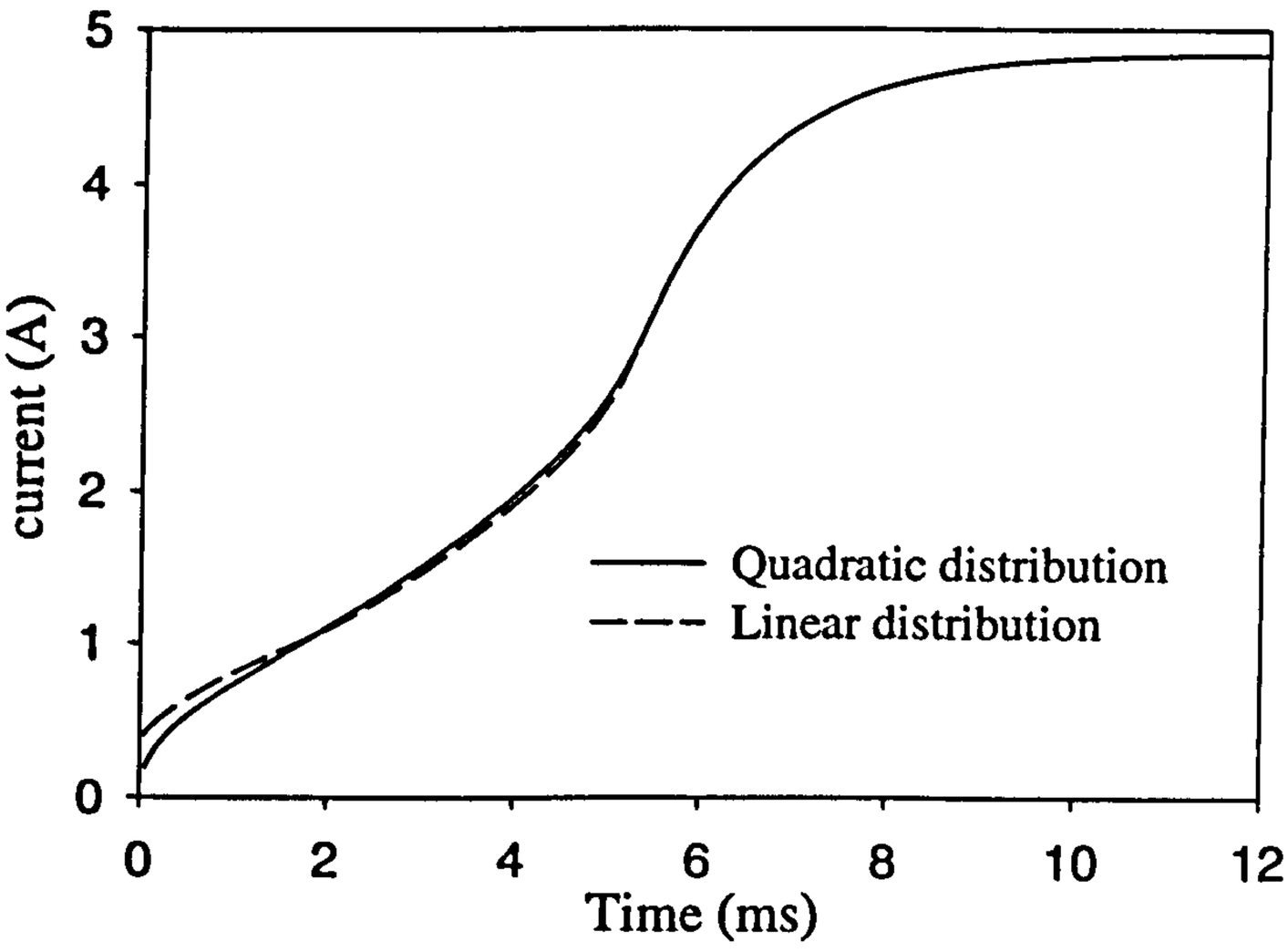

Figure 5.15: Transient current versus layer distributions. Step voltage of $10V$, $R1 = 2\Omega$, $G = 0.1mm$

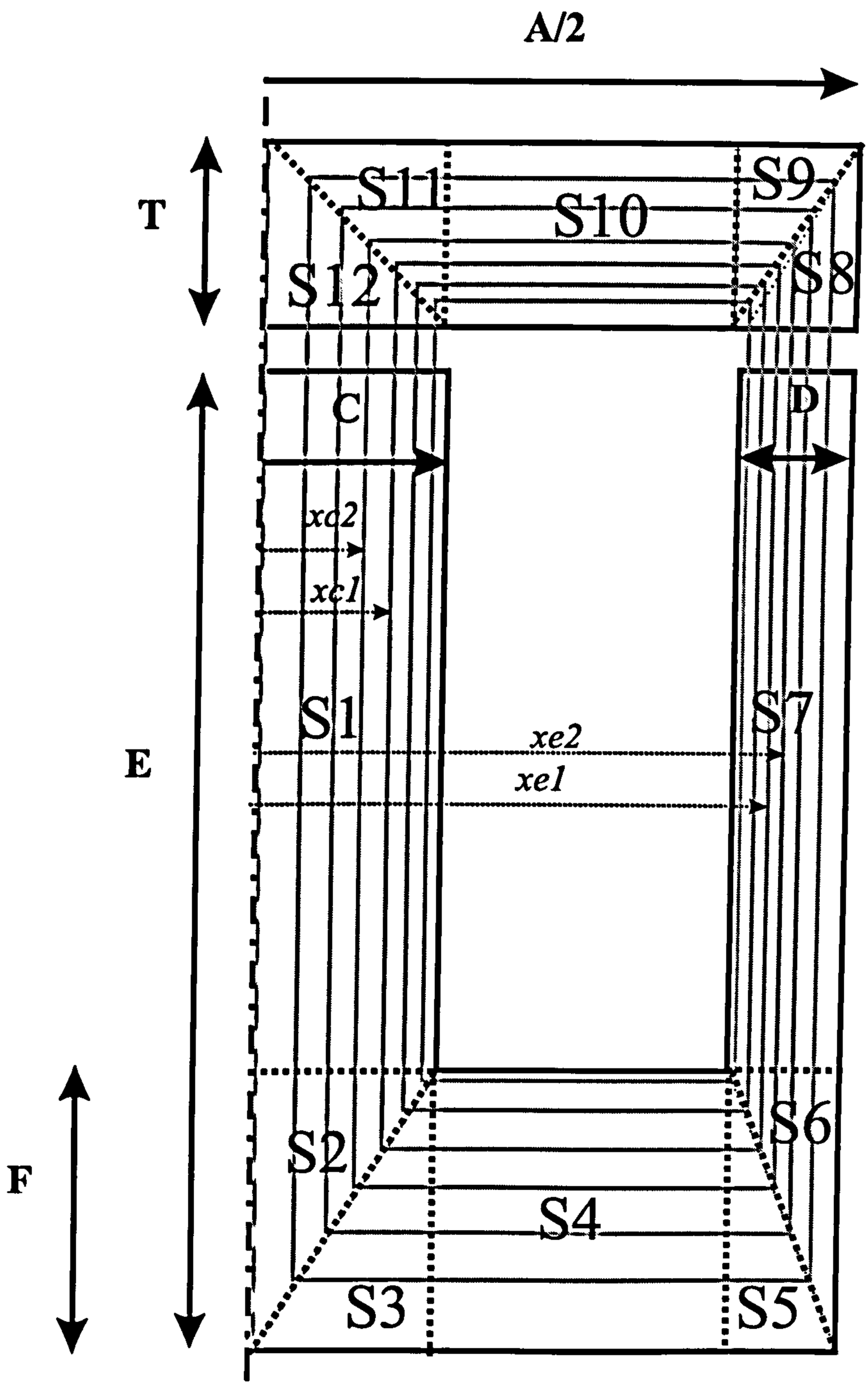

Figure 5.16: Sections defined for computing the iron resistance summarised in table 5.2.

the computation of the winding resistance changing significantly if the test was repeated several times. The resistance value in the simulation was kept constant at a value read just after each test using an HP high precision multimetre. However this approach does not take into account of the resistance variation during the test itself. Also the amount of eddy current is an increasing function of the step voltage magnitude which was kept rather low, under 12V for any measurements. It is therefore difficult to judge from these results how well or how badly the simulation performs.

For this reason, the series of tests have been completed with a finite element analysis for which a 90 V step voltage was chosen. This comparison is shown in fig. 5.19 including also the results corresponding to the ideal case (without eddy currents) [6]. From fig. 5.19, it can be observed that the effects of eddy currents are significant on both current and force waveforms and also that the simulation results are in excellent agreement with finite-elements.

From this last simulation, the following variables have been also plotted :

1. The transient eddy current density for each layer up to 1.3ms in fig 5.20 and 5.21 for Nc=15 and Nc=30 respectively. The eddy current density per layer J_{ei} is equal to:

$$J_{ei} = \sqrt{\frac{R_{2i}\, I_{ei}^2}{\rho\, Vol_i}}, \tag{5.35}$$

where I_{ei} is the current flowing through the iron resistance R_{2i}; Vol_i is the volume of the closed flux tube i which can be computed from the volume of the flux tubes given for each section in table 5.2.

2. The total eddy current I_e related to the primary (I_{ep}) which is given in fig. 5.22 and is equal to:

$$I_{ep} = \frac{I_e}{N} = (I_1 - I_{L1}) + \sum_{2}^{Nc}(I_{Li-1} - I_{Li}) = I_1 - I_{LNc}. \tag{5.36}$$

[6]The winding resistance was set to 0.92 Ohms leading to a steady-state current of about 97 A, which is too high for the device under consideration (see table 5.1). For this reason the comparison shown in fig. 5.19 has been restricted to a maximum current of 40A.

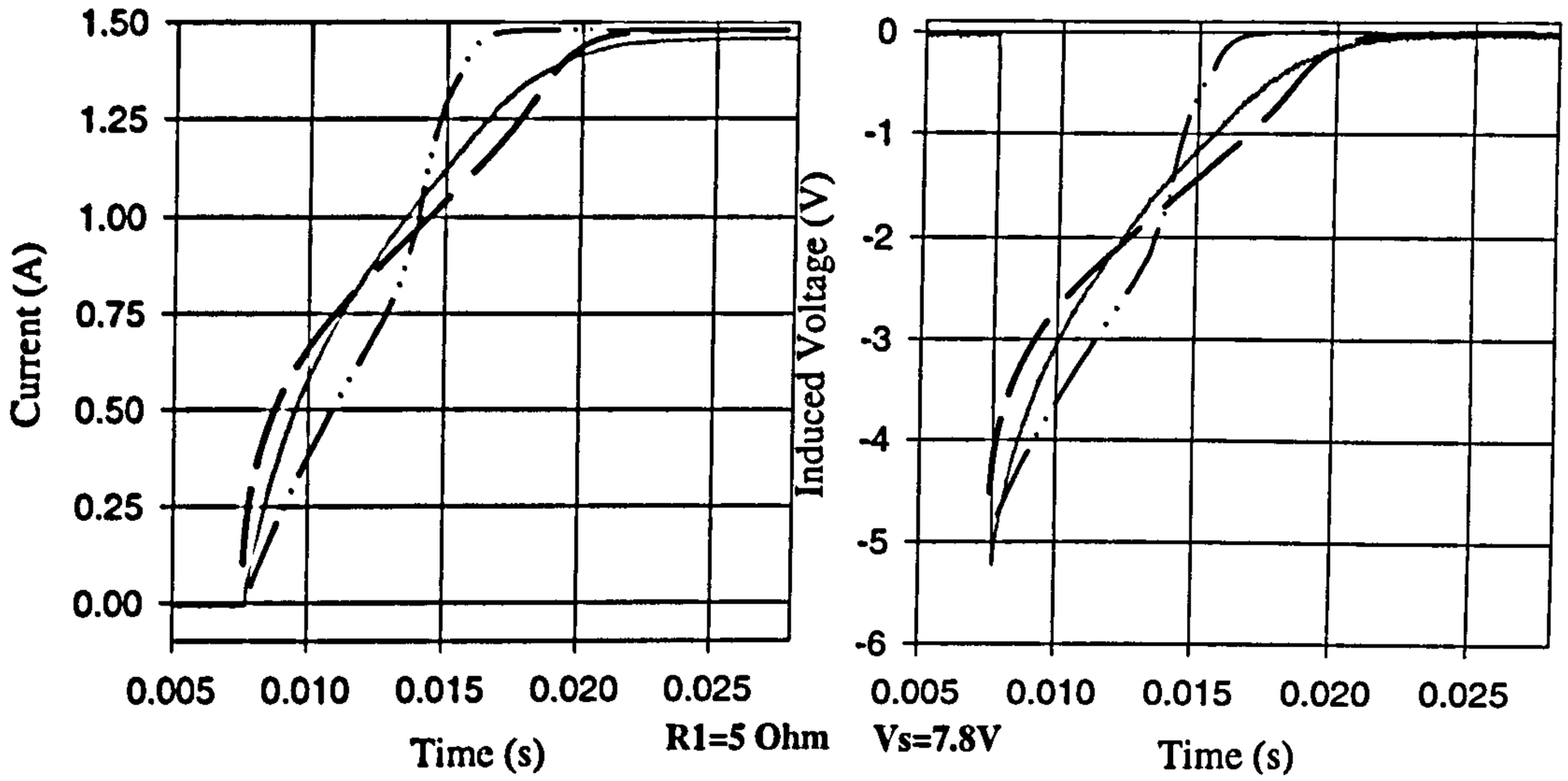

Figure 5.17: Current and induced voltage waveforms due to a step voltage at a gap length = 0.0508 mm. Measurements (solid lines) and simulation with eddy current (dashed lines) and simulation without eddy current (dashed lines + dots).

3. The circuit layer currents I_{Li} with $(i = 1..Nc)$ are given in fig. 5.22 for $Nc = 15$. The layer currents are shown in fig. 5.11.

It takes in this case about 0.5 ms for the eddy currents and for the flux to propagate through the overall actuator cross-sections. This corresponds to the time at which the eddy current density (fig 5.20) and then the flux start rising in the last layer. Indeed the last layer current $I_{L\,Nc}$ (fig. 5.22) is only a function of the flux flowing in the last closed tube of flux (see fig. 5.11).

During this first period the total amount of primary-related eddy current I_{ep} (fig. 5.22) is equal to the total winding current as the current in the last layer of the electromagnetic circuit, I_{LNc} (see fig. 5.11), is still equal to zero in eq. (5.36). This observation has however to be taken with caution. Indeed, as explained in section 5.2.2, the total amount of eddy current simulated by the network given in fig. 5.11 is overestimated by the amount of ampere-turns required for magnetising the airgaps in each closed flux tube. As soon as the last layer is affected by eddy currents and therefore generates some flux, the total amount of eddy current generated in the actuator starts decreasing significantly.

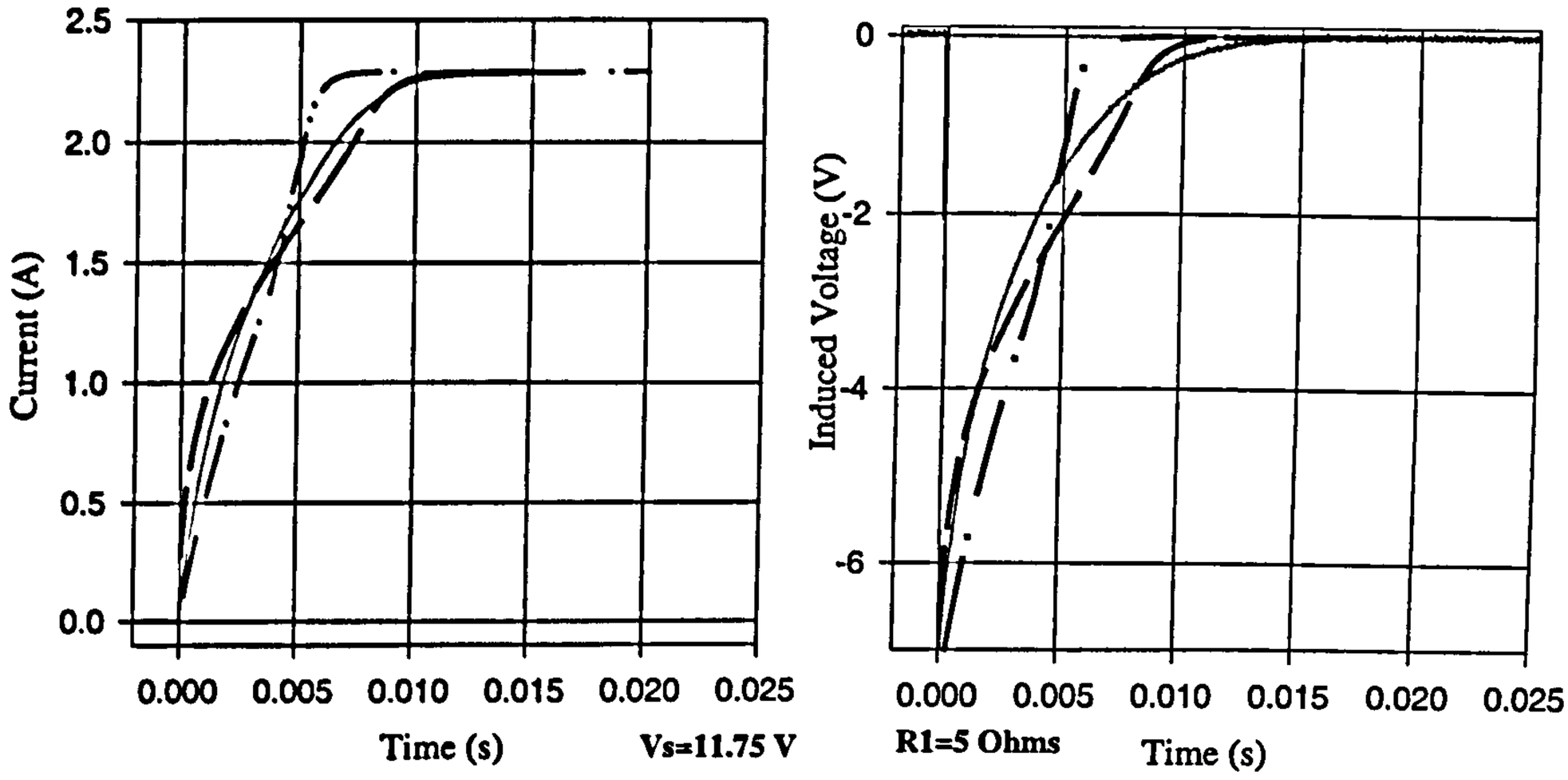

Figure 5.18: Current and induced voltage waveforms due to a step voltage at a gap length = 0.1016 mm with $R1 = 5\Omega$. Measurements (solid lines) and simulation with eddy current (dashed lines) and simulation without eddy current (dashed lines + dots).

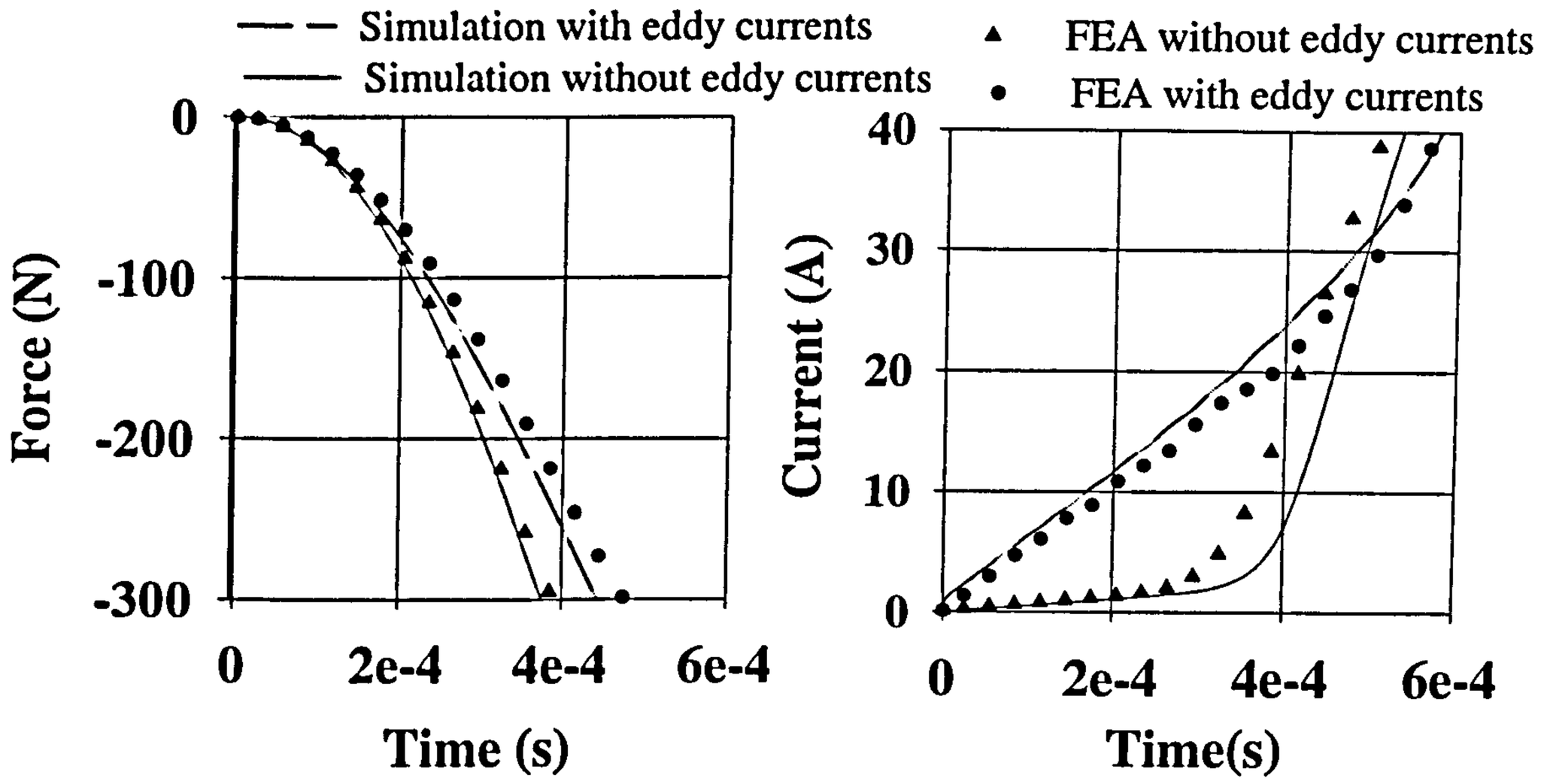

Figure 5.19: Current and force waveforms due to a step voltage at a gap length = 0.1 mm.

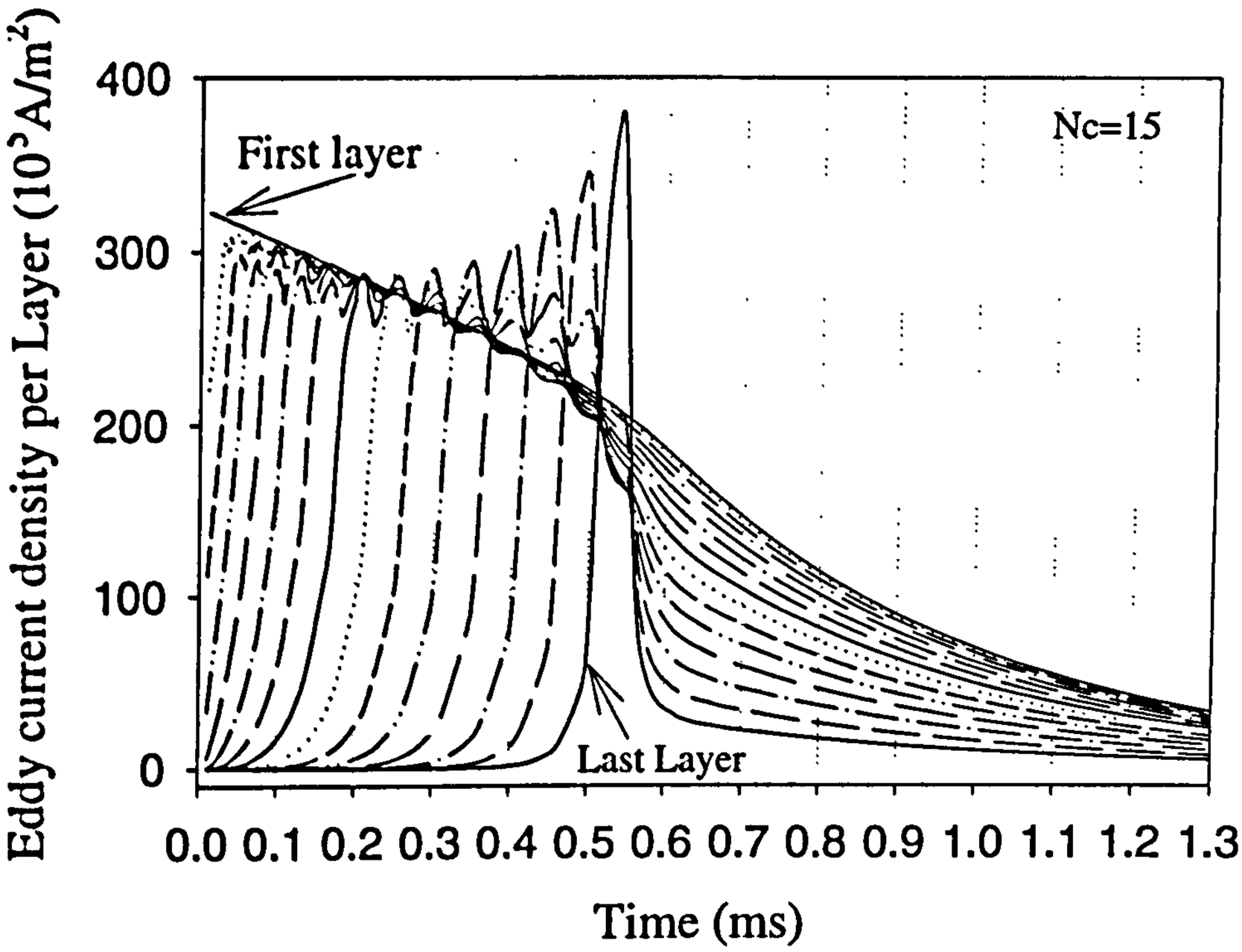

Figure 5.20: Eddy current density waveforms per layer. $Nc = 15$

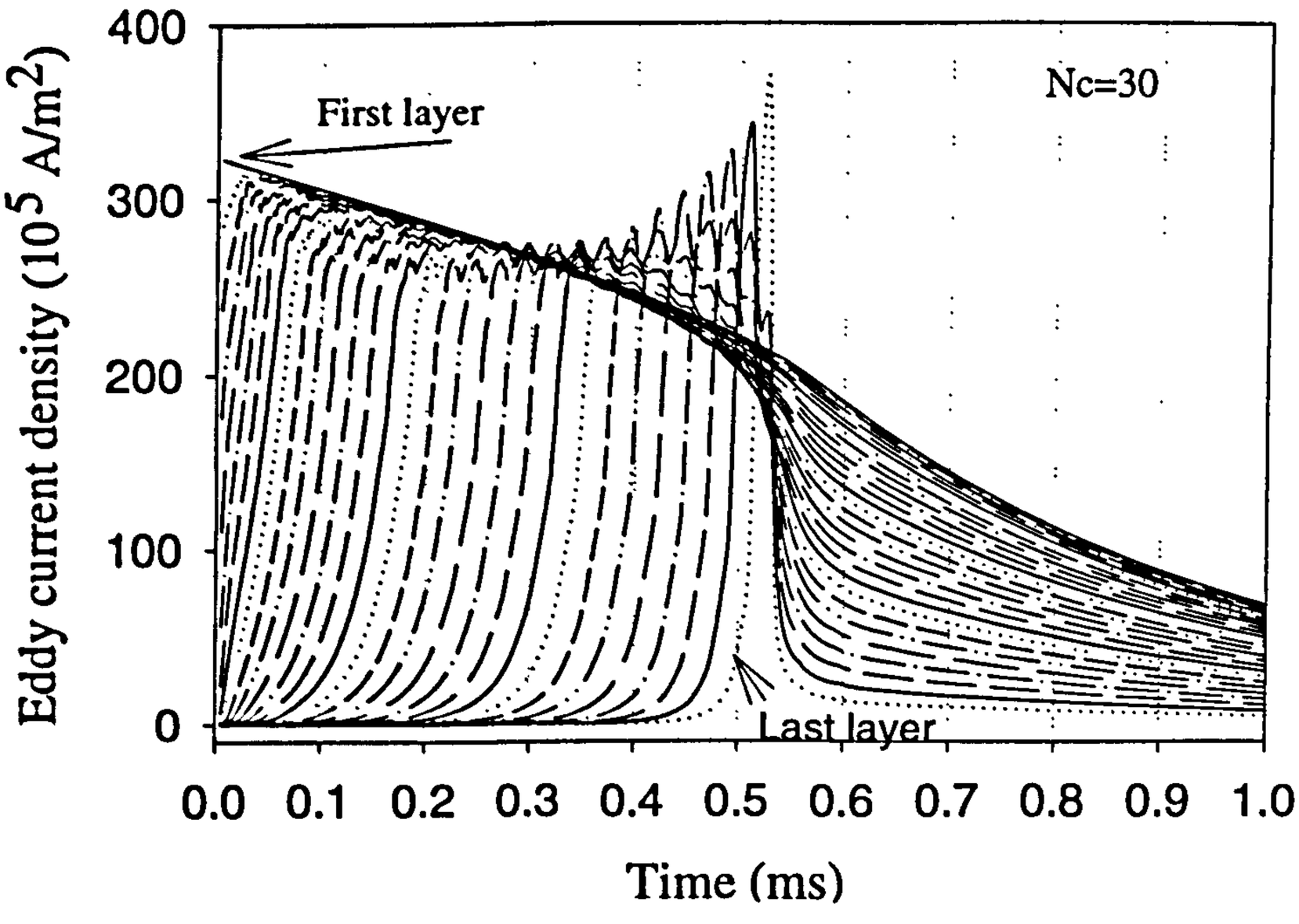

Figure 5.21: Eddy current density waveforms per layer. $Nc = 30$

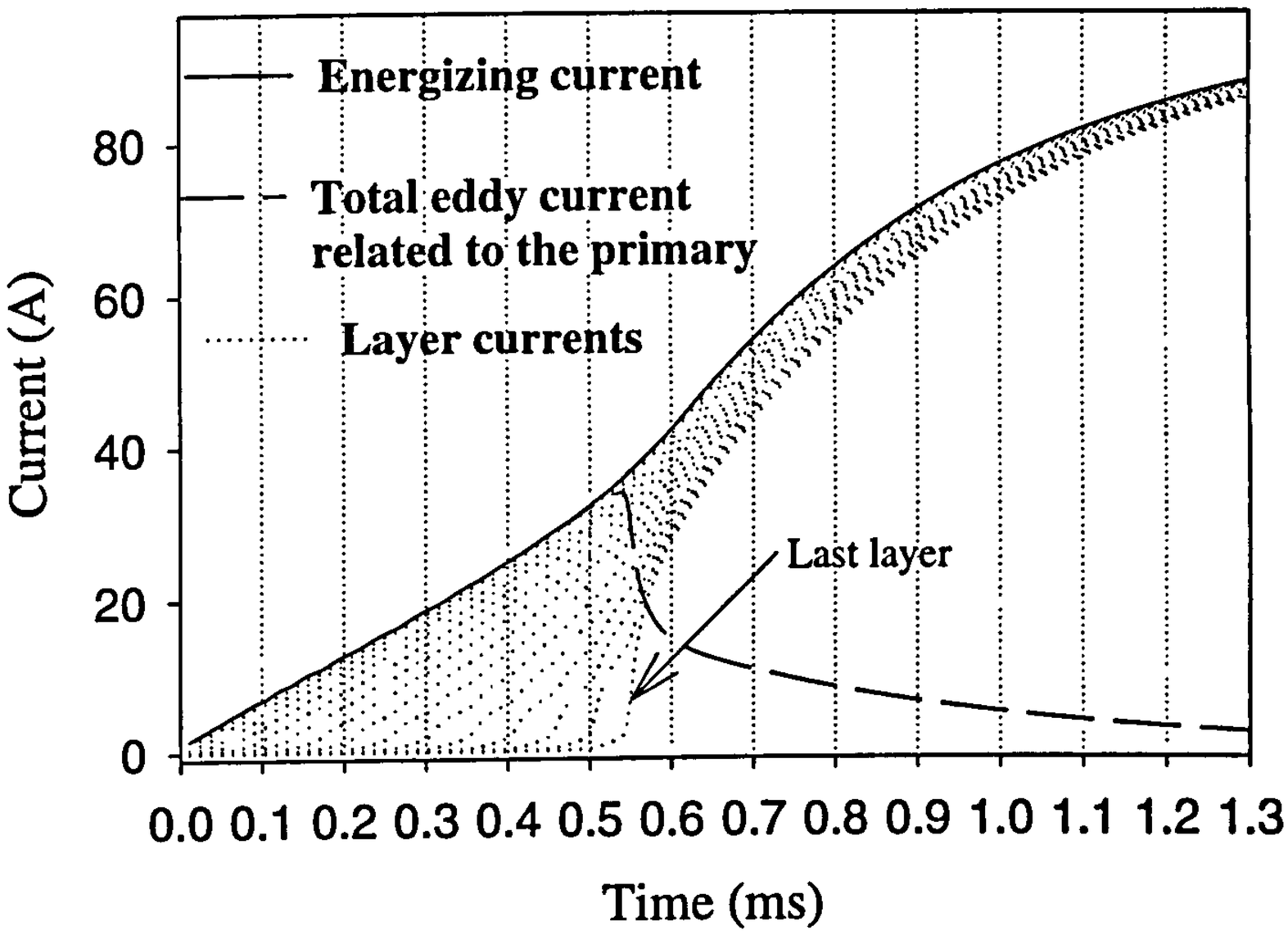

Figure 5.22: Layer currents in the electromagnetic circuit for $Nc = 15$, total current $I1$ and total eddy current related to the primary I_{ep}.

From fig. 5.21, it can be observed that the first layer jumps to its maximum value of eddy current density just after switching on. Then the eddy current density rises in the following layers, each with a different rising time which increases when the layer is further away from the iron surface (next to the coil). During this propagation time ($t < 0.5ms$), the maximum value of eddy current density reached by any layer is given by the value of the first layer eddy current density [7]. After the propagation time ($t > 0.5ms$), the eddy current generated in the last layers decreases very quickly, leaving only the eddy currents in the first layers decaying slower.

5.3.3 Conclusions

The eddy current analysis, as presented in this thesis, is more complex than what has been carried out in the past and it is clear from this new approach that this phenomenon can not be approximated with high accuracy by only one time constant, meaning also

[7] The higher value of eddy current density in the last layers are due to numerical errors during the computation and also probably to the first-order approximation of this analysis.

one resistance and one inductance.

Also the BH nonlinearities have a important role during the diffusion of flux and eddy currents. Indeed, from equation (5.28), it appears that the rate of flux variation in a layer $(i+1)$ is an increasing function of the current value I_{Li} flowing in the previous layer. However this current is linked to the flux linkage of the same layer i through a nonlinear magnetisation characteristic. Therefore when the flux tube i starts saturating, its respective layer current I_{Li} increases significantly, leading to a faster flux rise in the following flux tube.

The transient evolution of eddy currents and flux in each layer is also significantly affected by the driving conditions. The propagation time shown in the previous test is rather short due to the high step voltage. For comparison, an example of transient eddy current density and flux waveforms obtained at low step voltage (7.8V) is given in fig. 5.23 and 5.24 respectively. These results are actually obtained from the first comparison made with measurements shown in fig. 5.17.

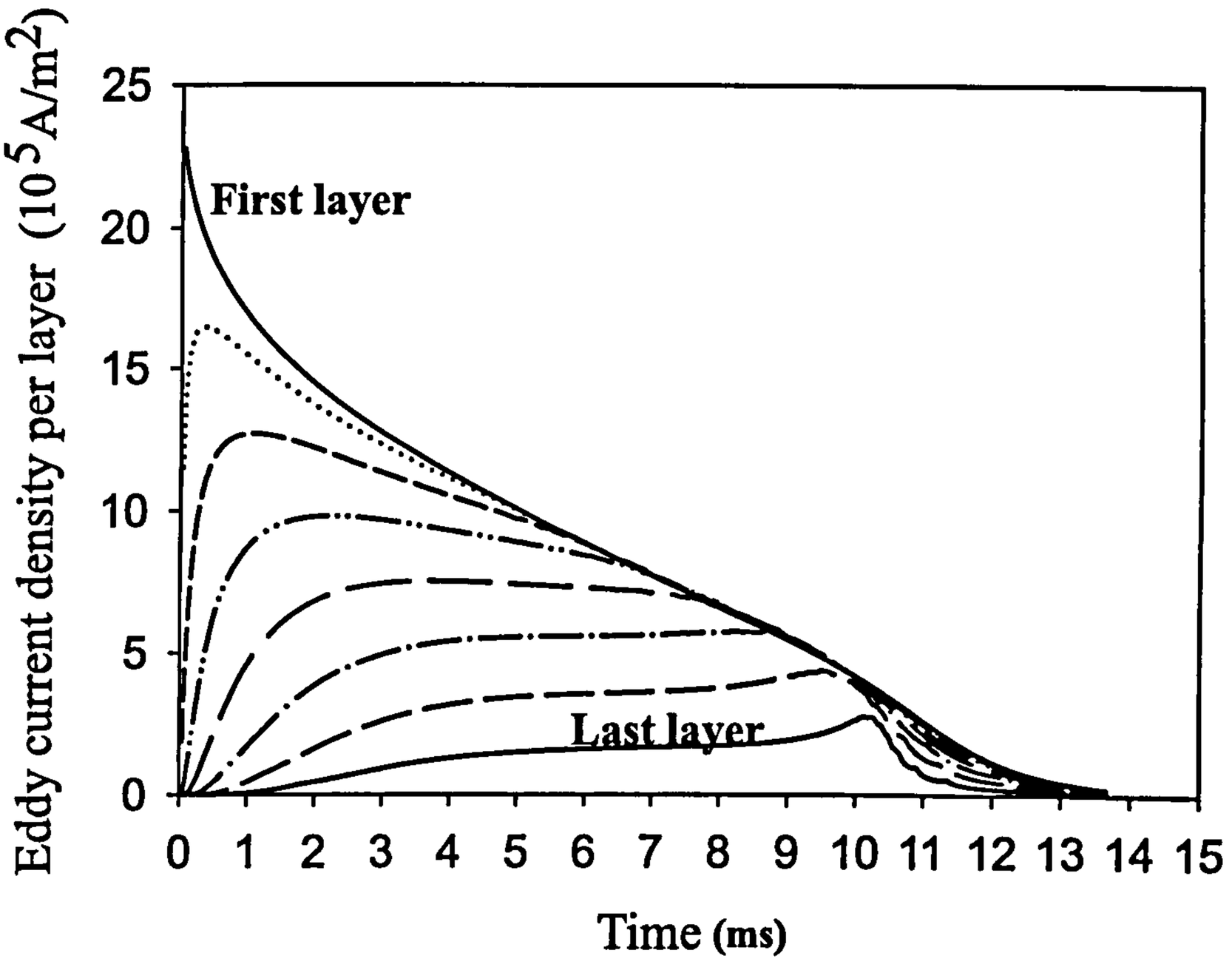

Figure 5.23: Eddy current density waveforms per layer. $Nc = 15$, $G = 0.0508mm$, $V = 7.8\ V$

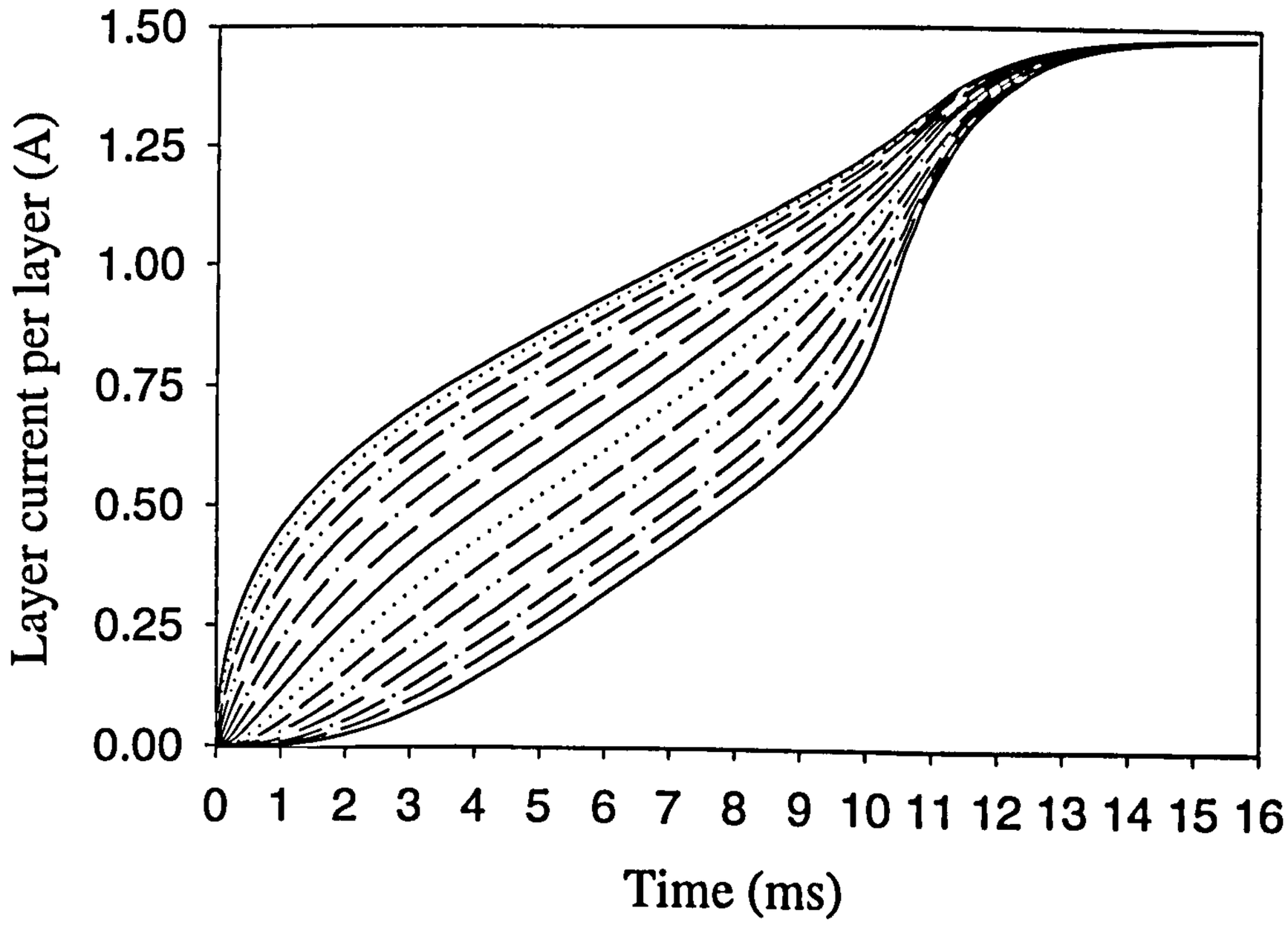

Figure 5.24: Layer currents for $Nc = 15,$, $G = 0.0508mm$, $V = 7.8\ V$

Sections	Resistance (Ω)	Volume (m^3)
S1	$\frac{2\pi\rho}{\ln(xc_1/xc_2)\,(E-F)}$	$\pi\,(xc_1^2 - xc_2^2)\,(E-F)$
S2	$\frac{2\pi\rho}{\ln(xc_1/xc_2)\,F\,(1-\frac{2}{C\,(xc_1+xc_2)})}$	$\pi\,(xc_1^2 - xc_2^2)\,F\,(1-\frac{2}{C\,(xc_1+xc_2)})$
S3	$\frac{2\pi\rho}{\ln(\frac{2\,C}{xc_1+xc_2})\,\frac{F}{C}\,(xc_1-xc_2)}$	$\pi\,(C^2 - \frac{(xc_1+xc_2)^2}{4})\,\frac{F}{C}\,(xc_1 - xc_2)$
S4	$\frac{2\pi\rho}{ln(\frac{A/2-D}{C})\,(\frac{F}{D}\,\frac{(xe_2-xe_1)}{2}+\frac{F}{C}\,\frac{(xc_1-xc_2)}{2})}$	$\pi\,((A/2-D)^2 - C^2)\,(\frac{F}{D}\,\frac{(xe_2-xe_1)}{2}+\frac{F}{C}\,\frac{(xc_1-xc_2)}{2})$
S5	$\frac{2\pi\rho}{ln(\frac{xe_1+xe_2}{2\,(A/2-D)})\,\frac{F}{D}\,(xe_2-xe_1)}$	$\pi\,(\frac{(xe_1+xe_2)^2}{4} - (A/2-D)^2)\,\frac{F}{D}\,(xe_2 - xe_1)$
S6	$\frac{2\pi\rho}{ln(xe_2/xe_1)\,\frac{F}{D}\,(\frac{xe_1+xe_2}{2}-(A/2-D))}$	$\frac{F}{D}\,\pi\,(xe_2^2 - xe_1^2)\,(\frac{xe_1+xe_2}{2} - (A/2-D))$
S7	$\frac{2\pi\rho}{ln(xe_2/xe_1)\,(E-F)}$	$\pi\,(xe_2^2 - xe_1^2)\,(E-F)$
S8	$\frac{2\pi\rho}{ln(xe_2/xe_1)\,\frac{T}{D}\,(\frac{xe_1+xe_2}{2}-(A/2-D))}$	$\pi\,(xe_2^2 - xe_1^2)\,\frac{T}{D}\,(\frac{xe_1+xe_2}{2} - (A/2-D))$
S9	$\frac{2\pi\rho}{ln\,\frac{xe_1+xe_2}{2\,(A/2-D)}\,\frac{T}{D}\,(xe_2-xe_1))}$	$\pi\,(\frac{(xe_1+xe_2)^2}{4} - (A/2-D)^2)\,\frac{T}{D}\,(xe_2 - xe_1)$
S10	$\frac{2\pi\rho}{ln\,\frac{(A/2-D)}{C}\,\frac{\frac{T}{D}\,(xe_2-xe_1)+\frac{T}{C}\,(xc_1-xc_2)}{2}}$	$\pi\,((A/2-D)^2 - C^2)\,\frac{\frac{T}{D}\,(xe_2-xe_1)+\frac{T}{C}\,(xc_1-xc_2)}{2}$
S11	$\frac{2\pi\rho}{ln\,\frac{2\,C}{(xc_1+xc_2)}\,\frac{T}{C}\,(xc_1-xc_2)}$	$\pi\,(C^2 - \frac{(xc_1+xc_2)^2}{4})\,\frac{T}{C}\,(xc_1 - xc_2)$
S12	$\frac{2\pi\rho}{ln\,\frac{xc_1}{xc_2}\,T\,(1-\frac{xc_1+xc_2}{2C})}$	$\pi\,(xc_1^2 - xc_2^2)\,T\,(1-\frac{xc_1+xc_2}{2C})$

Table 5.2: Expressions of the eddy current resistances in the different actuator sections

5.4 Dynamic Analysis

The previous comparisons are not sufficient to complete the validation of the electromagnetic equivalent circuit shown in fig. 5.11. A dynamic simulation, i.e with armature movement, is considered in this section involving different types of control sequence. This test is compared with time-stepping finite elements and gives more insight into the limits of the proposed network configuration.

5.4.1 Test Conditions

The driving conditions chosen for the new comparison are very close to what it could be expected in a real application. A high step voltage (90V) is used in order to accelerate the rise of eddy currents and flux in the actuator. The current is limited to a peak value of 6A. These conditions are only held during 0.55ms during which the armature is expected to move to its minimum airgap length position. Then a free wheeling operation starts and reduces progressively the current to its holding value of 2A, kept until 1ms. The last stage is the switch-off process obtained by reversing the voltage source on the winding. This should lead to a fast decay of the current and a return of the armature to its initial position.

The actuator dimensions considered in these tests are given in column D2 of table 5.1. The winding resistance R_1 is set to 3.8 Ohms. The voltage drops on the diodes or transistors are neglected. The steel is the same as for the magnetostatic and transient computation for which the iron resistivity ρ is $42.810^{-8}\,\Omega\,m$. The mechanical characteristics defined for this test are given in table 5.3.

A comparison is obtained by time-stepping finite elements implemented in MEGA by Lucas Varity [42]. The mesh developed for this purpose is given in fig. 5.25. The armature movement is obtained by stretching the airgap mesh. Within the iron the mesh has been mainly refined at the air/iron interface, where the diffusion phenomena are the most intense.

The results of this comparison are shown:

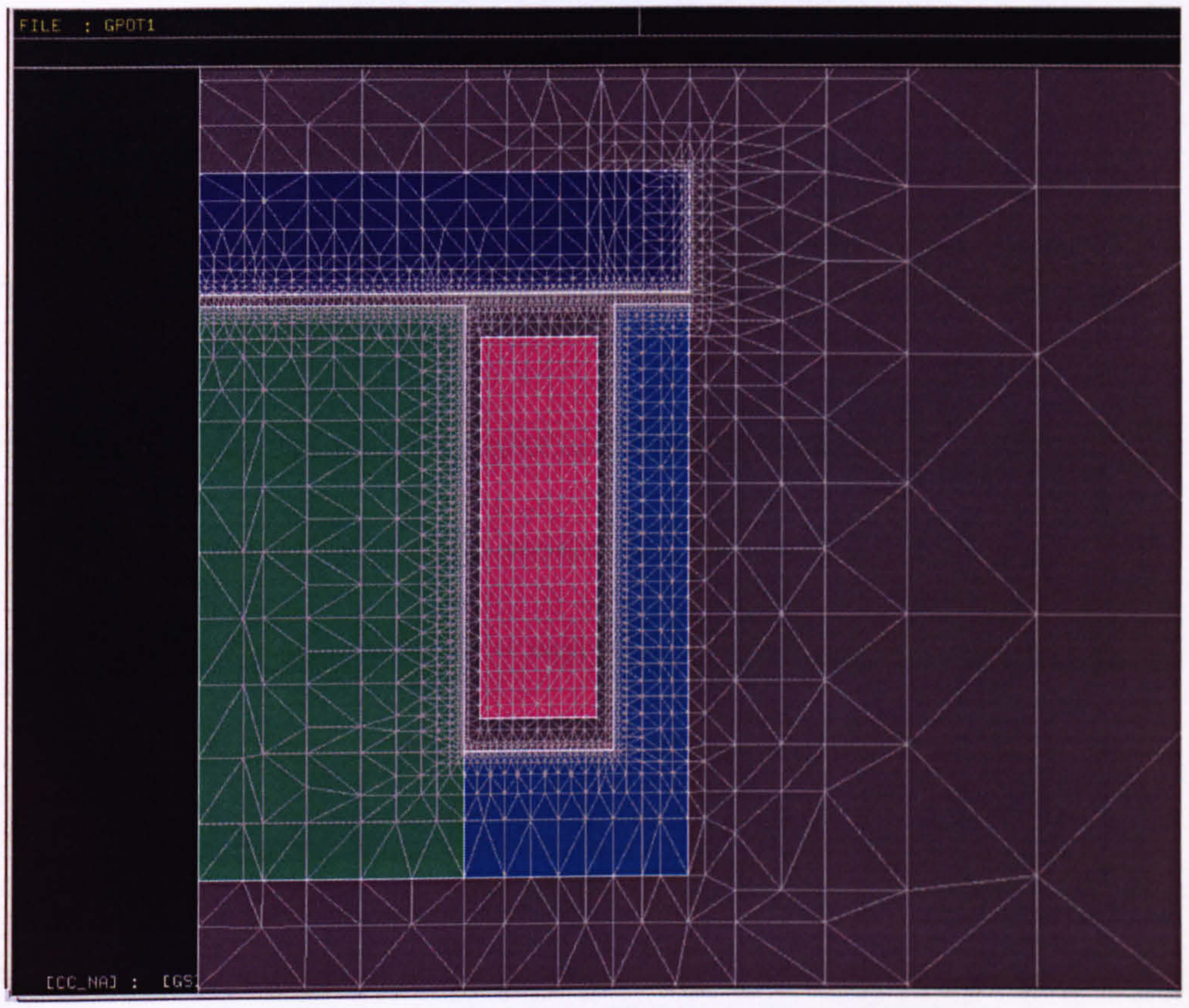

(A)

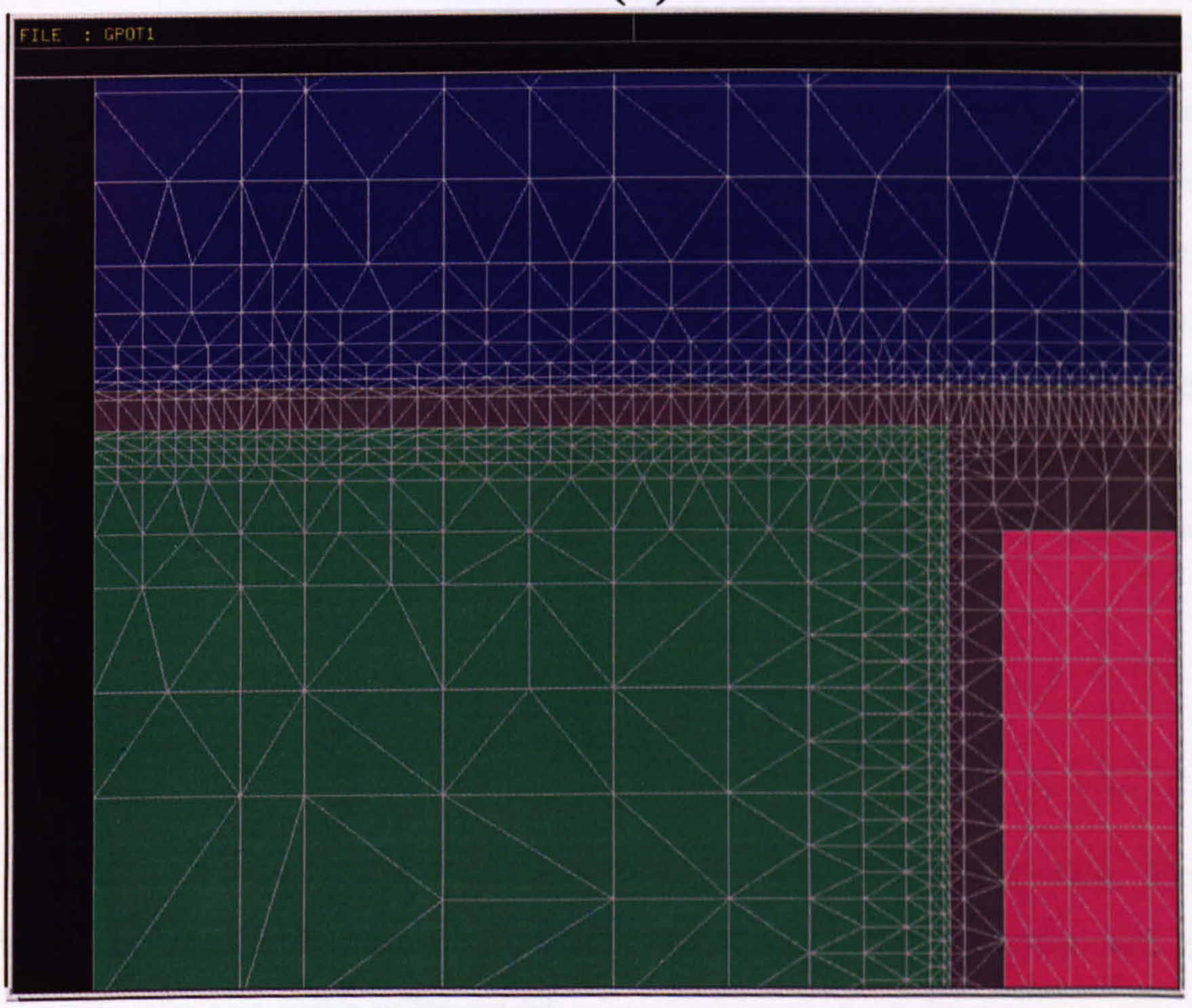

(B)

Figure 5.25: Mesh of the axisymmetric actuator developed for the dynamic analysis.

Moving mass	$10\,g$
Spring constant	$75\ 10^3 N/m$
Spring preload	$15N$
Minimum gap	$0.1mm$
Maximum gap	$0.3mm$

Table 5.3: Mechanical characteristics defined for the dynamic comparison.

- in fig. 5.26 for the transient current and magnetic force,
- in fig. 5.27 for the armature movement and the total flux linkage,
- and in fig. 5.28 for the total eddy current.

5.4.2 Result Discussion

For $I_1 > 0\,A$

The results obtained by the analytical simulation for the current, magnetic force, armature movement and flux linkage are in excellent agreement with the finite-element analysis. The total amount of eddy current is however larger than the one predicted by finite-elements, which confirms the previous discussion of section 5.2.2. The discrepancy between both curves corresponds to the amount of ampere-turns consumed by the airgaps. For the same reason, the effect of airgap variation is not visible in the analytical simulation but can be clearly observed in the FE case. The order of magnitude and the general trend of the analytically predicted eddy current is however satisfactory.

For $I_1 = 0\,A$

During the switch-off period, the winding current rapidly decreases to zero. However due to the presence of eddy currents, the flux still flows in the actuator and decays slowly during nearly one more millisecond.

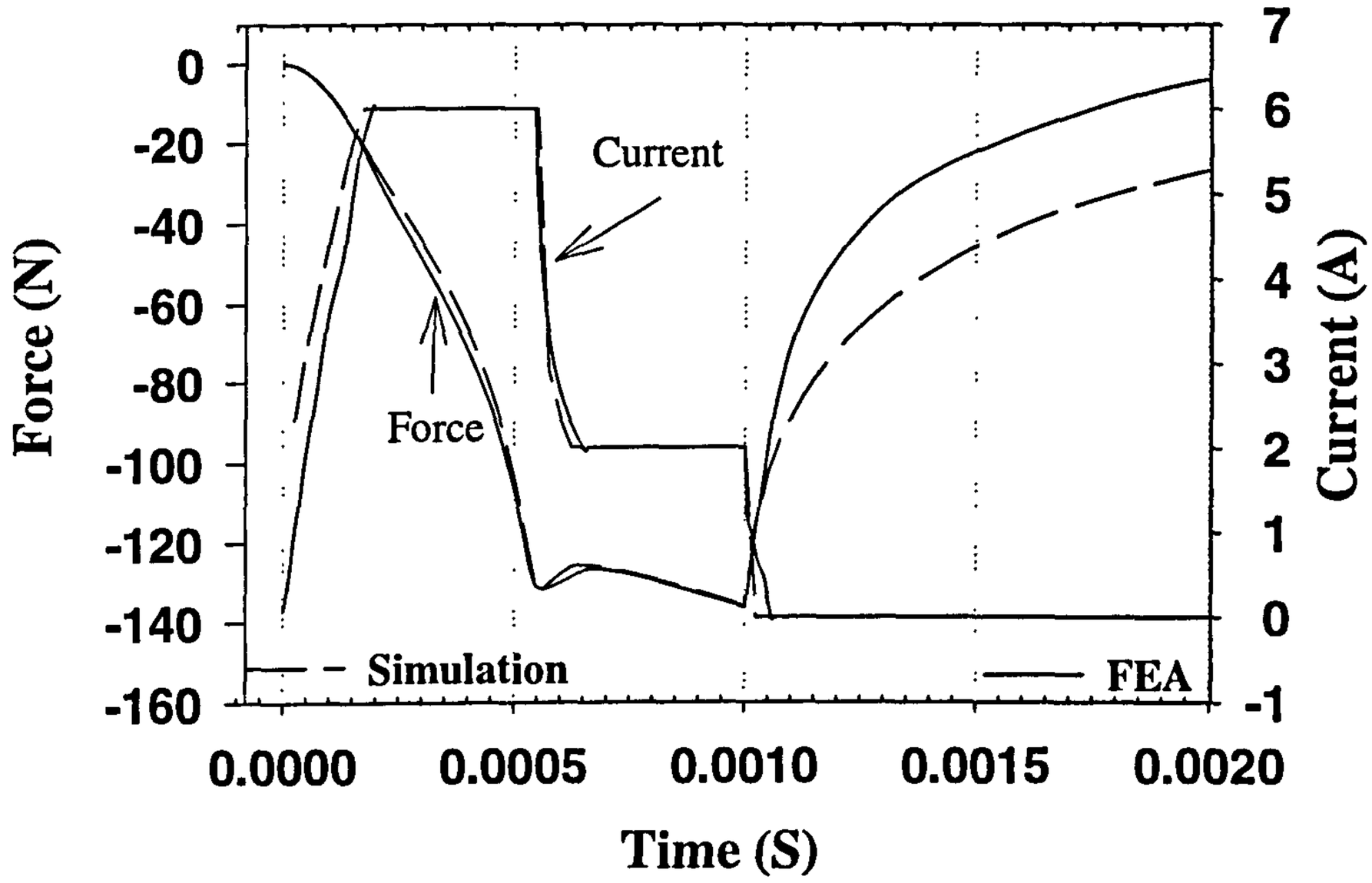

Figure 5.26: Current and force waveforms during the dynamic test.

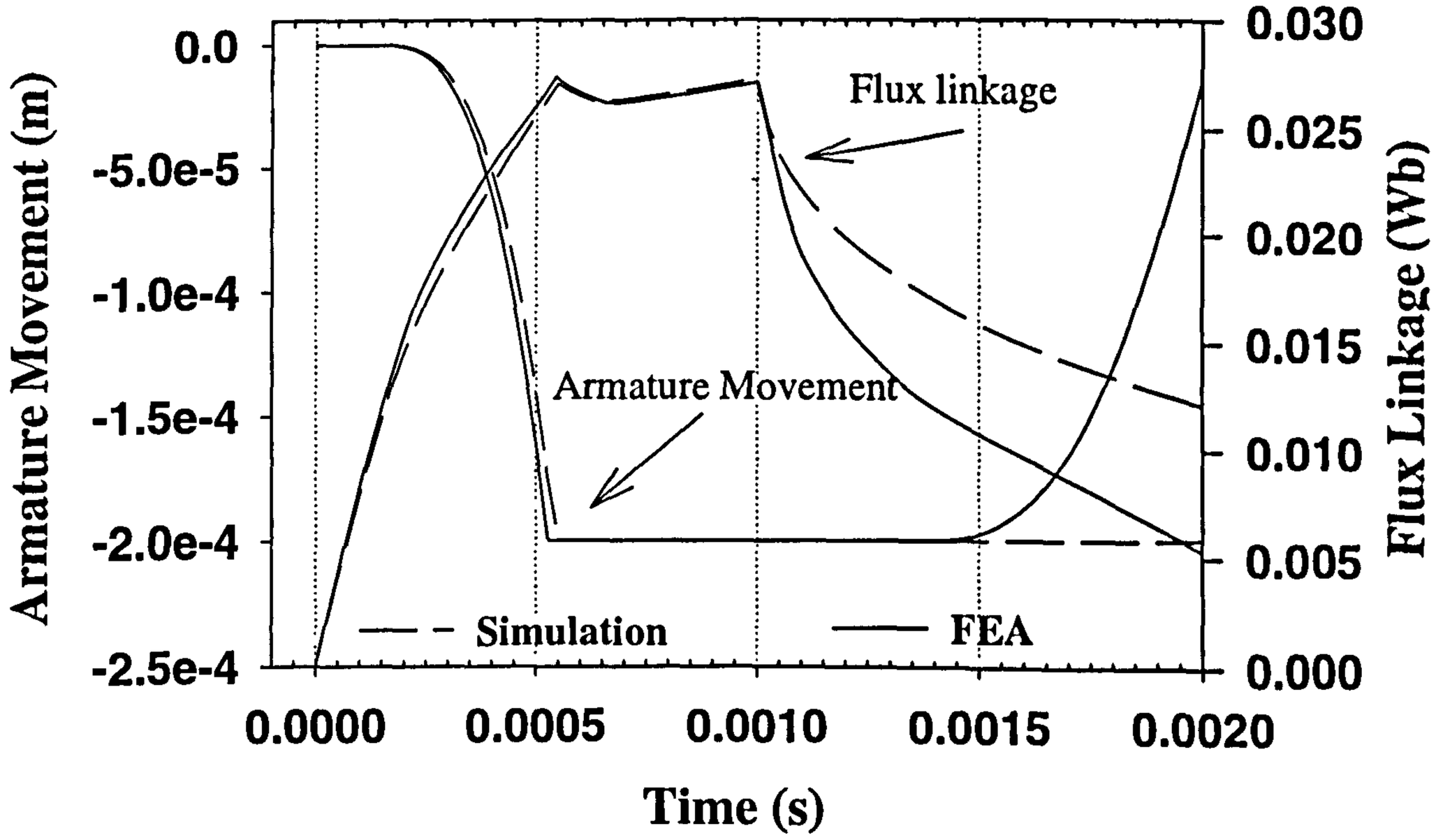

Figure 5.27: Armature movement and flux linkage waveforms during dynamic test.

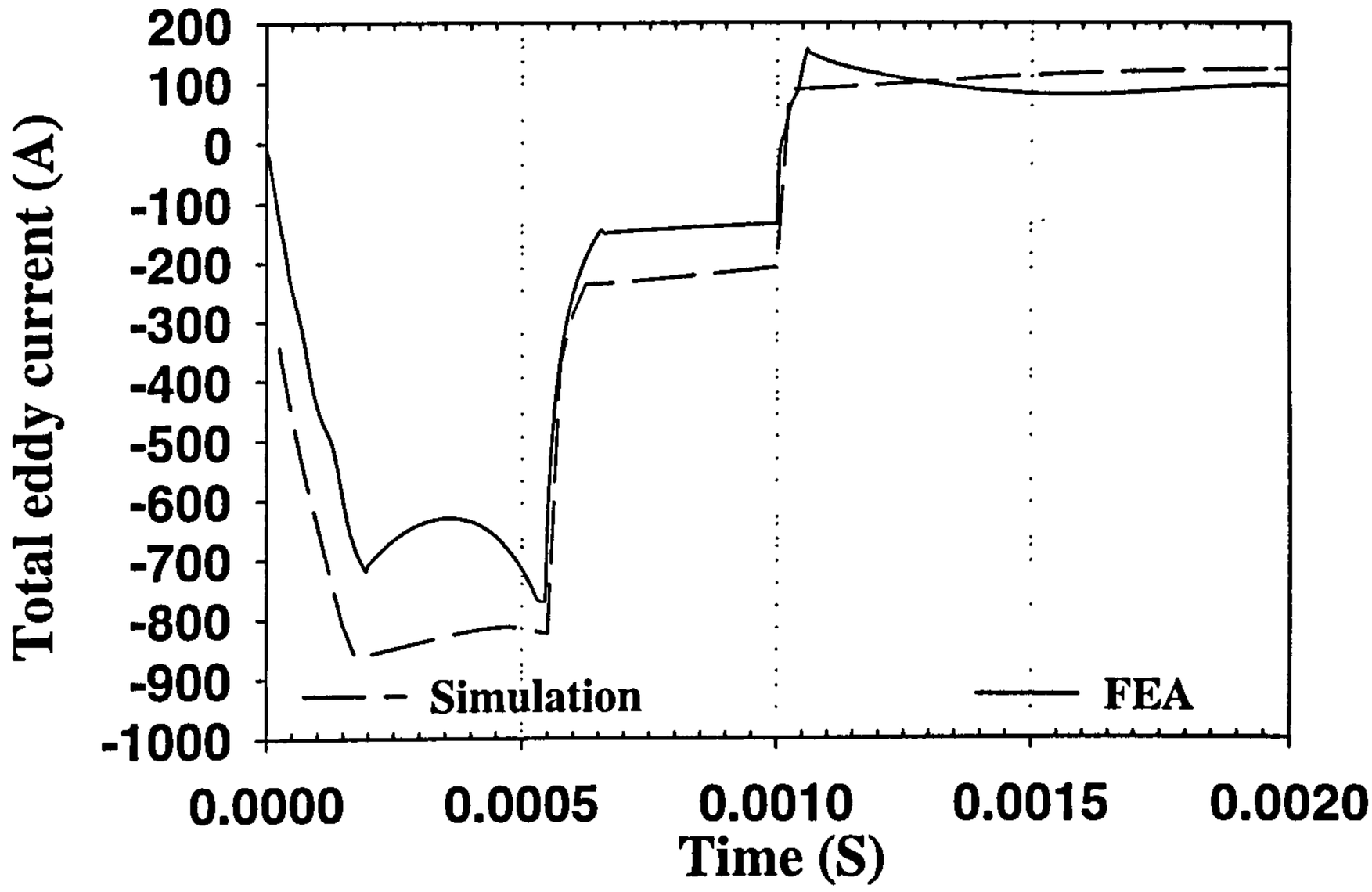

Figure 5.28: Eddy current waveform during dynamic test.

As soon as the current has returned to zero, the discrepancy increases significantly between both simulations. The natural flux/force decay predicted by the analytical model takes significantly more time than in the finite element case. Also the level of discrepancy suggests that a major assumption of the circuit development may be the cause of such a difference.

Figure 5.29 shows a flux plot retrieved from the finite element analysis at $t = 1.6ms$. It can be observed that a significant part of the flux does not flow any more through the airgaps but decays by forming closed loops within the core and the armature separately. This flux plot also suggests that this phenomenon starts within the first layers next to the coil and extends progressively to the following ones until complete decay.

The flux path configuration described above, is not possible within the electromagnetic circuit given in fig 5.11. This network assumes a fixed flux path going through the different actuator sections for any driving conditions including decay. During the natural decay, the flux simply decreases in magnitude in each layer but never changes direction. This can be observed in fig. 5.30 showing the layer current waveforms during the dynamic test. A change of sign in any of the layer current would indeed correspond

to a change of flux direction in the same layer. In fig. 5.30, there is clearly no change of the layer current sign during the natural decay period and therefore no change of flux direction.

It is concluded that the network topology as given in fig. 5.11 is not valid for simulating the natural flux decay and cannot be applied for computing the complete dynamic behaviour of actuators.

5.4.3 Electromagnetic Equivalent Circuit for Dynamic Computation

The problem highlighted in the previous section does not modify the diffusion network configuration. However it certainly throws some light on the interpretation that should be given to the circuit elements (iron resistances and nonlinear inductances). Indeed, if the assumption of dividing the actuator into closed flux tubes is not correct, it means that a diffusion network can only be associated with one part of the actuator. Therefore several diffusion networks should be used in parallel if required for simulating the complete flux path. The simplest network configuration complying with this new constraint is shown in fig. 5.31. In this new configuration, the actuator has been divided into two diffusion blocks, one for the armature and one for the core. The airgap inductance L_l simulates the slot leakage flux while L_g simulates the main airgap flux as well as the fringing flux.

Although this new configuration has not been completely implemented, it can be shown that there are some major differences with the first configuration, which should make it more accurate in the dynamic simulation:

- First of all, the computation of eddy currents provided with this new network will be more accurate. Indeed the nonlinear elements in each diffusion network correspond only to iron flux tubes; the linear inductances for the airgaps are modelled as separate elements in parallel or in series with the diffusion blocks. It follows that the total amount of ampere turns available for the iron losses is

reduced by the mmf drop required for magnetising the airgaps and then eq. (5.25) is in this case respected. A variation of airgap length will then also affect the total eddy current in this new configuration.

- The division of the electromagnetic equivalent circuit into several block enables the flux to diffuse differently in each block. The total amount of flux flowing at a time is limited by the configuration of the entire circuit. However the propagation within any actuator section is now a local function of the iron resistances and nonlinear inductances of the respective section.

  For this purpose a simple test has been implemented which shows the variation in the transient behaviour of the limbs only . The test consists of an impact excitation generated in the network configuration shown in fig. 5.32, in which the iron losses as well as the mmf drop in the yokes have been neglected . Each of the two diffusion blocks characterises in this case a different limb. The layer current waveforms obtained from this test for both limbs are shown in fig. 5.33. The propagation period of the outer limb is significantly smaller than for the central one. The overall transient behaviour of the axisymmetric actuator is mainly driven by the slow flux propagation time of the central limb. Indeed the same test conditions and actuator dimensions have been used in fig. 5.24 obtained with a 1-diffusion block circuit and in fig. 5.33 obtained with a 2-diffusion block circuit (except that the yokes have been neglected in the second case). The results obtained in the first case have nearly the same propagation time as for the central limb in the second case.

- More importantly, by fractioning the previous closed flux paths into sections, the flux is now able to modify its direction depending on the driving conditions such that during a natural decay period, a change of flux direction in the first layers of each diffusion block can be observed. This can be demonstrated using again the simplified network given in fig. 5.32. A natural decay period is simulated by applying a step voltage with a limited current ($2\,A$) and then reversing the voltage until complete decay of the winding current. Fig. 5.34 shows the winding current (above) and the layer currents (below) in the central limb obtained during this

test. As explained earlier, the change of a layer current sign indicates a change of the flux direction within the same layer. During the natural flux decay , the layer currents in the first layers of the central limb are becoming negative. The same phenomenon can be observed at the same time within the diffusion block of the outer limb. Some flux is still flowing however in the airgaps, generating an mmf drop proportional to I_g shown also in fig. 5.34. These general conditions look similar to what can be observed in fig 5.29.

Although the computation of the equivalent circuit shown in fig. 5.31 is still faster than a numerical analysis, the division of the actuator model in different blocks removes some of the computational advantages of the first network. Indeed with this new equivalent circuit, it is no longer possible to compute the magnetising current based on the gauge curve approach or simply based on the evaluation of the magnetisation characteristics of the actuator. At any time, the mmf drop in each layer within each actuator section has to be retrieved from the knowledge of the flux flowing within the corresponding tube and its geometrical and material characteristics. However the force computation is definitely easier than with the first circuit as the airgap flux is directly available during the computation. The total number of equations is multiplied by the number of diffusion networks considered in the equivalent circuit. In fact it is clear that more complex electromagnetic equivalent circuit could be defined in practice. For example, a possible but complex equivalent network for the pot-core actuator could be the electrical version of magnetic equivalent circuit developed for the magnetostatic analysis (fig. 2.16), in which each nonlinear inductance (permeance) is replaced by an appropriate diffusion network.

It should be however emphasised that a great amount of useful information can already be retrieved by the solenoid designers from the simplified but very fast electromagnetic equivalent circuit as shown in fig. 5.11. For example a set of dynamic simulations showing the effect of different parameter change is given in this section. The comparison is based on the previous dynamic test summarised in fig. 5.26, 5.27, 5.28 but limited here to the portion which has given a good agreement with FEA. The different simulations include:

1. **A variation of the number of turns such that the total amount of ampere-turns is kept constant.** The results are shown in fig. 5.35. The initial simulation which was compared with finite-element analysis is shown in dashed lines and corresponds to 152 turns. It can be seen that by multiplying the number of turns by a factor two, the inductive effect is dominant in the current and force rise leading to a significant delay in the armature movement. On the contrary, by dividing the number of turns by two, the armature moves quicker but not as fast as could be expected due to the generation of eddy current, delaying the force rise.

2. **A great variation of the iron resistivity.** The results are given in fig. 5.36. By multiplying the resistivity by a factor ten, the current and force rise are close to what it could be expected in an ideal material without eddy current. The actuator goes to saturation changing the slope of the current rise and also leading to a quicker decay of the already reduced amount of eddy currents. Then the armature also moves a lot faster.

3. **A variation of the limb length.** Although the limb length is constrained by the amount of copper in the slot, fig. 5.37 shows clearly the necessity to optimise this variable. Indeed the overall behavior of the actuator is dominated by the central limb iron resistance, a function of the limb length. The total amount of mmf drop required for magnetising the limb is also a function of this parameter. It follows that by reducing the limb length the iron resistance per layer is increased, the flux propagates faster within the iron and also more flux is available for the same amount of ampere-turns. Therefore the armature moves a lot faster.

4. **A simultaneous variation of resistivity and BH characteristics.** This test tries to give an idea about how much dynamic improvement could be expected from a change in the material characteristics. An arbitrary variation of both permeability and resistivity is then imposed on the material characteristics used in the original dynamic simulation (dashed lines in fig. 5.38). It is concluded from fig. 5.38 that a gain of 20% in resistivity leading to an equivalent decrease of the permeability of the steel will not lead to any dynamic improvement. However if

the trade-off leads to a different proportion of small variation between these both parameters, some small gain may be obtained in the dynamic response.

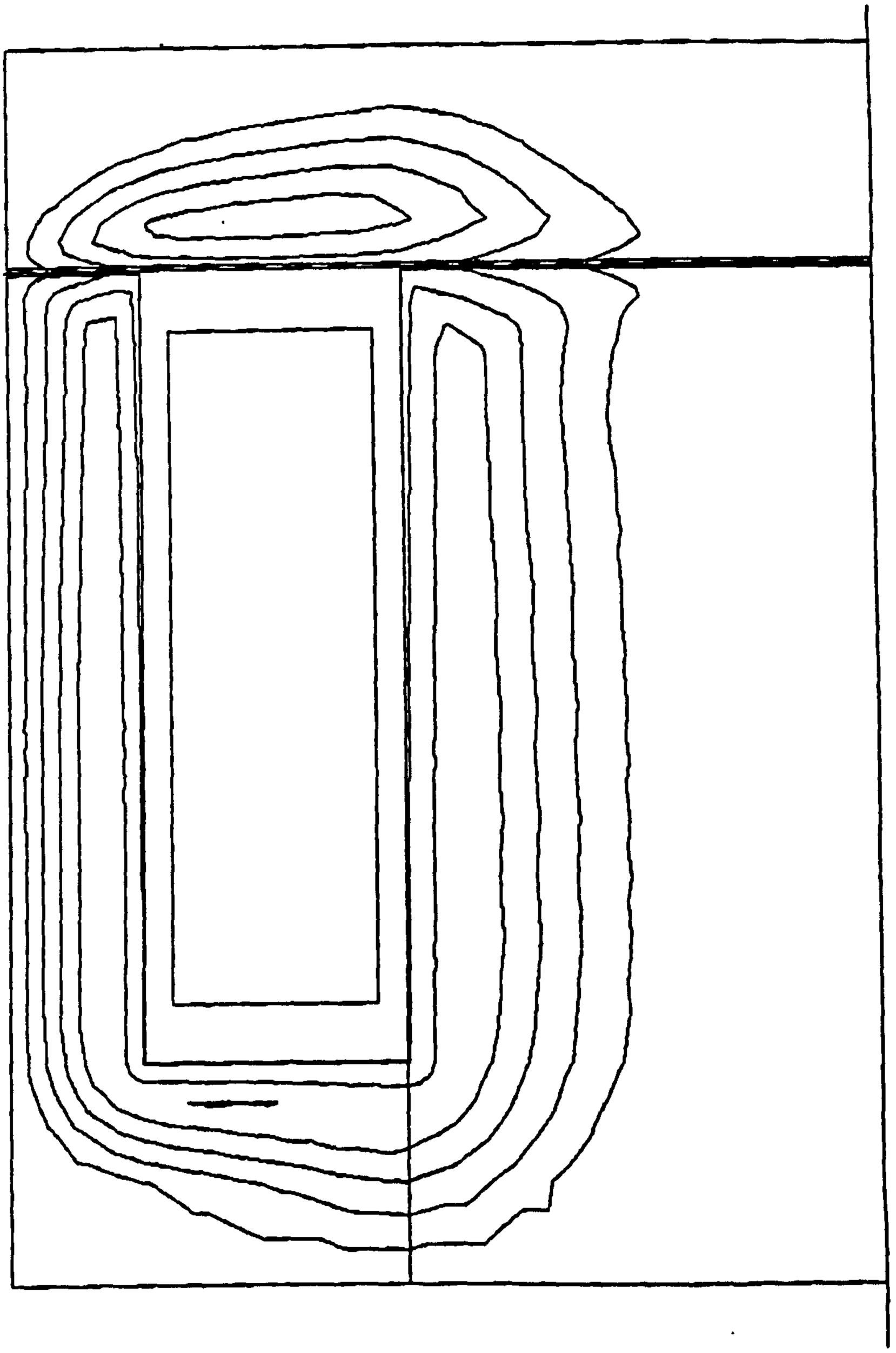

Figure 5.29: Flux plot at $t = 1.6ms$ during the natural flux decay

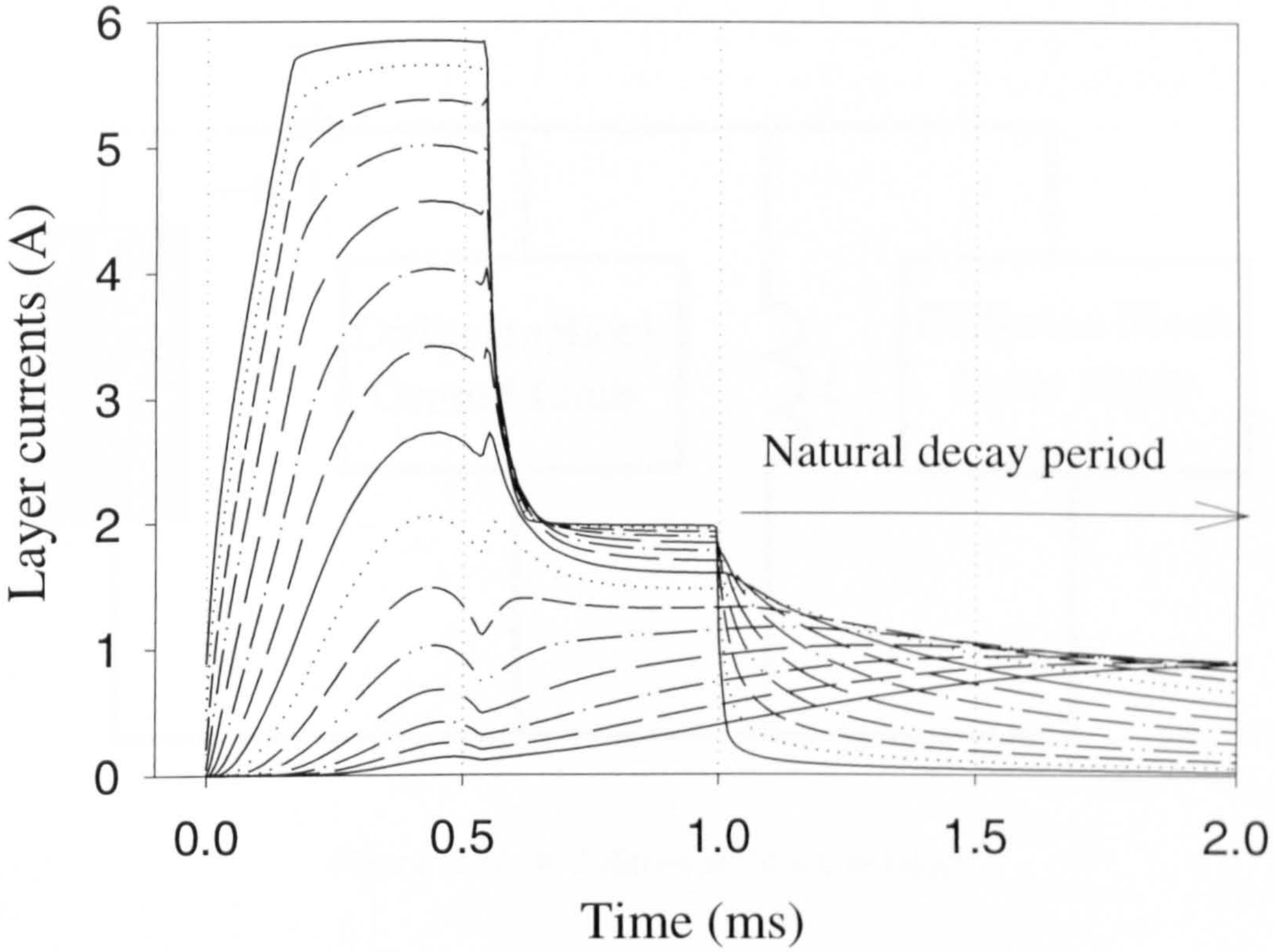

Figure 5.30: Layer currents during dynamic test.

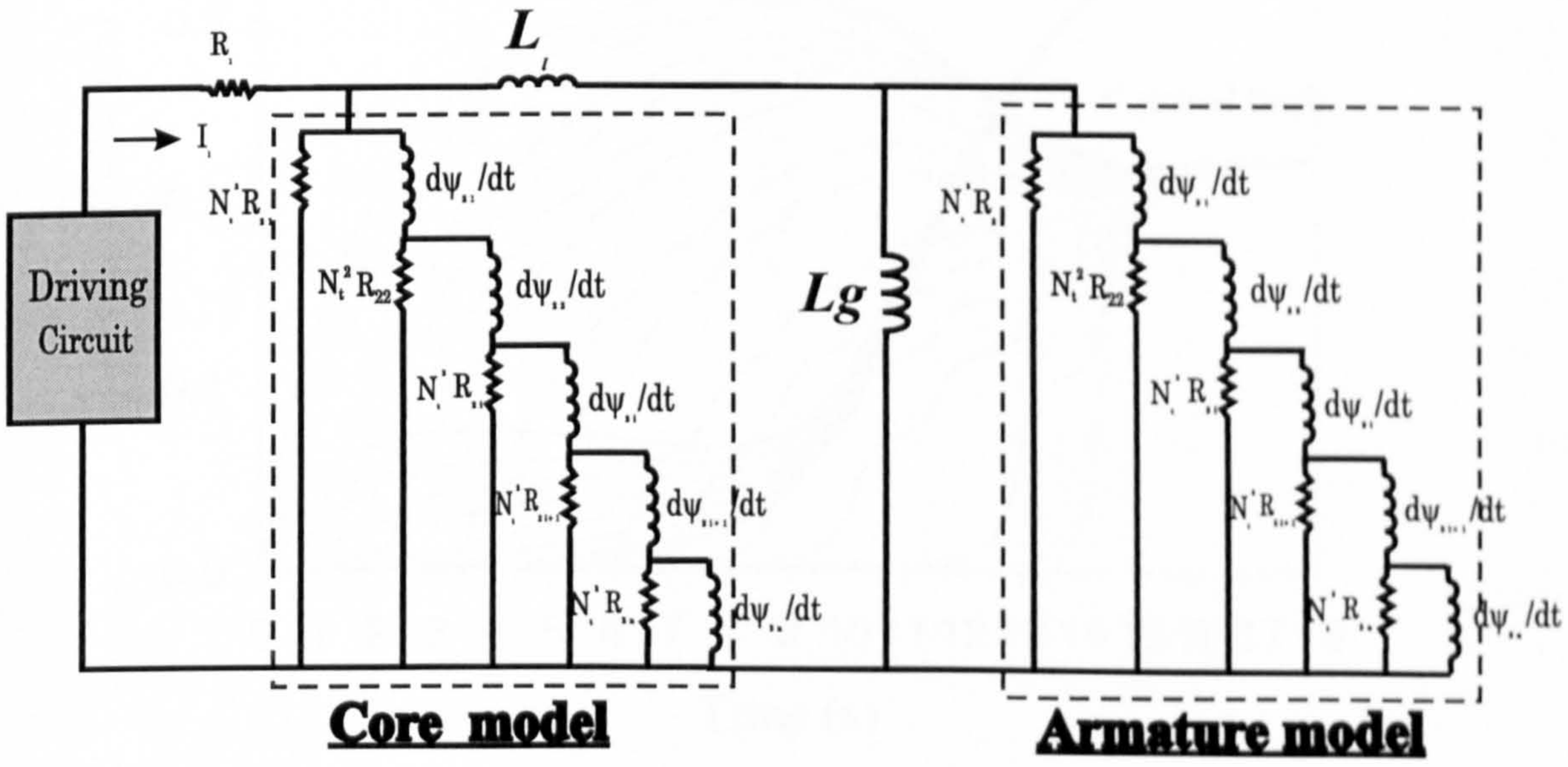

Figure 5.31: Electromagnetic equivalent network for dynamic analysis of axisymmetric actuators.

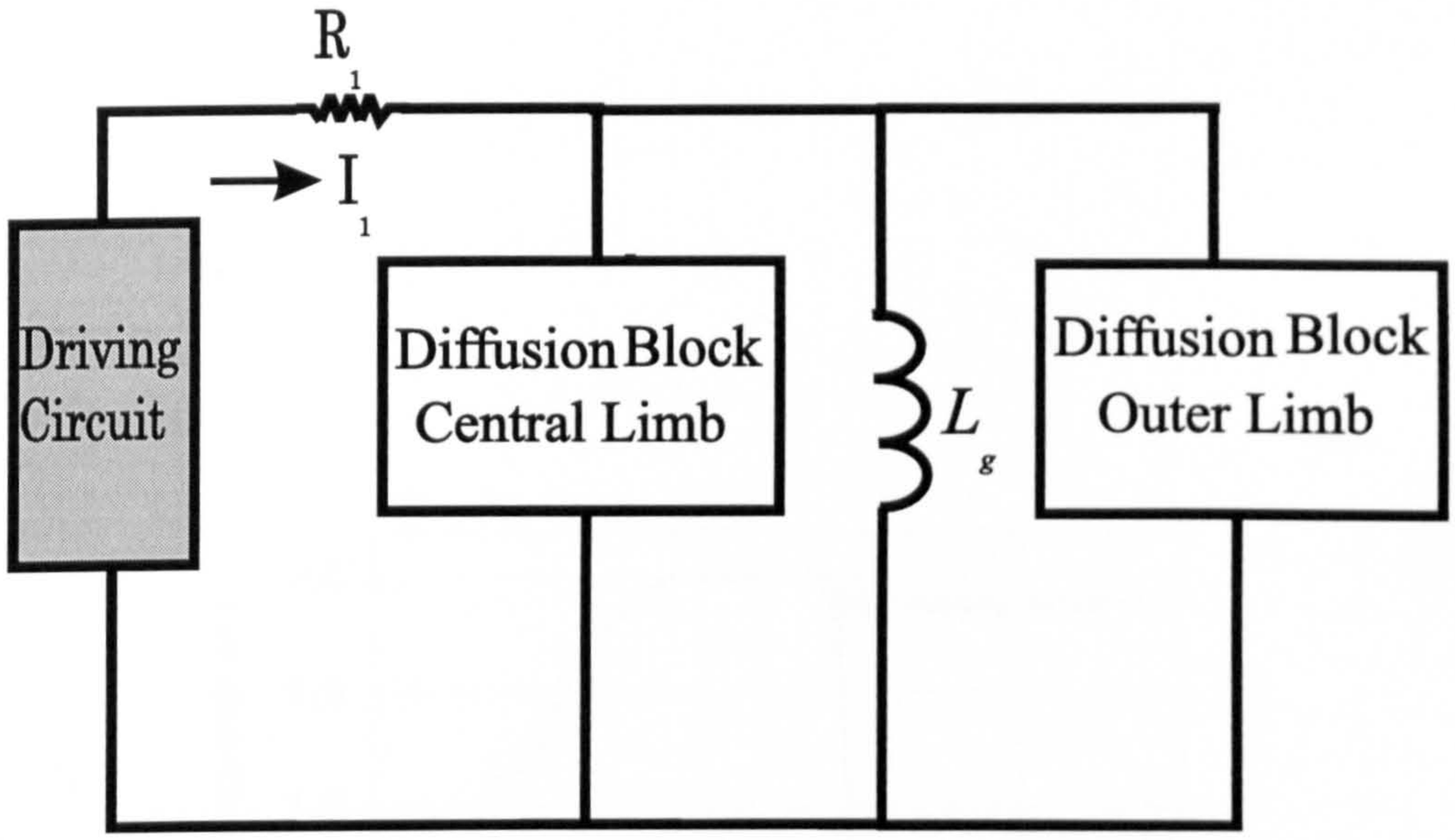

Figure 5.32: A 2-diffusion block network

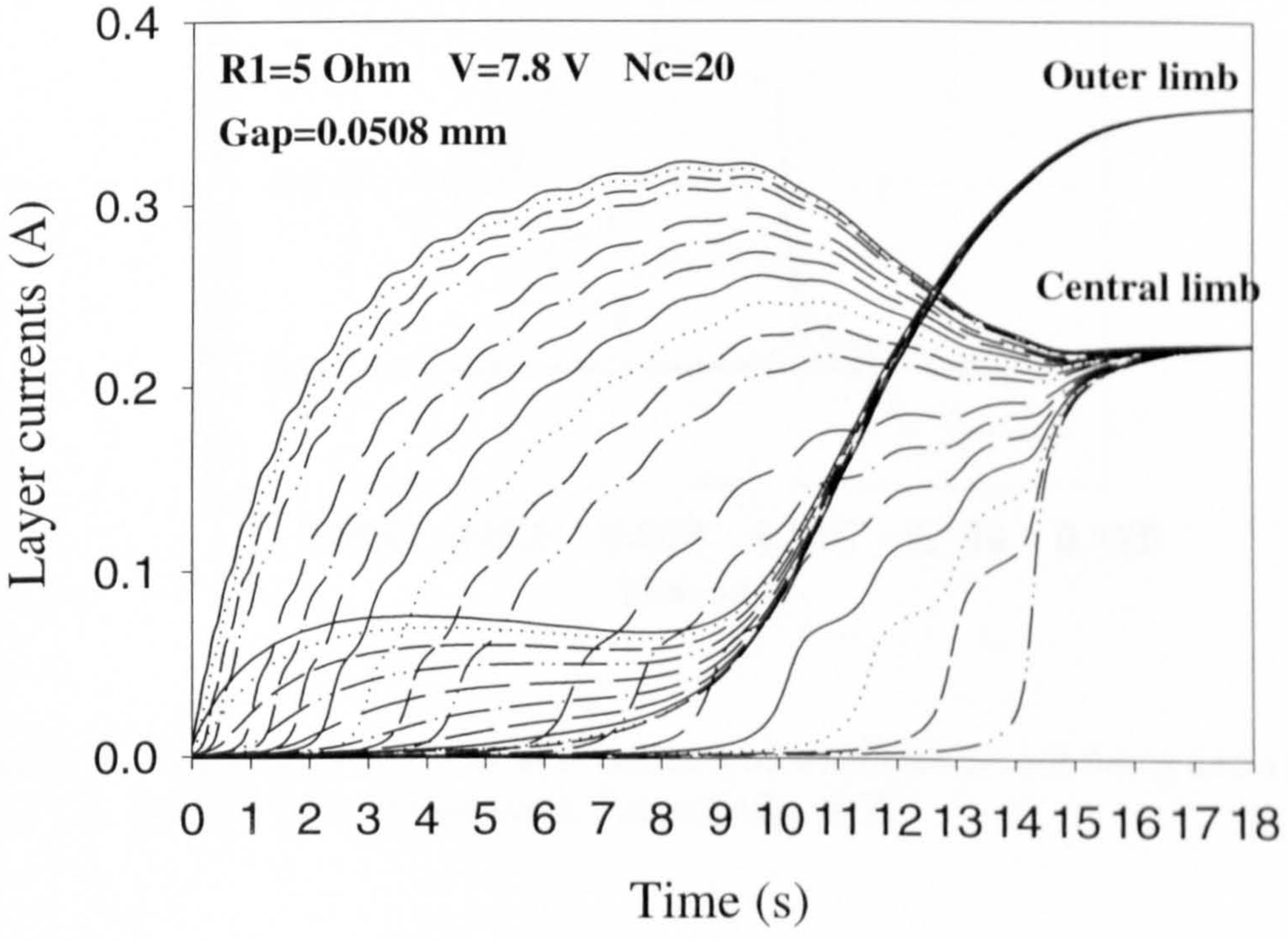

Figure 5.33: Layer currents in the central and outer limbs due to impact excitation. Network shown in 5.32

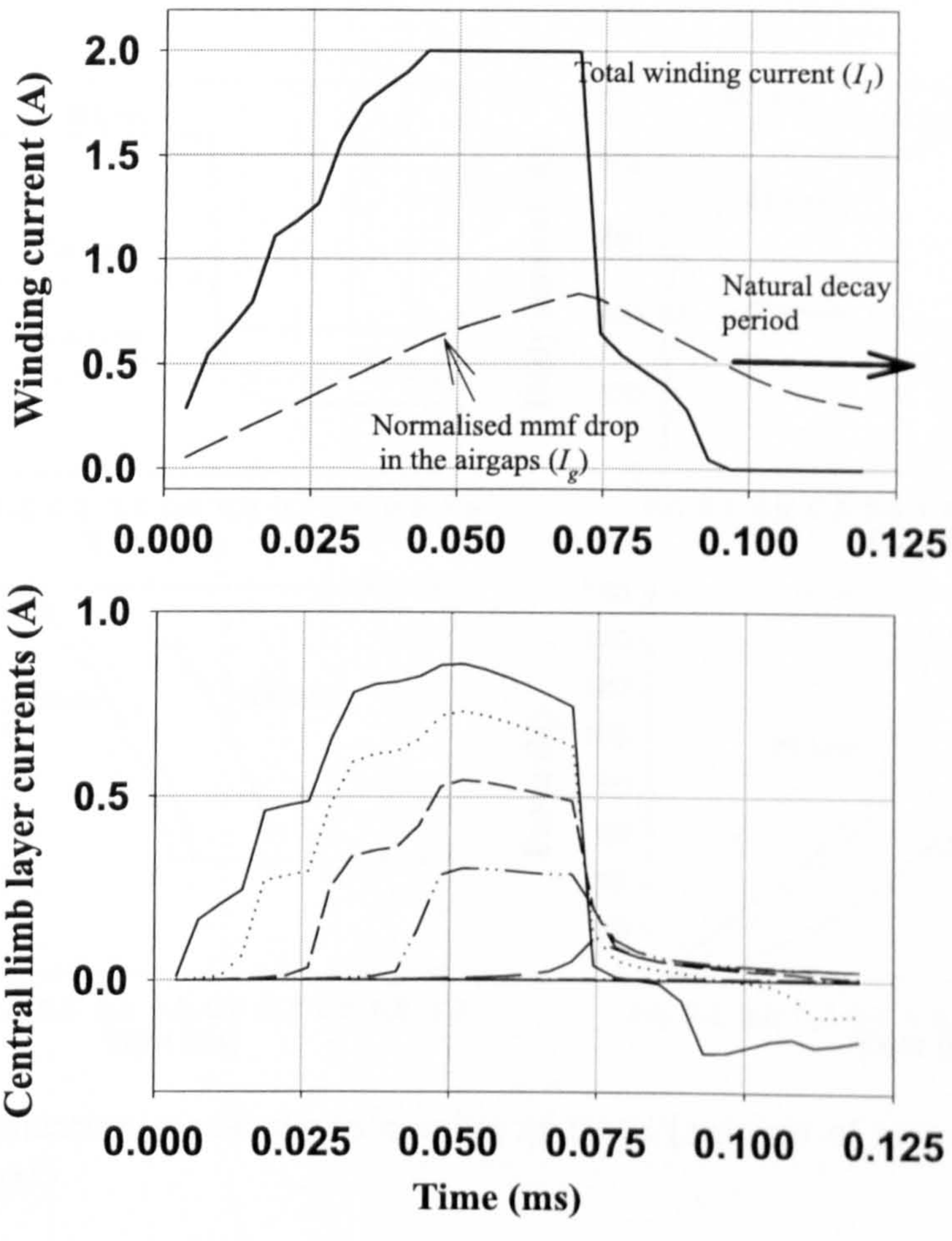

Figure 5.34: Winding current and layer currents obtained for $G = 0.3mm$ and a step voltage of $90V$ with the network shown in fig. 5.32

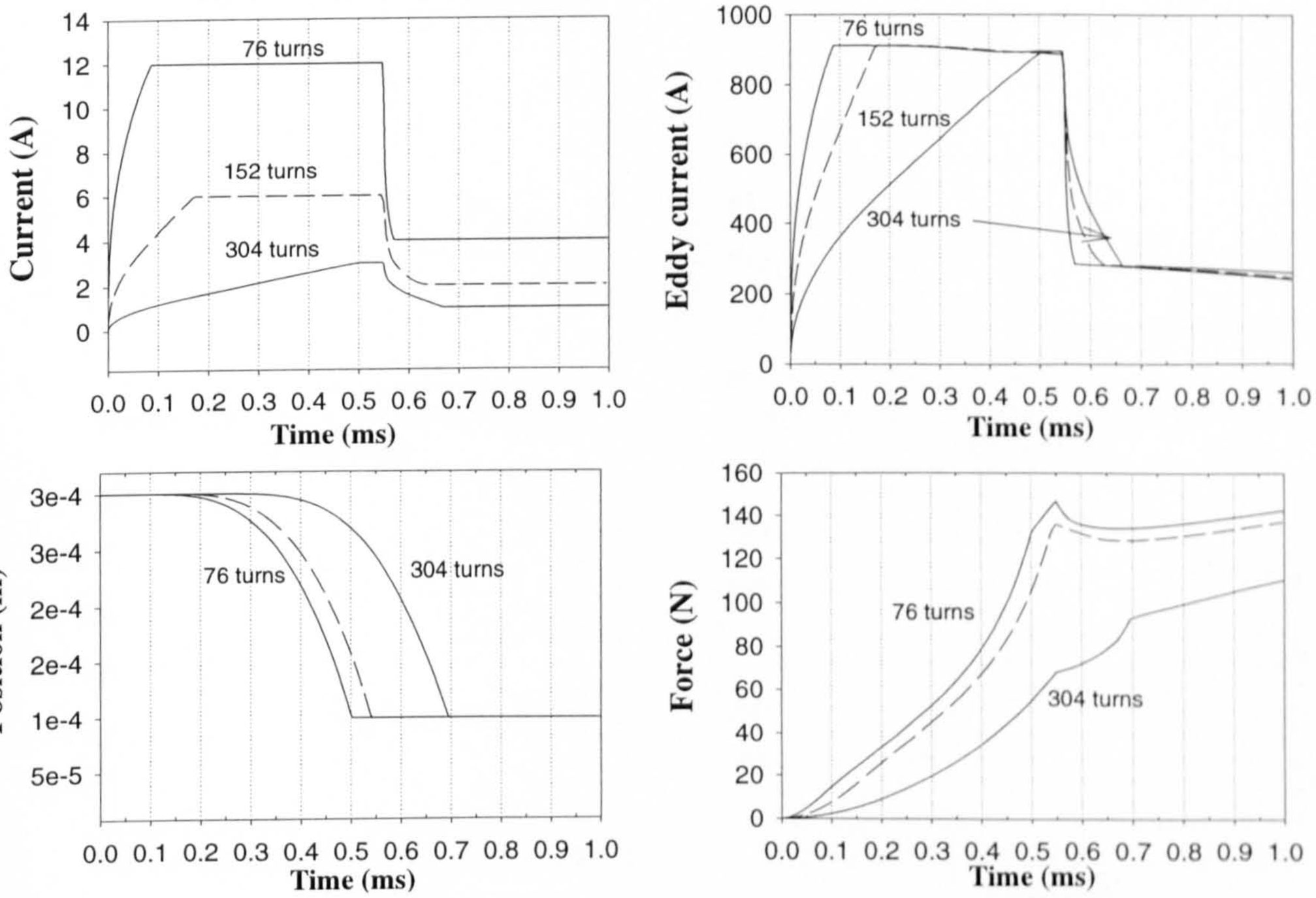

Figure 5.35: Simulation sensitivity to number of turns (amount of ampere-turns kept constant).

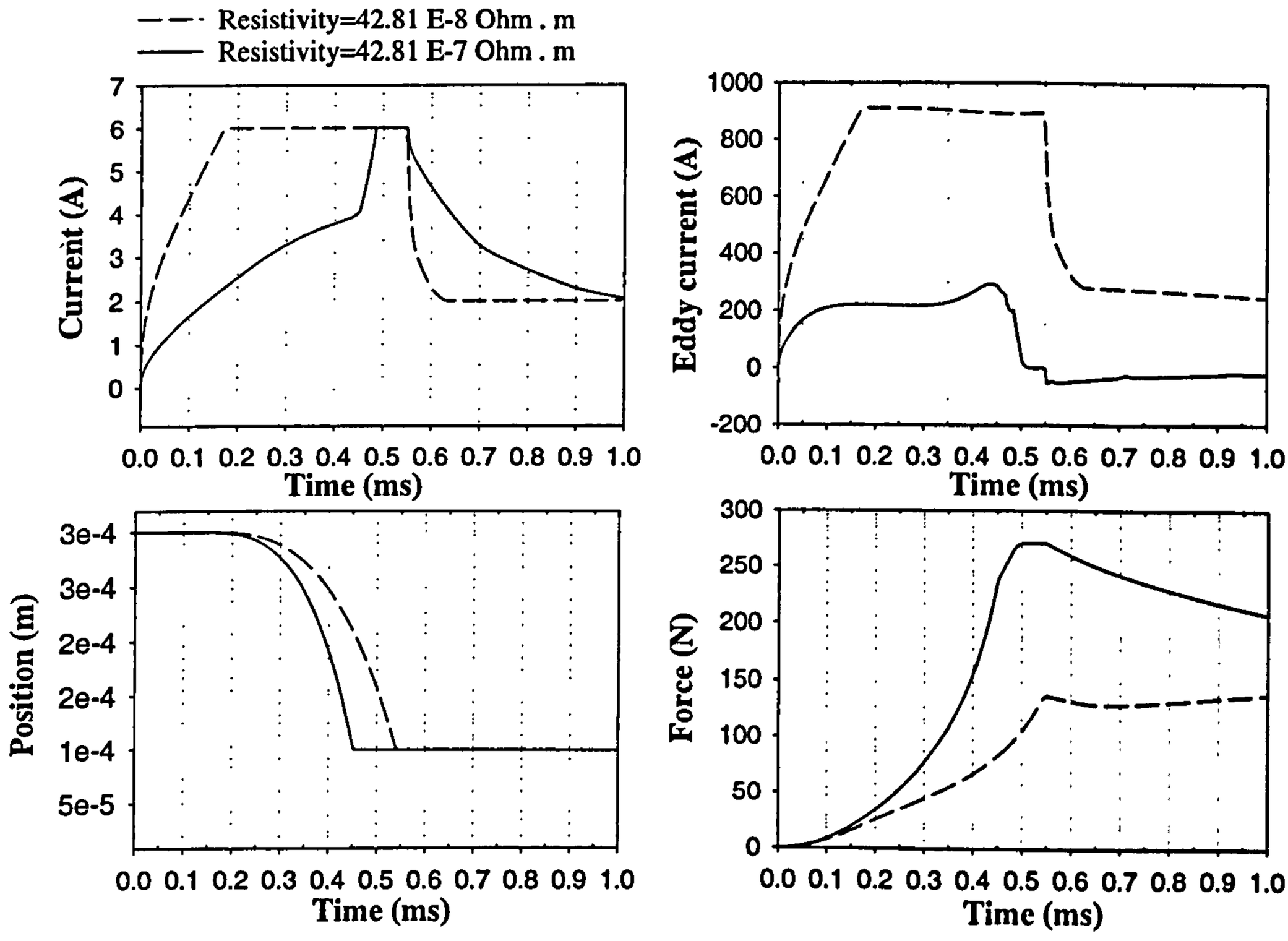

Figure 5.36: Simulation sensitivity to resistivity change.

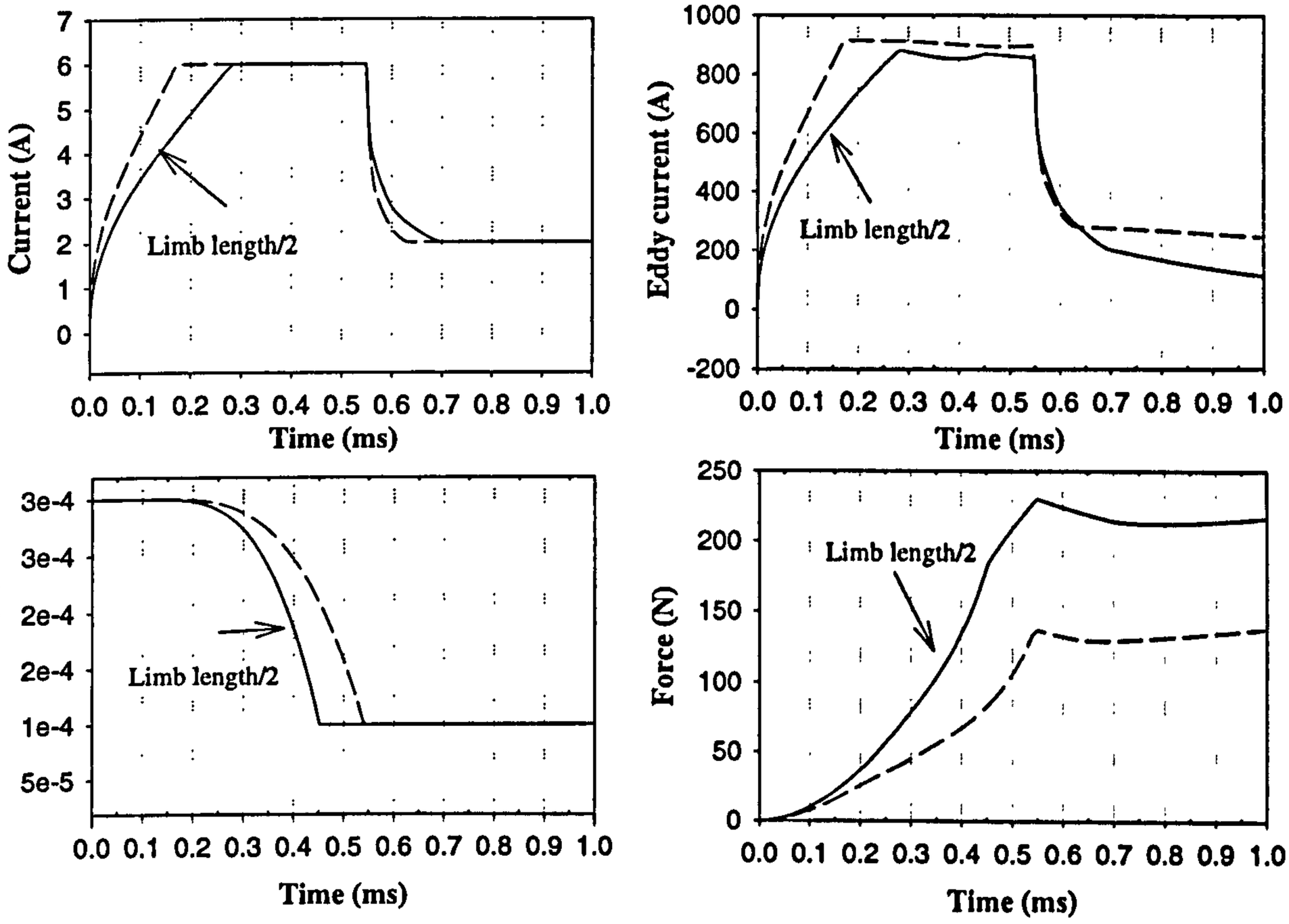

Figure 5.37: Simulation sensitivity to limb length. Dashed lines: $E = 14mm$, Solid lines: $E = 7mm$

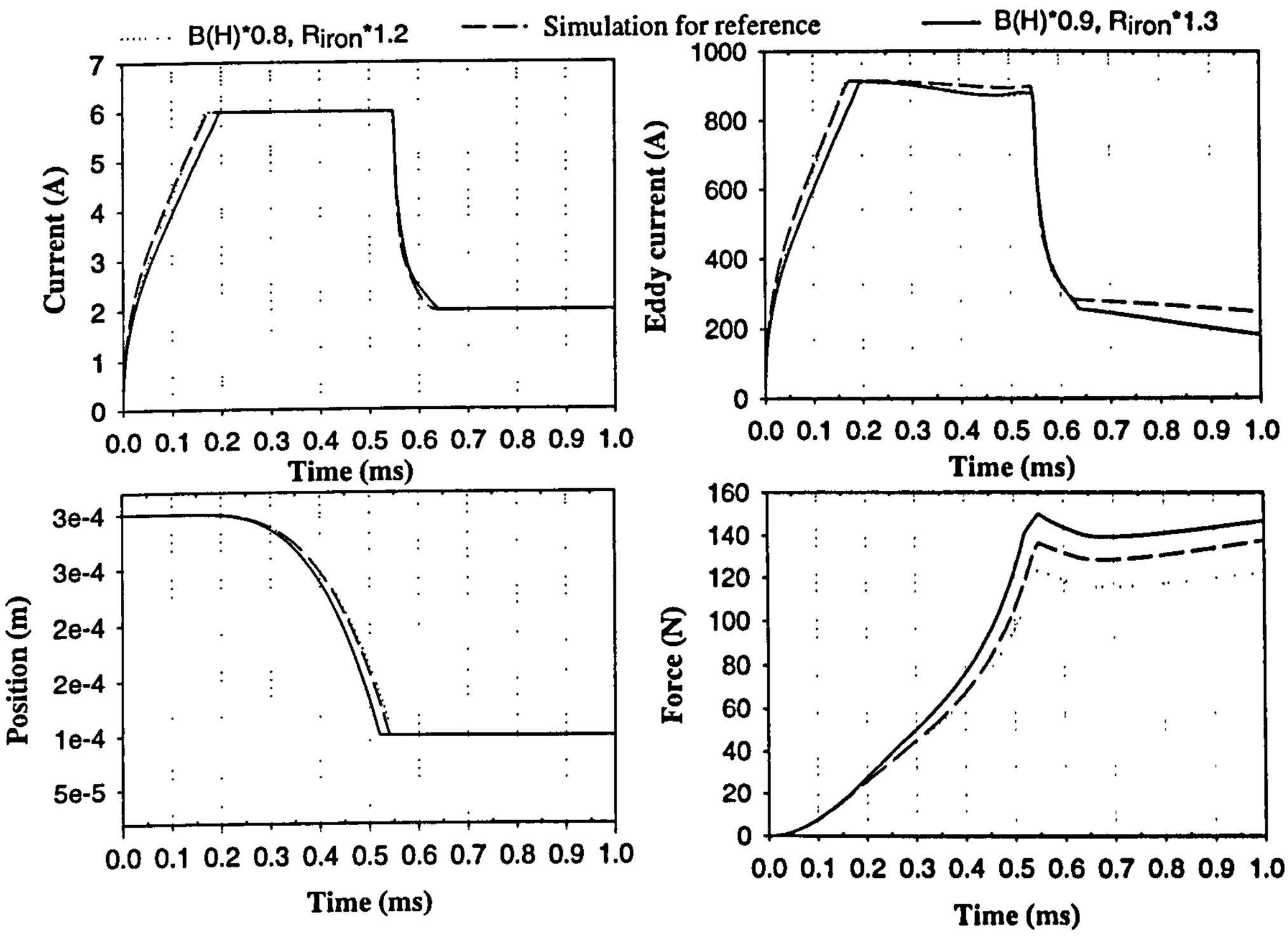

Figure 5.38: Simulation sensitivity to BH characteristic and resistivity.

5.5 Conclusions

A first-order model of the eddy currents generated in a solid iron bar have been developed from first principles and has lead to a so-called diffusion network. An electromagnetic equivalent circuit of the axisymmetric fast-acting solenoid was then obtained by assuming specific flux paths within the device leading to a first interpretation of the iron resistances and nonlinear inductances of the diffusion network. The transient and dynamic comparisons with measurements and finite-elements including the nonlinear characteristics of the solid iron and the armature movement (for dynamic only) show a very good agreement under impact excitation, constant current and free-wheeling operations. However the same network has not satisfactorily simulated the switch-off period due to the fixed closed flux path approximation. However it has also been shown that this previous assumption on the flux paths is not essential for defining a more appropriate electromagnetic equivalent network for the actuator. A different minimum circuit configuration has been proposed for dynamic analysis which removes all the physical contradictions of the first version.

Chapter 6

Rectangular Solenoid Actuators

6.1 Introduction

The dynamic model for the rectangular solenoid actuator has been developed using the same approach as for the axisymmetric case. This analysis is to some extend simpler as the eddy currents affect only one part of the device, the armature, which can not easily be built with laminated material. The amount of eddy currents generated in a E-core is comparatively less than for the pot-core actuator . However the transient delay in the force production is still significant as it can be observed in fig. 6.1 showing two 3D finite-element results computed with and without eddy current generation (90 V step voltage). The eddy currents produced within the laminated core are neglected in all following numerical or analytical simulations compared to those generated in the solid armature.

There is also some major differences with the axisymmetric problem. And it is shown that a major issue in the rectangular analysis is the approximation of the eddy current paths, significantly affected by the end-effects. Also the computation of the resulting network is based on a different approach requiring an iterative algorithm.

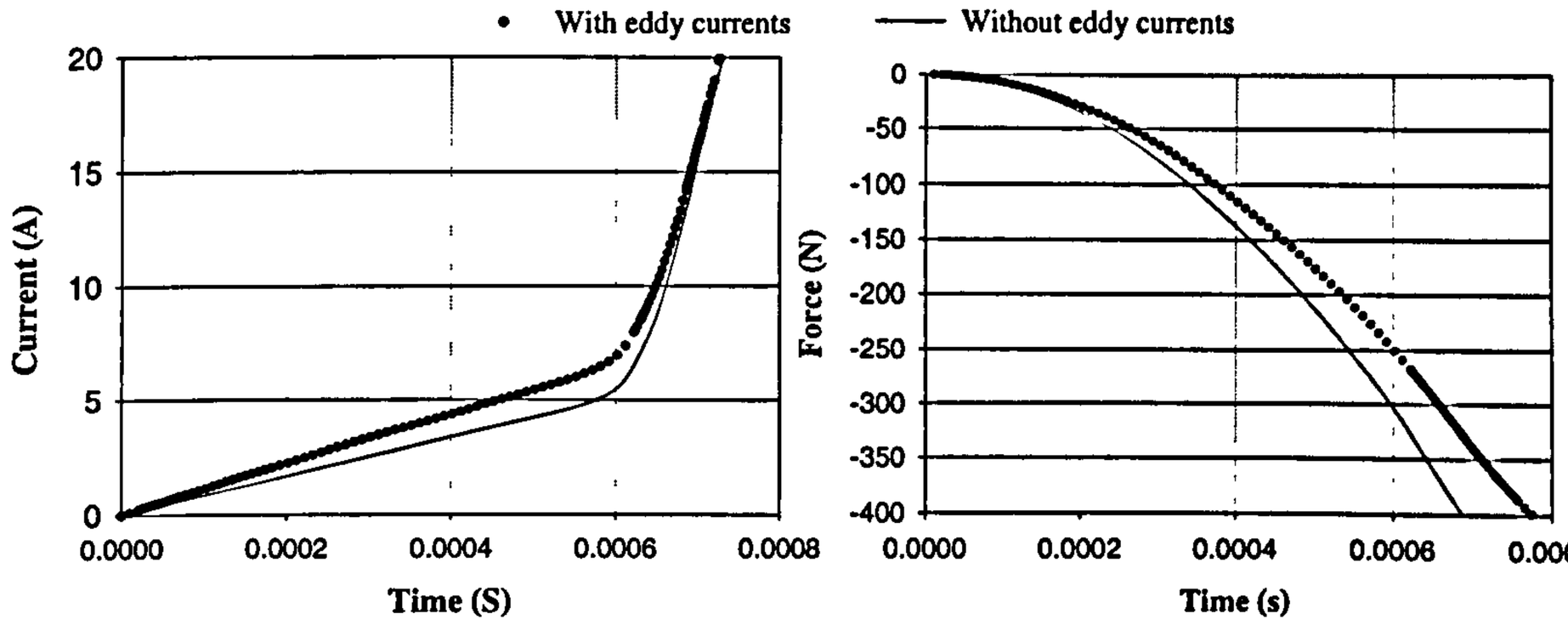

Figure 6.1: Finite-element results comparing the transient current and force waveforms due to a step voltage of $90V$, obtained with and without eddy current generation. $G = 0.3mm$

6.2 Electromagnetic Equivalent Circuit

The electromagnetic equivalent circuit proposed for the rectangular actuator is shown in fig. 6.2. The electromagnetic model of the core is unchanged from the magnetostatic analysis derived in chapter 2 and is obtained by transforming the magnetic equivalent circuit shown in fig. 2.24 into an electromagnetic equivalent [56]. However a factor 2 has been applied to all the circuit permeances as the magnetostatic model was only developed for half E-core. As some of the eddy current paths link both sides of the armature, it is preferable in this section to study the entire actuator.

The nonlinear inductances given in fig. 6.2 are a function of the permeance expressions developed in the magnetostatic analysis and correspond to the different subsections defined in the limbs and in the yoke. For example if P_{yt} is the total yoke permeance, then the corresponding inductance is equal to $N^2\,P_{yt}$. The linear inductances in series with the nonlinear components are the various slot leakage inductance elements obtained also from the corresponding permeance defined in fig. 2.24. The resistance R_1 is the winding resistance and the total airgap inductance L_G is computed as it follows:

$$L_G = 2\,N^2\,\frac{(P_{g1} + P_{fi1} + P_{fe1})(P_{g2} + P_{fi2} + P_{fe2})}{P_{g1} + P_{fi1} + P_{fe1} + P_{g2} + P_{fi2} + P_{fe2}}, \tag{6.1}$$

where

P_{g1} is the main airgap permeance for half of the central limb,

P_{fi1} is the inner fringing permeance half of the central limb,

P_{fe1} is the outer fringing permeance half of the central limb,

P_{g2} is the main airgap permeance of an outer limb,

P_{fi2} is the inner fringing permeance of an outer limb,

P_{fe2} is the outer fringing permeance of an outer limb.

In fig. 6.2, the dynamic model of the armature is based on designing an appropriate diffusion network. This configuration could be called 'minimum' as a combination of several diffusion networks is also a possible option for simulating separately the various flux and eddy current paths existing in the armature due to the end-effects. The assumptions associated with the development of this diffusion network are covered in the following section. The total airgap inductance is directly connected in parallel with the armature model such that the main airgap flux as well as the total fringing flux are arbitrarily assumed to flow at any time through the entire armature. This is an approximation which will be also discussed in a following section.

The computation of this dynamic network is not as straightforward as it was for the dynamic analysis of the pot-core device. And to some extend it is similar to the technique applied to evaluate the dynamic performance of a switched reluctance motor. However the magnetisation curves cannot in this context be computed in advance due to transient variations depending on the driving conditions applied to the device. In other words, an iterative approach is required for the electromagnetic model of the rectangular actuator presented in fig. 6.2.

Indeed the generation of eddy currents within the armature dissociates completely the magnetostatic link between current required and flux produced by the armature. It follows that more current (than flux) is actually consumed by the armature during the transient evolution. This excess of current is 'seen' by the core as a higher mmf drop required by the armature, which then leads to a higher production of slot leakage flux.

In practice the transient algorithm (i.e. at fixed gap) is divided into three steps summarised in fig. 6.3. The dynamic algorithm is obtained by also involving the mechanical equation simulating the armature movement.

Step 1. The first step consists in computing the general electric equation of the actuator winding and retrieving from it the actual flux linkage ψ_t available for the solenoid. The winding current at time $t = 0$ is usually set equal to zero. An iterative process then starts in order to evaluate which amount of flux ϕ_G in the main airgap and fringing paths would lead to this actual flux linkage ψ_t.

Step 2. Indeed, by making a guess of the airgap flux, ϕ_G^I, from which can be derived V_G, it is possible to evaluate the current I_{Ga} required for generating the flux within the airgaps and in the armature but also consumed by the eddy currents. These last parameters I_{Ga} and ϕ_G^I are the input parameters for the magnetic equivalent circuit of the solenoid core which can now be computed.

Step 3. By introducing these values within the magnetic model of the core, the total flux linkage ψ^I and total current I_1 required by the E-core for this given airgap flux I_{Ga} can be evaluated. The iterative process between step 2 and 3 stops when the actual flux linkage ψ_t and the predicted one ψ^I satisfy the convergence criterion.

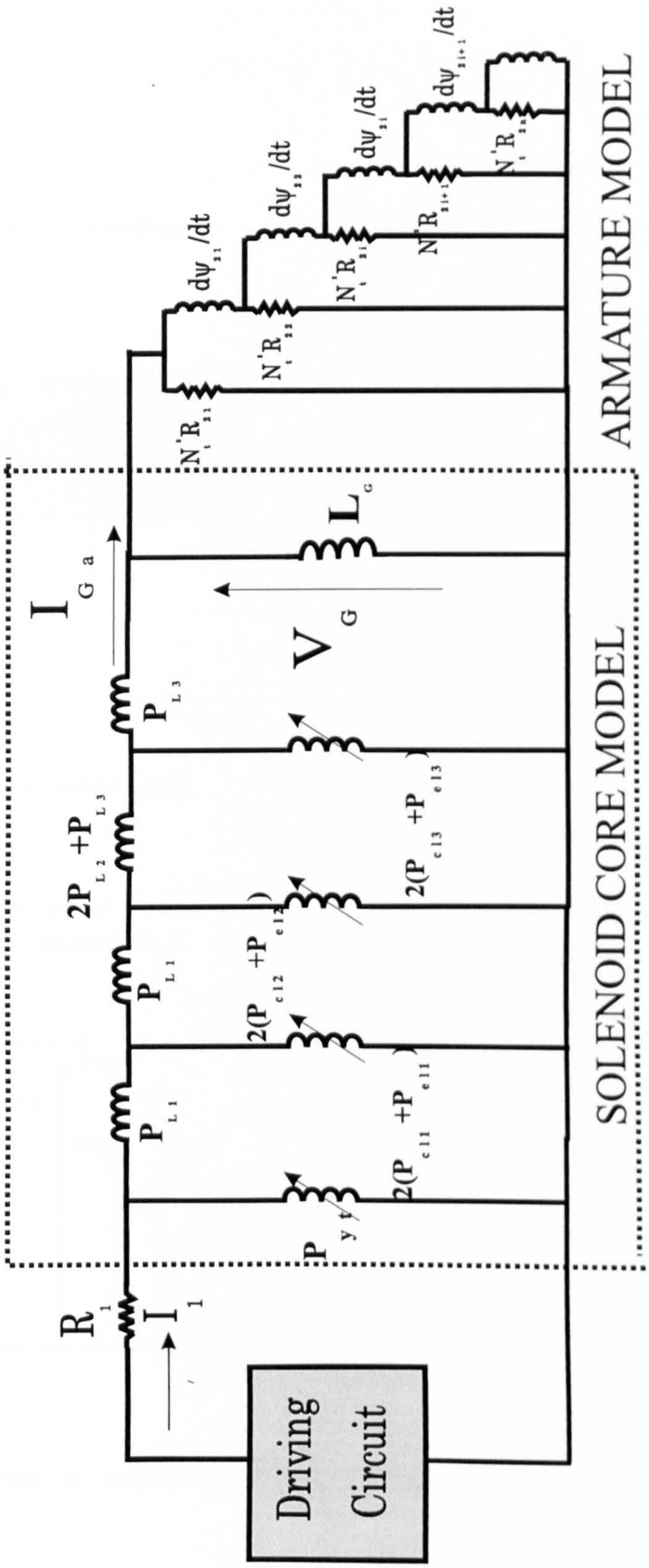

Figure 6.2: Electromagnetic equivalent circuit for a rectangular solenoid actuator

STEP 1...

Electric equation of the winding

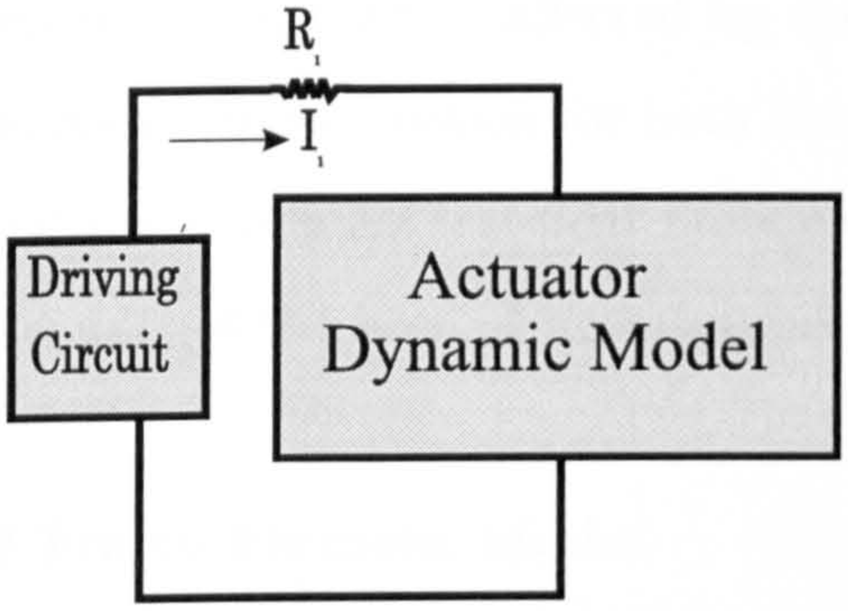

$$V = R_i I_i + \frac{d\psi_t}{dt} \longrightarrow \psi_t$$

Total flux linkage computation

STEP 2...

Electric equivalent circuit of the armature + airgaps (L_G)

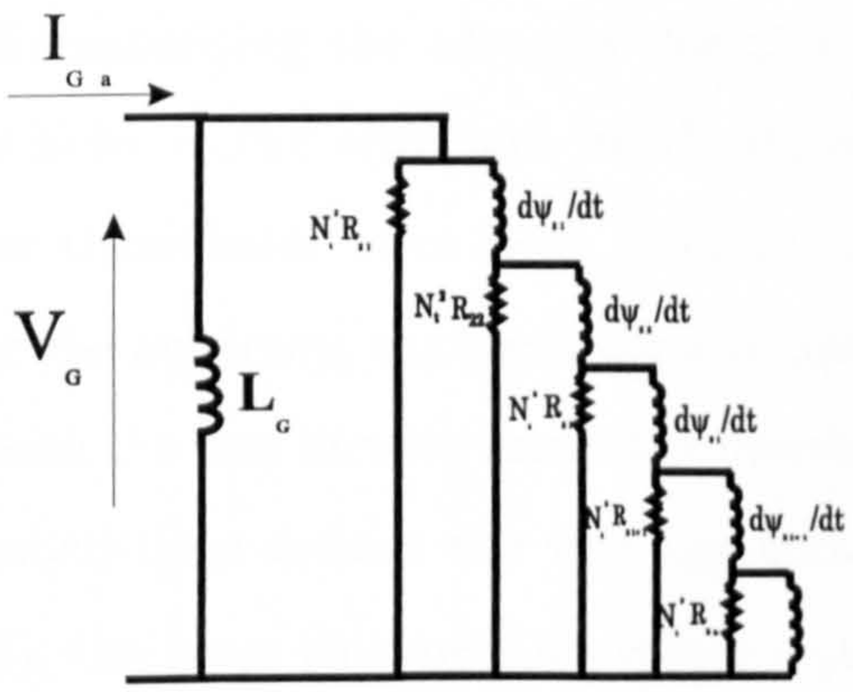

STEP 3...

Magnetic equivalent circuit of the half core

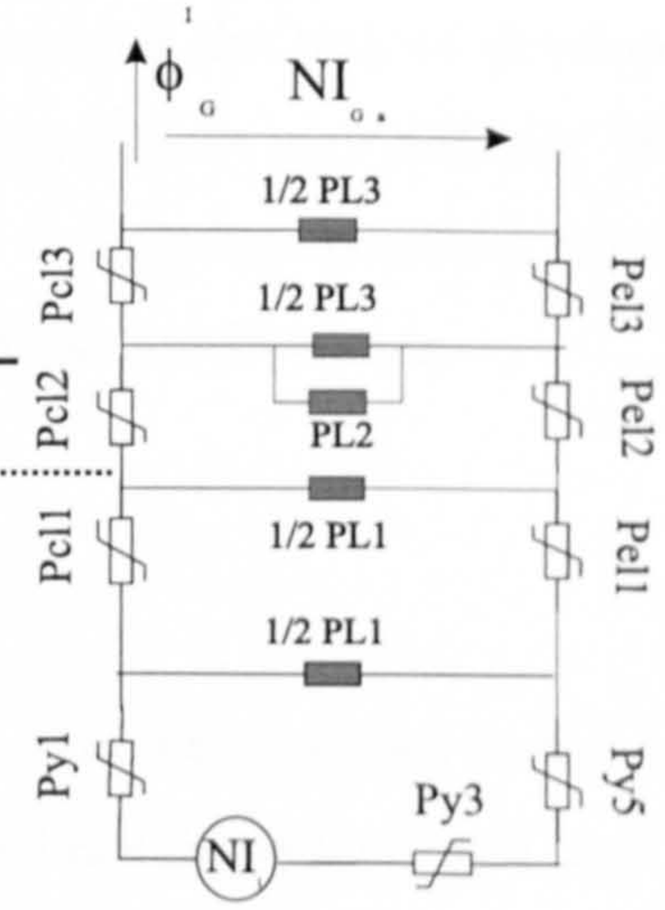

Iteration until ...

$$2\psi^{i} = \psi_t$$

...by changing $\psi_G{}^{i}$

$$\psi_G{}^{i} \longrightarrow V_G = 2\frac{\psi^{i}_{G,t+1} - \psi_{G,t}}{\Delta t}$$

$$\phi_G^{i} = \psi_G{}^{i}/N$$

Figure 6.3: Algorithm for computing the transient performance of rectangular devices

6.3 Armature Model

6.3.1 Transient Eddy Current and Flux Density Distribution

Actual designs of E-core actuators (fig. 1.4) are characterised by a relatively short stack length ($Lstk < 0.8\,A$). Therefore the transient electromagnetic behaviour of such devices is significantly affected by the end-effects, making the task of developing an analytical approximation for both flux and eddy current paths very difficult. However the support of a 3D transient finite-element analysis is nowadays possible, reducing to some extend the level of uncertainties in such analytical developments.

3D Finite Element Model

A 3D transient numerical analysis of the large E-core actuator shown in fig. 1.4 and whose characteristics are summarised in table 4.3 has been carried out by Lucas Varity using the 3D finite-element software MEGA [40] . Two slices of the 3D mesh developed for the transient analysis are given in fig. 6.4 and 6.5. A double symmetry reduces the numerical analysis to only a fourth of the total device volume. The 3D mesh was built around a constant pattern in the XY-plane (fig. 6.5), a function of the geometrical features characterising the actuator design under analysis. The original design included circular holes in the armature which explains the peculiar mesh element composition. However these holes have been filled in with steel for the purpose of this work. To increase the accuracy, the mesh density has been doubled on the contours of the armature where the flux density and eddy currents start their diffusion within the armature. The dashed lines defines the winding area around the central limb. In the ZY-plane (fig. 6.4), the layer thickness decreases significantly around the working airgap region.

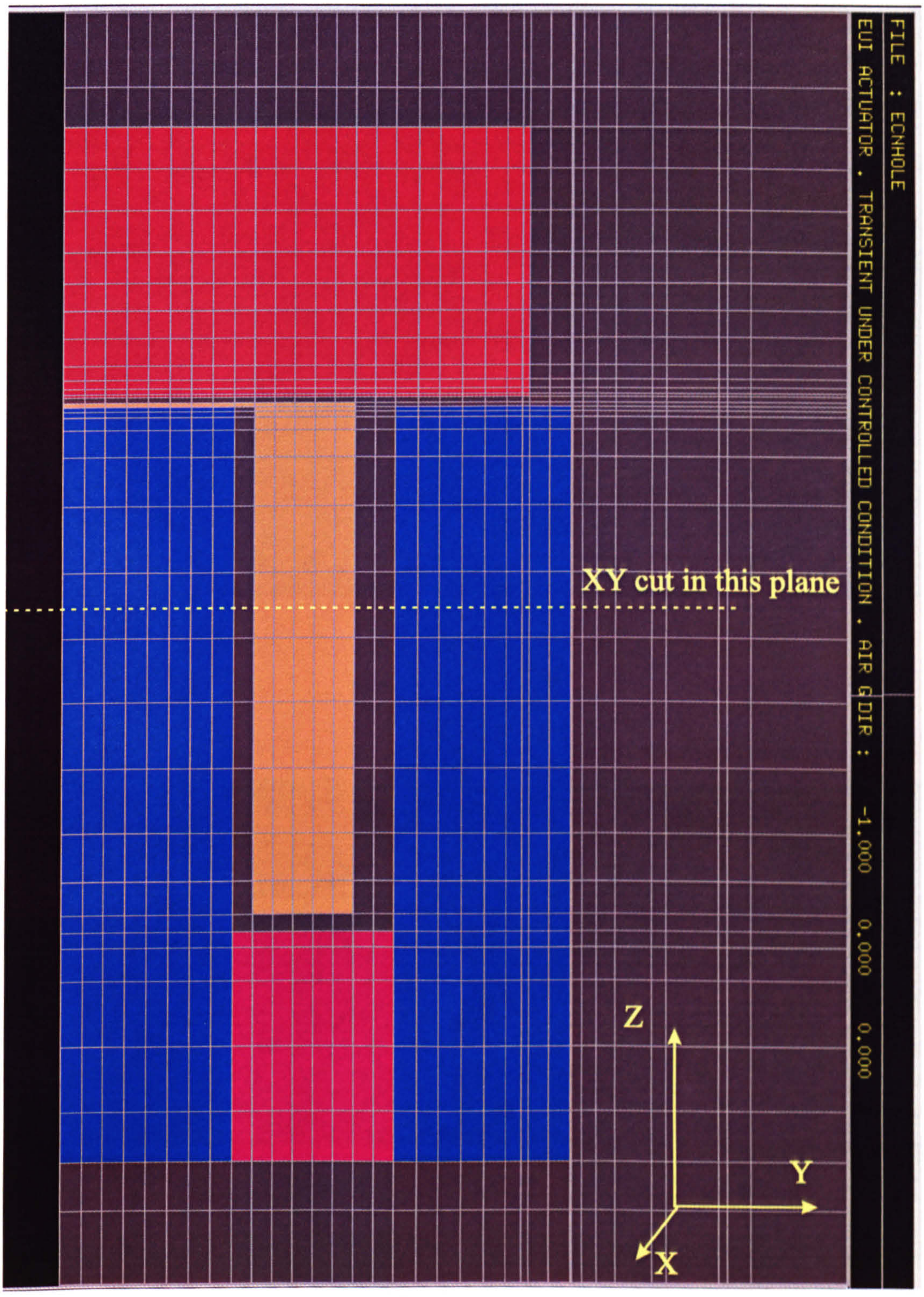

Figure 6.4: 3D finite-element mesh of an E-core actuator: cut at $X = Constant$.

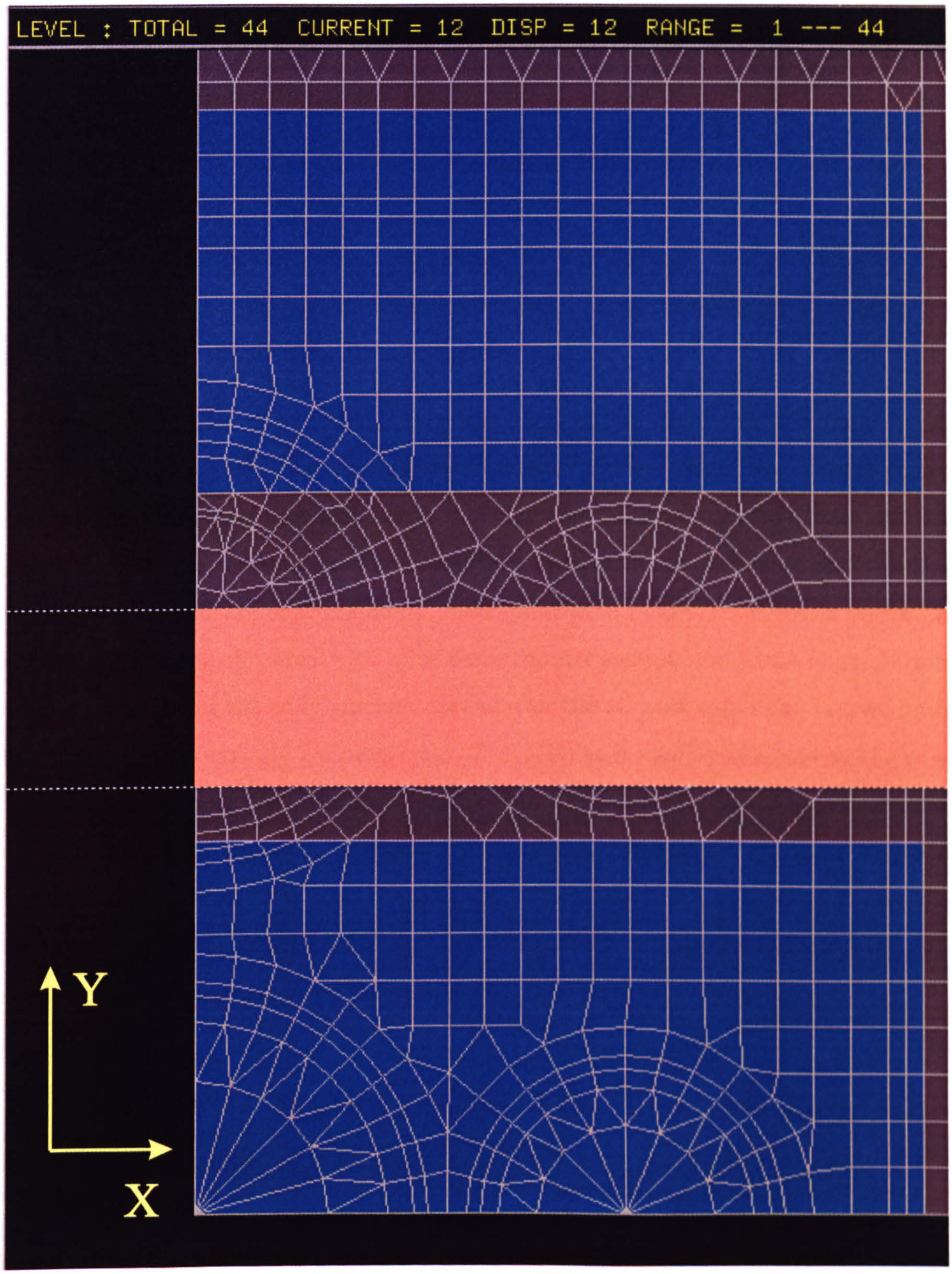

Figure 6.5: 3D finite-element mesh of an E-core actuator: cut at $Z = Constant$.

Postprocessing results

Some results of the transient 3D finite-element analysis, obtained by simulating a step voltage of 90V, are discussed in this section. The variables considered are the flux and eddy current densities. The gap was fixed at 0.3mm.

Figure 6.6 shows the flux density distribution at 50 and 200 μs after switching on. As expected the flux density distribution mainly occurs at the interface between the working airgap and the armature. At 200 μs the flux diffusion is also visible on the lateral sides of the armature due to the end-effects (outer fringing flux). Figure 6.7 captures nicely these both flux diffusion phenomena.

During this transient period the armature sections, in which the flux density has already diffused, are also characterised by high eddy current densities. This is shown in fig. 6.8 corresponding to a layer close to the airgap (at $Z = Cst$) for t =50 and 200 μs. These induced currents flow in eddies and in opposite direction to the winding current. Their paths are approximately rectangular with however a variable width i.e. very large above the slot area with a lot more thinner section above the central limb. With time increasing the eddy currents spread over the all area above the central limb. Their paths are not strictly 2 dimensional ($Z = Cst$) as it can be observed at the edge of the armature slide in fig. 6.9. The length of the arrows in this figure is proportional to the local eddy current density which varies in time. After analysing several cuts at different instants it has been observed that the eddy currents follow a relatively similar pattern in each layer defined at $Z = Cst$, from which a simplified electromagnetic model of the armature has been derived.

6.3.2 Analytical Approximation of the Flux and Eddy Current Paths

Similarly to the axisymmetric problem, the E-core armature has been divided into layers, simulating the propagation of flux and eddy currents within the armature. Figure 6.10 schematises the approximated flux and eddy current paths computed for

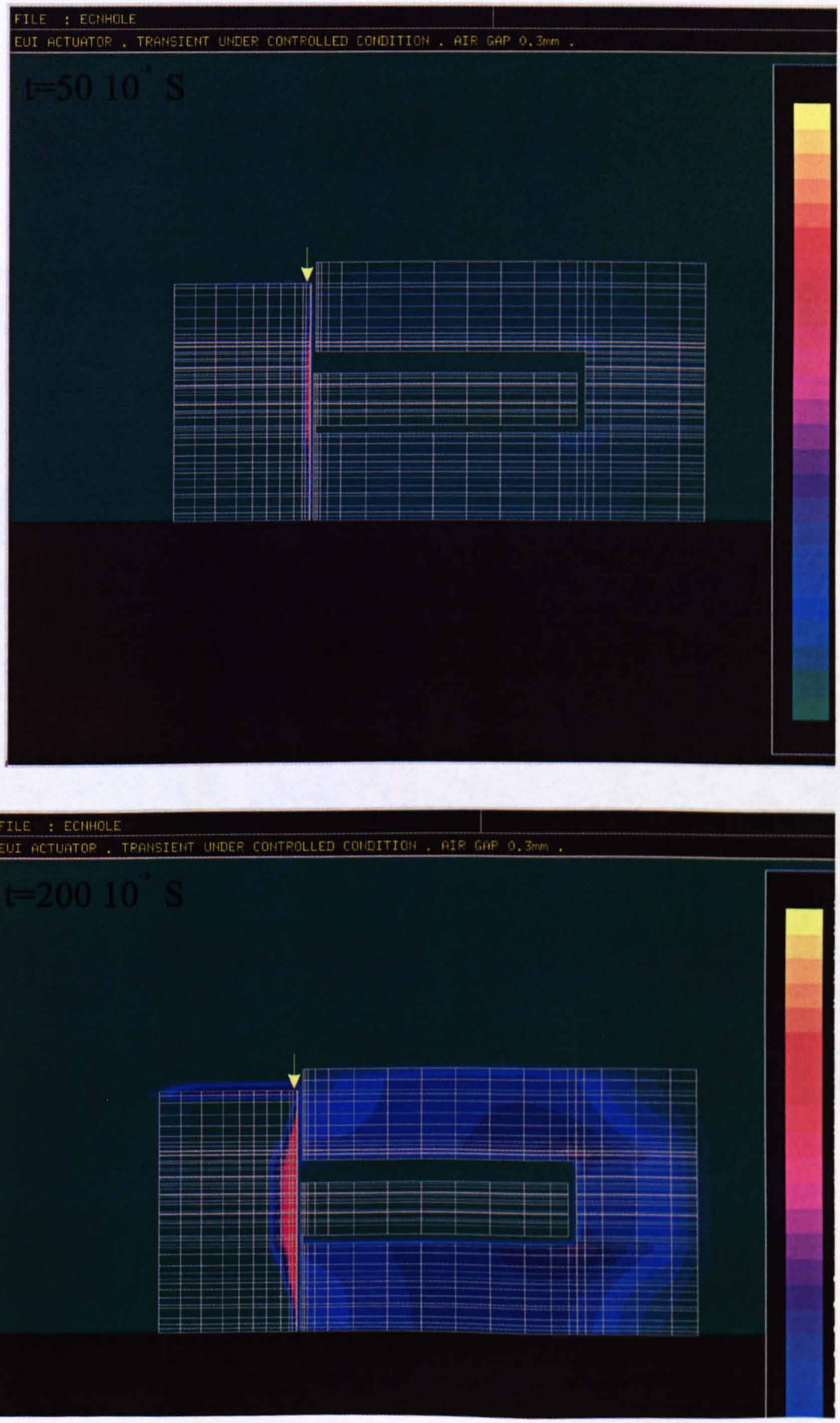

Figure 6.6: Transient flux density in a E-core design at $50\mu s$ and $200\mu s$ due to a step voltage of 90V.

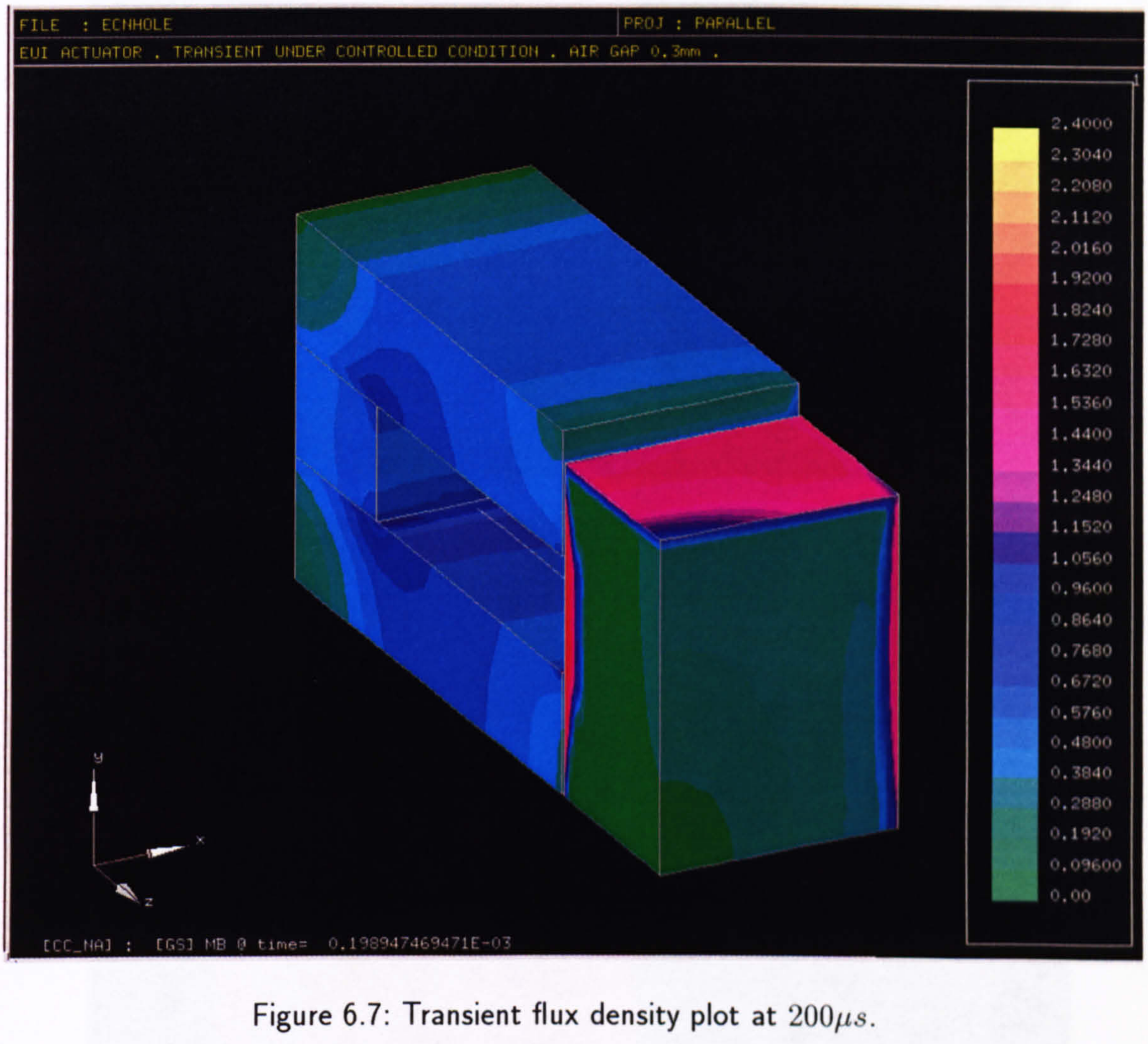

Figure 6.7: Transient flux density plot at $200\mu s$.

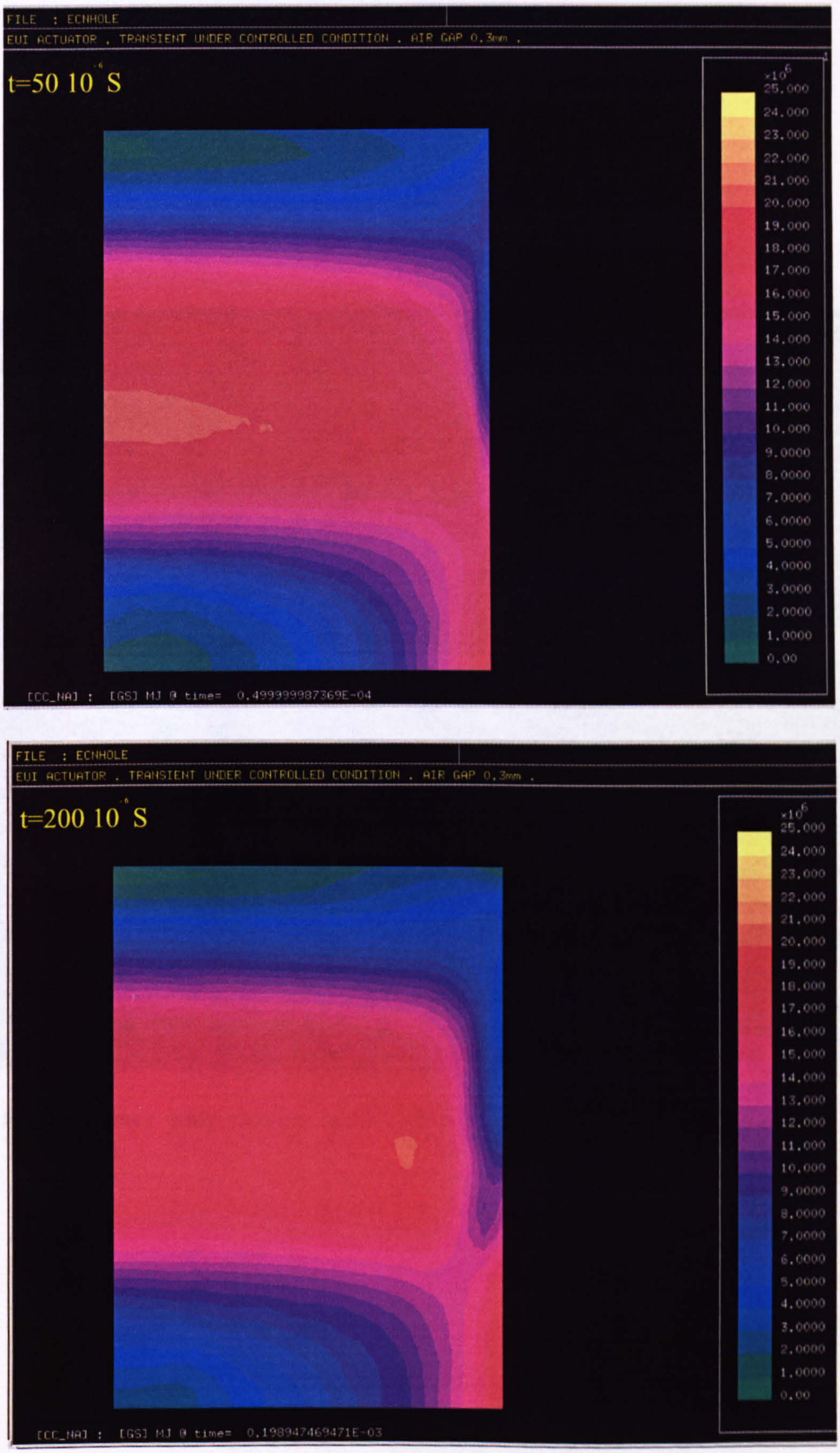

Figure 6.8: Transient eddy current density plot at $50\mu s$ and $200\mu s$ in the armature. Cut at $Z = Cst$. See yellow arrows in fig. 6.6

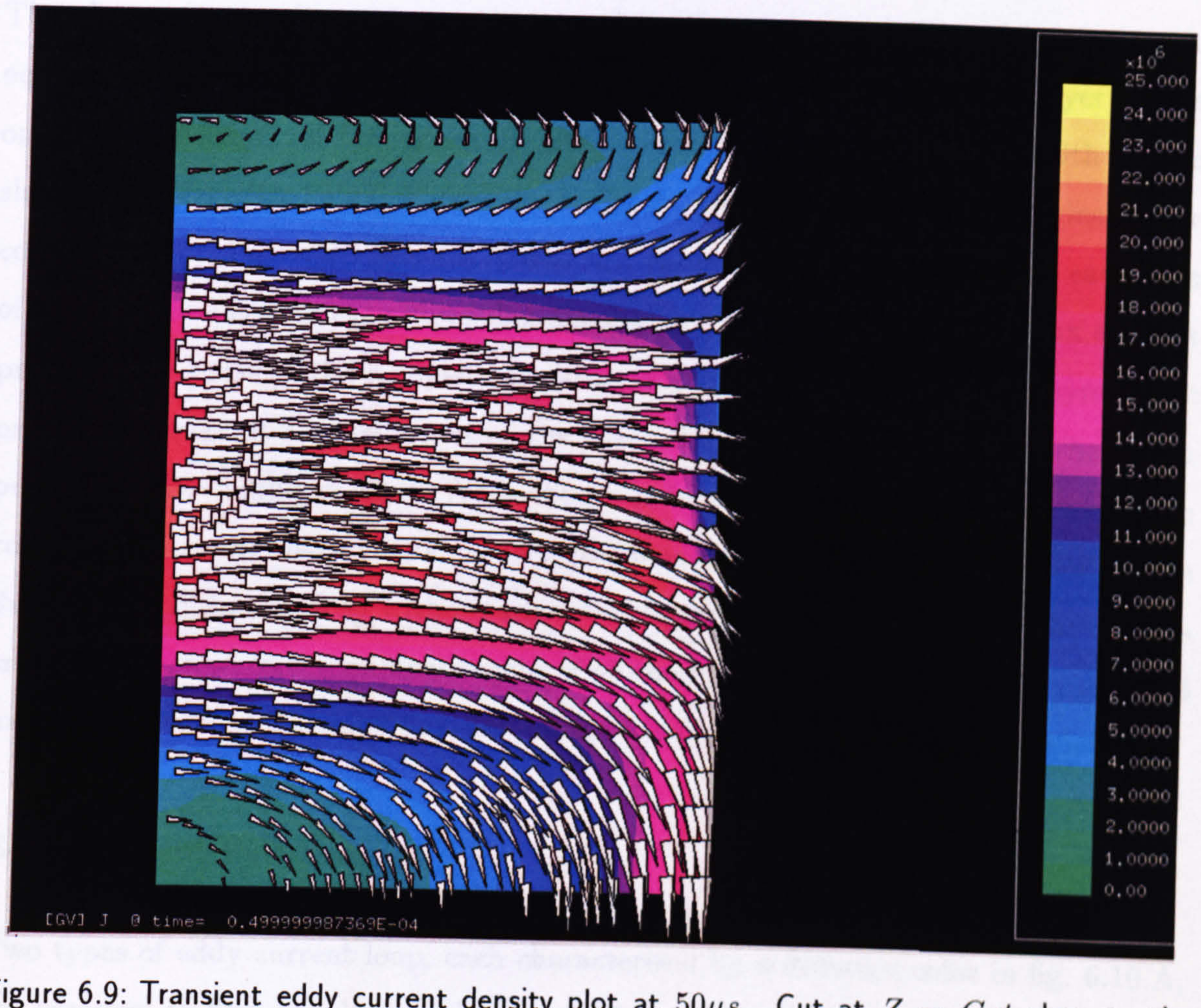

Figure 6.9: Transient eddy current density plot at $50\mu s$. Cut at $Z = Cst$ close to the airgap

these layers in the analytical model. The end-effects make particularly difficult the development of a relatively simple model. For this reason they have only been partly accounted for in the iron resistance computation but not in the flux path evaluation, leading then to some physical inconsistencies.

Flux Paths

The chosen flux paths, corresponding to the different layers in the electromagnetic equivalent circuit of the armature, are shown in fig. 6.10.(B). The first layer covers only a small height of the armature and is essentially limited to the width of the slots. The developed model respects obviously the symmetry of the device under consideration. Therefore the flux paths are assumed to be the same on each side of the E-core. The following flux tubes (layers) are defined such that the flux spreads progressively through the complete armature volume. Similarly to the axisymmetric problem, a quadratic distribution of the layer thickness (Th_j for layer j) has been preferred. The number of layers Nc is chosen as being the minimum one for which the computation results become steady (see previous chapter). The computation of the flux density and mmf drop within each tube requires the computation of the various cross-sections and corresponding lengths of all the flux tube sections. In this simplified model the lateral diffusion of flux due to end-effects has been arbitrarily neglected.

Eddy Current Paths

Two types of eddy current loop, each characterised by a different color in fig. 6.10.A, are assumed to flow simultaneously in each flux layer. It is obvious from fig. 6.10.B that the first flux layers should not contain any iron resistance from the blue sections shown in fig. 6.10.A. However due to the level of complexity and also the fact that the central iron section is generating most of the eddy currents, this approximation is acceptable. The arrows, shown in each coloured section, approximate the eddy current paths within each of them. The inner solid or dashed lines within each section, are a geometric support for breaking down the sections into eddy current paths in order to

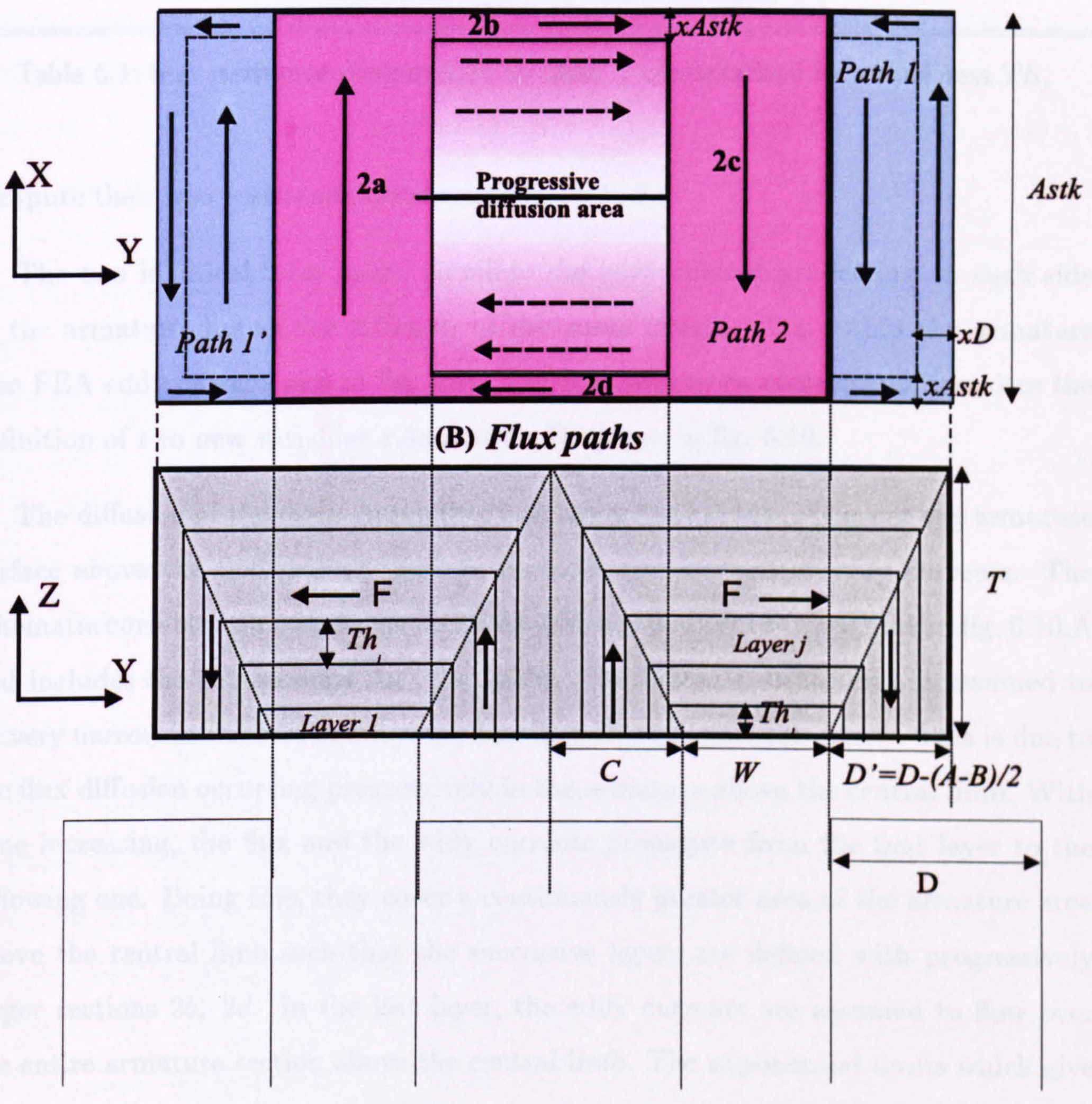

Figure 6.10: Analytical approximation of the flux and eddy current paths within the rectangular armature.

Eddy Current Paths (fig. 6.10)	for layer J
Paths 1+1'	$R_{2j} = 0.5\ \rho(\frac{Astk - 2\ xAxtk}{Th_j\ (D' - xD)} + 2\ \frac{D'}{Th_j\ xAstk} + \frac{Astk}{Th_j\ xD})$
Path 2	$R_{2j} = 2\ \rho \frac{Astk - 2\ xAxtk}{Th_j\ W} + 2\ \rho \frac{2\ C + W}{Th_j\ (xAstk + (\frac{Astk}{2} - xAstk)\frac{e\sqrt{j}}{e\sqrt{Nc}})}$

Table 6.1: Iron resistance computation for layer J characterised by a thickness Th_j

compute their iron resistance summarised in table 6.1.

The two identical 'blue loops' simulate the eddy current generating on each side of the armature due to the diffusion of the outer fringing flux within the armature (see FEA eddy current plot in fig. 6.9). The iron resistance computation requires the definition of two new variables $xAstk$ and xD, shown in fig. 6.10.

The diffusion of the main airgap flux into the armature takes place at the armature surface above the slot area and generates the major amount of eddy currents. The schematic current path associated with this diffusion is shown in dark pink in fig. 6.10.A and includes the sub-sections $2a$, ,$2b$, $2c$ $2d$. The subsections $2b$, $2d$ are assumed to be very narrow in the first flux layer, a function of the parameter $xAstk$. This is due to the flux diffusion occurring progressively in the armature above the central limb. With time increasing, the flux and the eddy currents propagate from the first layer to the following one. Doing this, they cover a continuously greater area of the armature area above the central limb such that the successive layers are defined with progressively larger sections $2b$, $2d$. In the last layer, the eddy currents are assumed to flow over the entire armature section above the central limb. The exponential terms which give the width variation of $2b$, $2d$ with layer are given in table 6.1 and involve a degree of empiricism. The total iron resistance per layer j is equal to the iron resistance of the three eddy current paths connected in parallel.

6.4 Parameter Evaluation and Underlying Assumptions

Based on the previous developments the transient (and dynamic) performance of the E-core can in theory be computed by following the algorithm presented in section 6.2. However the computation of the iron resistance for each layer of the new electromagnetic model of the armature has involved the definition of two unknown variables $xAstk$ and xD. In practice these variables should be evaluated as being equal to a certain percentage of the armature stack length $Astk$ and of the armature overlap D' with the outer limbs respectively, such that their value changes accordingly with the E-core armature dimension being considered. For simplification, it is also assumed that the ratios $xAstk/Astk$ and xD/D' will be equal. This assumption is sensible considering the task difficulty and also the fact that the eddy current resistance is mainly determined by the eddy current paths in the central part of the armature, a function of $xAstk$ only. However the importance of setting a value to these parameter ratios should not be underestimated as it does modify significantly the order of magnitude of the layer iron resistances (especially the first ones) and also the resistance range covered between the first and the last layer. Therefore the attributed value will also determine the amount of iron loss generated in the armature.

This current issue is certainly a major difference with the axisymmetric problem in which the eddy current paths were clearly defined; and this difficulty results simply from the 3D nature of the E-core actuator. The practicality of solving analytically the rectangular problem will then depend on how these parameters can easily and accurately be defined and also on the fact that the series of assumptions underlying this technique are reasonably applicable. These assumptions are:

1. The eddy current paths do not vary with the airgap length.

2. The eddy current paths are independent of the driving conditions as preconised by Silvester [53].

3. The eddy current paths and therefore the iron resistance can be simply scaled

with the E-core dimensions involved in their computation.

A first attempt to evaluate these parameters involved fitting a transient finite-element solution with the analytical prediction. The available results included the current and force waveforms due to a step voltage of 90V with an airgap of 0.3 mm. It occurred that by tuning the parameters $xAstk$ and xD, it was impossible to obtain a satisfactory agreement for both traces simultaneously: a proper response for the current induced a too fast force response and a proper response for the force induced a too high winding current due to too much iron losses[1].

This major difficulty was not due to the armature model but to other assumptions made in the electromagnetic equivalent network of the E-core. Indeed after studying more closely the finite element results, it appears that the inner fringing does play a important role in the transient process by acting rather more as a leakage component. In steady-state conditions, the inner fringing flux has a minor action. However in this transient process, the armature volume above the coil is literally saturated of flux and eddy currents such that a significant portion of flux crosses the airgap region above the slot without linking the armature, producing no useful force. This transient phenomenon is shown in fig. 6.11 gathering the airgap flux density (module) distribution at three different heights. In the airgap layer close to the limbs a concentration of flux density appears on each side of the slot. This amount of flux is not flowing in direction of the armature; otherwise a peak of intensity would have also appeared in the other waveforms or at least the flux density should have been in average higher in the two other distributions under each limb . Therefore this peak of flux density crosses the slot following a path at some stage parallel to the armature.

To take approximately this phenomenon into account within the analytical model, the inner fringing permeances included in the computation of L_G in eq. 6.1 were removed and put instead, in parallel with the slot leakage permeance P_{L3} shown in fig. 6.2. In this way, the flux dragged by the inner fringing permeances does not link any more the armature. Although the force computation before the circuit modification did not

[1]The force in the E-core problem is computed by following the same approach as for the pot-core: at any time increment, the total flux flowing through the main gaps is evaluated from the electromagnetic model and eq. 5.29 is applied.

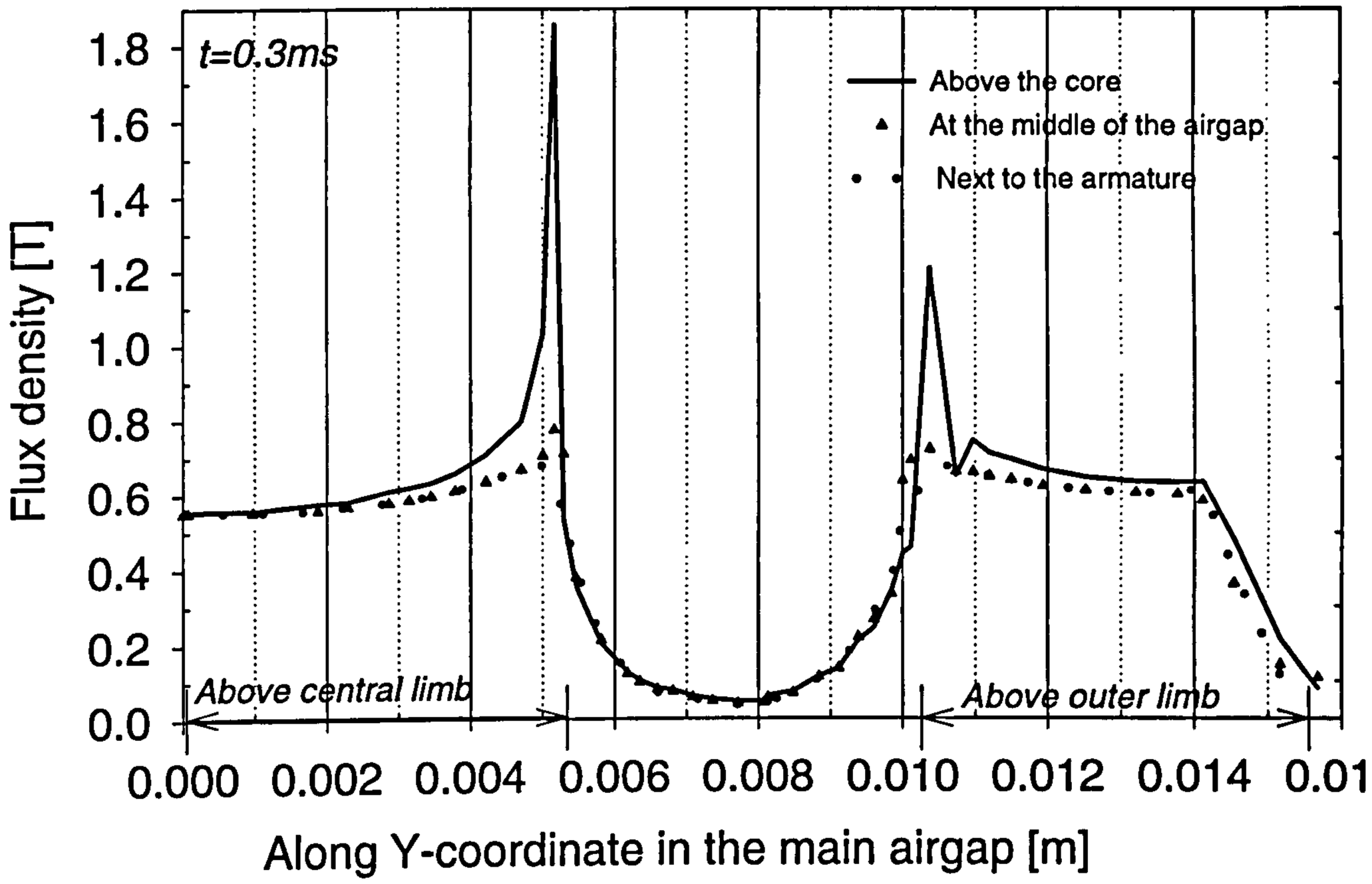

Figure 6.11: Flux density distribution in the airgap at three height levels.

involve the flux within these inner fringing permeances, an great improvement has been observed in the results obtained with the modified electromagnetic network. And a proper fit for both current and forces waveforms could then be easily obtained with:

$$xAstk = 0.02\ Astk, \tag{6.2}$$

and

$$xD = 0.02\ D'. \tag{6.3}$$

The corresponding transient waveforms are shown in fig. 6.12 for the current, in fig. 6.13 for the force and in fig. 6.14 for the eddy current losses.

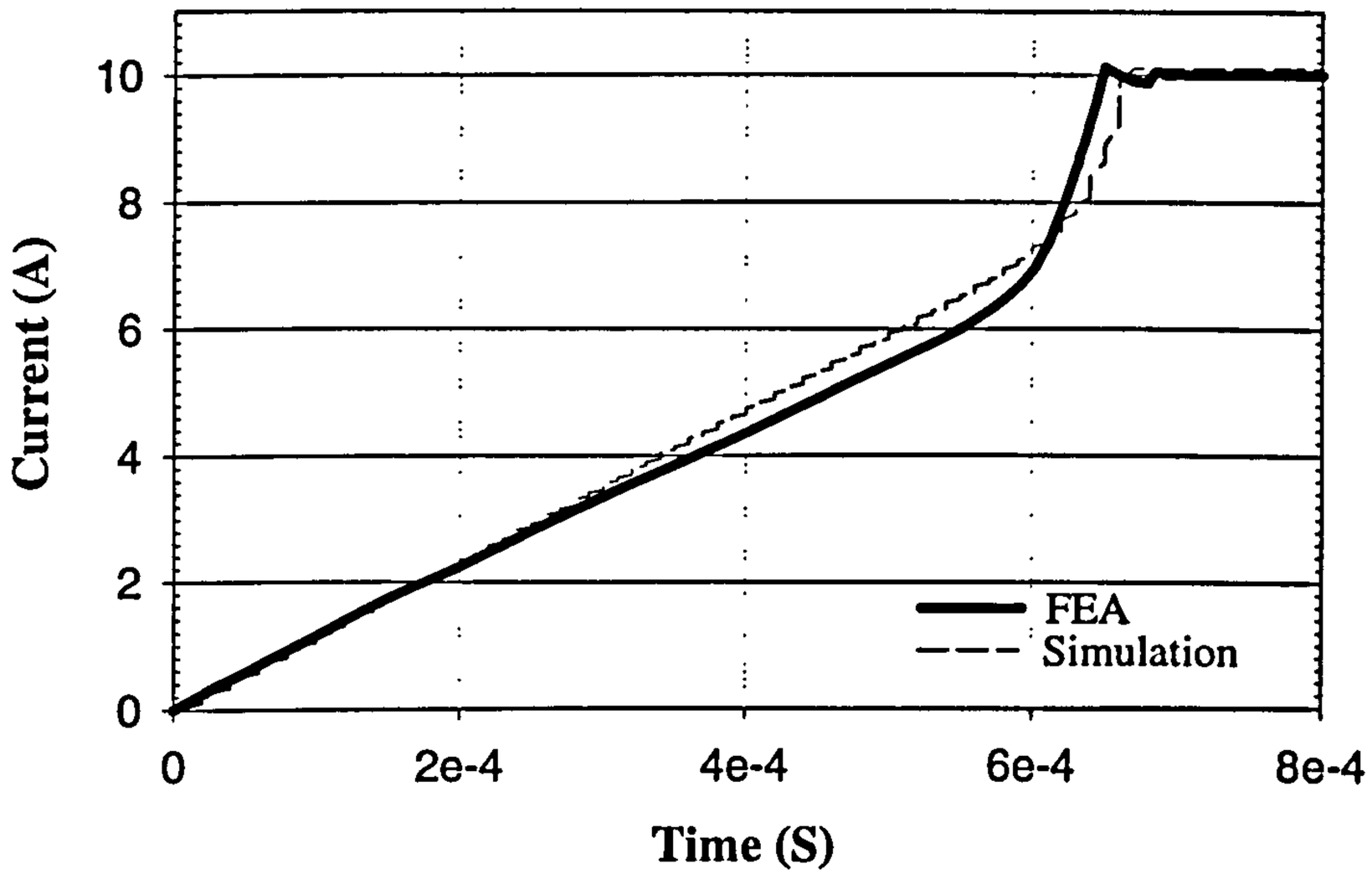

Figure 6.12: Transient current waveform resulting from a step voltage of 90V and a current limit of 10A.

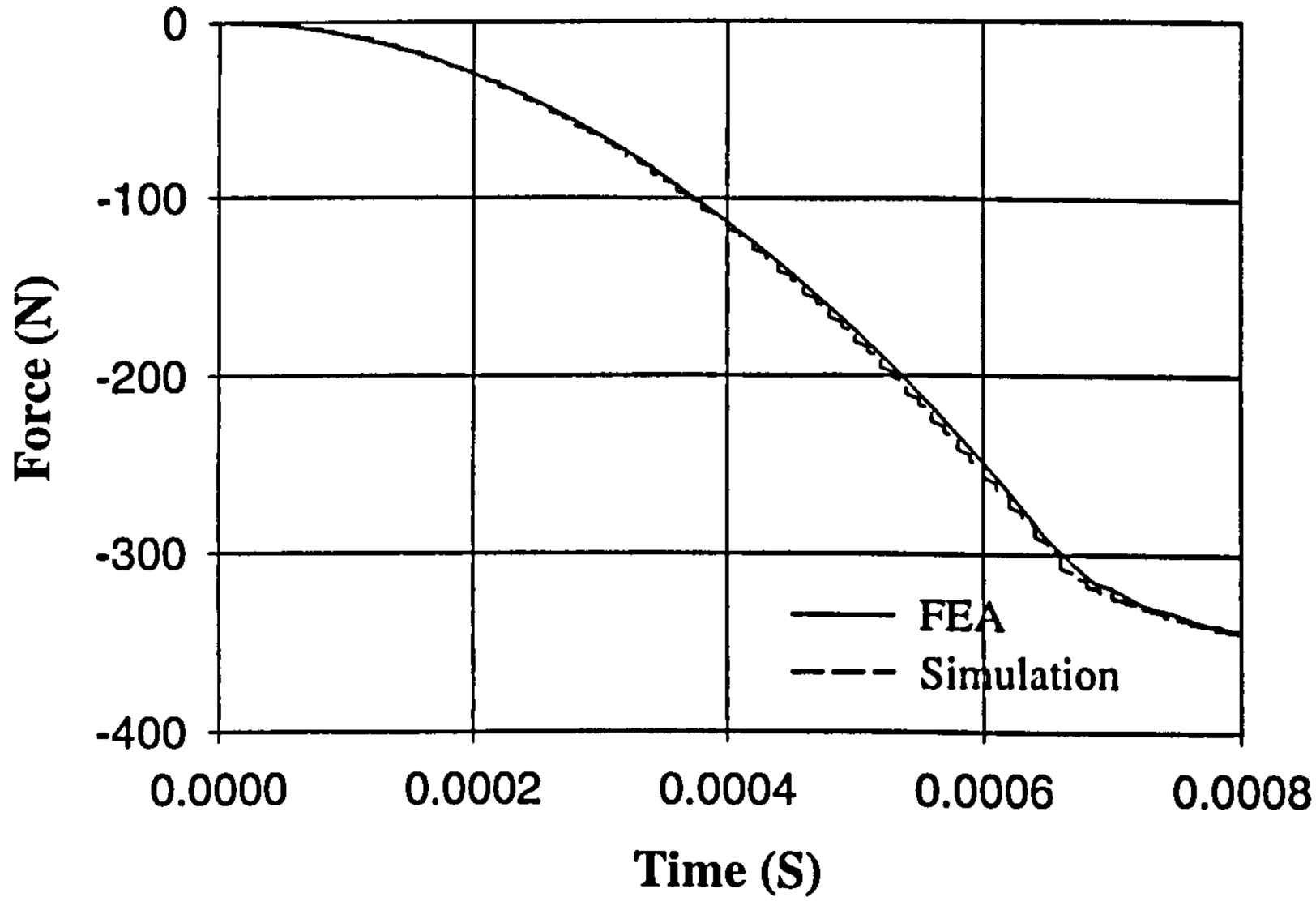

Figure 6.13: Transient force waveform resulting from a step voltage of 90V and a current limit of 10A.

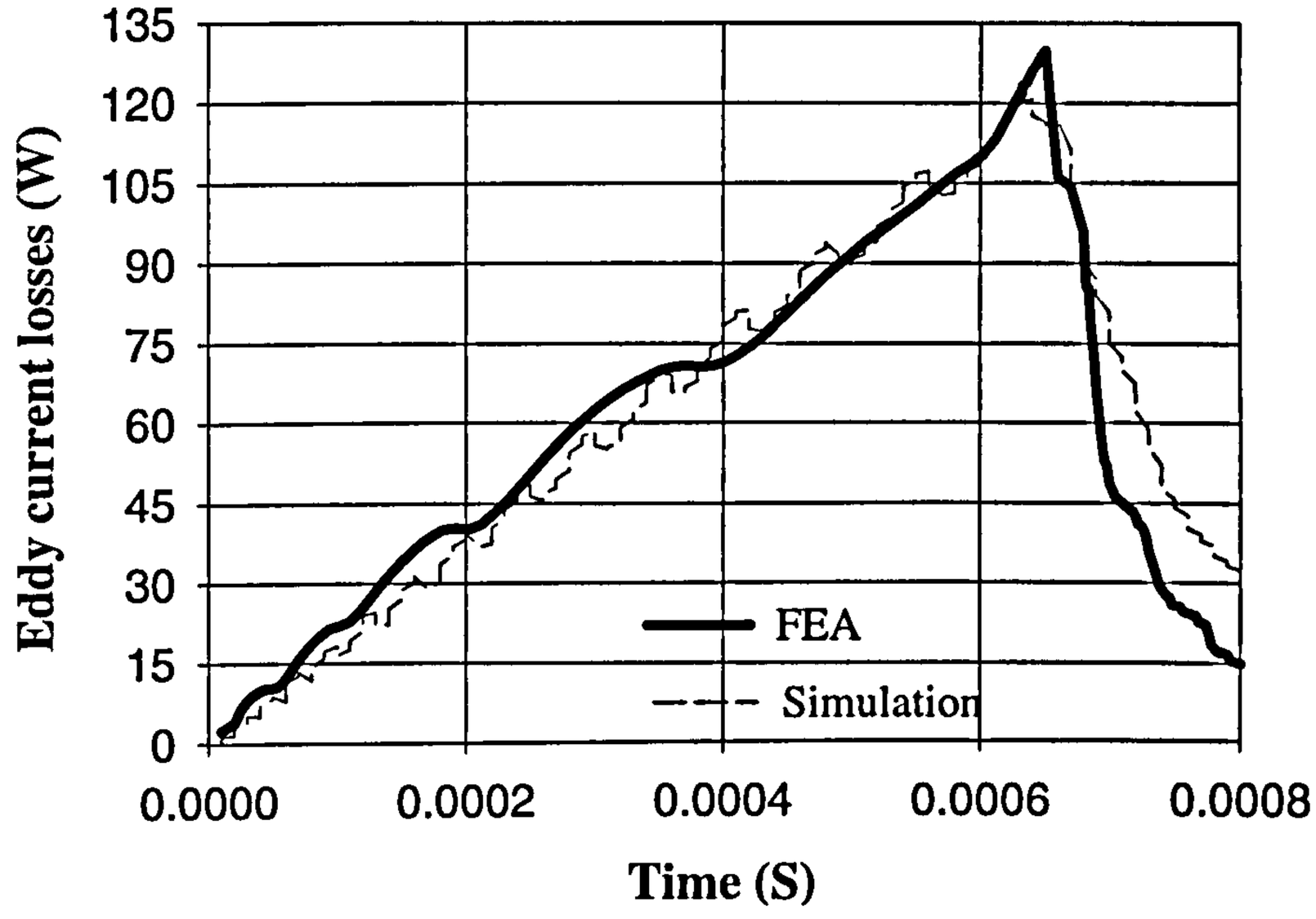

Figure 6.14: Iron losses resulting from a step voltage of 90V and a current limit of 10A.

6.5 Conclusions

The satisfactory agreement obtained in the last three figures tends to demonstrate that the proposed electromagnetic equivalent network is a promising technique for simulating dynamically the E-core actuator. The generation of eddy currents within the armature is modelled with a diffusion network. The computation of the iron resistance and nonlinear inductance per layer is derived from a simplified analytical model of the flux and eddy current paths based on finite-element results. Although an iterative approach is required, the overall computation is significantly faster than a corresponding 3D finite-element analysis. Therefore the proposed method is a potential complementary design tool to the latter.

However it is also too early to make any definitive conclusions concerning the performance of the electromagnetic equivalent network as, if this development has certainly benefited from the experience acquired in the axisymmetric analysis, it does also leave some important questions without any answer. For example,

1. What would be the analytical results for a different gap or a different control

strategy?

2. Is it possible to develop a more accurate armature model with less or none unknown parameters?

3. How would be the accuracy affected by a design modification?

Unfortunately these questions will not be answered in this thesis. However a comparison of this analytical technique with measurement is given in the following chapter, for which the variables $xAstk$ and xD are computed with eq.(6.2) and (6.3). It involves a different E-core design with an average airgap of 0.1mm and also a different control strategy.

Chapter 7

Transient and Static Force Measurements

7.1 Introduction

A comparison of the analytical force computation with finite-elements has already been presented in the previous chapters for both pot- and E-core devices.

The validation for static force was given in fig. 3.7 and fig. 3.8 for a pot-core and an E-core design respectively. In both cases a satisfactory agreement was concluded. The computation of the analytical force involved using the co-energy approach summarised in chapter 2 and also the gauge curve technique presented in chapter 3. A good agreement was obtained between these two methods, again for both axisymmetric and rectangular devices.

A transient and dynamic force comparison with finite-elements has also been presented for the axisymmetric problem and is summarised in fig 5.19 and fig. 5.26. The control sequence for both tests consisted in a step voltage ($90V$) with, for the dynamic problem only, a current limit of $6A$. In both cases a satisfactory agreement between the finite-element method and the analytical model was concluded although the electromagnetic equivalent circuit in fig. 5.11 was not shown to be appropriate for

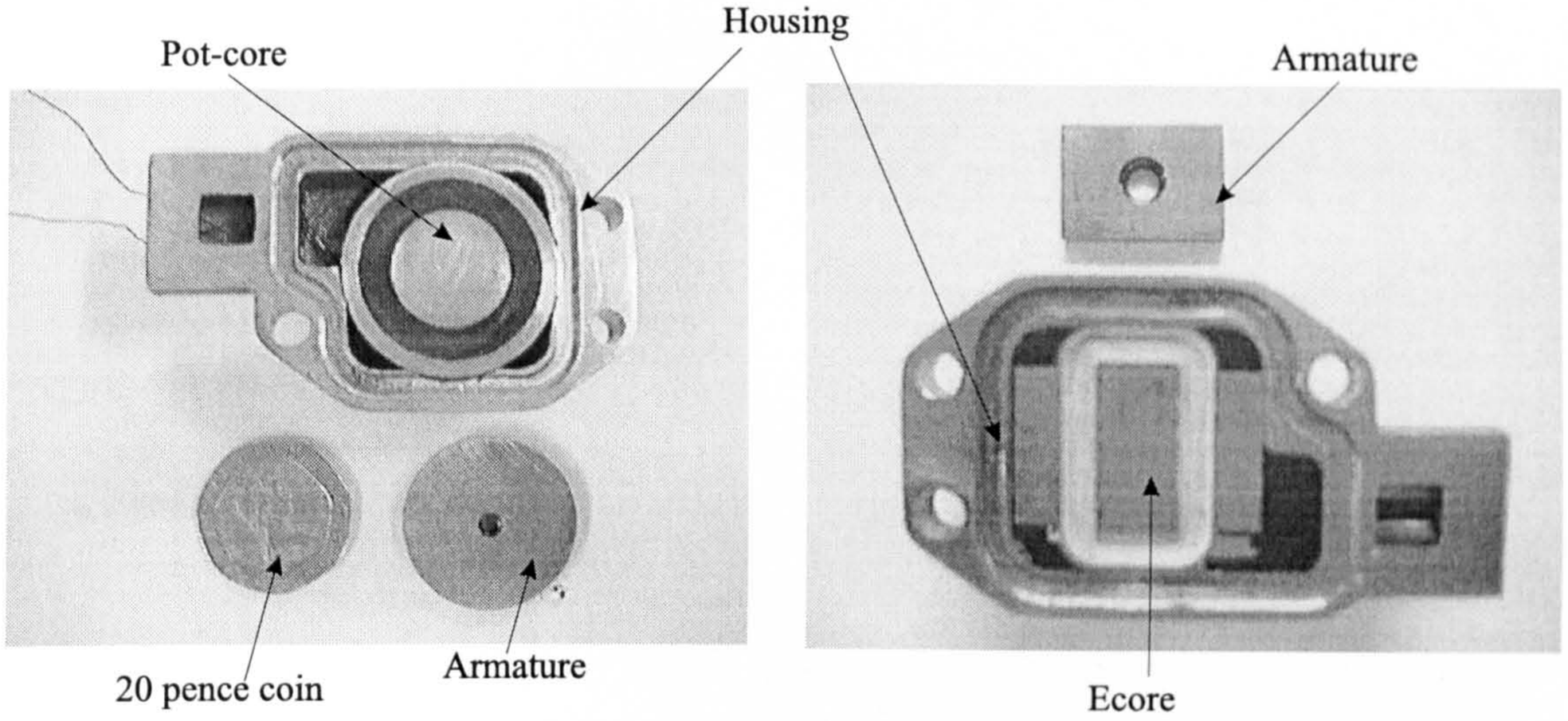

Figure 7.1: Pot-core and E-core actuators in their housing component for force measurements.

simulating flux decay due to the variation of flux paths.

A transient test for a rectangular device was also given in fig. 6.12 and 6.13, showing a good agreement between the analytical model and finite-elements. The control sequence also involved a step voltage of $90V$ with a current limit of $10A$.

The validation of the analytical force computation is completed in this chapter by adding some static and transient measurement results. The dimensions of the pot-core actuator considered in these measurements are summarised in table 5.1 while its measured material characteristics, a 2.5% SiFe steel, are given in fig. 4.2. Fig. 7.1 and 1.4 shows a photo of this prototype. Similarly the E-core design considered for the measurements is summarised in table 7.1. Its laminations are made of a grain oriented steel whose measured BH curves are plotted in fig.2.23. The solid armature is made of a 2.5% SiFe steel. Figure 7.1 shows also a photo of this prototype. Only the lamination stacks of the limbs and the top part of the bobbin is visible from the core molded within its housing. The armature, slightly shorter than the core, includes a relatively large hole for fixing the armature to the rig. Figure 1.4 shows more clearly the variation of dimensions between the core and the armature.

Variables	$[mm]$
A	20.4
B	18.29
C	3.25
E	19
D	3.5
F	5
T	3.5
$Lstk$	14.12
$Astk$	14.46
$Sins$	0.5
$abcoil$	3.0
$uncoil$	1.0
$Fstk$	0.95
Lamination material	Unisil 35 M7
Armature material	2.5% SiFe Steel
N	130
Resistance	1.5 Ohm

Table 7.1: E-core actuator dimensions for force measurements.

7.2 Test Rig Set-Up

7.2.1 Force Rig

The force rig presented in fig. 7.2 was conceived by Lucas Diesel. The armature, placed above the top plate, is fixed to the piezo-electric force transducer placed between the two plates. A hole has been drilled into the top plate such that there is no contact between this plate and the armature assembly. The core housing is fixed to the top plate through a smaller stainless steel rectangular plate screwed on to the top plate around the armature as shown in fig 7.3 . The stainless steel plate height is slightly greater than the armature to ensure that an airgap is kept constant between the core fixed to the top plate and the armature fixed to the transducer. With this particular setup, the airgap length can be easily measured using a clock gauge, and also modified by changing the height of the spacer inserted into the armature and transducer assembly.

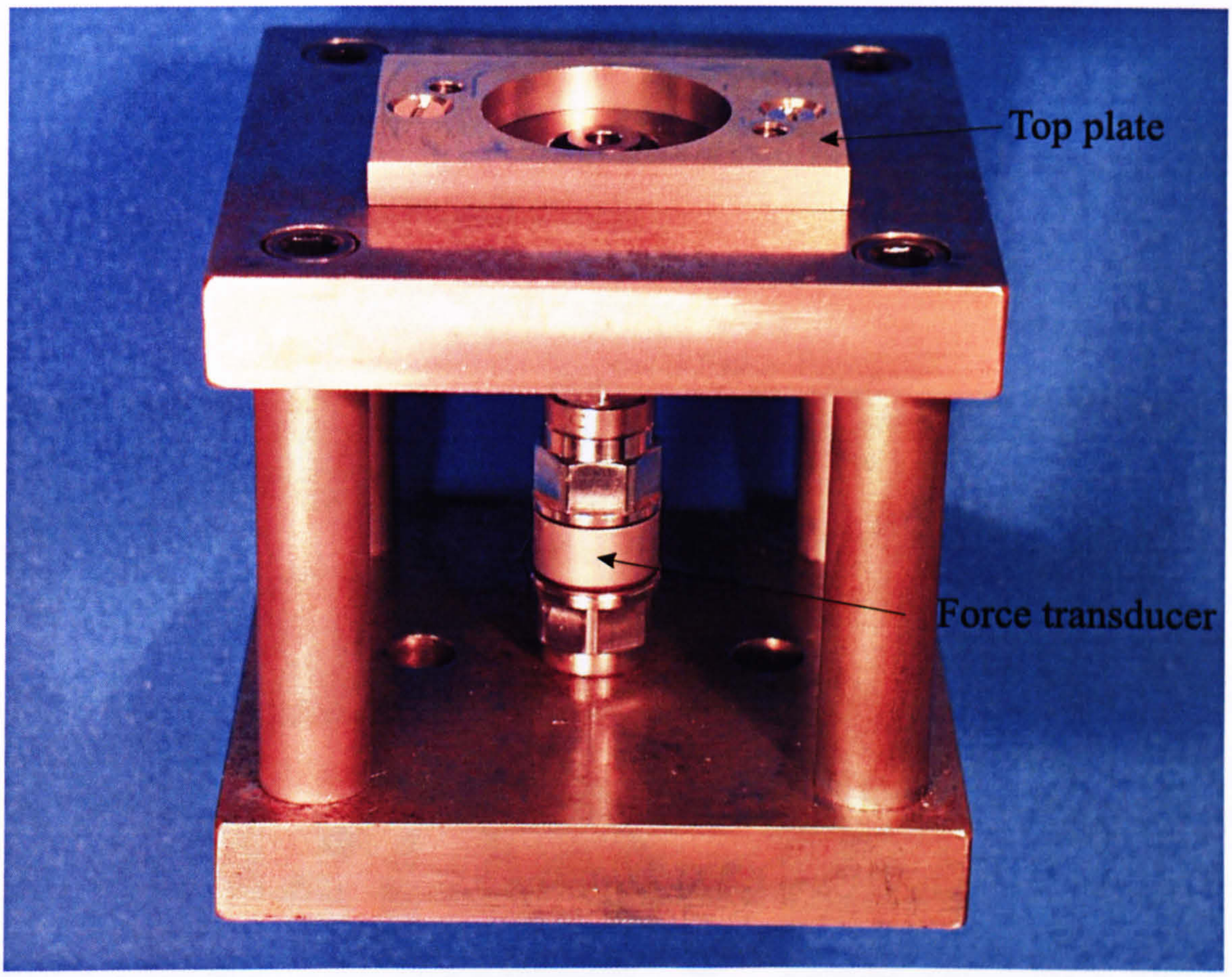

Figure 7.2: Force rig for transient measurements.

Possible sources of error with such a force rig could result from problems of alignment and parallelism between the core and the armature.

7.2.2 Test Rig

The complete test rig used for transient measurement includes:

1. the force rig using a Kistler piezo-electric force transducer type 9311B,
2. a HP 6010 A *DC* power supply ,
3. a switched reluctance phaseleg plus associated gate drives,
4. a SPEED FC3 flexible Controller (+ PC),

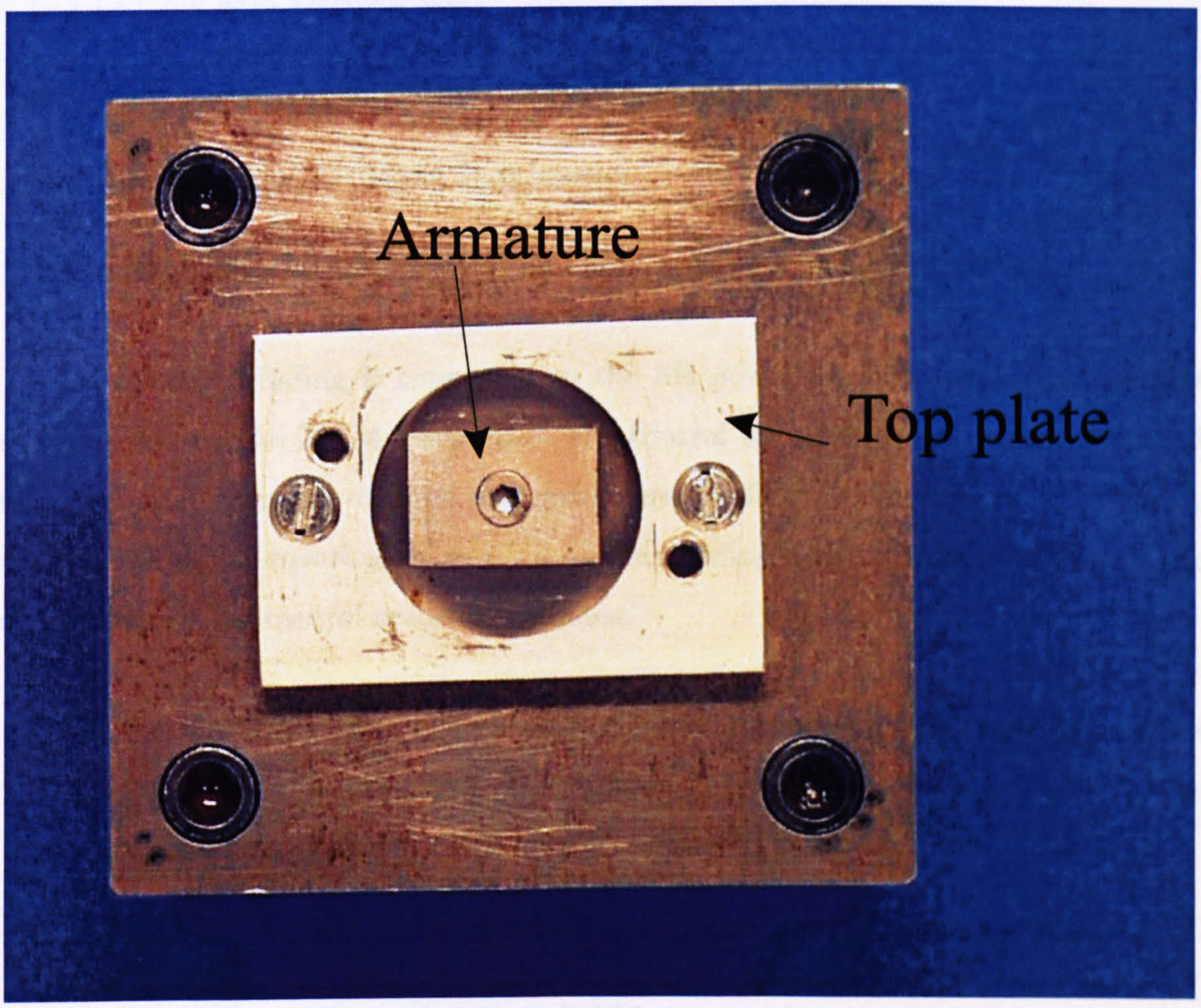

Figure 7.3: Top plate set up for the force rig.

5. two small *DC* power supply for the current sensor and gate drives.

The instruments for measurements include:

1. a Kistler charge amplifier type 5011A,

2. a Tek Am503 current amplifier,

3. a Le Croy 9414 Oscilloscope,

4. a TEK A6302 current probe,

5. a High precision HP 3457A multimeter,

6. a clock gauge and a base plate (precision $1\,\mu m$) for measuring the gap.

The actuator winding is connected to the SR power phaseleg whose gate drives are controlled by the PWM controller. The control set up is summarised in fig. 7.4 and generates a sequence of three successive periods of 2ms followed by a significantly longer 'dead time', ensuring no heating of the winding and a complete decay of the eddy currents. The control sequence includes:

- During the first period, a 60V step voltage is applied to the winding until a current limit of 2A is reached. Then a fixed PWM duty cycle is applied until the end of this period.

- The second period corresponds to a free wheeling operation during 2 ms.

- In the third period, another fixed PWM duty cycle is applied (half of the first one).

- At the end of the third period, both switches are turned-off and the voltage is reversed.

The choice of the control sequence for the transient measurement is purely arbritrary and results from a trade-off between varying the control to extend the range

of validation and also keeping it as simple as possible to simulate it with sufficient accuracy. The soft switching frequency is 31.25KHz.

The steady state measurements are based on a slightly different test rig in which the current was kept constant at each measurement by adjusting the DC voltage.

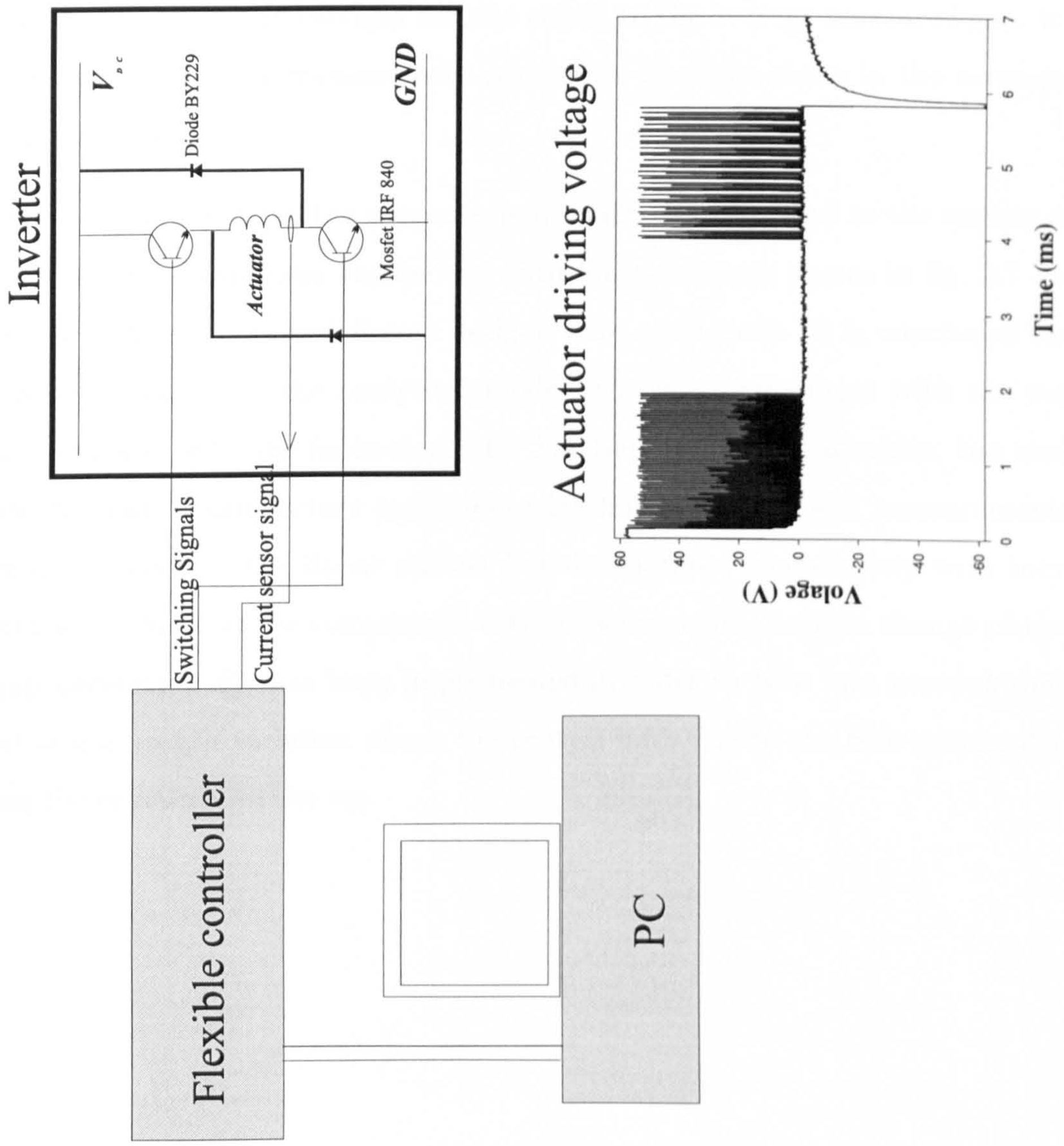

Figure 7.4: Driving set up for transient measurements.

7.3 Static Forces Measurements

The static force measurements are presented in fig. 7.5 and 7.6 for several airgap lengths. For some of the measured airgaps, two simulated curves are plotted for slightly different gap lengths. Indeed, the force sensitivity to gap length variation changes significantly within the gap range (0.05 to 0.5mm). Therefore by drawing two simulated curves corresponding to two gap lengths closed to the average measured gap, it shows how sensitive the force measurement results are to slight errors in the corresponding airgap measurements.

For each device type, the measurement results seem to lead to the similar conclusions as in the comparison carried out with finite-elements shown in fig. 3.7 and 3.8 although different pot- and E-core designs were considered. It is concluded that, for the pot-core actuator, the analytical model is in good agreement with the measurements and also with the finite-elements. For the rectangular actuator, the analytical model has only a satisfactory agreement with finite-elements and measurements. The accuracy is good in the linear section but deteriorates progressively with increasing saturation[1]. Also, in the comparison with measurements, a slight change of the main airgap permeance P_{g1} has been implemented in order to take into account the significant airgap length variation above the central limb due to the hole within the screw fixing the armature to the rig.

[1]The variable *limbsec* was set to 4 during the simulation compared to measurements.

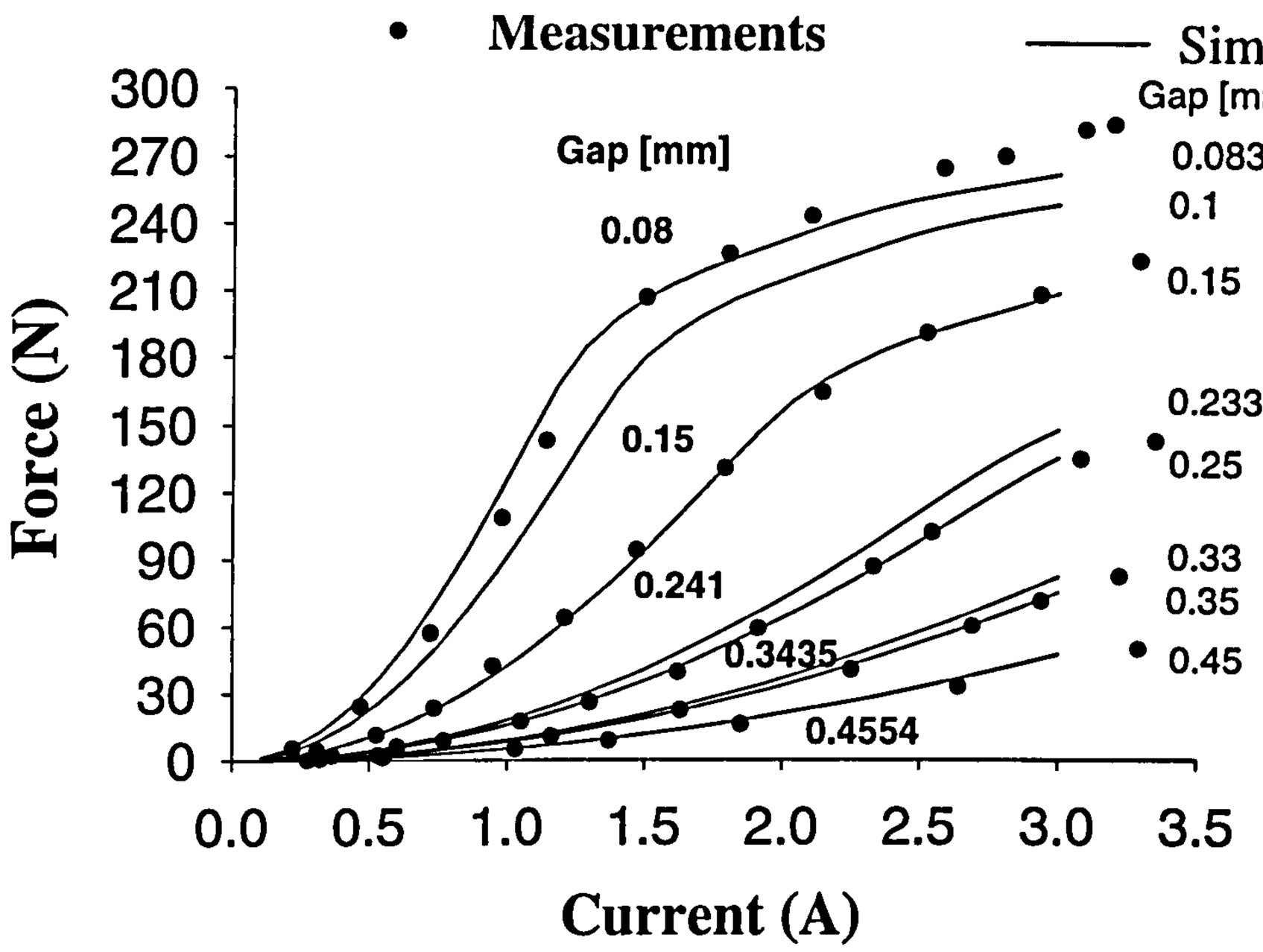

Figure 7.5: Pot-core actuator: static force versus current

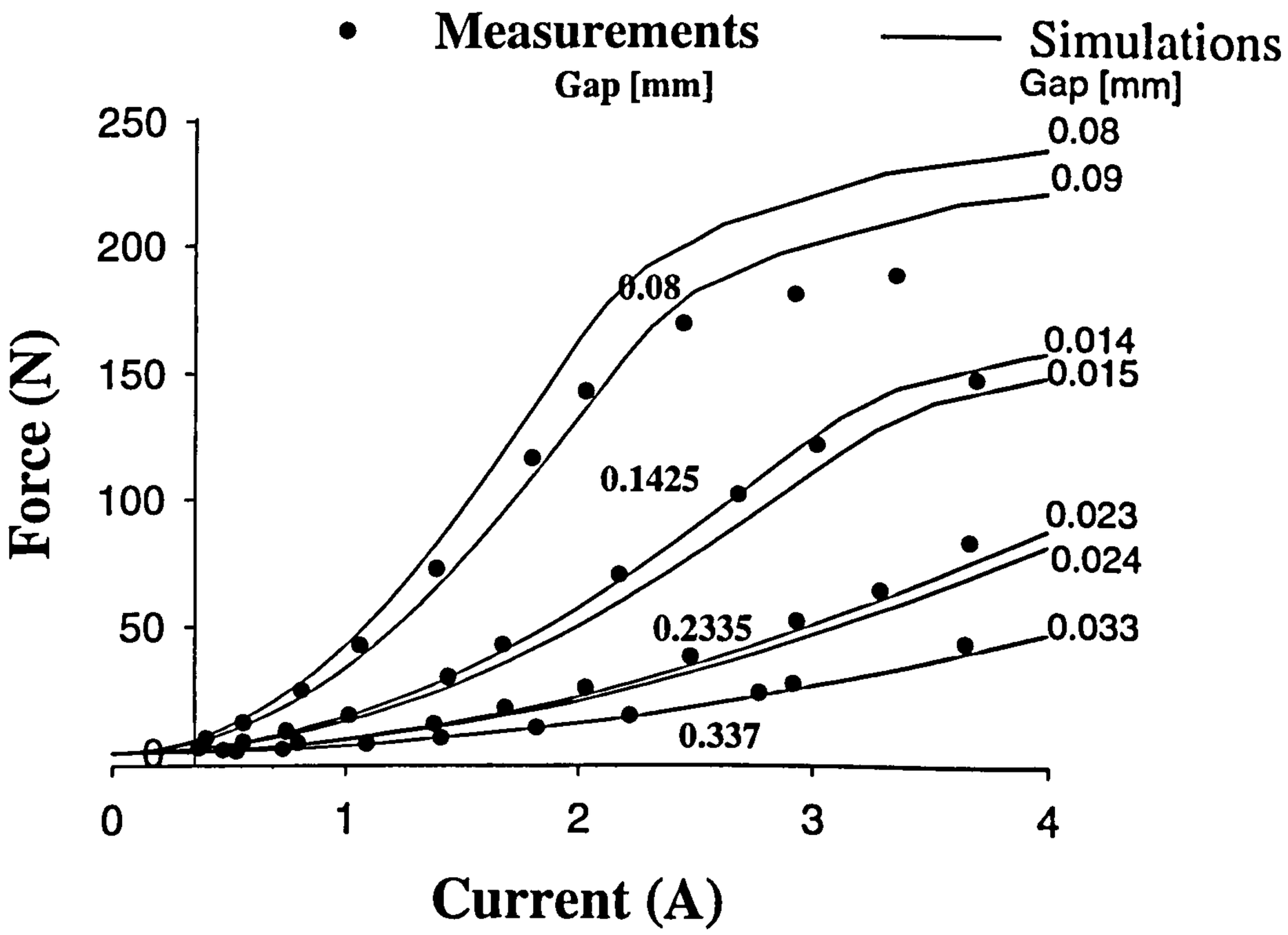

Figure 7.6: E-core actuator: Static force versus current

7.4 Transient Forces Measurements

7.4.1 Axisymmetric Actuator

The transient measurements obtained by applying the previous control sequence are shown in fig. 7.7, 7.9, 7.11 for the current corresponding to three different gap lengths along with the analytical simulation results. Figures 7.8, 7.10, 7.12 gather the corresponding transient force results.

The transient measurements lead to new conclusions concerning the range of driving conditions for which the simplified electromagnetic network shown in fig. 5.11 can be applied with a certain level of accuracy. However before developing this point, it is important to mention the difficulties encountered during this validation which may influence the way the results should be interpreted. The period corresponding to a constant PWM duty cycle have been simulated by applying to the simulated actuator an average voltage obtained by multiplying the source voltage (60V) with the duty cycle. Unfortunately it was found after measurements that the switching devices (Mosfet IRF840) as well as the diodes (BY229) could generate a significant voltage drop in the circuit. The periods the most affected by these drops could be the fixed PWM duty cycle and free-wheeling sequences . An attempt has been made to model these nonlinear drops. However the technical information for the transistor was not very helpful for such low levels of current characterising the results obtained for two first gaps at least. The voltage drop for each diode was fixed to 0.5 V and to 0.1 V for the transistors. The duty cycle period however involves another difficulty as the active electric circuit does vary with the duty cycle e.g. if the duty cycle was set to 20, two transistors should be simulated switched-on during 20 % of the switching period while only one and a diode are switched on during 80 % of the same time. In practice, the simulation assumes simply two transistors switched continuously on when the average voltage is applied. In summary it is rather difficult to compare in absolute terms the given results and the discussion here should be limited to the general trends of the transient current and force curves.

The transient current and force measurements obtained for the three different airgaps have a relatively similar waveform. During the initial step voltage, the measured current response is affected by the iron losses and also the generation of flux in the different airgap paths, leading to a simultaneous jump in the force waveform. Indeed by comparing fig. 7.8, 7.10, 7.12, it can be observed that the level of this force jump is an inverse function of the the gap length. Due to the high initial iron resistance and the low total airgap inductance, the current rises rapidly to its peak value starting the PWM fixed duty cycle mode. During the same period, the simulated current for each gap shows an even faster growth with no significant inductive behaviour. This result was anticipated from the simplified electromagnetic equivalent circuit shown in fig. 5.11 as the total airgap inductance is hidden within the diffusion network. By dividing the actuator into closed flux tubes, it has been implicitly assumed that the flux diffuses simultaneously in both airgaps and iron. In this case the simulated force 'jump is significantly smaller than the real one. Also the PWM duty cycle mode starts earlier (more than two time faster) as the peak current is reached a lot quicker. In order to compensate this effect, the PWM duty cycle mode for the simulation results in the given figures has been delayed in order to start at the same time as for the measured results. This correction was obtained by retrieving from the measured voltage waveform the time during which a constant step voltage was applied to the actuator. This has been done for each gap. Even so, the initial simulated force jump is still significantly lower due to the required simultaneous diffusion of the flux within the iron and the airgaps. Such particular effects were not visible in the previous dynamic test validated against FEA as the step voltage, also higher (90V), lasted long enough to allow a fast and complete propagation of the flux within the iron and therefore to allow the transient simulated force to 'catch up' with the finite-element force response.

For each gap, the force waveform is characterised by a two peak shape as the duty cycle reduces greatly the average voltage on the winding, leading to a lower diffusion of flux within the iron compared to the dynamic test for example. The discrepancy between the simulated and measured force waveforms during the first PWM duty cycle mode is mainly due to the variation in the initial jump. The following sections of the transient waveforms of current and waveform may be significantly affected by the

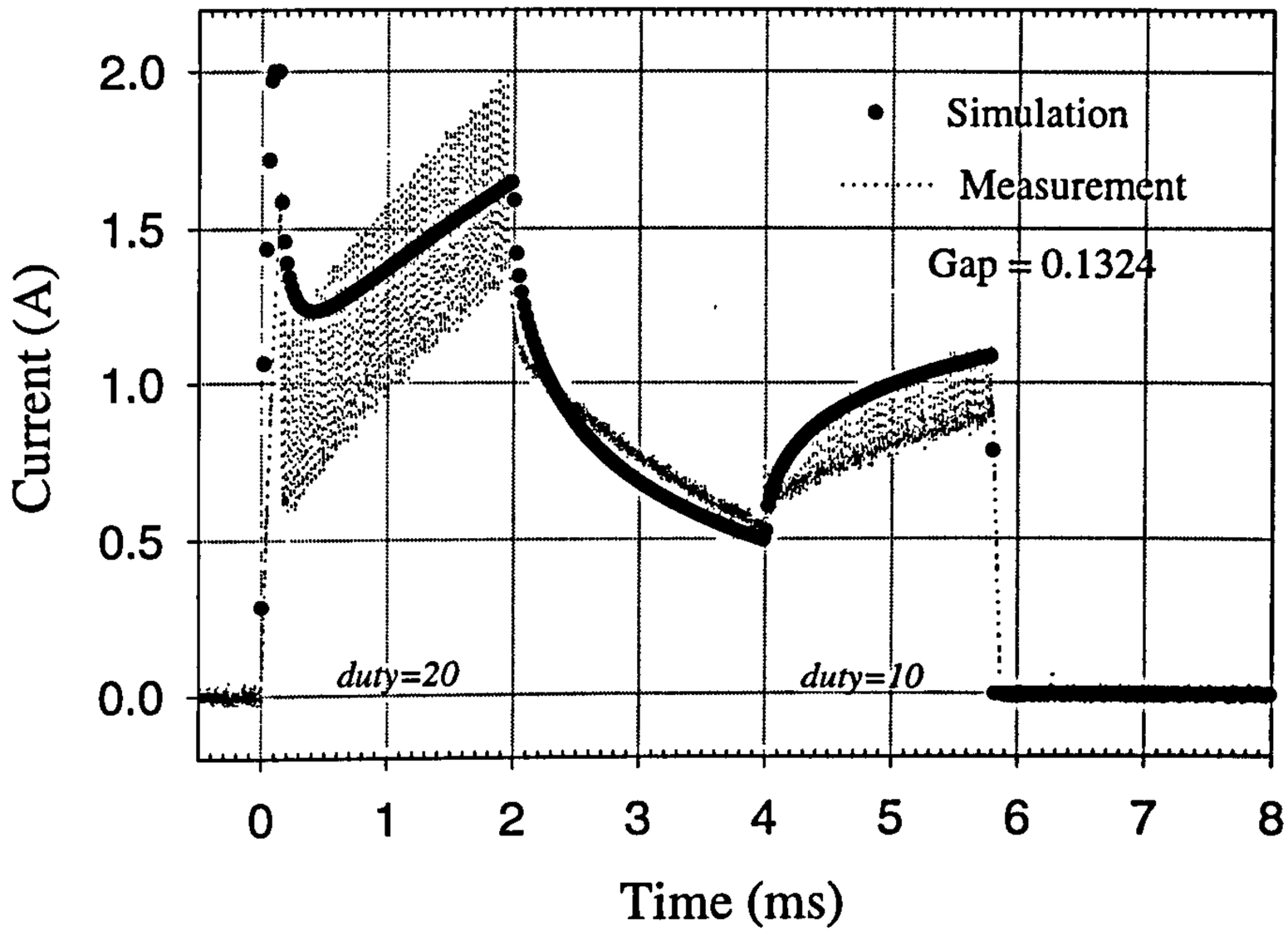

Figure 7.7: Pot-core actuator: transient current versus time

rather unknown drops occurring in the active circuit and therefore it is not appropriate to draw any conclusions. However the slower decay of the simulated transient force, already commented in the finite-element validation, can once more be observed in this section against the measurements.

7.4.2 Rectangular Actuator

Due to the difficulty encountered in the validation against measurements for the axisymmetric problem, only the airgap has been tested for the rectangular actuator (0.24mm). The level of current being in average higher than in the pot-core experiment, the diode drop has been set to 1V and the transistor drop has been approximated by a resistance of 0.5 Ω taking partially into account the fact that both transistors are not on during the complete PWM duty cycle periods.

First it is important to underline that the tested E-core has a smaller overall design than when compared in the previous chapter with the finite-element analysis. However the same number of layers (20) and the same assumptions on the eddy current paths

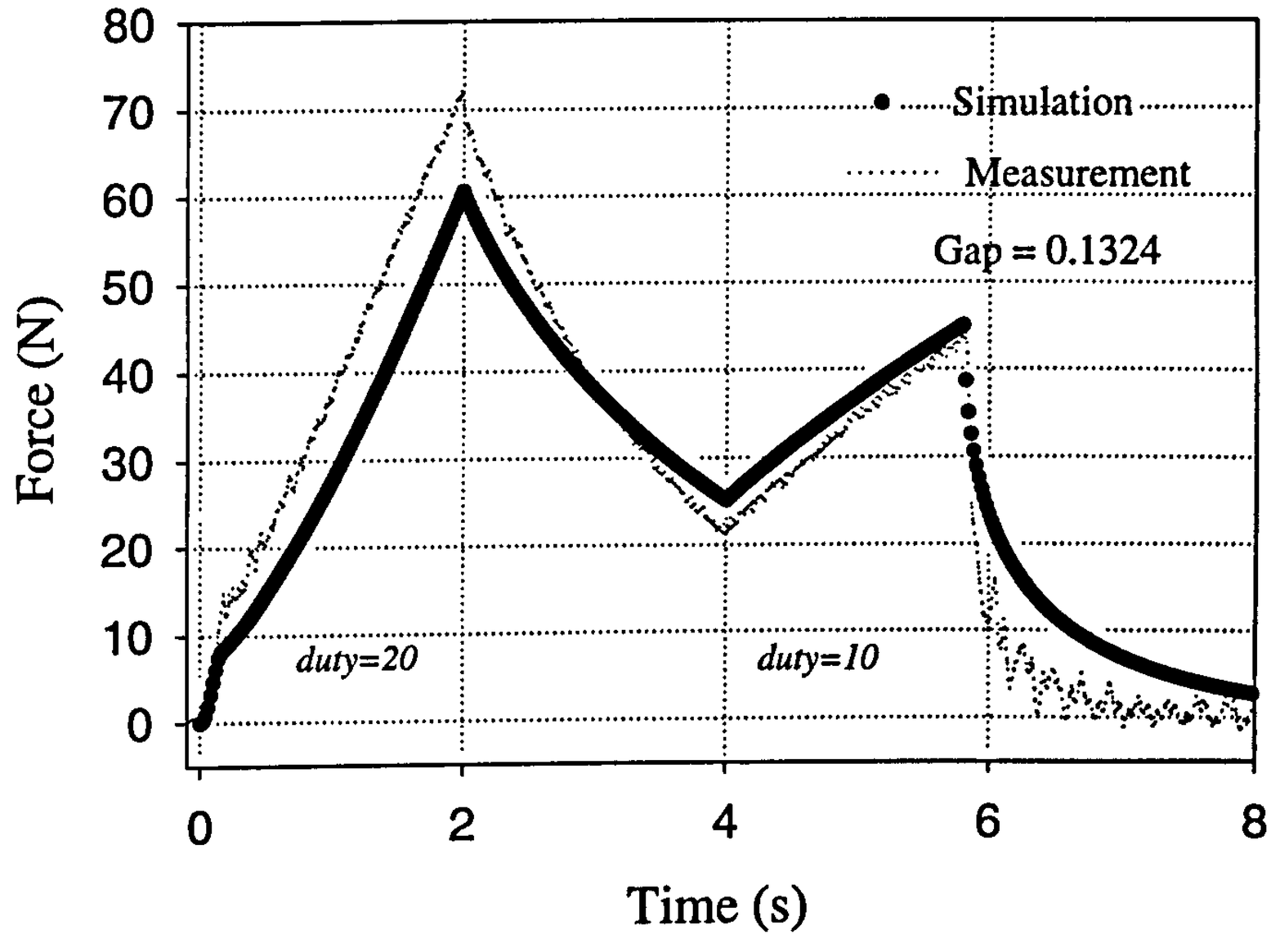

Figure 7.8: Pot-core actuator: transient force versus time

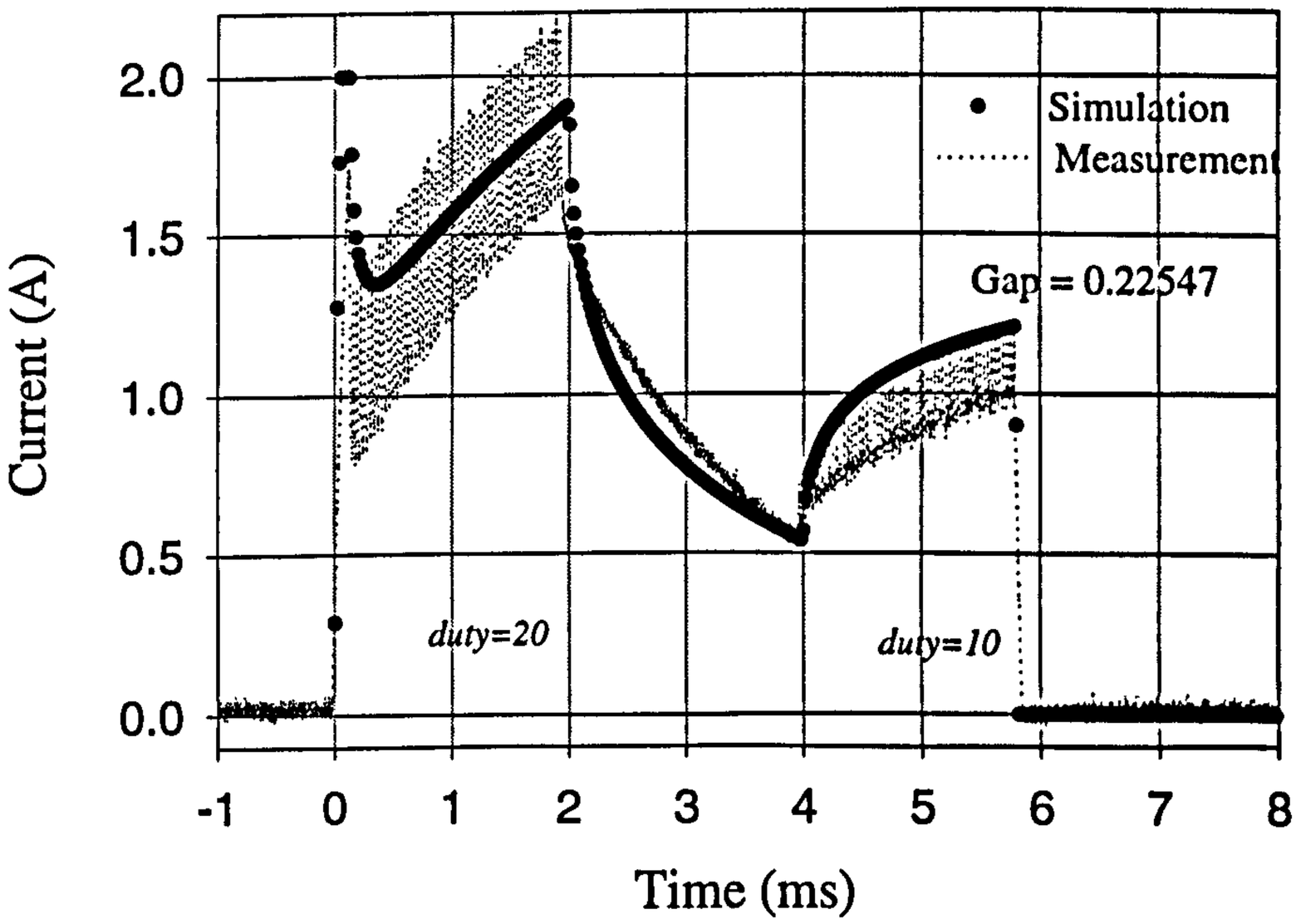

Figure 7.9: Pot-core actuator: transient current versus time

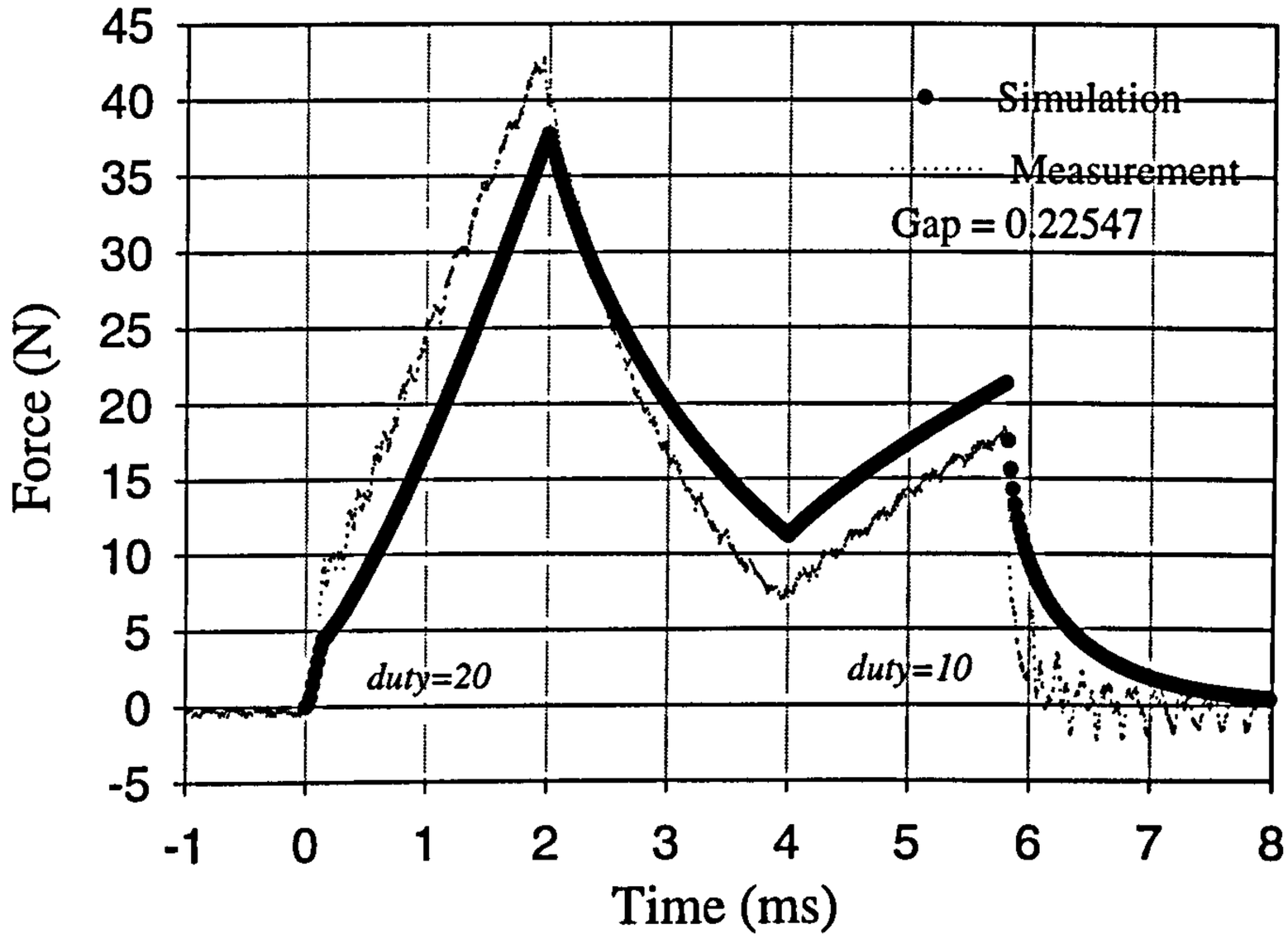

Figure 7.10: Pot-core actuator: transient force versus time

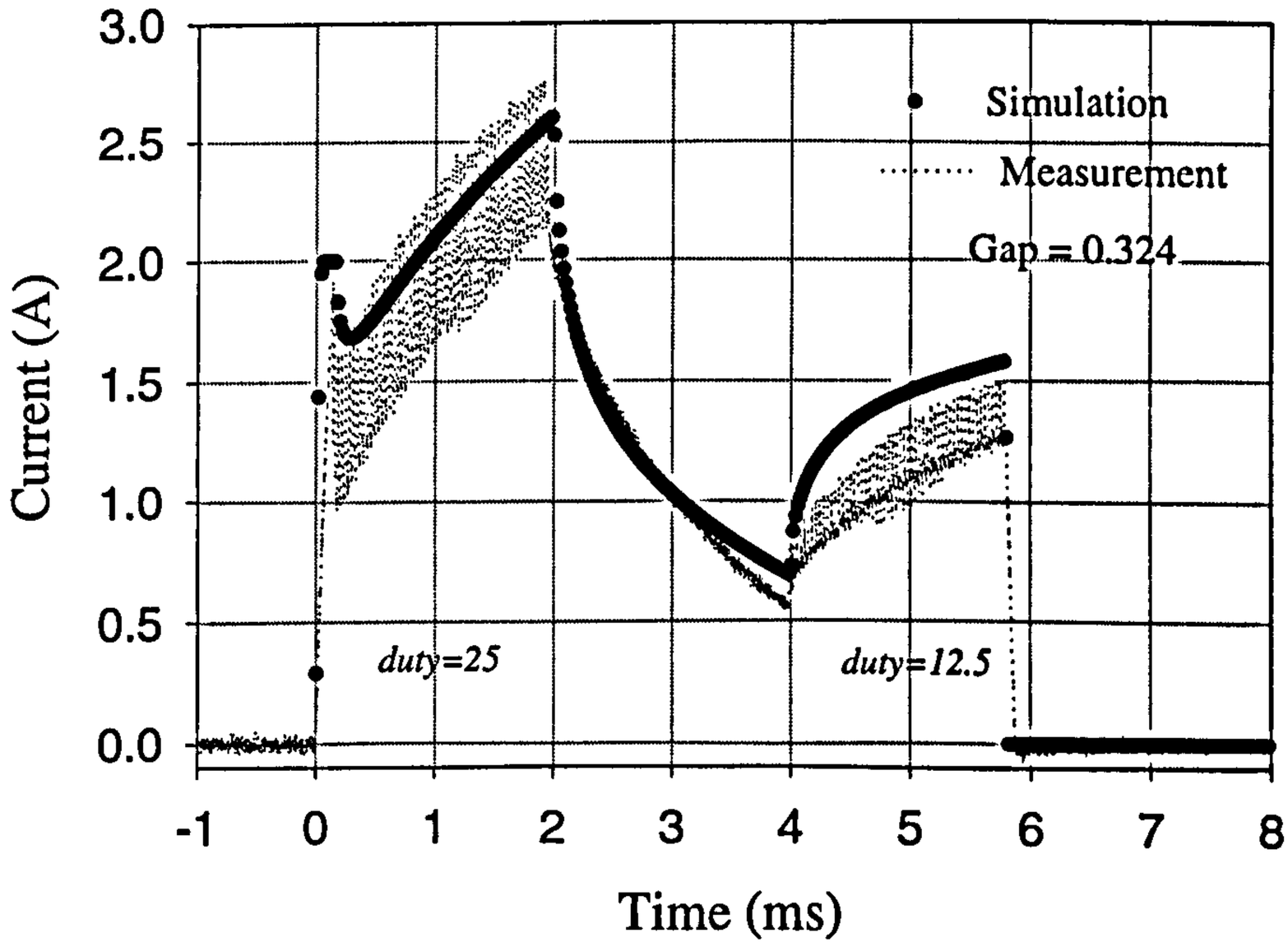

Figure 7.11: Pot-core actuator: transient current versus time

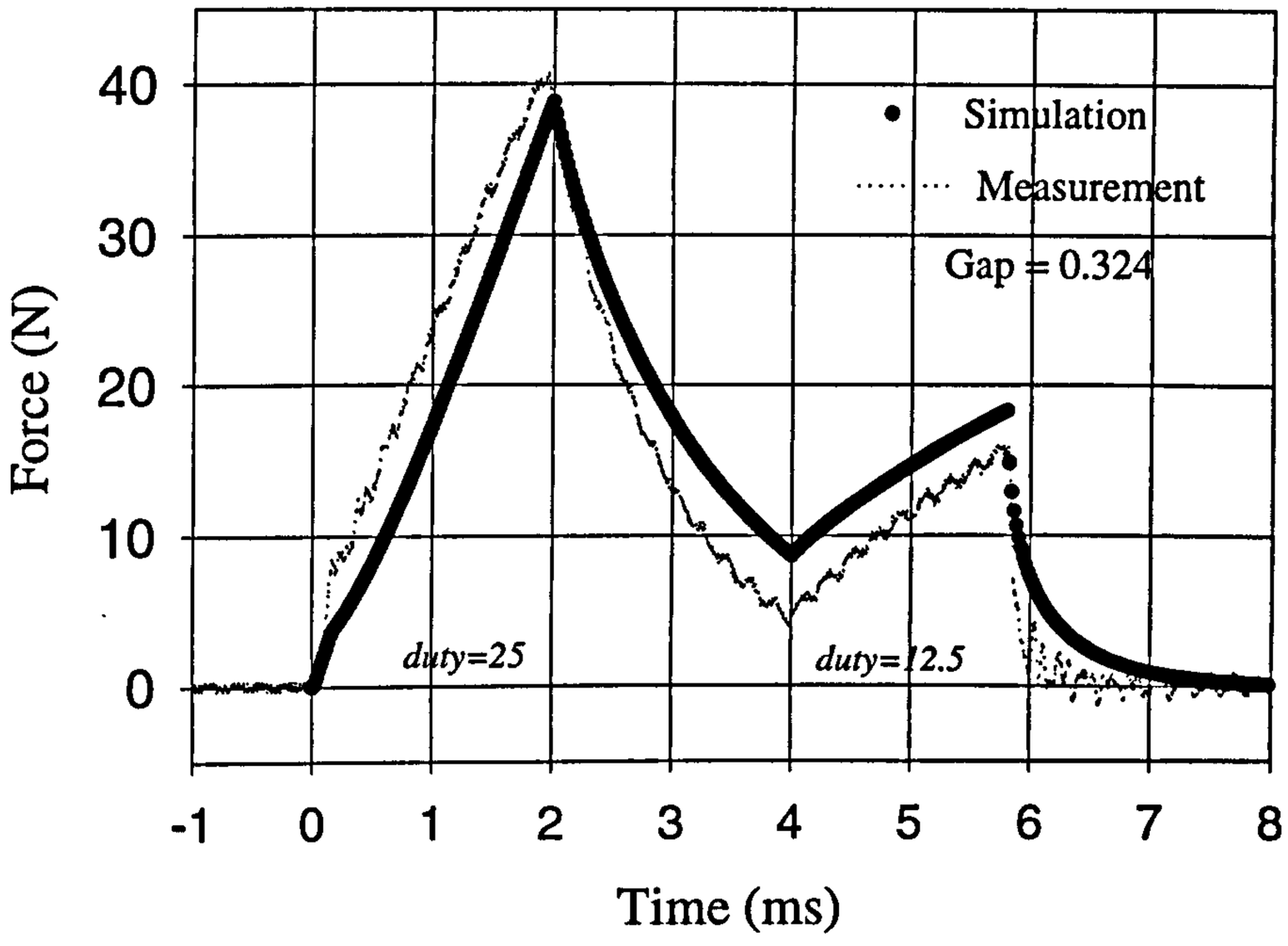

Figure 7.12: Pot-core actuator: transient force versus time

have been used. The iron resistances, being a function of the actual armature dimensions have however a different final value. From the comparison shown in fig. 7.13 for the transient current and in fig. 7.14 for the transient force, the analytical electromagnetic model looks a promising technique although it is clear that more validation should be undertaken. The E-core dynamic model does not involve the aforementioned strong assumption underlying the simplified pot-core model. Therefore to some extent, a better agreement between simulation and measurement was expected for the rectangular device. Fig. 7.15 shows that the total simulated eddy current corresponding to this transient test. And the corresponding iron losses computed as

$$W_{loss} = R_{21}\, I_{R21}^2 + \sum_{2}^{N_c} R_{2i}\, (I_{2i-1} - I_{2i})^2, \tag{7.1}$$

where I_{R21} is the current flowing through the first iron resistance R_{21} in the electromagnetic equivalent circuit shown in fig. 6.2.

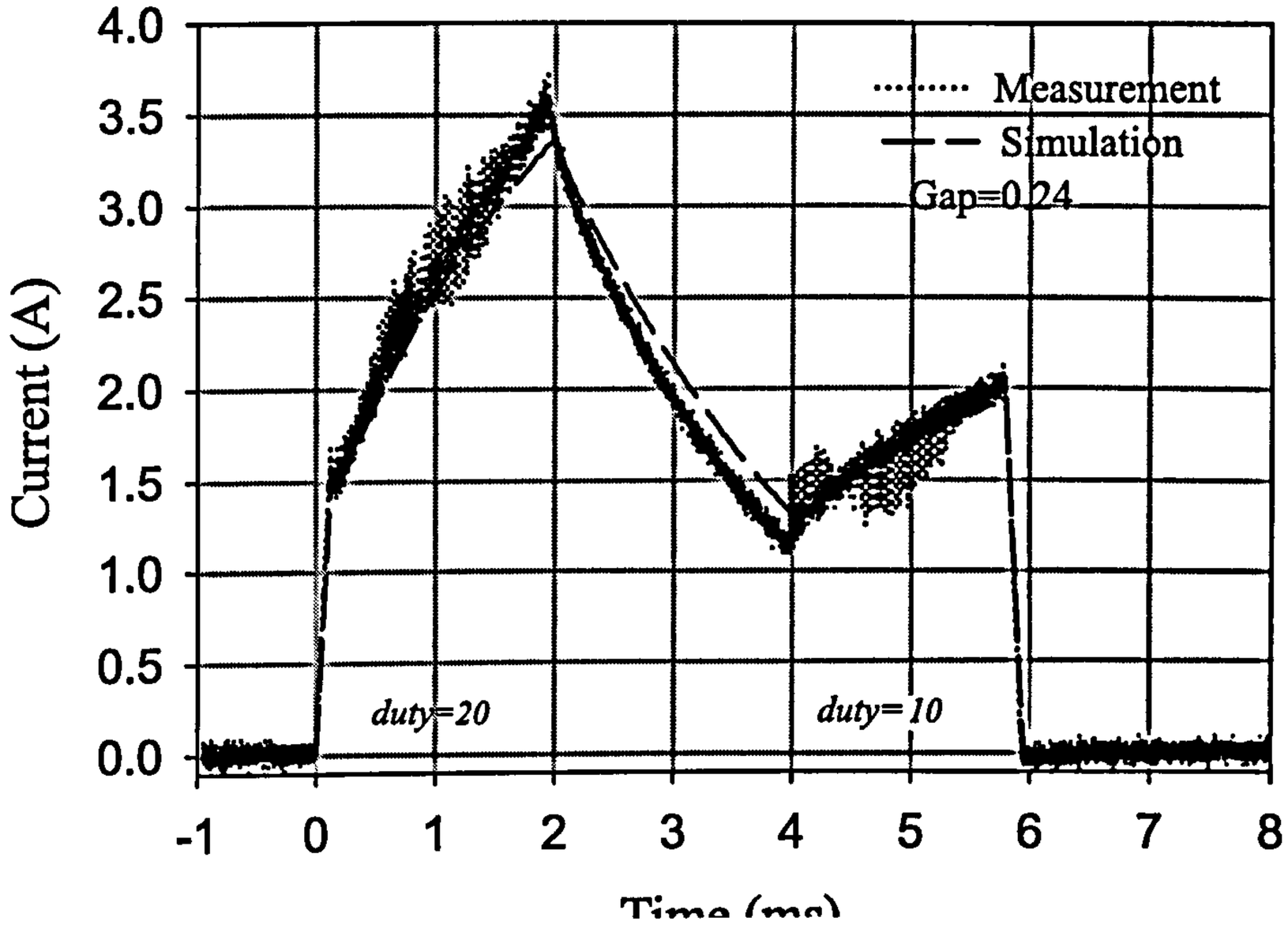

Figure 7.13: E-core actuator: transient current versus time

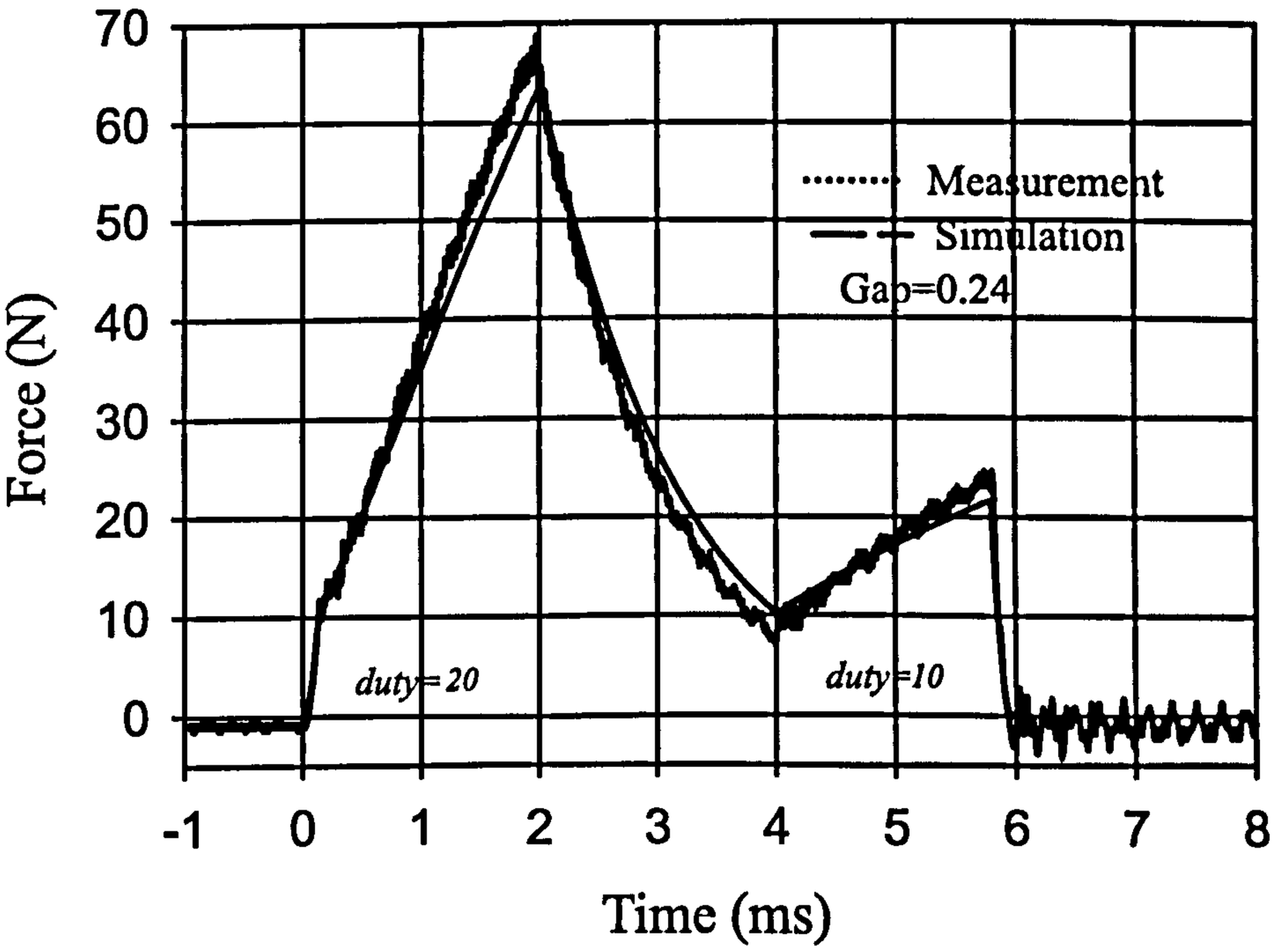

Figure 7.14: E-core actuator: transient force versus time

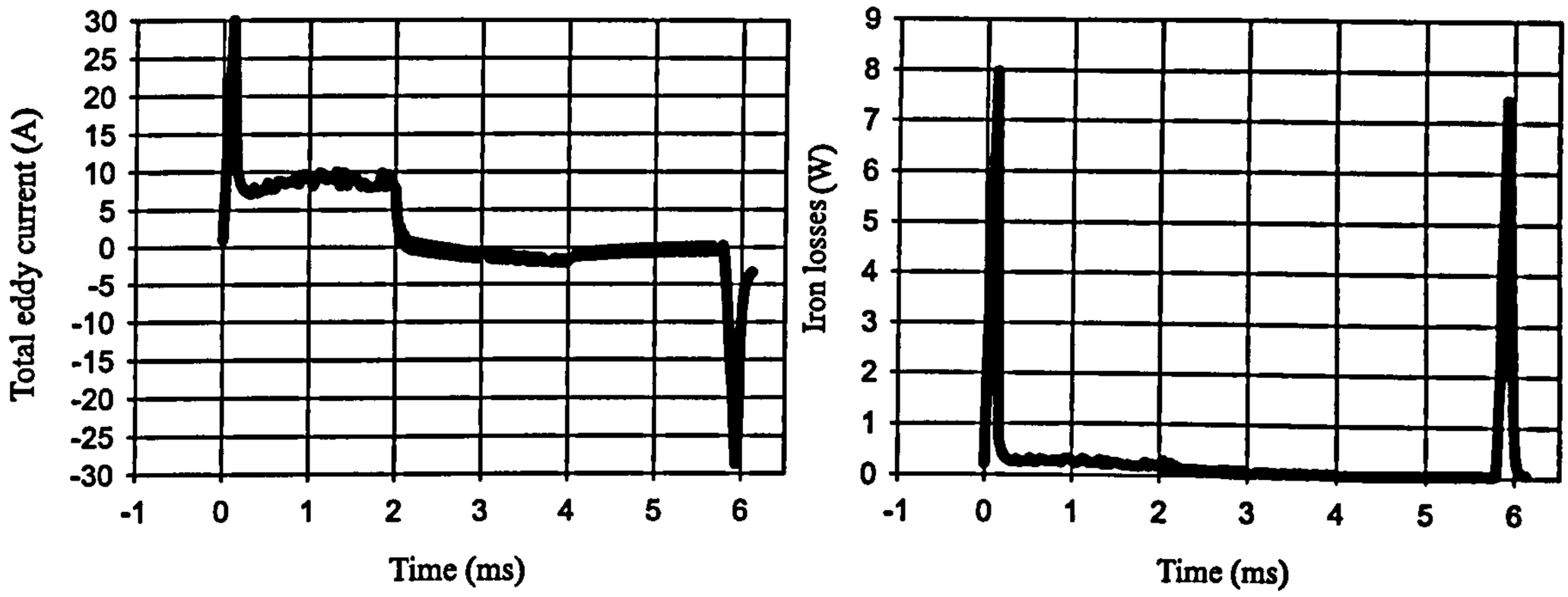

Figure 7.15: Total eddy current and corresponding loss

7.5 Conclusions

The dynamic simulation of the axisymmetric actuator based on the simplified electromagnetic network demonstrates a significant variation of its accuracy level depending on the driving conditions. The origin of the discrepancy has however been identified in each case as being the previous assumption made on the flux paths (the closed flux tube configuration) leading to this first electromagnetic model. However it has been shown in chapter 5 that this assumption is not necessary and a more refined and accurate electromagnetic equivalent network can be developed for the axisymmetric problem. At this point, it is relevant to mention that most of the previous authors [15], [47], [52], [48] have limited their validation to simple control sequence typically a step voltage. It can be seen from this thesis that these tests may not be sufficient to validate their proposed dynamic or transient methods.

In the rectangular problem, the unknown parameters associated with the eddy current paths have been determined in the previous chapter by fitting the simulated iron losses to the finite-element results for a certain gap. The measurements provided in this chapter however have been provided for a very different E-core design involving a different armature dimension and also a different airgap length. From the satisfactory agreement obtained with the simulation results, it can be concluded that the proposed electromagnetic equivalent circuit shown in fig. 6.2 for rectangular device is a promising

analytical technique for simulating the dynamic behaviour of these types of device. The more sophisticated electromagnetic equivalent circuit presented in fig. 5.31 for the pot-core actuator eliminates the inadequate assumption of the first model and should also be considered as an equally promising and powerful technique for simulating the dynamic performance of the solid-iron axisymmetric devices.

Chapter 8

Conclusions

The magnetostatic (i.e. without eddy currents) and magnetodynamic (i.e. with eddy currents) models presented in the thesis must be seen as complementary design tools. The magnetostatic analysis allows a quick appraisal of the actuator dimensions necessary to produce the required force within the constraints imposed on the dimensions and weight. A rough estimation of the number of turns, switch size and armature mass is also possible by combining the magnetostatic model with an appropriate model of the inverter as well as the spring and fluid forces interacting with the armature movement. The analytical fluid force model may derived from a 3D numerical analysis (finite or boundary elements) of the fluid flow around the system. The effect of eddy current generation can then be assessed by replacing the magnetostatic model with the proposed magnetodynamic model of the actuator. This process will lead to a better optimisation of the previously mentioned parameters and also to a final choice of the steel type.

This chapter summarises the findings of the thesis and highlights the advantages and disadvantages of using the proposed analytical methods within a rapid computer-aided design tool. Particular attention was given to two types of actuators: an axisymmetric and a rectangular configuration with both a flat-faced armature. The applicability of the findings to other actuator types as well as recommendations for future work are also discussed.

8.1 Magnetostatic Analysis

Two methods have been presented for the magnetostatic analysis of solenoid actuators: the magnetic equivalent circuit in chapter 2 and the magnetic gauge curve in chapter 3.

8.1.1 Magnetic Equivalent Circuit

The Axisymmetric Problem

A detailed magnetic equivalent circuit of the axisymmetric solenoid actuator with a flat-faced configuration has been presented. All the airgap paths were modelled: the working airgaps, the inner and outer fringing as well as the slot leakage. A more flexible model of the fringing permeance was obtained by combining conventional design techniques and new ideas based on conformal transformations. The effect of saturation was modelled by dividing the flux paths within the iron in several slices. The division was refined in the armature and the core yoke characterised by a wide spectrum of saturation intensities. The mmf drop in the limb due to leakage was also modelled. As the permeance expressions are all a function of the actuator dimensions and do not include any correction factor, the magnetic equivalent circuit was shown to be relatively accurate in spite of dimension change within a sensible current range. The static force was derived from the computation of the coenergy. A validation of the analytical results included a comparison of the magnetisation characteristics and static forces, for several airgap lengths and designs, with finite-elements and measurements. In all cases a good agreement was obtained.

In order to increase the range of accuracy to highly saturated devices (above 2T), it was proposed that the model should also simulate the more complex mechanisms of de-saturation, which mainly involve short-circuiting the saturated limbs by an increasing proportion of flux through the constantly evolving outer fringing and leakage paths. In practice, a more refined model of the limbs could be implemented in which the leakage and outer fringing permeances are broken into several tube elements covering the entire limb length. This approach would also lead to an increase in the computation time as

several simultaneous iterative processes would then be required.

MEC as a Preliminary Design Method for Pot-Core Actuators

The development of a magnetic equivalent circuit for the magnetostatic analysis of axisymmetric solenoid actuators could be easily argued. Indeed, a 2D finite element analysis with a well-defined mesh density can nowadays reach a high computational speed. Therefore one could easily imagine a link between a finite-element package and a preliminary design tool. The design developments would be implemented in the CAD tool; the device geometry and material properties would then be transferred through a software link to the finite-element package leading to a refined computation of the magnetisation characteristics and also static forces.

This is certainly an interesting option for the magnetostatic analysis of the axisymmetric solenoid actuators. However the development of the magnetic equivalent circuit was motivated by:

1. The overall objective of this project which was the evaluation of the dynamic performance of solenoid actuators including armature movement and eddy current generation. This could not be accurately implemented on the post-processing results of a magnetostatic numerical analysis (independent of its computational speed).

2. This speed off-set between the numerical methods and the MEC is still highly relevant for designers doing repeated design trials.

3. The magnetisation curve and static force results obtained from the MEC agree within 5% with finite-elements and measurements. This accuracy is excellent for a preliminary design evaluation.

Therefore, although the MEC can only model the general basic geometric characteristics of the actuator, a good understanding of the magnetostatic performance of the solenoid actuator can already be achieved with this method. A more refined evaluation can then be obtained with the help of a numerical technique. The magnetic equivalent

circuit approach has however an important drawback: high development costs.

MEC and Other Actuator Types

The magnetic equivalent circuit is in theory applicable to any type of solenoid actuators [18]. The good performance of the MEC developed for the cylindrical flat-faced armature type tends to confirm the great potential of this method for any axisymmetric solenoid actuator. However the static performance of some plunger-type solenoid actuators may also be significantly affected by local saturation, occurring during partial overlap between the plunger and the core. In the case of the switched reluctance machines, it was shown that the analytical evaluation of these local nonlinear phenomena was rather difficult. Therefore the accuracy of the MEC may be affected by this problem.

The Rectangular Problem

A similar magnetic equivalent circuit was conceived for computing the magnetostatic performance of the E-core solenoid actuator. All the airgap paths including end-effects were modelled as well as saturation and mmf drop in the limbs due to leakage. The magnetic effect of a small variation between armature and core width (increasing the outer fringing flux) was also incorporated in the model.

At low saturation, the magnetisation characteristics and static forces computed with the MEC agreed within 5% with 3D finite-element and measurement results. However the computation of the static force based on the magnetisation characteristics significantly deteriorates with saturation increasing such that, at the smaller validated gap length, a difference of 23% was observed between the analytical and numerical results. The static performance of the rectangular device are more affected by the model weakness which is the simulation of the interaction between flux paths in the iron and in the surrounding air (end-effects). This is reflected in the analytical force prediction at higher currents.

A more accurate analytical model of the E-core actuators, characterised by very

short stack lengths, would require a better understanding and modelling of the end-effect flux paths in the MEC.

However, it was shown that the predictions of the MEC were significantly better than with a 2D finite-element analysis which certainly requires an end-effect correction factor.

MEC as a Preliminary Design Method for E-Core Actuators

Although the level of accuracy is not as high as in the pot-core case, the MEC for rectangular solenoid actuators is still a valuable method for rapid computer aided design considering the time required for running a 3D finite elements analysis. The designer should however be aware of the margin of error expected in the saturation region.

MEC and Other Actuator Types

The E-core actuator and the U-shape type [18, 46] are the most common fast-acting rectangular solenoid actuator configurations. The development of the previous work to a U-core solenoid actuator would be relatively straightforward. Also the magnetic equivalent circuit for both types of actuator would share the same advantages and disadvantages: fast computation, good accuracy at low currents, characterised by a decreasing trend with saturation increasing.

8.1.2 Magnetic Gauge Curve

The concept of gauge curve was introduced in chapter 3. More than a mathematical tool, it was shown that the gauge curve, based on a normalised current model, is an efficient way to store the magnetic information specific to the intermediate positions of the moving part. The complete magnetic data of the actuator is then restored by evaluating just two magnetisation curves corresponding to the minimum and maximum airgap lengths, containing the bulk saturation information, and the gauge curve. It was

shown that this method could in principle be applied to any type of variable reluctance machine.

For the axisymmetric and rectangular solenoid actuators with a flat-faced armature, it was shown that the gauge curve method could perform as well as the MEC. These results were partly expected as the gauge curve was computed from the MEC permeance elements.

Although it is not demonstrated in the thesis, it is very probable that this method would outperform the MEC if the two magnetisation characteristics and the gauge curve itself were computed directly from finite-elements. Only a linear 3D numerical analysis would then be required for the gauge curve corresponding to the rectangular device which would therefore include an accurate 'picture' of the end effects.

Also this method leads to an analytical expression of the static force as a function of flux linkage and armature position, meaning an instantaneous static force evaluation.

Gauge Curve Method as a Preliminary Design Method

From the previous findings, it is clear that this approach has great potential within a rapid computer aided design tool due to its computational advantages.

Gauge Curve Method and Other Actuator Types

The gauge curve method is a general technique applicable to any type of variable reluctance device. The final expression of the gauge curve is a function of the magnetic characteristics of the actuator at its intermediate plunger/armature positions. In the case of the rectangular and axisymmetric actuators with a flat-faced armature, the gauge curve was reduced to a single curve, a function of the armature position. In general, the gauge curve will depend on armature/plunger position and also flux linkage (due to local saturation).

8.2 Dynamic Analysis

The dynamic performances of solid iron or partly solid iron solenoid actuators are significantly affected by the magnetic damping caused by the eddy current generation. For this reason the analysis of eddy currents was limited to the thick iron pieces and assumes an 'ideal' nonlinear magnetic behaviour within the laminated parts.

8.2.1 Axisymmetric Solenoid Actuator

The first step in the evaluation of the dynamic model involved the development of an electromagnetic model of the flux and eddy current diffusion within an infinitely long bar of solid iron (1D problem). The latter was directly derived from first principles such that the nonlinear properties of the material were modelled accurately.

Based on finite-element results computed during an impact excitation, it was proposed to divide the actuator into closed flux tubes and associate to each of them a 'layer' (i.e. an eddy current resistance and a nonlinear inductance) of the diffusion network derived for an infinitely long bar. This approach was physically valid as each closed flux tube contained its own eddy current loops in each of the actuator subsections. The eddy current resistance per layer was then evaluated analytically based on the closed flux tube dimensions and steel resistivity. The nonlinear relationship between the flux linkage produced in each flux tube (layer) and the magnetising current was retrieved from the static magnetisation characteristics of the actuator by applying a scaling factor to the closed flux tube flux linkage. This scaling factor was simply the ratio of the actuator cross-section area to the closed flux tube area, constant for each actuator subsection (limbs, yokes). The relation between the driving circuit and the actuator diffusion network was derived from Ampere's law and leads to the same expressions as the ones relating the secondary to the primary winding of a transformer. In this case the secondary had only one turn.

In order to model more accurately the diffusion of the flux and eddy currents through the iron, a quadratic distribution of the layers within the actuator was chosen

such that the first layer, closed to the slot, was extremely thin leading to a very high iron resistance. The total number of layers was deduced from computation and was chosen as the minimum number of layers leading to steady current and force waveforms. In general the actuator dimensions and driving conditions should be taken into account for choosing an appropriate value for this variable.

This electromagnetic equivalent network for axisymmetric actuators has many computational advantages:

1. The number of equations for the dynamic analysis is reduced to $Nc + 2$: the mechanical equation modelling the armature movement, the electrical equation of the driving circuit and Nc equations for the Nc network layers.

2. The computation does not require any matrix handling or iterative approach.

3. The evaluation of the magnetising current in each layer from the corresponding flux linkage can be based on the magnetisation characteristics of the actuator. This operation repeated Nc times per time step is accelerated by using the gauge curve method.

4. A particular algorithm for evaluating the transient force was proposed with this network leading to a minimum data storage, a rapid computation and a high level of accuracy.

5. Force, eddy currents, total current as well as iron loss waveforms can be easily and rapidly retrieved for the network.

The proposed network is therefore a very suitable algorithm for rapid-computer aided design.

During validation, several driving schemes were tested:

An impact excitation

The transient analytical current and flux linkage (or induced voltage) waveforms were compared with transient finite-elements and measurements and lead to a

good agreement in both cases. Various step voltages and airgap lengths were tested. In the measurements, the step voltages were relatively low due to a winding temperature rise which limited the eddy current generation. However, in the finite-element comparison, the step voltage was set to 90V, leading to a significant amount of eddy currents.

A dynamic sequence

The sequence included an impact excitation with current control followed by a free-wheeling period before switching off. The comparison was obtained using finite-elements. Current, total eddy current, force and armature displacement waveforms formed the basis of the discussion. It was observed that while the current was still flowing in the winding, both simulations agreed well in terms of current, force and displacement. Although the general trends were respected, the analytical model lead to a larger generation of eddy currents. During the switch-off period, a large discrepancy in the force prediction could also be observed as soon as the current dropped to zero. The analytical simulation gave a force decay response which was too slow. Based on finite-element results, it was shown that both problems were linked to a previous assumption: the division of the actuator into closed flux tubes leading to a single diffusion network for the entire actuator.

A transient test

This test involved a step voltage, a fixed duty cycle control following by a free-wheeling period before switching off. The simulation results, compared with the measurement data, included the current and force waveforms and mainly confirmed the conclusions deduced from the previous validation.

Therefore this electromagnetic equivalent circuit is only valid for modelling impact excitations. However it was shown that relevant design information could already be retrieved from the computation of this network such as a comparison of different material performance, an evaluation of the armature dimension or the number of turns. An accurate evaluation of the magnetic damping, under any driving conditions, requires a more complex circuit representation of the actuator dynamic characteristics.

In order to accurately evaluate the eddy currents, it was concluded that the airgap permeances should be removed from the diffusion network and stand as separate elements in the equivalent circuit. In this case, the amount of ampere-turns available for magnetising the iron or generating eddy currents is then equal to the total amount provided by the source (which was the case with the first network), less the ampere-turns required for magnetising the airgaps.

In order to solve the flux decay discrepancy it was concluded that the electromagnetic equivalent circuit should give more flexibility to the flux path direction varying with the imposed driving conditions. A modified electromagnetic equivalent circuit was then proposed. This network included two diffusion networks, one for the armature and one for the core. Both are connected in parallel with the main airgap and fringing permeances, and connected in series with a total leakage permeance. Although these modifications are logical, the new network configuration has not been validated as such and is therefore a recommendation for future work.

Other Actuator Types

Based on these findings, similar development should be possible for any configuration of axisymmetric solenoid actuators. The computation of the iron resistance for each diffusion network should be relatively straightforward as eddy currents are flowing in well-defined circular loops. The support of a transient finite-element analysis is however recommended during the development of the analytical model.

Depending on the required level of accuracy, more refined models could be developed by dividing the actuator iron sections into more pieces, each represented by a different diffusion network. Based on this approach, a more refined airgap permeance distribution can therefore be considered. However such an approach would automatically lead to a slower and more complex computation algorithm.

A Preliminary design Method

This method is certainly a relevant analytical technique for rapid computer-aided dynamic analysis as it models accurately the nonlinear magnetic material properties, the

entire actuator geometry and dimensions. It also simulates the generation of eddy currents dues to any driving conditions as well as their variation caused by armature movements. Transient force and eddy current loss can also be retrieved easily.

8.2.2 Rectangular Solenoid Actuator

Based on the experience gained from the axisymmetric problem, a similar approach was followed in order to evaluate the dynamic performance of rectangular solenoid actuators. However, the eddy currents were neglected in the laminated core compared to those generated in the solid iron armature (at the origin of the magnetic damping).

An electromagnetic equivalent network of the rectangular actuator was proposed and included a diffusion network for the armature and a series of linear and nonlinear permeances for modelling the iron core sections and surrounding airgap paths. It was found that this network required an iterative algorithm, slowing down its computation.

The evaluation of the diffusion network elements was obtained by dividing the armature into flux tubes and approximating the eddy current paths in each of them. This task was relatively difficult due to the presence of end-effects affecting both eddy current and flux paths and was achieved with the 'visual' support of a transient 3D finite-element solution corresponding to an impact excitation, computed at a fixed airgap length.

Although some simplifications were introduced in the armature diffusion model, it appeared that the eddy current paths were still a function of an unknown parameter $xAstk$, significantly affecting the magnitude of eddy current resistances as well as their relative variation in the successive layers. An evaluation of this parameter was easily obtained by tuning the analytical prediction of the iron loss waveform with the finite-element solution computed for an impact excitation. This parameter was defined as a function of the armature depth.

During this development it was also found that the inner fringing flux could not flow through the armature due to the high eddy current and flux density in the armature

layers above the slot. It was concluded that the inner fringing permeance should be replaced by an equivalent leakage element, short-circuiting the armature. Although this has not been demonstrated, this assumption should not greatly affect the steady state prediction of the network as the inner fringing flux is, in steady state, negligible compared to the other airgap flux.

Based on these assumptions, a good agreement was obtained for the transient current and force waveforms computed with the electromagnetic equivalent circuit and 3D finite-elements. In this approach, the eddy current paths and therefore resistances per layer are implicitly assumed to be a function of the armature dimensions and not the driving conditions. This property could be observed in the transient finite-element results obtained for the axisymmetric actuator. The transient analytical current and force waveforms corresponding to a different actuator design and airgap length were compared with measurement data and lead to a good agreement.

So far the results obtained in the thesis tend to demonstrate that this method has some great potential for computing the dynamic performance of rectangular solenoid actuators. The model development is however relatively tedious, and although an iterative algorithm is required for solving the equivalent circuit, the proposed model is significantly faster than a time-stepping 3D finite element analysis. The support of the latter was however essential in the construction of the armature model.

More validation has still to be provided in order to establish real confidence in the applicability of this dynamic model for rectangular solenoid actuators. In particular the field of validation should include various driving conditions, different airgap lengths and armature dimensions. It should also be noted that the proposed armature model is a simplified 2D model of a 3D complex diffusion problem. New ideas for a more accurate and practical evaluation of the eddy current resistances could also be sought.

Appendix A

Double Salient Rotary Machine

The evaluation of a gauge curve for switched reluctance machines is at the other end of the 'difficulty scale'. Their complex nonlinear magnetic behaviour makes them a very good complementary test to the gauge curve application, from which the case of 'intermediate' devices (e.g. plunger type actuator) may be more easily extrapolated.

A.1 Gauge Curve for SR Machines

The gauge curve analysis for SR motors is demonstrated on a set of magnetisation curves obtained by measurement on a 4 phase 8/6 SR motor. The main characteristics of this conventional machine are stated in table A.1. Based on the general theory, the gauge curve for the given SR motor is evaluated graphically by computing eq. (3.1) at several constant flux linkages. The result of this operation is given in fig A.1.

The normalised current is a complex function of both rotor position and flux linkage in the case of the SR motor. However equation (3.3) shows that, at very low flux linkage, the gauge curve can be approximated with fair accuracy as a function of the total airgap permeance only. This particular curve which is labelled 'reference curve' on fig. A.1 corresponds therefore to:

$$I_N(\theta,\psi) \approx I_N(\theta) = \frac{\frac{1}{P_{gtot}(\theta)} - \frac{1}{P_{gtot}(\theta_a)}}{\frac{1}{P_{gtot}(\theta_u)} - \frac{1}{P_{gtot}(\theta_a)}}, \qquad (A.1)$$

Stator outer diameter (mm)	120.7
Stator slot-bottom diameter	96.8
Rotor outer diameter	60.0
Rotor slot-bottom diameter	43.2
Air gap	0.3
Shaft diameter	25.4
Stack length	75
Stator pole arc	22.6
Rotor pole arc	23.0
Steel	29GM19
Turns per pole	38

Table A.1: 8/6 Switched Reluctance Motor Data.

where θ defines the rotor position.

By increasing the flux linkage, this curve changes position due to an mmf drop occurring in the iron which is different from the bulk saturation. The origin of this mmf drop is analysed by substracting the content of the reference curve from the other curves. The result of this operation is plotted on fig A.2 where every curve is still defined at constant flux linkage.

It is observed in fig A.2 that:

1. The greatest change in normalised current occurs over a relatively small range of rotor positions; this range being characterised by a relatively small overlap.

2. The number of positions affected by this mmf drop increases with the flux linkage level.

The variation of the gauge curve with flux linkage reflects therefore the local saturation occurring at the poles as they partially overlap. Due to a large fringing effect around the pole tips, the magnetic overlapping starts slightly earlier than the physical one and is also completed earlier. The bulk saturation occuring in the stator and rotor yoke has been removed from (3.3) as this is a common mmf drop for any position at constant flux linkage.

A.1.1 Magnetic Circuit

A magnetic equivalent circuit has been developed to model the mmf drop in the poles of the given motor. For this purpose, eq.(3.3) is modified as follows:

$$I_{Ni}(x,\phi) = \frac{\frac{1}{P_{gtot}(\theta_i)} - \frac{1}{P_{gtot}(\theta_a)} + (K_{si}(\phi,\theta_i) - 1)\sum_j H_{aj}\, l_{aj}/\phi}{\frac{1}{P_{gtot}(\theta_u)} - \frac{1}{P_{gtot}(\theta_a)} + (K_{su}(\phi,\theta_u) - 1)\sum_j H_{aj}\, l_{aj}/\phi}, \tag{A.2}$$

where K_{si} is defined as a local saturation coefficient given by:

$$K_{si}(\phi,\theta_i) = \frac{\sum_j H_{ij}\, l_{ij}}{\sum_j H_{aj}\, l_{aj}}, \tag{A.3}$$

defined at constant flux linkage. In (A.2), the mmf drop in the poles at the aligned position, divided by the total flux, is approximated by using the geometric characteristics of the motor:

$$\sum_j H_{aj}\, l_{aj}/\phi = \frac{4\, la}{\mu(\phi/A_p)\, A_p}, \tag{A.4}$$

where la is chosen as the average of the stator and rotor pole lengths, Ap the smallest iron cross-section between stator and rotor poles [1]. $\mu(\phi/A_p)$ is the absolute permeability computed from the iron BH characteristic. The computation of the total airgap permeance $P_{gtot}(\theta_i)$ is deduced from the measurement set at very low flux linkage, by assuming an infinite permeability in the iron.

Computation of Ksi

The computation of the local saturation coefficient Ksi is the core of this problem. The SR motor poles are divided into three regions in which the mmf drop is separately computed (see fig A.3).

Region I. The mmf drop at any intermediate position is computed as follows:

$$H_{iI}\, l_{iI} = H(\frac{\psi\, Prop}{N A_p})\,(la - l_{YP}), \tag{A.5}$$

where N is twice the number of turns per pole (connection in series) and l_{YP} the distance between Y and P. The magnetic field H is computed from the BH

[1] For simplification, the stack factor F_{stk} has been neglected in the computation of the gauge curve but could be easily introduced by replacing A_p with $F_{stk}\, A_p$.

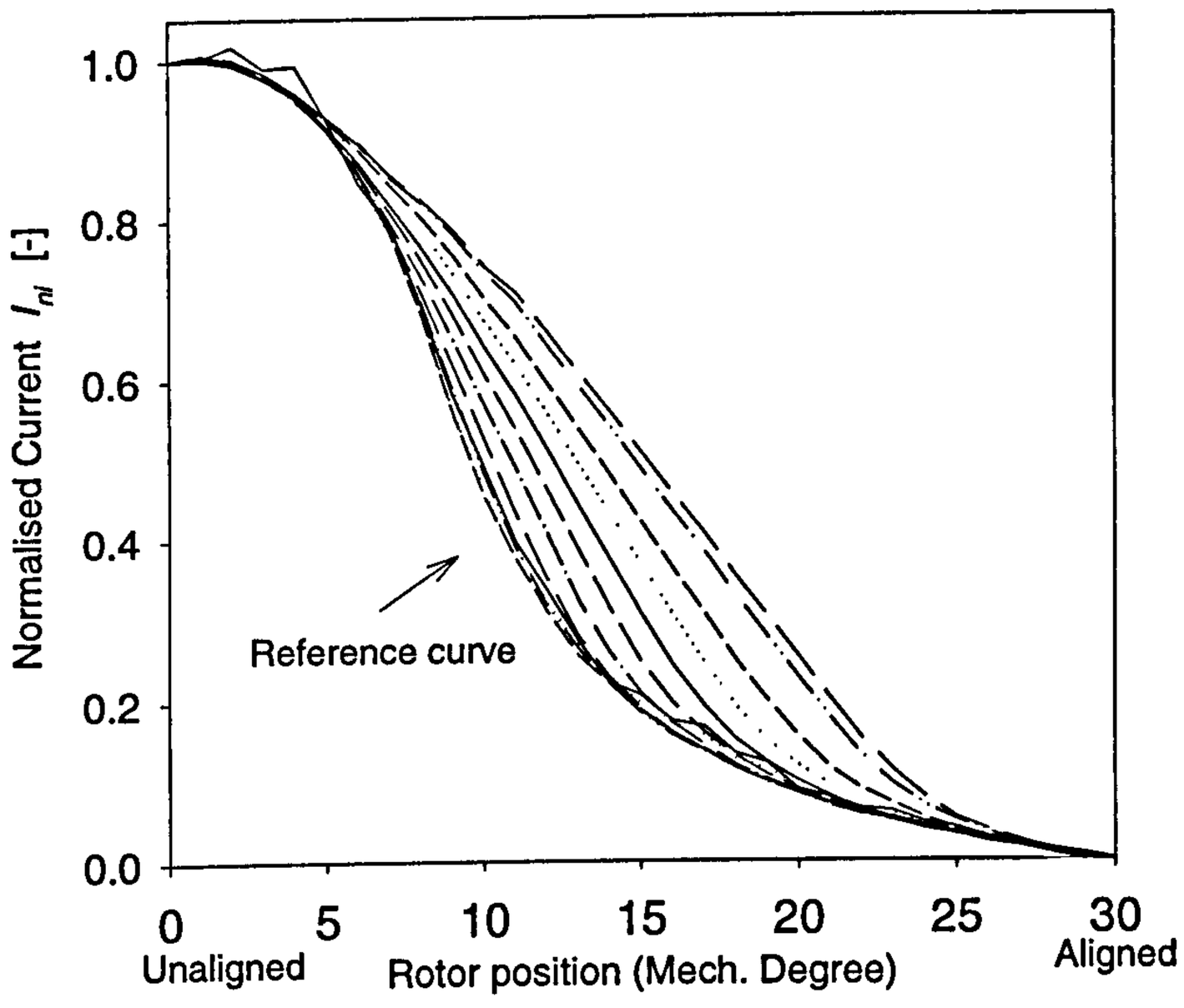

Figure A.1: Measured Gauge Curve for 8/6 SR Motor

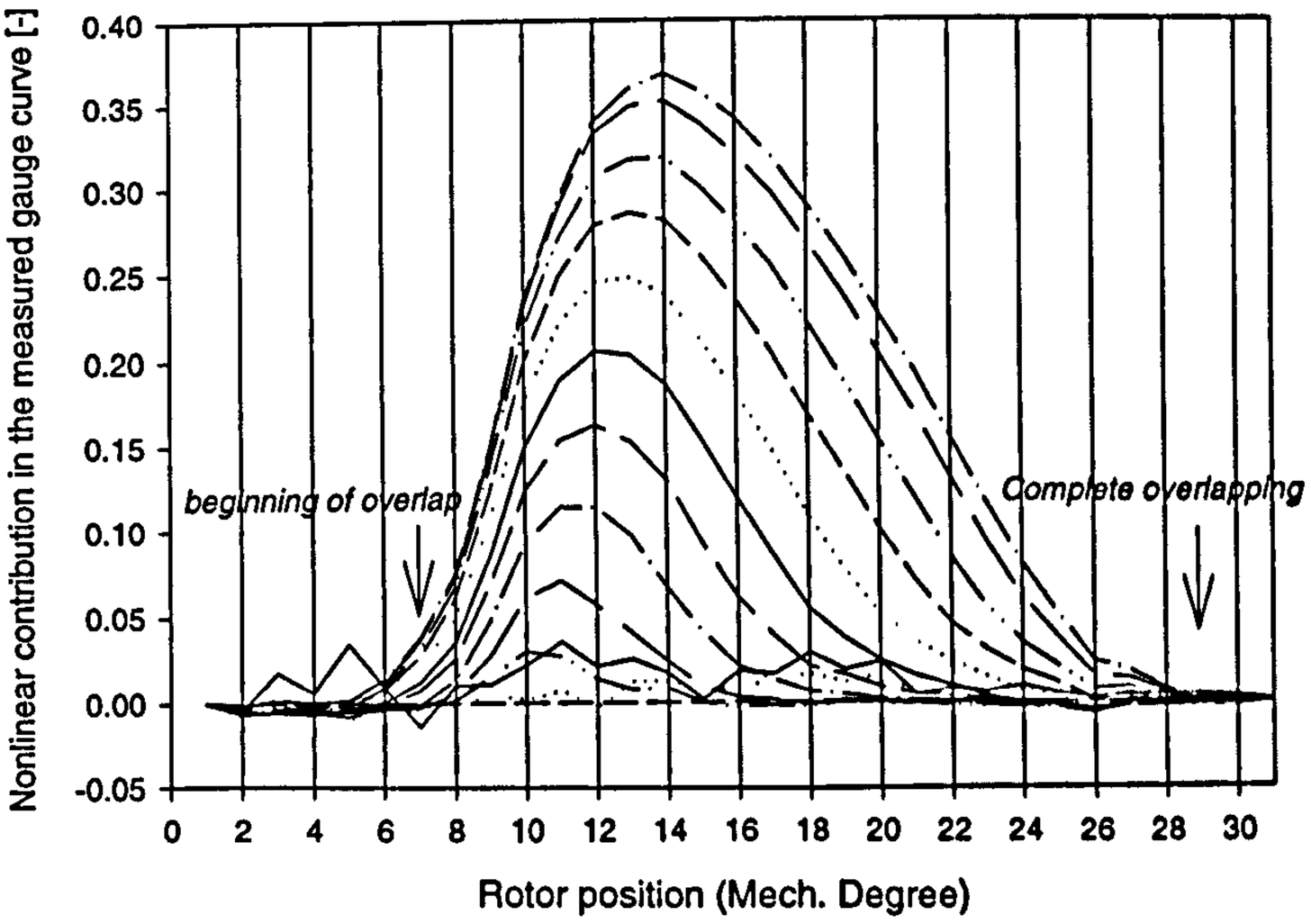

Figure A.2: Nonlinear contribution in the measured gauge curve.

characteristic. The function *Prop* is given on fig. A.4 and simulates the effect of the slot leakage as a function of position.

Region II. The average magnetic field length starts within region II at $P2$ at half pole width, and finishes with $P3$ whose position varies with the rotor position and is defined by the function Wp (equal to $YP3$). The mmf drop in region II is computed by replacing the line $P2P3$ by several arc sections of different radii:

$$H_{iII}\, l_{iII} = \sum_{k}^{N_{sections}} H\left(\frac{\psi\, Prop}{N A_p}\right)\left(l_{YP2} + \frac{(l_{YP3} - l_{YP2})\, k}{N_{sections}}\right) \frac{A_l}{N_{section}}, \qquad \text{(A.6)}$$

where $N_{sections}$ gives the number of sub-sections in region II, l_{Ypi} defines the distance between Y and Pi, and A_l corresponds to the angle beween $YP2$ and $YP3$.

Region III. Compared to the two previous regions, the analysis of region III is relatively complex and is based on a series of assumptions.

If the effective overlap is first assumed equal to the physical overlap (no fringing effect), the area of possible local saturation, at a given rotor position, is approximated by a triangle YPT [57] (see fig. A.3) whose :

- base Ax is equal to the partial overlap existing at this position ,
- and hypotenuse (YT) is equal to Ap.

The choice of Ap as the hypotenuse of the triangle of local saturation results from the fact that the local saturation means, in this context, a higher saturation than the one obtained at the aligned position for the same flux linkage. Therefore considering the total flux flowing through the hypotenuse of the triangle, the latter should be either less than Ap for small flux level (no saturation at the aligned position) or equal to Ap for high flux level (with saturation at the aligned position).

The computation of Ksi also requires the evaluation of an average magnetic field path within the triangle (line $P3P4$ in fig. A.3). This path varies within the triangle as a function of rotor position θ and also flux level ϕ. But the difficult task is simplified by assuming that:

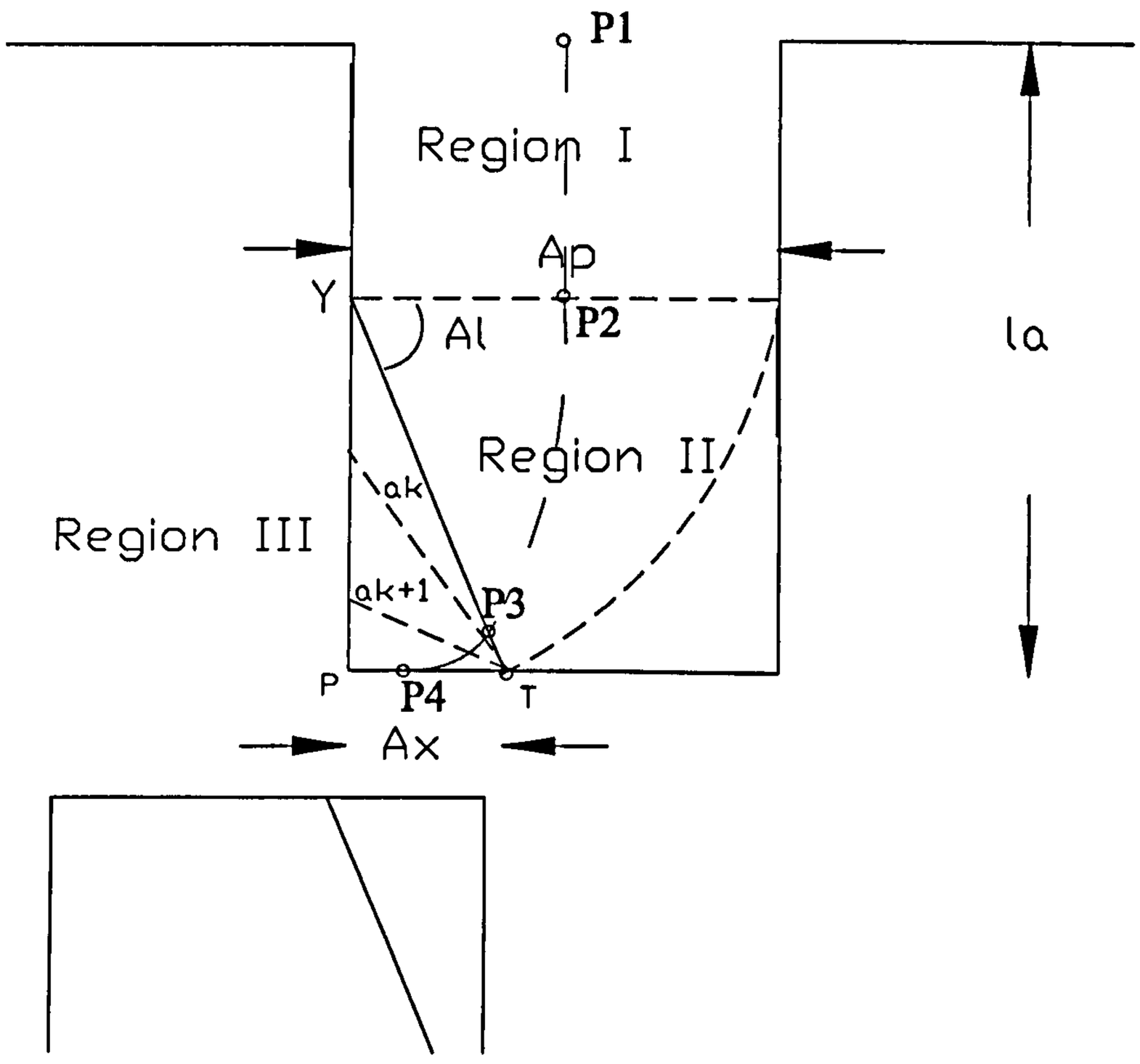

Figure A.3: Model of the local saturation at the pole tips

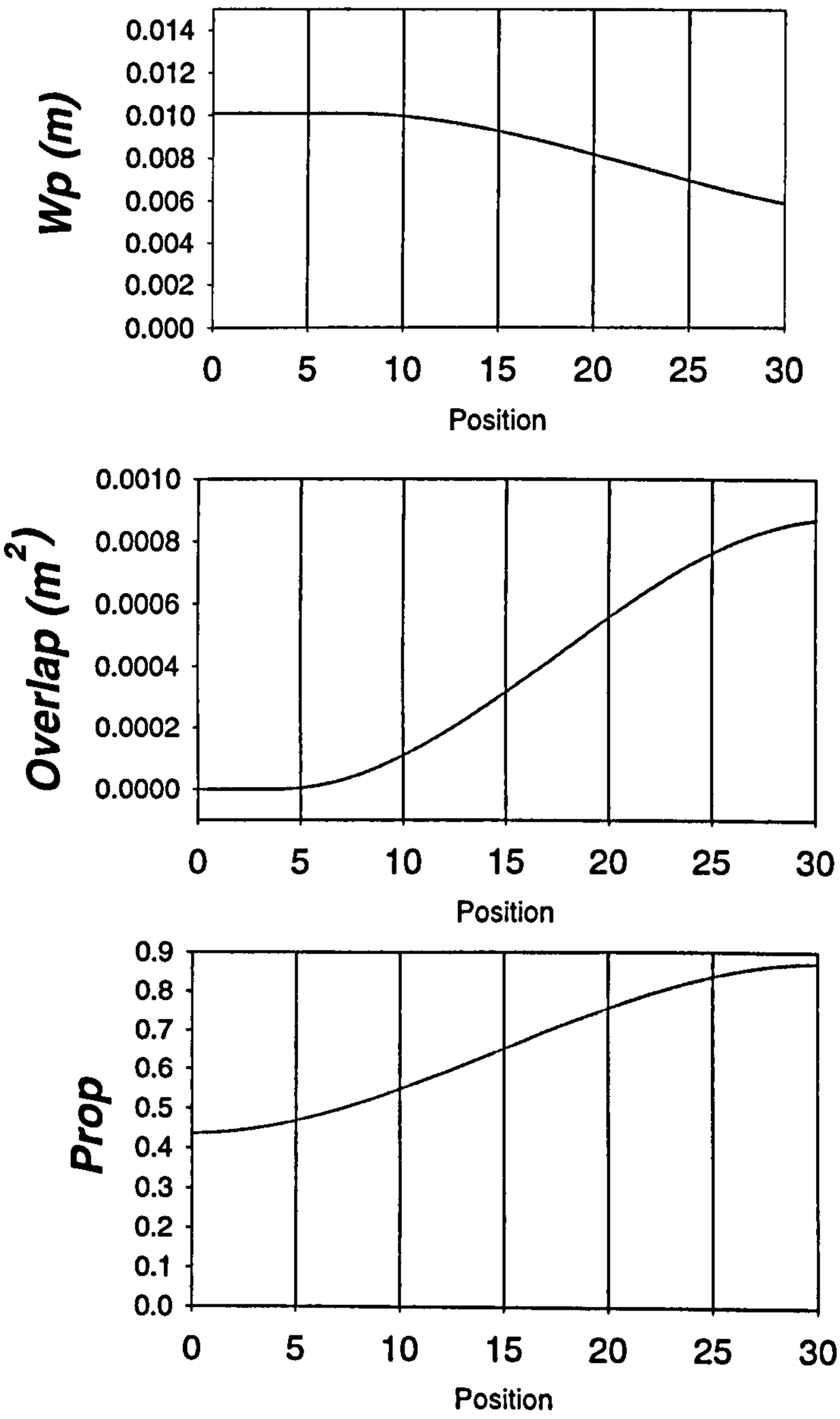

Figure A.4: Variation of variables $Wp, Overlap, Prop$ with rotor position θ

- There is no variation due to flux level.
- The path is approximated by an arc; its centre corresponds to Y in fig. A.3 and its radius Wp (equal to $YP3$) varies continuously from one rotor position to another.

The computation of Wp is such that:

- Approaching the aligned rotor position, the value of Wp converges to half of the pole width.
- The unaligned rotor position (θ_u) is characterised by a symmetric flux distribution between two rotor poles for one stator pole.

When the rotor moves from the unaligned position to the aligned, $P3$ is assumed to move from point T towards the middle of the hypotenuse, giving a variation of arc length within the triangle as a function of rotor position. The resulting variation of Wp with rotor position is given in fig. A.4.

The triangles of saturation, defined in the four active poles (2 stator and 2 rotor poles) are also assumed to be exactly the same. This choice is partly justified by the nearly similar width of the stator and rotor poles in SR motors. The computation of mmf drop within the triangle is obtained by dividing the triangle into sub-sections defined by the lines ak, $ak+1$. These lines, multiplied by the stack length $Lstk$, are equivalent in the model to cross-sections $Ak, Ak+1$ through which the flux is flowing. The smallest area Ax is defined either by the overlap for this position when the average magnetic field path ($P3P4$) reaches the base of the triangle or by the intersection of the arc with the triangle side (YP) for one end and T for the other end. The value of magnetic field H_i in each sub-section is evaluated from the BH curve by computing the corresponding flux density B_k as:

$$B_k = \frac{\phi}{ak\ Lstk} = \frac{\phi}{Ak} \tag{A.7}$$

The associated length l_i (for computing the mmf drop) corresponds to the arc length between ak and $ak+1$.

The overlap is a continuous function of rotor position. It should also reflect the fact that the effective overlap starts before the physical overlap. The chosen function for simulating the variation of overlap is shown in fig. A.4.

Similarly, the quantity of flux flowing through the triangle varies with position. For this reason, a fringing/leakage function, called *Prop*, has been defined (see fig. A.4) which varies with position.

The three functions $Wp, prop, Ax$ are the only three variables which have been considered for fitting the gauge curve model to the measured one. The result is shown on figure A.5, while the computed saturation factor is given in fig. A.6 . The computed magnetisation curves, based on this model and on the knowledge of the aligned and unaligned magnetisation curves, are compared with the measured ones on fig. A.7. The satisfactory agreement between the computed magnetisation curves and the measurements tends to demonstrate that the highly nonlinear magnetic behaviour is then due to the saturation at the pole tips. However, in order to use such a model for any design of SR machines, the fitted functions $Wp, Prop, Overlap$ should be replaced by analytical expressions varying with the geometry and BH characteristics of the motor. Realistically this task is too difficult to be considered seriously.

A.1.2 Piecewise Polynomial Interpolation

In this section, the gauge curve is modelled by using piecewise polynomial equations. The gauge curve has been divided into 5 sections as shown in fig. A.8 where sections II, III, IV correspond to the magnetic overlap. The gauge curve is fitted in these sections with:

$$I_{Ni}(\theta, \psi) = a(\psi)\,\theta^3 + b(\psi)\,\theta^2 + c(\psi)\,\theta + d(\psi) \qquad (A.8)$$

and in sections I, V the computation of the gauge curve is based on eq. (A.1).

The computation of the gauge curve requires the minimum following information:

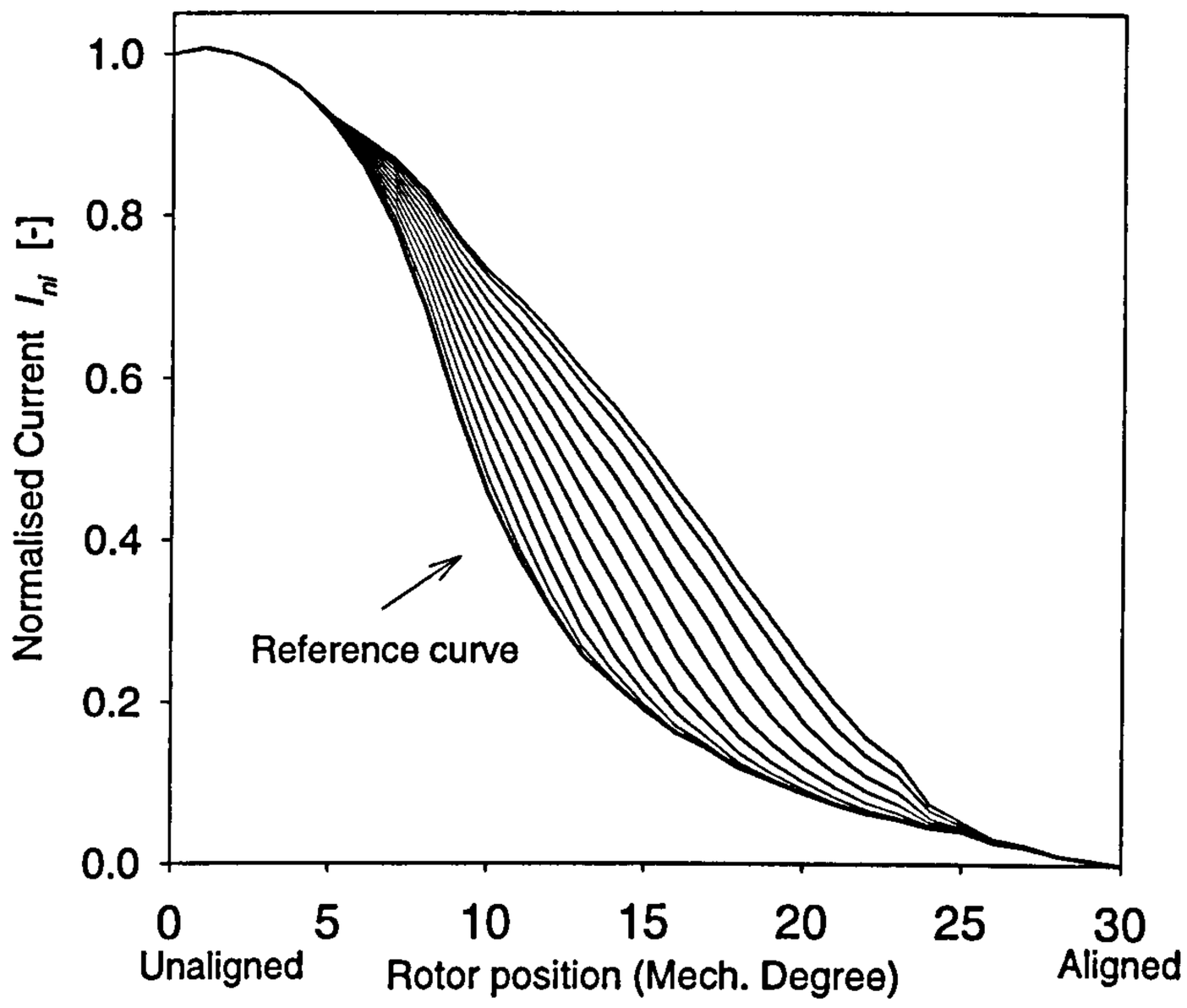

Figure A.5: Computed gauge curve for the 8/6 SR motor

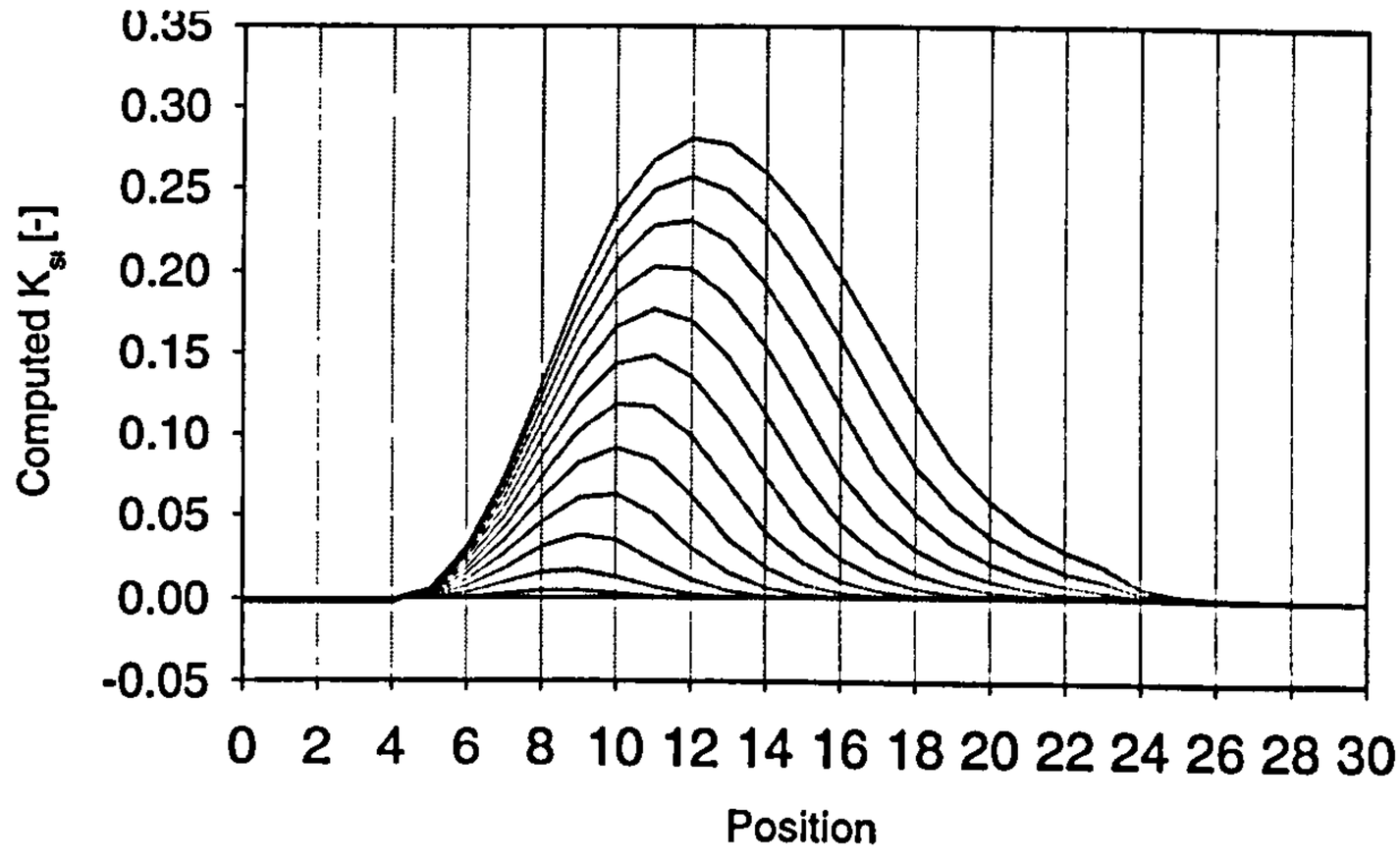

Figure A.6: Computed Saturation Factor Ksi at Different Flux Linkages

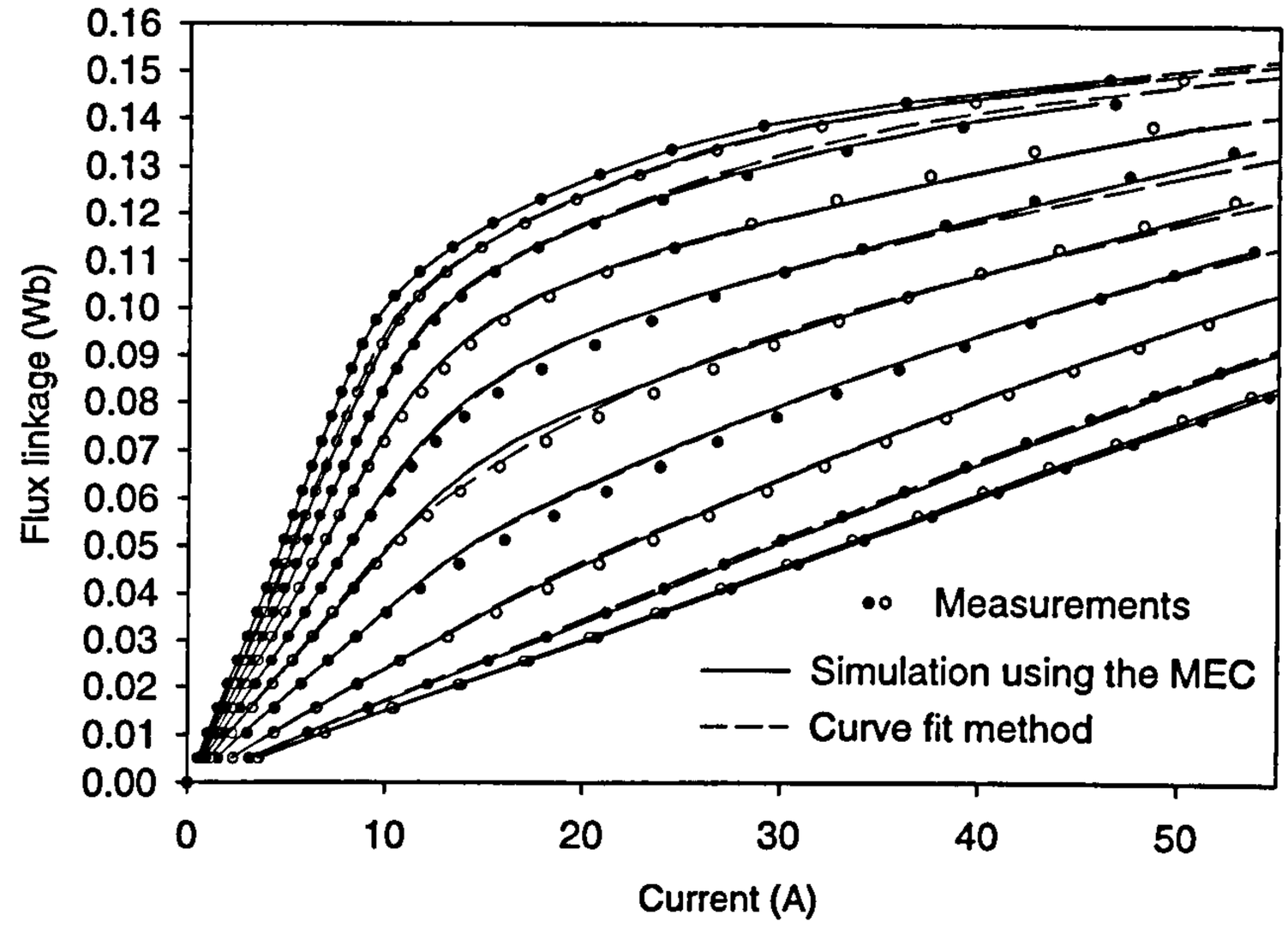

Figure A.7: Magnetisation curves for the 8/6 SR motor obtained from the gauge curve model and compared with measurements

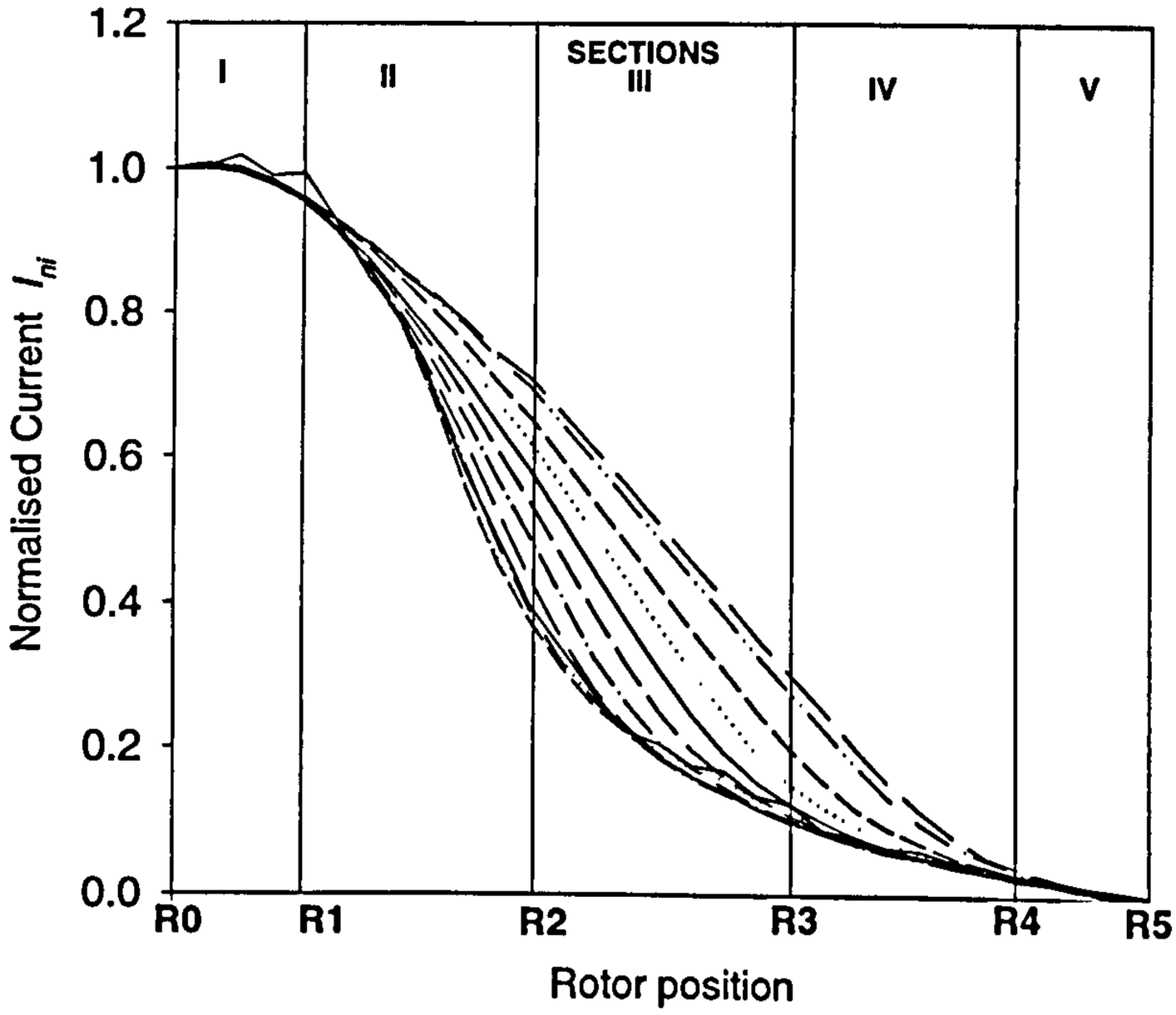

Figure A.8: Gauge curve division for polynomial curve fitting

Section R0-R1 and R4-R5.

The gauge curve at rotor position R0 is equal to 1 and its slope can be approximated to be 0.

Similarly the gauge curve at position R5 is equal to 0 and its slope can be approximated to be 0.

At the rotor positions R1 and R4, the gauge curve can be approximated with only one value if the positions are chosen just outside the effective overlap. Their slope computation requires the evaluation of the gauge curve at 2 different but close positions e.g. R1 and R1$-\delta$R1 (R4 and R4$+\delta$R4).

At R2 and R3

The entire magnetisation curve is required at each of these positions as well as at R2$+\delta$ R2 (or R2$-\delta$R2) and at R3$+\delta$R3 (or R3$+\delta$R3) for computing the corresponding slope.

Fig. A.7 shows the magnetisation curves evaluated from the piecewise analytical gauge curve in dashed lines. The method has been also tested on a 3 phase 6/4 SR motor and fig. A.9 gives a satisfactory agreement which could probably be improved by optimising the choice of rotor positions R1, R2, R3, R4.

The piecewise polynomial approximation for I_{Ni} requires then more magnetic information than the model presented by Miller [37]; but a higher level of accuracy is also expected when computing the intermediate magnetisation curves and also the static torque.

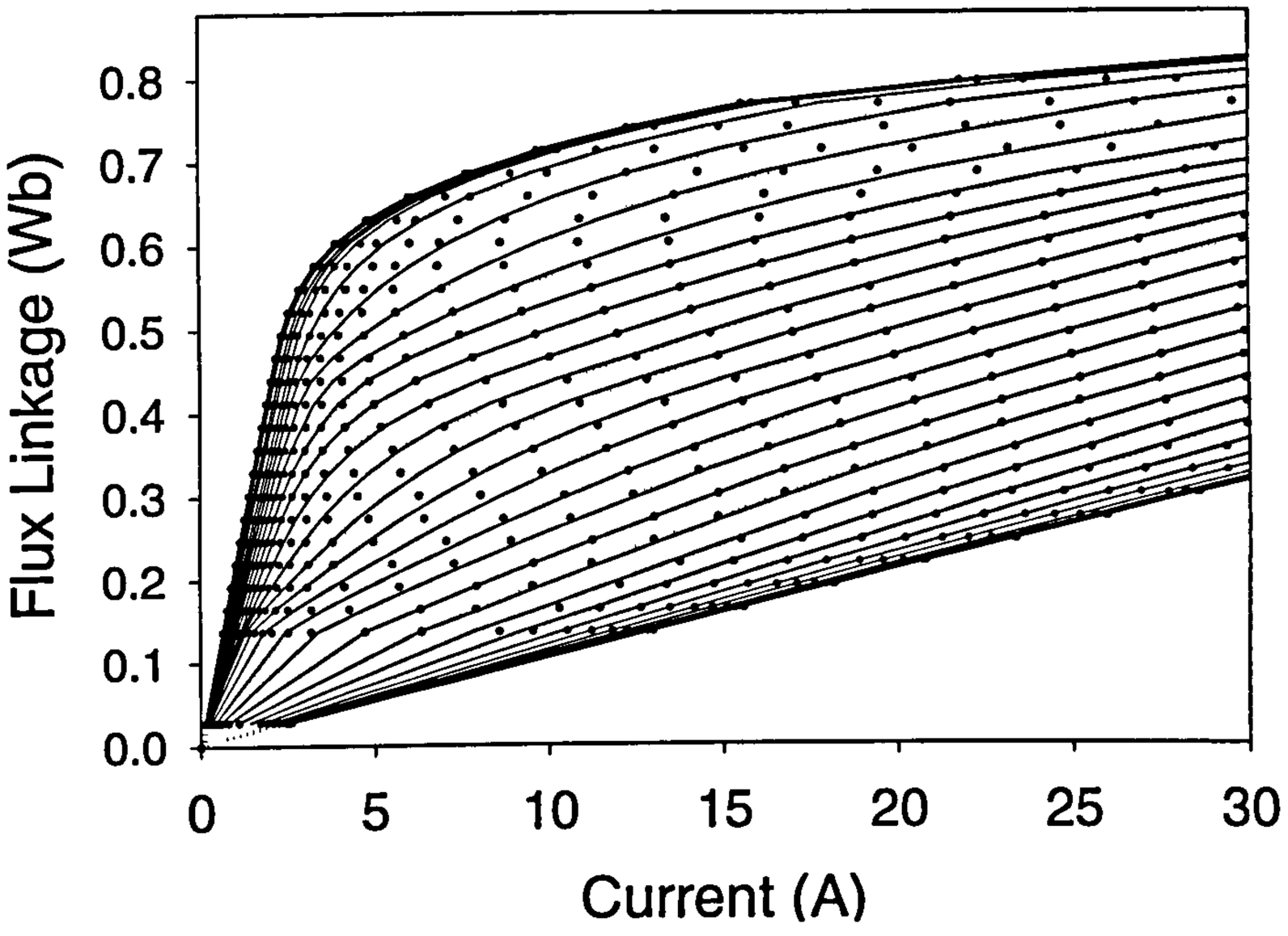

Figure A.9: Magnetisation characteristics for 3 phase 6/4 SR motor. FEA (dotted lines), gauge curve method (solid lines).

A.2 Magnetostatic Torque Computation

The slope continuity between two successive curve sections is important for computing the static torque Te, which is based on the same formulation as developed for solenoid actuators (section 3.2.3). Depending on the rotor position however, the gauge curve is expressed differently such that:

- In the effective overlap position range:

$$Te = -\int_0^{\psi} \frac{\partial I_{Ni}(\theta,\psi)}{\partial \theta}\,(I_u(\psi) - I_a(\psi))\,d\psi, \tag{A.9}$$

in which I_{Ni} is replaced with (A.8) and differentiated in function of θ:

$$Te = -\int_0^{\psi} (3\,a(\psi)\,\theta^2 + 2\,b(\psi)\,\theta + c(\psi))\,(I_u(\psi) - I_a(\psi))\,d\psi, \tag{A.10}$$

A complete analytical force computation would require an analytical approximation for both aligned and unaligned magnetisation characteristics [37, 22, 25].

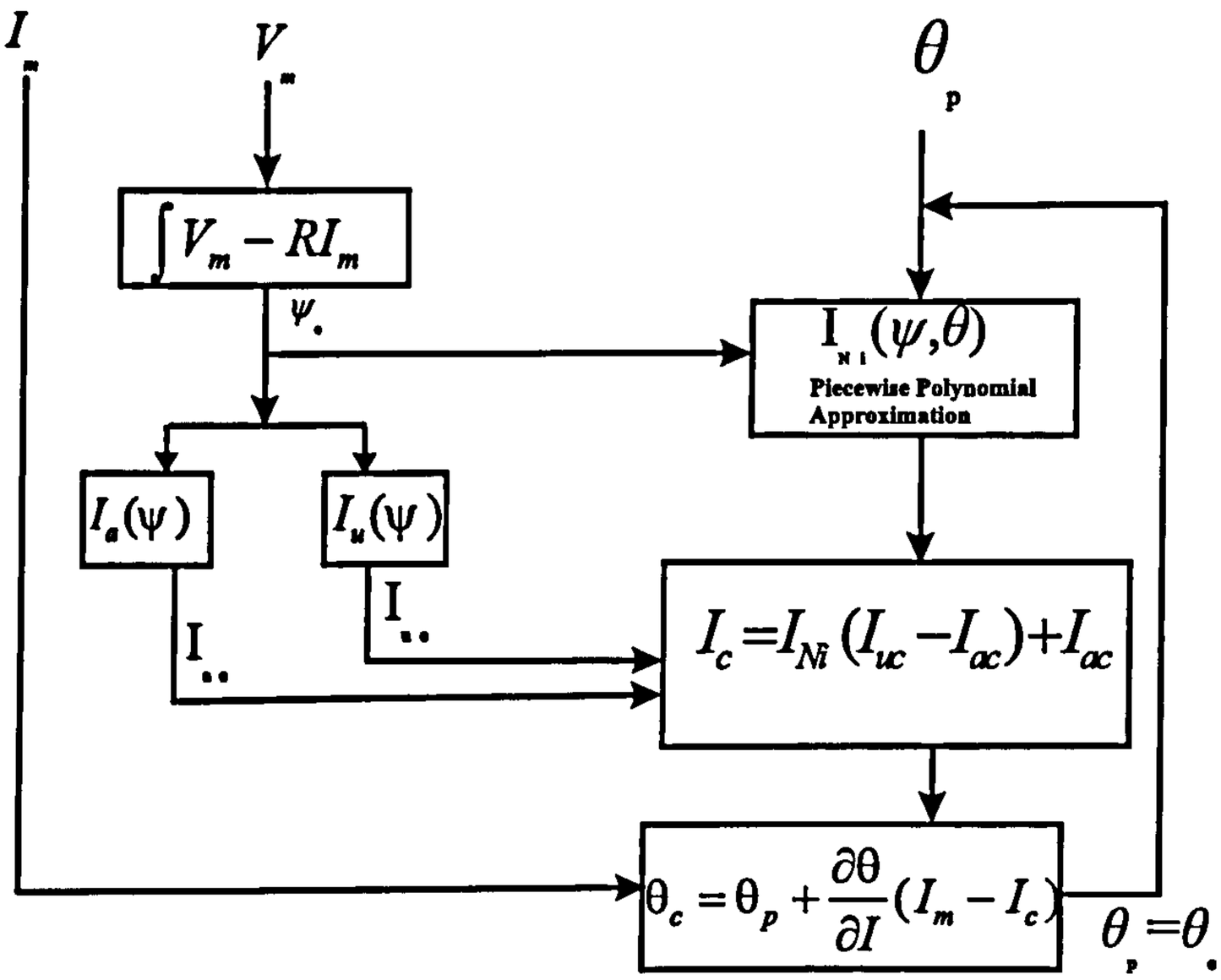

Figure A.10: Simplified rotor position detection scheme for SR motors

- Outside the effective overlap position range, the gauge curve is only a function of θ and the magnetostatic torque is computed from:

$$Te = -\frac{\partial I_{Ni}(\theta)}{\partial\theta}\int_0^{\psi}(I_u(\psi) - I_a(\psi))\,d\psi. \tag{A.11}$$

A.3 Rotor Position Detection Scheme

Although it is not demontrated here, the polynomial approximation of the gauge curve may also give new opportunities for improving high-grade position estimation (and detection) scheme based on the knowledge of the magnetisation data [38]. The application of the gauge curve would lead in this case to a drastic decrease in the required amount of stored information. Indeed the analytical gauge curve gives a direct access to the magnetic data $I(\theta,\psi)$ and also to $\frac{dI}{d\theta}$. The computation speed would also be improved which is an important issue for real-time implementation.

An example of possible rotor detection algorithm, based on the gauge curve, is given

in fig. A.10. The scheme includes the following steps:

1. At every sampling time, the flux linkage ψ_c is computed from the measured voltage V_m and current I_m (R being the total circuit resistance).

2. Then at ψ_c, the magnetisation currents (I_{ac}, I_{uc}) are computed from the known magnetisation curves corresponding to the aligned and unaligned positions.

3. The normalised current $I_{Ni}(\theta_c, \psi_c)$ is then evaluated from the known piecewise gauge curve model with a predicted value of the rotor position θ_p.

4. From eq. (3.1), an estimated current I_c is computed and the difference between I_c and I_m is introduced in the position corrector scheme, leading to a corrected value of rotor position $\theta_p = \theta_c$ [2].

[2]This scheme could be based on $(\frac{\partial I}{\partial \theta})$ estimated at ψ_c and at θ_p as it can be directly derived from the gauge curve.

Appendix B

Publications

Only two papers have been published on the material presented in this thesis.

- The first one entitled "**The Application of Magnetic Gauge Curves to Linear Motion Solenoid Actuators and Rotary Doubly Salient Reluctance Machines**" was presented last September at the International Conference on Electric machines (ICEM'98) organised in Istanbul. The author is: M.Piron.

- The second one entitled "**Rapid Computer-Aided Design Method for Fast-Acting Solenoid Actuators**" was presented last October at the IEEE Industry Application sociaty (IAS) at St. Louis, US. This paper is also scheduled for publication in the IEEE transactions, Sept./Oct. 1999. The authors are: M.Piron, P. Sangha, G. Reid, T.J.E. Miller, D.Ionel, J. Coles.

Bibliography

[1] D.C. White and H.H Woodson. *Electromechanical Energy Conversion.* John Willey & Sons, Inc 1959.

[2] M.F.Russell and O.Hulot. *Improvements to Diesel Passenger Car Refinement.* SAE Technical Paper Series, No 981033.

[3] N.Guerrassi and P.Dupraz. *A Common Rail Injection System for High Speed Direct Injection Diesel Engines.* SAE Technical Paper Series, No 980803.

[4] J.E.Mardell and R.K.Cross. *An Integrated, Full Authority, Electrohydraulic Engine Valve and Diesel Fuel Injection System.* SAE Technical Paper Series, No 880602.

[5] J.P.Andrighetti and D.R.Gallup. *Design-Development of The Lucas CAV Multipoint Gasoline Injector.* SAE Technical Paper Sesries, No 870127.

[6] A.R.Stockner M.A.Flinn and F.A.Camplin. *Development of the IIEUI Fuel System-Integration of Design, Simulation, Test, and Manufacturing.* SAE Technical Paper Series, No 930271.

[7] J.S.Taylor P.S.Sangha H.M.D.Smith and Q.I.M.B.Akhtar. *Lucas EUI Actuator Solenoid: Investigation of Electromagnetics and Magnetic Materials Technologies.* Report No ADVE/S-E-0389, November 1994.

[8] D.H.Smith and D.A. Spinweber. *A General Model for Solenoid Fuel Injector Dynamics.* SAE Technical Paper Series, No 800508.

[9] D.S.Smith. *High Performance Actuators for Automotive and Aerospace Applications.* University of Sheffield, Department of Electronic and Electrical Engineering.

[10] Y.Okada K.Matsuda B.Nagai. *Application of a High Speed Solenoid Actuator to Linear Hydraulic Servo-Mechanism.* Conference proceedings on Fluid Control and Measurement in Tokio japan, Vol. I, pp. 83-88, Sept.85., Pergamon Press Oxford.

[11] J.G.Abrahamsen P.Ennemark F.Jensen. *A Novel Electromagnetic Model of A Linear Reluctance Actuator.* Proc. of ICEM'94, Paris, September 1994, Vol.II.

[12] J.P. Karadis and S.R. Turns. *Fast-Acting Electromagnetic Actuators - Computer Model Development and Verification.* SAE Technical Paper Series, No 820202.

[13] A.M. Pawlak and T.W. Nehl. *Transient Finite Element Modeling of Solenoid Actuators: The coupled Power Electronics, Mechanical and Magnetic Field Problem.* IEEE Transactions on Magnetics, Vol. 24, No 1, january 1988, pp.270.

[14] K.Y.Yuan S.C.Chen. *A New Algorithm for Coupled Solutions of Electric, Magnetic, and Mechanical Systems in Dynamic Simulation of Solenoid Actuators.* IEEE Transactions on Magnetics, Vol. 26, No 3, May 1990.

[15] Dr. B. Lequesne. *Dynamic Model of Solenoids under Impact Excitation Including Motion and Eddy Currents (Part II).* IEEE Transactions on Magnetics March 1990 Vol 26 No 2 pp. 1107-1116.

[16] k.Harmer G.W.Jewell and D.Howe. *Experimental Validation of a Finite Element Based Dynamic Simulation Technique for Fast-Acting, Short-Stroke, Linear Actuators.* Proceedings of The Second International Symposium on Linear Drives for Industry Applications (IEE of Japan), April 8-10,1998, Tokio.

[17] J.G. Zhu S.Y.R. Hui and V.S. Ramsden. *Discrete Modelling of Magnetic Cores Including Hysteresis Eddy current and Anomalous Losses.* IEE Proceedings Part A, Vol. 140, No 4, July 1993.

[18] H.C. Roters. *Electro-Magnetic Devices.* John Wiley & Sons, New-York 1961.

[19] T.J.E. Miller and M. McGilp. *PC-CAD for Switched Reluctance Drives.* IEE-EMD.

[20] T.J.E. Miller and M. McGilp. *PC-SRD 6.2 User's Manual.* Glasgow University SPEED Laboratory, 1995.

[21] T.J.E. Miller. *Switched Reluctance Motors and their Control.* Magna Physics Publishing, Clarendon Press, 1993, ISBN 1-881855-02-3.

[22] J.M.Stephenson and J.Corda. *Computation of torque and current in doubly salient reluctance motors from nonlinear magnetisation data.* Proc.IEE Vol 126 No.5 May 1979.

[23] V. Ostoviéc. *Dynamics of Saturated Electric Machines.* Springer-Verlag, ISBN 0-387-97079-7 or 3-540-97079-7.

[24] N.C.Chueng M.F.Rahman and K.W.Lim. *Position Estimation in Solenoid Actuators.* IEEE Transactions on Industry Applications, vol. 32, No 3, May/june 1996.

[25] Jeremiah O'Dwyer and Eberhard Vonhof. *Saturable Variable Reluctance Motor Simulation using Spline Functions.* Proc. ICEM 94, Vol 3, pp 176-180.

[26] J.V.Byrne and J.B. O'Dwyer. *Saturable Variable Reluctance Motor Simulation using Exponential Functions.* Proc. Intl. Conf. on stepping motors and systems, pp 11-16, Leeds, September 1976.

[27] J.M. Kokernak and D.A. Torrey. *Magnetic Circuit Model for the Mutually Coupled Switched Reluctance Machine.* IEEE IAS Conf. Proceedings. 1997, Vol 1, pp. 302-309.

[28] P. Materu and R. Krishnan. *Analytical Prediction of SRM Inductance Profile and Steady-State Average Torque.* IEEE IAS Conf. Proceedings 90.

[29] M.Tolikas J.H.Lang and J.L.Kirtley. *Algebraic Dual-Energy Magnetic Analysis with Application to Variable Reluctance Motor Design.* IEEE IAS conf. record, 1995, Vol 1, pp 412-418.

[30] H. Smith. *Spreadsheat Solenoid Modelling.* Internal Memo, Lucas Electrical and Electronics Systems, July 96.

[31] K.J.Binns P.J.Lawrenson and C.W.Trowbridge. *The Analytical and Numerical Solution of Electric and Magnetic Fields.* John Wiley & Sons, New-York 1992.

[32] F.W. Carter. *The Magnetic Field of the Dynamo-Electric Machine.* Journal IEE, 1926, pp. 1115-1138.

[33] H.Kober. *Conformal Representations.* Dover Publications, INC 1952.

[34] D.A. Torrey X.M. Niu and E.J. Unkauf. *Fast, Accurate Modeling of Variable-Reluctance Machine Magnetization Characteristics.* IEE Proceedings: Electric Power Applications, Jan 95, Vol. 142, No1,pp14-22.

[35] Longua Xu and Jianrong Bu. *Position Transducerless Control of a Switched Reluctance Motor Using Minimum Magnetizing Input.* IDC 97, Vol.36.

[36] Erkan Mese and David A. Torrey. *Sensorless Position Estimation for Variable-Reluctance Machines Using Artificial Neural Networks.* IDC 97, Vol.36.

[37] Prof.T.J.E. Miller and M.McGilp. *Nonlinear Theory of the switched reluctance motor for rapid computer-aided design.* IEE Proceedings Vol 137 Pt. B.

[38] G. Gallegos lópez P. Kjaer and T.J.E. Miller. *High-Grade Position Estimation for Switched Reluctance Motor Drive Using Flux Linkage/Current Correction Model.* IEEE IAS Conf. Proceedings 98.

[39] Vector Fields. *PC-OPERA, Reference/User Manuals.* Vector Fields Limited, Oxford 1996.

[40] P.J.Leonard R.J.Hill-Cottingham and D.Rodger. *3D Finite Element Models and External Circuits using the Aψ Scheme with Cuts.*

[41] C.Cossar and T.J.E. Miller. *Electromagnetic Testing of Switched Reluctance motors.* ICEM'92, Conf. Proceedings, Manchester,pp.470-474.

[42] P. Sangha and D. Rodger. *Design and Analysis of Voltage Fed Axisymmetric Actuators.* IEEE Transactions on Magnetics, Vol. 30, N0 5, pt. 2, September 1994, pp.3240.

[43] T. Tarhasaari A.Koski K. Forsman and L. Kettunen. *Hybrid Formulations for Eddy Current Problem With Moving Objects.* IEEE Transactions on Magnetics, Vol. 34, N0 5, September 1998, pp. 2660.

[44] N. Allen H.C. Lai D. Rodger and P.J. Leonard. *On the Validity of two A-ψ Finite Element formulations For Modelling Eddy current Problems With Velocity.* IEEE Transactions on Magnetics, Vol. 34, N0 5, September 1998, pp. 2535.

[45] R.Pohl. *Rise of Flux due to Impact Excitation: Retardation by Eddy Currents in Solid Parts.* Proc.IEE Paper No 776 S, February 1949 (96, part II, p. 57).

[46] R. Rüdenberg. *Transient Performance of electric Power Systems.* McGraw-Hill Book Company, INC 1950.

[47] N. Kesavamurthy and P.K. Rajagopalan. *Rise of Flux in Iron Core due to Impact Excitation.* Proc.IEE 1959, Vol 106 Part C, p.189.

[48] N. Kesavamurthy and P.K. Rajagopalan. *Effect of Eddy Currents on the Rise and Decay of Flux in Solid Magnetic Cores.* Proc.IEE 1962, 109 C, p.63.

[49] F. Brailsford and J.M. Burgess. *Internal Waveform Distorsion in Silicon-Iron Laminations For Magnetization at 50 c/s.* The Institution of Electrical Engineers, Monograph No 446 M, May 1961.

[50] J. Roberts. *Analogue Treatment of Eddy Currents and Magnetic Flux Penetration in Saturated Iron.* The Institution of Electrical Engineers, Monograph No 505, Feb. 1962.

[51] V. Subba Rao. *Eddy-Current Losses in Finite Sections of Solid Iron under Saturation.* Proc.IEE Vol 111 No 2 February 1964.

[52] V. Subba Rao. *Equivalent Circuit of Solid core for Impact Excitation Problems.* Proc.IEE Vol 111 No 2 February 1964.

[53] P. Silvester. *Eddy-Current Modes in Linear Solid-Iron Bars.* Proc. IEE, Vol. 112, No 8, August 1965.

[54] R.L.Stoll. *The Analysis of Eddy Currents.* Clarendon Press - Oxford 1974.

[55] S.Seely. *Electromechanical Energy Conversion.* Electrical and Electronic Engineering Series, McGraw-Hill Book Company, 1962.

[56] E.R. Laithwaite. *Magnetic Equivalent Circuits For Electrical Machines.* Proc.IEE Vol 114 No.11 November 1967.

[57] J. Tasker T.Collyer and A.Wearing. *Cogging Torques.* IEE conf. publication, 1997, No 444, pp 205-209.